UNIVERSIDAD DE VALENCIA
Departamento de Física Aplicada y Electromagnetismo

Simulations of Piezoelectric, Electronic and Optical Properties of Nanowires

By

Heruy Taddese Mengistu

Ph. D. Thesis supervised by:

Alberto García Cristóbal

Programa Oficial de Doctorado en Física 3026

Valencia, Spain
July 2016

ICMUV
INSTITUT DE CIÈNCIA DELS MATERIALS de la Universitat de València

Alberto García Cristóbal
Departmento de Física Aplicada e
Instituto de Ciencia de Materiales
Universidad de Valencia
Tfno.: +34 963543600
Fax: +34 963543633
Email: Alberto.Garcia@uv.es

D. ALBERTO GARCÍA CRISTÓBAL, Profesor Titular de Física Aplicada de la Universidad de Valencia,

CERTIFICA

Que la presente memoria, titulada Simulations of Piezoelectric, Electronic and Optical Properties of Nanowires, ha sido realizada bajo mi dirección en el Instituto de Ciencia de Materiales de la Universidad de Valencia (ICMUV) por D. HERUY TADDESE MENGISTU, y constituye su Tesis para optar al grado de Doctor en Física.

Y para que así conste, en cumplimiento de la legislación vigente, autorizo la presentación de la referida Tesis Doctoral a la Universidad de Valencia para su depósito y defensa, firmando el presente certificado

en Valencia, a 8 de julio de 2016,

Fdo.: García Cristóbal

This thesis was done within the framework of
Nanowiring: European Marie Curie Initial Training Network (ITN)

Abstract

Nanowires have attracted increasing interest due to their potential applications in electronics, optics and photonics. To understand the properties of nanowires, it is necessary to know their electronic structure. Moreover, it is important to understand how this electronic structure depends on the nanowire composition, crystal structure, orientation and geometry (shape and size), as well as on the eventual presence of some built-in deformation. The aim of this Ph.D. thesis is to develop theoretical models and computational methodologies that are realistic enough but also efficient to study piezoelectric, electronic and optical properties of nanowires.

In the first place, we have formulated a consistent two-dimensional (2D) theoretical framework to solve fully-coupled piezoelectric problems with translational symmetry. For these problems all transverse sections of the system are in identical state, and therefore the strain and piezoelectric fields depend only on the in-plane coordinates. With this sole input a very general procedure, able to encompass a wide range of in-plane geometries, compositions, loads, charges, and boundary conditions, is developed. This framework is here called the *generalized plane piezoelectric*, *GPP*, *problem*. This problem is expected to be a good approximation to three-dimensional (3D) systems with high aspect-ratio, such as the nanowires we are interested in. We have further developed an efficient and flexible numerical implementation by means of the finite element method. By means of it, we have examined the strain and piezoelectric fields in various cases of lattice-mismatched core-shell nanowires. In particular, a systematic comparison of the 2D problem with exact 3D calculations in long finite nanowires has been presented. The analysis shows that the behavior of the 3D solutions (strain and electric fields) at distances $\geq 1.25D$ from the end surfaces (where D is the largest size of the cross section) is very well approximated by the predictions of the 2D generalized plane approaches, in both non-piezoelectric and piezoelectric nanowires.

In a second research line, a theoretical model for the study of the single-particle electronic structure and linear optical absorption in semiconductor nanowires has

been developed. It is based on the envelope function approximation combined with the eight-band $\boldsymbol{k} \cdot \boldsymbol{p}$ (Kane-like) Hamiltonian. If there is a strain distribution in the system, its effects on the electronic structure are included by using the Bir-Pikus Hamiltonian. When the model is applied to nanowires with an axially symmetric (e.g., cylindrical) geometry made of zincblende and wurtzite and oriented along appropriate directions, it is possible to classify the electronic states in terms of the total (envelope plus intrinsic) angular momentum, what facilitates the computation and interpretation of the band structures. The resulting equations have been solved by means of an eigenfunction expansion methodology. The model has been applied to the study of the electronic structure and optical absorption of free-standing (InAs, GaAs, InN, ZnO) and core-shell (AlGaAs/GaAs and GaAs/InAs) nanowires. In each case, a detailed study has been made of the geometry-dependence of the energies and symmetries of the conduction and valence band states, as well as the polarization-dependent optical spectra. In the case of core-shell nanowires, we have investigated the influence of the shell thickness in both lattice-matched and lattice-mismatched nanowires. The impact of an applied uniaxial stress on ZnO nanowires has also been investigated. Various distinctive effects of the confinement have been found in all systems for the range of very narrow nanowires.

Acknowledgements

First of all, I would like to thank God the almighty for giving me the strength and courage to finish this work.

I would like to extend my gratitude to many people who helped to bring this research work to end. First of all, I would like to express my special appreciation and thanks to my academic advisor Prof. Alberto García-Cristóbal, you have been a tremendous mentor for me. I would like to thank you for encouraging my research and for allowing me to grow as a research scientist. Your advice on both research as well as on my career have been invaluable. I also would like to thank Prof. Giancarlo Cicero from Politecnico Torino for giving me the chance to work in his group. In addition, thank you Prof. Nuria Garro for the works in collaboration.

This journey would not have been possible without the support of my family. Thank you for encouraging me in all of my pursuits and inspiring me to follow my dreams. To my friends Aemro, Maribel, Ruben, Miranda, Jose, Felix, Amsalu, Yoseph, Dilu, Mintesinot, Atinafu, Addisu, Dagim, Fanuel, Tamene, Merid, Aynu and Aouchenni, thank you for supporting me through this entire process. Many thanks to Eleonora for helping me to settle housing and immigration processes.

Finally, I would also like to thank all the members of the NANOWIRING network. The group has been a source of collaboration and friendship. And last but not the least, I would like to thank the European Union for the financial support.

Table of Contents

Chapter 1

Introduction to Nanowires

Nanostructures have attracted steadily growing interest due to their fascinating properties, as well as their unique applications relative to their bulk counterparts[1–3]. The ability to generate such structures is now central to the advance of many areas in modern science and technology. There are a large number of new opportunities that could be realized by down-sizing currently existing structures or by making new types of nanostructures. The most successful examples are in microelectronics, where 'smaller' has always meant greater performance ever since the invention of transistors: higher density of integration, faster response, lower cost, and less power consumption.

In the past decades, significant progress has already been made in the field of zero-dimensional (0D) and two-dimensional (2D) nanostructures (i.e., quantum dots and quantum wells, respectively). Nanoscale one-dimensional (1D) materials also have stimulated great interest due to their importance in basic scientific research and potential technology applications[4,5]. Other than carbon nanotubes, 1D nanostructures (nanowires or quantum wires) are ideal systems for investigating the dependence of electrical transport and mechanical properties on size and dimensionality. They are expected to play an important role as both interconnects and functional components in the fabrication of nanoscale electronic and optoelectronic devices. Many unique and fascinating properties have already been proposed or demonstrated for this class of materials, such as higher luminescence efficiency[6], enhancement of thermoelectric figure of merit[7] and lowered lasing threshold[5].

Nanowires (NWs), by definition, are quasi-one-dimensional materials with a high aspect ratio (length/diameter ratio). Generally, they would have diameters of 1-200 nm and lengths up to several tens of micrometers. One immediate consequen-

ce is the increased surface-to-volume ratio in these nanostructures with respect to their bulk counterparts, leading to an increasingly important role of the surface effects on many system properties. Their one-dimensional geometry on the nanometer scale provides an extremely high surface area with a nanoscale radius of curvature and great mechanical flexibility. The geometry also provides anisotropic properties that should be interesting from the point of view of nanomaterial science and engineering. Their length makes them easy to manipulate for device fabrication. Owing to their nanoscale dimensions in the radial direction, they may exhibit size confinement effects that give them novel physical properties as compared to bulk materials. Consequently, semiconductor nanowires have attracted intense research interest within the past decade. A wide range of nanowire-based electronic and photonic devices have already been developed, including nanowire solar cells[1], photodetectors[2], light emitting diodes[3,4] and lasers[5,6].

Nanowires can be fabricated via a number of approaches. These are classified into two broad categories: top-down and bottom-up. Top-down methods begin with bulk material, from which nanowires are patterned via a combination of lithography and etching, for example using electron beam lithography and plasma etching or focused ion beam milling. Top-down methods have underpinned the microelectronics industry to date, but as the length scale of the devices shrink according to Moore's law, top-down methods become increasingly problematic. The lithographic and etching techniques are resolution limited, which makes it difficult to define smaller features, and the quality of the nanostructures diminishes. The etching and patterning processes introduce surface defects, which adversely affect nanostructure properties.

Bottom-up methods, on the other hand, involve the chemical synthesis of nanowires whose properties can be carefully controlled and tuned during growth. These nanowires are themselves building blocks, which ideally could be subsequently assembled into more complex nanoscale devices and architectures. This bottom-up paradigm offers opportunities for the fabrication of atomically precise, complex devices not possible with conventional top down technologies. Consequently, this paradigm is expected to lead the next generation of nanoscale electronics and optoelectronics. In many ways, bottom-up methods mimic the growth of living organisms, whereby macro-molecules are assembled into larger, more complex structures.

It is practical to distinguish between growth mechanisms and growth methods. The growth mechanism is the general phenomenon that explains how the thermodynamics and kinetics ensure that nanowires with a filament morphology and single crystallinity are obtained, while the growth methods refer to the experi-

mental chemical processes that employ the appropriate environment to synthesize the nanowires. So it is possible to utilize different chemical processes to grow different species of nanowires using the same growth mechanism. Among the different nanowire growth mechanisms, the vapor-liquid-solid mechanism (VLS) growth mechanism is so far the most versatile and extensively used to grow a variety of semiconducting nanowires. The VLS synthesis requires a catalyst. For nanowires, the best catalysts are liquid metal droplets or nanoclusters, which can either be self-assembled from a thin film by dewetting, or purchased in colloidal form and deposited on a substrate. The source enters these nanoclusters and begins to saturate them. On reaching supersaturation, the source solidifies and grows outward from the nanocluster. Simply turning off the source can adjust the final length of the nanowire. Morales and Lieber demonstrated that very small diameter Si and Ge nanowires (3-20 nm in diameter) and several μm in length could be grown using a pulsed laser to vaporize the semiconductor and Fe needed in the growth seed. This so-called pulsed laser vaporization (PLV) method provides nanometer-sized Fe particles and Si/Ge vapor supply.[14] It was this landmark paper that arouse worldwide research on semiconducting nanowires. Besides PLV method, several other methods such as metal-organic chemical vapor deposition (MOCVD), vapor transport using solid source or molecular precursors and physical evaporation have been used to provide the necessary vapor source to initiate the VLS growth. Several other solution phase synthesis growth mechanisms have also been explored to synthesize semiconductor nanowires such as the so-called solution-liquid-solid (SLS) mechanism and the super-critical fluid-liquid-solid mechanism. Other growth methods based on beam epitaxy of various kinds and not needing the presence of a catalyst have also been reported. Many NWs have been grown successfully with these methods, although without a clear understanding of the growth mechanism.

The composition, crystal structure,[15–17] growth direction,[18] and lateral shape and size[19,20] of the nanowires dominate their electronic and optical properties. In this work we are interested in studying from the theoretical and computational point of view some aspects of these influences for the case of small semiconductor nanowires (with a radius range of 1-120 nm). We will ultimately focus on nanowires with the crystalline structure of diamond, zincblende (ZB) and wurtzite (WZ), grown along different orientations. Two types of systems will be analyzed: simple, uniform nanowires composed of a single material (we will call these systems here *free-standing* nanowires) and bimaterial nanowires composed of a central core material surrounded coaxially by a shell made of a different material (*core-shell* nanowires).

Just for illustration purposes, below we will comment on the growth techniques

and possible applications of selected zincblende (ZB) and wurtzite (WZ) nanowires studied in this thesis.

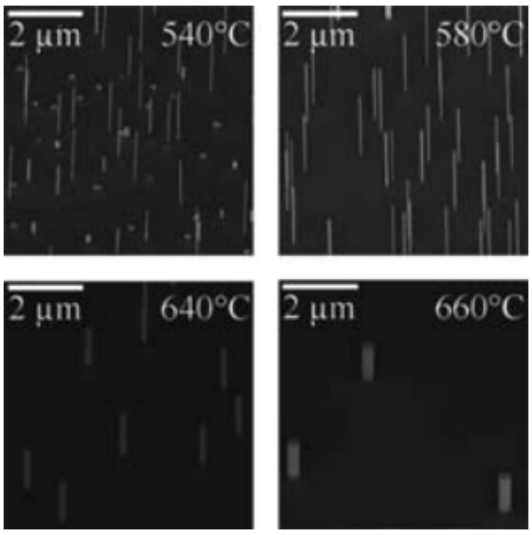

Figure 1.1: InAs nanowires grown on InP by MOCVD at various temperatures. Reproduced from Ref.[21].

1.1. Zincblende Nanowires

In this section we will review some growth techniques and possible applications of InAs and GaAs NWs.

1.1.1. InAs Nanowires

InAs exhibits a narrow (low temperature) energy band gap of 0.43 eV[22] and high electron mobility (33000 cm^2/V s). There have been several reports on the preparation of InAs nanowires[21,23–27]. For example, Mandl et al.[21] demonstrated growth of InAs nanowires by MOCVD without using Au or other metal particles as a catalyst. Instead, prior to growth, a thin SiO_x layer is deposited on the substrates. Figure 1.1 shows scanning electron microscopy (SEM) images of InAs nanowires on InP substrates. The wires are normal to the substrate and exhibit constant diameter along the entire height without any tapering. An increase in growth temperature results in an increase in wire diameter and a decrease in density.

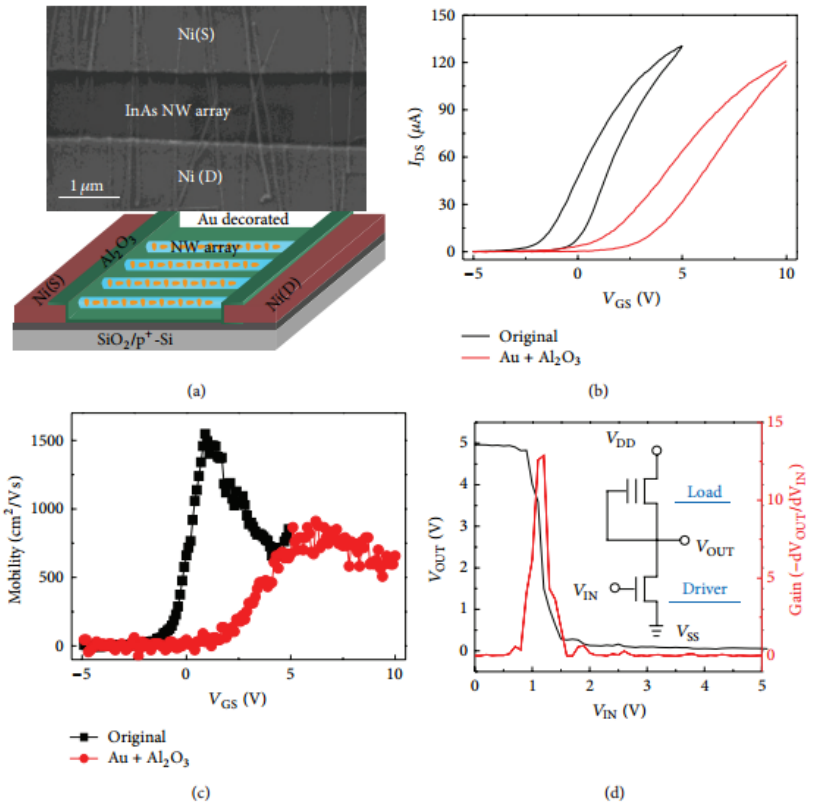

Figure 1.2: Application of the metal decoration method in transforming printed NW parallel array devices into E-mode and in the fabrication of NMOS inverters composed of E-mode and D-mode NWFETs. (a) SEM image and schematic illustration of an Au-cluster-decorated InAs NW array FET. (b) I_{DS}-V_{GS} curves before and after decoration. (c) Field-effect mobility of an InAs NW array FET before and after decoration. (d) The voltage transfer characteristics (red) and the corresponding gain (black) of the representative NMOS inverter. Reproduced from Ref. [28].

Applications as field-effect transistors (FETs)

The most intriguing property of III-V NWs lies in the possibility they offer to achieve ultrahigh carrier mobilities, making them highly attractive materials for next generation electronic devices. Especially, recent advances of NW contact printing technology have provided a useful platform for NW assembly and integration[29]. Combining the contact printing approach with the 'metal-cluster-decoration' method, one can obtain both depletion mode (D-mode) and enhancement mode (E-mode) FETs with parallel NW arrays at well-defined locations. Based on that, n-channel metal oxide-semiconductor (NMOS) inverters are constructed, with Au-decorated E-mode InAs NW FETs as the drivers and original D-mode InAs NW FET as the loads. Figure 1.2 shows the device structure of NW array FETs and the electrical characteristics of FETs as well as the NMOS

inverters[28]. The transfer curve in Figure 1.2(d) demonstrates clearly that the input signal is inverted with a high gain of ∼13. More importantly, due to the high electron mobility and low operating voltage of these InAs NWs, the static power dissipation of this III-V NW NMOS inverter is found to be as low as ∼4 μW, which is comparable to the lowest NW NMOS reported values and far lower than their planar counterparts.

1.1.2. GaAs Nanowires

GaAs is a direct band gap semiconductor with a band gap of 1.51 eV.[22] It has been grown in the nanowire form by laser-assisted catalytic growth[30,31], MBE[32,33], MOCVD[31,34,35] and template-guided approach[36]. In the MOCVD experiment reported in Ref.[37], growth temperatures between 380°C and 520°C are explored to understand the impact on morphology. Undoped or Si-doped GaAs(111) substrates are used with gold deposited as a thin layer (0.1, 1.0, and 10 nm). Figure 1.3 shows a view of the grown samples: Figures 1.3(a), (b) and (c) show the particle size distribution after the gold film is heated to 500°C for 10 min to allow the film to break into droplets. The SEM images on the right, (d), (e) and (f), present the corresponding GaAs nanowire morphology For a gold film thickness of 0.1 nm, the particle size ranges from 8 to 30 nm and the nanowires appear to be like needles with the diameter at the midpoint approximately 20-30 nm. The nanowires are not vertical, instead appear to be brush-like. When the Au film thickness is increased to 1 nm, the particle size distribution is $10-40$ nm and the nanowires are cylindrical with a diameter of $70-80$nm. Finally, for a 10 nm thick gold film, the resulting particles are fairly large at $80-500$ nm, yielding correspondingly thick nanowires of $70-400$ nm in diameter. In this case, as well as for 1 nm film, the nanowires are vertical on the substrate. In Fig. 1.3(f), the presence of gold particles at the tip is evident, which confirms the VLS mechanism.

Applications as Photodetectors and Sensors

In typical III-V NWs the large density of surface states pin the surface Fermi energy, limiting carrier mobility. These surface states can be 'passivated' by placing a shell around the nanowire. Dai and co-workers have developed a nanowire photodetector using a GaAs-AlGaAs core-shell nanowires.[38] The GaAs-AlGaAs systems are found to be significantly more sensitive as a photodetector than the GaAs nanowire alone. On the other hand, Peng and co-workers have developed single GaAs nanowires as microscopic coherent THz sensors.[39] These single GaAs

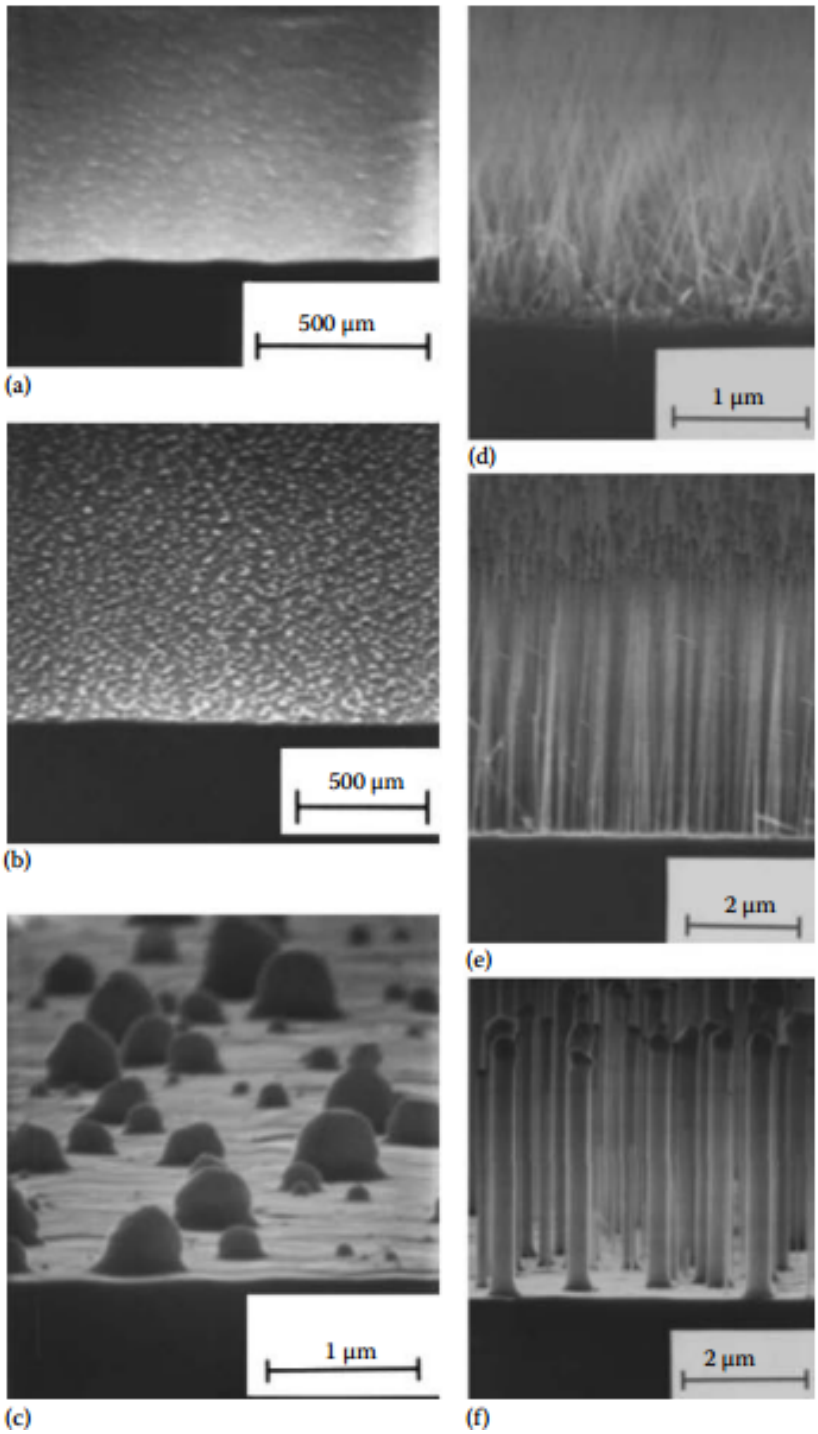

Figure 1.3: GaAs nanowires grown by MOCVD at 420°C. The effect of the gold film thickness on growth morphology is shown. The images on the left show particle size distribution for gold films of thickness: (a) 0.1 nm, (b) 1 nm, and (c) 10 nm. The images on the right show the corresponding nanowire growth results. Reproduced from Ref. [37].

nanowire detectors were fabricated using a direct laser lithographic technique and were even used as a spectrometer to measure the transmission spectrum of a 290 GHz low pass filter.

1.2. Wurtzite Nanowires

Here we discuss the properties and possible applications of InN and ZnO nanowires.

1.2.1. InN Nanowires

Group III-nitride usually grow with the wurtzite structure, although occasionally zincblende nanowires are obtained. These compound semiconductors exhibit unique electrical and optical properties, including high electron mobility, large saturation velocity, large electric breakdown field, extreme chemical stability, and direct energy band gap encompassing the entire solar spectrum[40–42]. Compared to other III-nitrides, InN exhibits the highest electron mobility ($\sim$ 4400 cm $^2V^{-1}s^{-1}$ at 300 K), the smallest effective mass, and the highest saturation velocity, making it an excellent candidate for a new generation of nanophotonic and nanoelectronic devices, including chip-level nanoscale lasers and high-speed field effect transistors. InN nanowires have been grown using quartz tube furnace[43], molecular beam epitaxy (MBE)[44,45] and MOCVD[46]. The resulting InN nanowires sometimes exhibit tapered morphology, with large variations in the wire diameter along the wire length, as shown in Fig. 1.4a.[47]. The poorly defined surface morphology severely limits the structural, optical and electrical properties of InN nanowires[48]. Recently, a novel growth technique using plasma-assisted MBE with *in situ* deposited In seeding layers has been shown to achieve non-tapered and nearly homogeneous InN nanowires.[49] In this growth process, a thin ($\sim$ 0.5 nm) In layer is first deposited on the substrate at elevated temperatures, prior to the introduction of nitrogen species. Shown in Fig. 1.4b, these wires are remarkably straight, with identical top and bottom sizes. They also exhibit a homogeneous height. The wires are well-separated, with the c-axis oriented vertically to the Si(111) substrate. With increasing growth temperature, InN nanowires generally exhibit reduced areal densities and larger diameters. Detailed high resolution TEM studies confirm that the entire wire exhibits a wurtzite crystal structure and is relatively free of dislocations.

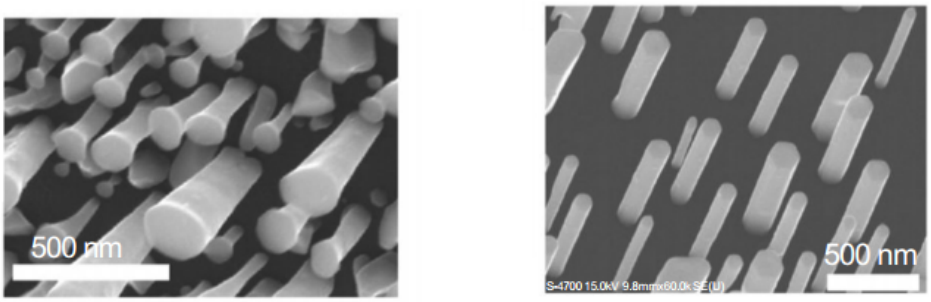

(a) (b)

Figure 1.4: SEM images of InN nanowires grown on Si(111) at 480 ^{o}C (a) without and (b) with the use of an *in situ* deposited In seeding layer. Reproduced from Ref.[49].

Methods	Diameter (nm)	Reference
MOCVD	40-400	[50]
MBE	20-80	[51]
MBE	50-150	[48]
VS	70-150	[52]

Table 1.1: Summary of growth methods and typical size of InN nanowires.

Applications as Light Emitting Diodes (LEDs)

To date, it has remained challenging to realize III-nitride nanowire LEDs beyond red color, due to the difficulty in In incorporation. In order to address this issue, Kishino et al.[53] developed the selective area growth of InGaN nanowires, wherein In incorporation can be enhanced by controlling the nanowire diameter. They have further demonstrated InGaN nanowire LEDs with an emission wavelength of $\sim$1.46 μm. Previously, the realization of electroluminescence emission from InN *p-i-n* diodes had been limited by the presence of surface electron accumulation and the lack of *p*-type conduction. The surface charge properties of InN nanowires can be well controlled by tuning the growth parameters. Under optimum growth conditions, the grown surfaces of nearly defect-free InN nanowires can be completely free of surface electron accumulation. Conduction of *p*-type conduction has been further demonstrated in Mg-doped InN nanowires.[54] The free hole concentration was measured to be $\sim 10^{17}$ cm^3, with a mobility around 100 cm^2 V s[54]. Illustrated in Fig. 1.5a is a single InN nanowire *p-i-n* diode, which was fabricated using standard e-beam lithography and metallization processes[55]. Shown in Fig. 1.5b is the I-V curve measured at 77 K. It is seen that the device has a turn on voltage around 0.7 V. The electroluminescence spectrum under a continuous wave

operation is shown in the inset, showing a peak emission peak around 0.7 eV (1.77 μm).

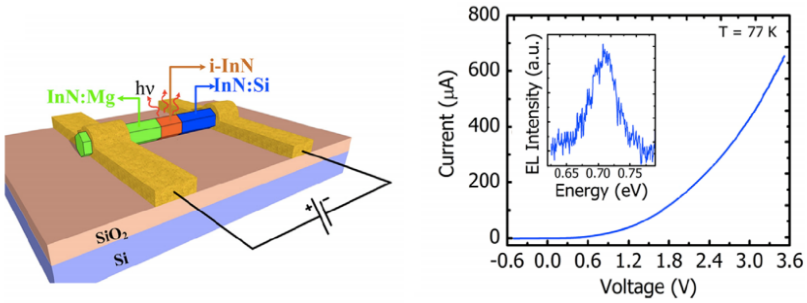

(a) (b)

Figure 1.5: (a) Schematic of the InN single nanowire LED. (b) *I-V* characteristics of the LED, with the inset showing the electroluminescence (EL) spectrum. Reproduced from Ref. [55].

1.2.2. ZnO Nanowires

ZnO is a direct band gap semiconductor with a band gap of about 3.4 eV.[56,57] The relatively large band gap of ZnO makes it a material with superior features, such as low electronic noise, high breakdown voltage, and good stability under high temperature and large electric field conditions. ZnO nanowires can be either grown independently or on certain substrates. A vertically aligned growth on a substrate has more advantages in many applications. The anisotropy of the ZnO crystal structure assists the growth of nanowires. The anisotropic growth of the nanowires takes place along the polar c-axis, in the [0001] direction[58]. The basal plane (0001) can be terminated in partially positive Zn lattice points or partially negative oxygen lattice points. The synthesis methods of ZnO nanowires reported so far can be roughly classified as vapor phase and solution phase. Vapor phase synthesis is probably the most extensively explored approach in the formation of 1D nanostructures[59]. A typical vapor phase synthesis method takes place in a closed chamber with a gaseous environment. Vapor species are first produced by evaporation, chemical reduction, and gaseous reaction. After that, the species are transferred and condensed onto the surface of a solid substrate. Generally, the vapor phase synthesis process is carried out at higher temperatures from 500 ^{o}C to 1500 ^{o}C and produces high-quality nanowires. Among the vapor phase synthesis methods, VLS[60] and MOCVD[61] are two of the most important methods for synthesis of ZnO nanowires. A SEM image of the ZnO NWs synthesized by the MOCVD method are shown in Fig. 1.6. The average length ranges from 1.5 to 10

μm and the diameters are in the range of 144 $\pm$ 8 nm. The overall average areal density of the ZnO NWs is 18.2 $\pm$ 0.5 NWs/μm^2.

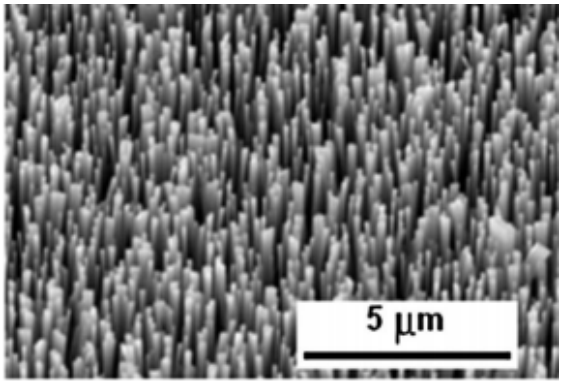

Figure 1.6: SEM image of ZnO NWs synthesized by MOCVD. Reproduced from Ref.[61].

Solution phase synthesis has some advantages when compared to vapor phase synthesis, such as low cost, low temperature, scalability, and ease of handling. Generally, solution phase reactions occur at relatively low temperatures ($< 200^oC$) compared to vapor phase synthesis methods. Thus, solution synthesis methods allow for a greater choice of substrates including inorganic and organic substrates. Due to these advantages, solution phase synthesis methods have attracted increasing interest. In solution phase synthesis, the growth process could be carried out in either an aqueous or organic solution or a mixture of the two[62,63].

Methods	Diameter (nm)	Reference
CVD	25	[64]
Electrodeposition	20-30	[65]
VLS	12-31	[66]

Table 1.2: Summary of growth methods and typical sizes of ZnO nanowires.

Applications as UV Detectors

UV detection is a promising optical application of ZnO nanowires[67]. The UV detector utilizes the change of the electric potential of the ZnO nanowires under UV irradiation. Chen et al.[68] constructed a UV photodetector by contacting a circular spiral structure containing ZnO nanowires with IrO_2 electrodes. The I-V measurement showed that the curve corresponded to the Schottky metal-semiconductor contacts with the photo-generated current reaching 5.11 $\times$ 10^{-7}A, under a bias voltage of 5 V (See Fig. 1.7) Li et al.[69] proposed a method of fabricating a ZnO

bridging nanowire structure exhibiting nanowatt UV detection. The electrodes were formed by the thick ZnO layers covering the Au-catalyst-patterned areas on the substrate, and the sensing elements consisted of the ultra long ZnO nanowires bridging the electrodes. The device exhibited drastic changes (10-105 times) in current under a wide range of UV irradiance ($10^{-8} - 10^{-2}$ W cm^{-2}). Moreover, the detector showed fast response (rise and decay times of the order of 1 s) to UV illumination in air.

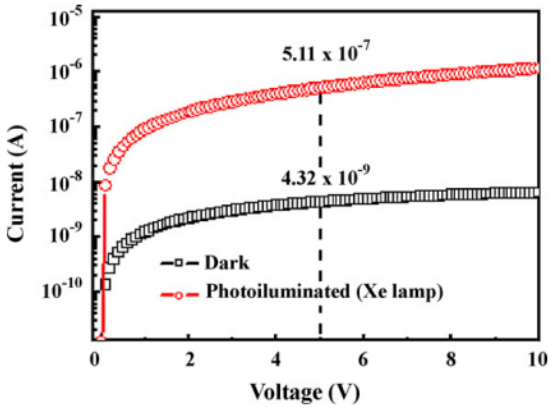

Figure 1.7: *I-V* characteristics of a ZnO NW photodetector in the dark and taken under illumination by a Xe lamp. Reproduced from Ref.[68].

Chapter 2

Theoretical Modeling of Nanowires

In Chapter 1 we have commented different properties and applications of nanowires. To better understand those and other properties, it is important to first understand the electronic and vibrational spectra of the nanowires. Particularly, one needs to understand how these properties are modified with respect to their bulk counterparts due to the new nanowire configurations (in size and shape), and to the presence of deformations (internal and external) and electric fields. Several theoretical methods have been developed in the past to study the electronic, piezoelectric and optical properties of semiconductor nanostructures. Below we summarize the most widely used approaches.

2.1. Overview of Theoretical Methods

The theoretical approaches available are roughly divided into two groups: atomistic and continuum methods. We examine them in turn.

2.1.1. Atomistic Methods

In the atomistic methodology the system structure is specified by giving the chemical signature and position of all the atoms in the system and modeling the interaction between them. From this common starting point several strategies are possible.

- *First principle* or *ab initio methods*: First principle calculations rely solely on the basic laws of physics. Specifically, this kind of calculations take into

account all the atoms and all types of interactions for the entire system to solve the Schrödinger equation. The advantage of this approach is that it is conceptually straightforward, starting from the basic laws of quantum mechanics, without the addition of adjustable parameters. The paradigm of the atomistic methods for the study of the electronic structure is the density functional theory (DFT).[70] However, the DFT has the following prominent difficulties: (i) the complexity of the calculation increases exponentially with the increase in the number of atoms; (ii) the bandgaps of insulating bulk solids are systematically underestimated; (iii) strongly correlated systems are poorly treated; and (iv) DFT, being an electronic ground state theory, does not offer a good scheme for the calculation of the electronic excitations. In the context of nanostructures, the *ab initio* methods are usually used only to calculate properties of very small size materials because larger sizes are computationally prohibitive. As such, it would be impractical to use first principle calculations to study elastic, electronic and optical properties in large nanowires. Thus, in the nanowire research field one can find DFT calculations only for small radius nanowires.[19,71–74]

- *Semi-empirical methods*: In these approaches the electronic structure of the material is also obtained by solving the one-particle Schrödinger equation with the explicit consideration of the atomic positions. However, contrary to the *ab initio* methods, the interactions between the atoms are now simulated by a set of judiciously chosen parameters, thus avoiding the need of self-consistent calculations. The computation time for the calculations is now much shorter than in the case of *ab initio* methods and their use has become very common in the study of all kinds of nanostructures. One of the most important semi-empirical atomistic methods is the tight-binding approach which has been widely used to study electronic and optical properties of nanowires[75–78]. One of the drawbacks of the semi-empirical methods is that they can be used only for systems whose parameters have been obtained previously, and that their accuracy is very sensitive to the quality of the parameters used.

- *Molecular dynamics simulations*: In this approach one predicts the trajectories of a system of classical particles using the Newton's laws of motion. Using the positions and momenta, one can investigate a variety of problems including thermal transport at the atomic level. The only required inputs are the atomic structure and an appropriate potential model describing the interatomic interactions. The interatomic potentials are usually obtained by fitting experimental data or results of *ab initio* calculations. Some of the

potentials more widely used include the Stillinger-Weber[79] and Tersoff potentials[80]. The drawback of molecular dynamics simulations is that they can only be used for systems where the appropriate interatomic potentials have been developed. The required computational resources and the size of the systems amenable to simulations are other limitations. In the field of nanowires, molecular dynamics simulations have recently been used to study the thermal conductivity of both free-standing and core-shell nanowires[81–83].

2.1.2. The Nanostructure as a Piezoelectric Continuum Body

Unlike the atomistic methods, the continuum approaches assume that matter is continuously distributed over the material body in a (piece-wise) homogeneous manner. There are several models that treat the system of ions as a continuum. The most popular among them is the linear piezoelectric continuum model, which is able to accommodate a wide range of phenomenology described by internally or externally induced strain and electric fields with both static and dynamic behaviors. The dynamic problem is intimately associated with the acoustic phonon modes of the system. In this work we will only focus on the static piezoelectric fields.

Under small deformation and electrostatic approximation the strain ε_{ij} and electric field E_m are expressed as:

$$\varepsilon_{ij} = \frac{1}{2}\left(\frac{\partial u_i}{\partial x_j} + \frac{\partial u_j}{\partial x_i}\right) , \tag{2.1a}$$

$$E_m = -\frac{\partial \phi}{\partial x_m} . \tag{2.1b}$$

where u_i and ϕ are the elastic displacement and electric potential respectively. Moreover, under the regime of linear piezoelectricity, the stress tensor σ_{ij} and the piezoelectric displacement vector D_m can be expressed in terms of ε_{ij} and E_m by means of the standard linear constitutive relations:[84,85]

$$\sigma_{ij} = C_{ijkl}\varepsilon_{kl} - e_{nij}E_n , \tag{2.2a}$$

$$D_m = e_{mkl}\varepsilon_{kl} + \epsilon_{mn}E_n , \tag{2.2b}$$

where C_{ijkl} is the elastic stiffness tensor, e_{nij} is the piezoelectric tensor, and ϵ_{mn} is the dielectric tensor.

In this approach the distribution of strain and electric field are obtained by minimization of the energy stored in the medium or, equivalently, by solving the equations of equilibrium:

$$\frac{\partial \sigma_{ij}}{\partial x_i} = -f_j \,, \tag{2.3a}$$

$$\frac{\partial D_m}{\partial x_m} = \rho \,, \tag{2.3b}$$

where f_j and ρ are body forces and electric charge respectively.

The continuum models are attractive since the computational resources required for their solution do not scale in general with the system size. Besides, the continuum models admit analytical solutions in highly idealized situations that serve to develop an intuition that can be useful for the treatment of more complicated structures. The continuum piezoelectric approach has been used in the field of nanostructures to study piezoelectric properties of quantum dots[86,87]. In the field of nanowires most of the efforts have been addressed to model single nanowire nanogenerators.[88,89] Recently, it has also been used to study the lattice-mismatch induced piezoelectric properties of core-shell nanowires[90–92] using direct three-dimensional calculations.

In Chapter 3 of this thesis we will present a theoretical two-dimensional formulation for solving the fully-coupled piezoelectric problem in wire-like systems.

2.1.3. The Envelope Function Approach to the Electronic Structure

We have also included in the category of the continuum methods the envelope function approach for the calculation of the electronic structure, to be described below in detail. Although this approach is ultimately based on the Schrödinger equation containing the potential created by all the atoms in the system, and therefore is not strictly a continuum method, the processing of that equation within the envelope function theory leads to an envelope function equation where the details of the microscopic potential are in part merged into a set of kinetic parameters and in part transformed into a smoother potential profile. In the simplest version, the electron is assumed to move in vacuum with a renormalized mass (known as effective mass) that depends on the material. The problem is then reduced to the calculation of a slowly varying field (the envelope function) whose computational requirements are essentially independent of the nanostructure size. This makes the method computationally very efficient and therefore more preferable than atomistic

calculations, particularly in nanostructures which are composed of a large number of atoms. In the field of nanowires, it has been used recently to study electronic and optical properties of both free-standing and core-shell nanowires[18,93–95]. In this thesis we have also chosen the envelope function approximation to calculate the electronic structure of nanowires.

The envelope function approach is usually implemented in combination with a description of the underlying bandstructure of the constituent bulk materials as provided by the $\boldsymbol{k}\cdot\boldsymbol{p}$ method. In the rest of the chapter we explain in further detail: (i) first, the $\boldsymbol{k} \cdot \boldsymbol{p}$ method and its specific form in zincblende and wurtzite crystals, (ii) then, the envelope function approximation as applied to one-dimensional systems, and (iii) finally, the fundamentals of the matter-radiation interaction necessary to describe the optical response in nanostructures.

2.2. The $\boldsymbol{k} \cdot \boldsymbol{p}$ Method

In this section, we will start with the general formulation of the $\boldsymbol{k}\cdot\boldsymbol{p}$ method and then the special formulations for bulk zincblende and wurtzite crystal structures will follow.

2.2.1. General formulation

The standard starting point for the study of the electronic structure of a solid is the Schrödinger-Pauli equation:[96]

$$H\Psi(\boldsymbol{r}) \equiv \left\{ \frac{\boldsymbol{p}^2}{2m_0} + V_0(\boldsymbol{r}) + \frac{1}{2}\,\frac{1}{m_0^2 c_0^2}\,[\boldsymbol{\nabla} V_0(\boldsymbol{r}) \times \boldsymbol{p}] \cdot \boldsymbol{s} \right\} \Psi(\boldsymbol{r}) = E\Psi(\boldsymbol{r}), \qquad (2.4)$$

where m_0 is the free electron mass and c_0 is the speed of light in vacuum. The linear momentum operator is $\boldsymbol{p} = -i\hbar\boldsymbol{\nabla}$. The solution of the eigenvalue problem (2.4) for the Hamiltonian operator H yields the energies E and associated wavefunctions $\Psi(\boldsymbol{r})$ of the electron in the solid. The potential $V_0(\boldsymbol{r})$ results from two contributions: first, there is the superposition of the potentials of the ion cores forming the solid, and second, there is the self-consistent potential that accounts for the electron-electron interaction in a mean field sense.[97] The third term in the Hamiltonian H in (2.4) represents the so-called spin-orbit interaction, where $\boldsymbol{s} = \frac{\hbar}{2}\boldsymbol{\sigma}$ is the electron spin operator, which is expressed in terms of the Pauli matrices $\boldsymbol{\sigma} = (\sigma_x, \sigma_y, \sigma_z)$.[96]

Therefore, $\Psi(\boldsymbol{r})$ is actually an spinor wave function:

$$\langle \boldsymbol{r} \mid \Psi \rangle \equiv \Psi(\boldsymbol{r}) = \begin{pmatrix} \Psi_\uparrow(\boldsymbol{r}) \\ \Psi_\downarrow(\boldsymbol{r}) \end{pmatrix} = \underbrace{\Psi_\uparrow(\boldsymbol{r})}_{\equiv\langle \boldsymbol{r} \mid \Psi_\uparrow \rangle} |\uparrow\rangle + \underbrace{\Psi_\downarrow(\boldsymbol{r})}_{\equiv\langle \boldsymbol{r} \mid \Psi_\downarrow \rangle} |\downarrow\rangle = \langle \boldsymbol{r}| \left(|\Psi_\uparrow\rangle |\uparrow\rangle + |\Psi_\downarrow\rangle |\downarrow\rangle \right) ,$$

where $|\uparrow\rangle$ and $|\downarrow\rangle$ indicate basic spinors corresponding to $s_z = +\frac{1}{2}$ and $s_z = -\frac{1}{2}$, respectively.

In the case of a cristalline solid that we are interested in here, the potential $V_0(\boldsymbol{r})$ reflects, among other system-specificic symmetries, the translational invariance of the crystal, and is therefore periodic, i.e.,

$$V_0(\boldsymbol{r} + \boldsymbol{R}_n) = V_0(\boldsymbol{r}) \qquad \text{for any Bravais lattice vector } \boldsymbol{R}_n \quad . \tag{2.5}$$

Then, by using the Bloch theorem, the solution of (2.4) can be written as a Bloch function:

$$\begin{aligned} \Psi(\boldsymbol{r}) \to \Psi_{b\boldsymbol{k}}(\boldsymbol{r}) &= \frac{1}{\sqrt{\mathcal{V}}}\, e^{i\boldsymbol{k}\cdot\boldsymbol{r}}\, u_{b\boldsymbol{k}}(\boldsymbol{r}) \,, \\ E \to E_b(\boldsymbol{k}) &\,, \end{aligned} \tag{2.6}$$

where $\mathcal{V} = N\Omega$ is the crystal volume, formed by N unit cells of volume Ω, $\boldsymbol{k}$ is a wave vector inside the first Brillouin zone (BZ), and b is the *b*and index. The energy spectrum of the crystal is organized in the band structure $\{E_b(\boldsymbol{k})\}_b$. The Bloch function $\Psi_{b\boldsymbol{k}}(\boldsymbol{r})$ consists of a plane wave $e^{i\boldsymbol{k}\cdot\boldsymbol{r}}$ multiplied by a (Bloch) amplitude $u_{b\boldsymbol{k}}$ (which is itself a spinor function) showing the same lattice periodicity as $V_0(\boldsymbol{r})$:

$$u_{b\boldsymbol{k}}(\boldsymbol{r} + \boldsymbol{R}_n) = u_{b\boldsymbol{k}}(\boldsymbol{r}) \qquad \forall\, \boldsymbol{R}_n \quad . \tag{2.7}$$

Note that, if we require the Bloch functions to be orthonormal:

$$\int_{\mathcal{V}} d\boldsymbol{r}\, \Psi^*_{b\boldsymbol{k}}(\boldsymbol{r})\, \Psi_{b'\boldsymbol{k}'}(\boldsymbol{r}) = \delta_{bb'}\, \delta_{\boldsymbol{k}\boldsymbol{k}'} \quad ,$$

we are lead to the following orthogonality relation for the Bloch amplitudes with the same $\boldsymbol{k}$:

$$\int_{\Omega} d\boldsymbol{r}\, u^*_{b\boldsymbol{k}}(\boldsymbol{r})\, u_{b'\boldsymbol{k}}(\boldsymbol{r}) = \Omega\, \delta_{bb'} \quad .$$

Substituting (2.6) into (2.4) yields, for each $\boldsymbol{k}$, the following eigenvalue problem

for the Bloch amplitudes and energies:

$$H(\boldsymbol{k})\, u_{b\boldsymbol{k}}(\boldsymbol{r}) = E_b(\boldsymbol{k})\, u_{b\boldsymbol{k}}(\boldsymbol{r}) \quad , \tag{2.8}$$

with

$$H(\boldsymbol{k}) = \frac{(\boldsymbol{p}+\hbar\boldsymbol{k})^2}{2m_0} + V_0(\boldsymbol{r}) + \frac{1}{2}\,\frac{1}{m_0^2c_0^2}\,(\boldsymbol{p}+\hbar\boldsymbol{k})\cdot[\boldsymbol{s}\times\boldsymbol{\nabla}V_0(\boldsymbol{r})] \quad , \tag{2.9}$$

which can be conveniently rewritten as:

$$H(\boldsymbol{k}) = H(\boldsymbol{0}) + \frac{\hbar}{m_0}\boldsymbol{k}\cdot\left\{\boldsymbol{p} + \frac{1}{2}\,\frac{1}{m_0c_0^2}\,[\boldsymbol{s}\times\boldsymbol{\nabla}V_0(\boldsymbol{r})]\right\} + \frac{\hbar^2\boldsymbol{k}^2}{2m_0} \quad , \tag{2.10}$$

with

$$H(\boldsymbol{0}) = \underbrace{\frac{\boldsymbol{p}^2}{2m_0} + V_0(\boldsymbol{r})}_{\equiv H^{(0)}} + \underbrace{\frac{1}{2}\,\frac{1}{m_0^2c_0^2}\,[\boldsymbol{\nabla}V_0(\boldsymbol{r})\times\boldsymbol{p}]\cdot\boldsymbol{s}}_{\equiv H_{\mathrm{so}}} \quad . \tag{2.11}$$

The usual way to deal with (2.8) starts by formally expanding $u_{b\boldsymbol{k}}$ in terms of a (yet unspecified) orthonormal basis of lattice periodic spinor functions $\{\chi_h\}_h$:

$$u_{b\boldsymbol{k}}(\boldsymbol{r}) = \sum_h c_{b\boldsymbol{k},h}\,\chi_h(\boldsymbol{r})\,, \tag{2.12}$$

which allows to reformulate (2.8) as a matrix eigenvalue problem,

$$\sum_{h'} H_{hh'}(\boldsymbol{k})\, c_{b\boldsymbol{k},h'} = E_b(\boldsymbol{k})\; c_{b\boldsymbol{k},h}\,, \tag{2.13}$$

with:

$$H_{hh'}(\boldsymbol{k}) = H^{(0)}_{hh'} + \Delta_{hh'} + \frac{\hbar}{m_0}\,\boldsymbol{k}\cdot(\boldsymbol{p}_{hh'} + \boldsymbol{\vartheta}_{hh'}) + \frac{\hbar^2\boldsymbol{k}^2}{2m_0}\,\delta_{hh'}\,, \tag{2.14}$$

where[1]

$$H^{(0)}_{hh'} = \left\langle \chi_h \left| H^{(0)} \right| \chi_{h'} \right\rangle\,, \tag{2.15}$$

$$\Delta_{hh'} = \langle \chi_h \left| H_{\mathrm{so}} \right| \chi_{h'} \rangle = \frac{1}{2}\,\frac{1}{m_0^2c_0^2}\,\langle \chi_h \left| [\boldsymbol{\nabla}V_0(\boldsymbol{r})\times\boldsymbol{p}]\cdot\boldsymbol{s} \right| \chi_{h'} \rangle\,, \tag{2.16}$$

[1]The following compact definition is used hereafter for the matrix elements of operators $\mathcal{O}(\boldsymbol{r},\boldsymbol{p},\boldsymbol{s})$ between lattice periodic spinor functions:

$$\langle \chi_h \left| \mathcal{O}(\boldsymbol{r},\boldsymbol{p},\boldsymbol{s}) \right| \chi_{h'} \rangle = \int_\Omega d\boldsymbol{r}\, \chi_h^*(\boldsymbol{r})\, \mathcal{O}(\boldsymbol{r},\boldsymbol{p},\boldsymbol{s})\, \chi_{h'}(\boldsymbol{r})\,.$$

$$\boldsymbol{p}_{hh'} = \langle \chi_h \left| \boldsymbol{p} \right| \chi_{h'} \rangle \ , \tag{2.17}$$

$$\boldsymbol{\vartheta}_{hh'} = \frac{1}{2} \frac{1}{m_0 c_0^2} \ \langle \chi_h \left| [\boldsymbol{s} \times \boldsymbol{\nabla} V_0(\boldsymbol{r})] \right| \chi_{h'} \rangle \ . \tag{2.18}$$

Note that the matrix $H_{hh'}(\boldsymbol{k})$ depends parametrically on the wavevector $\boldsymbol{k}$. Therefore, *a priori*, its diagonalization for all the values of $\boldsymbol{k}$ would provide the band structure $\{E_b(\boldsymbol{k})\}_b$ throughout the Brillouin zone as well as the corresponding eigenvectors $c_{b\boldsymbol{k},h}$ which determine the Bloch amplitudes $u_{b\boldsymbol{k}}$. However, we must immediately point out that the matrix $H_{hh'}(\boldsymbol{k})$ has infinite dimension, its specification requiring therefore an infinite number of parameters: $H^{(0)}_{hh'}$, $\Delta_{hh'}$, $\boldsymbol{p}_{hh'}$ and $\boldsymbol{\vartheta}_{hh'}$. In practice it is necessary to find a procedure that allows to transform (2.13) into an effective eigenvalue problem of finite dimension. One systematic procedure to achieve this is provided by the so-called $\boldsymbol{k} \cdot \boldsymbol{p}$ method.[98] It can be summarized as follows:

- In the first place, we formally assume that we have *solved* the eigenvalue problem (2.8) at $\boldsymbol{k} = 0$ (Γ-point), in the absence of spin-orbit interaction:

$$H^{(0)} \, u_b(\boldsymbol{r}) = \left[\frac{\boldsymbol{p}^2}{2m_0} + V_0(\boldsymbol{r}) \right] \, u_b(\boldsymbol{r}) = E_b^{(0)} \, u_b(\boldsymbol{r}) \, , \tag{2.19}$$

  and know the corresponding energies $E_b^{(0)} \equiv E_b^{(0)}(\boldsymbol{k} = \boldsymbol{0})$ and Bloch (spinor) functions $u_b(\boldsymbol{r}) \equiv u_{b\,\boldsymbol{k}=\boldsymbol{0}}(\boldsymbol{r})$. The Γ-point Bloch functions $\{u_b\}_b$ form an orthogonal basis for the space of lattice periodic functions, and therefore it seems convenient to choose in the above treatment for $\{\chi_h\}_h$ the set of orthonormal functions

$$\{\chi_h\}_h \quad \longrightarrow \quad \left\{ U_b \equiv \frac{1}{\sqrt{\Omega}} \, u_b \right\}_b \quad .$$

  This leads to a simplified form of (2.14):

$$H_{hh'}(\boldsymbol{k}) \longrightarrow H_{bb'}(\boldsymbol{k}) = \left(E_b^{(0)} + \frac{\hbar^2 \boldsymbol{k}^2}{2m_0} \right) \, \delta_{bb'} + \Delta_{bb'} + \frac{\hbar}{m_0} \, \boldsymbol{k} \cdot (\boldsymbol{p}_{bb'} + \boldsymbol{\vartheta}_{bb'}) \ , \tag{2.20}$$

  where the Hamiltonian matrix has now a convenient structure: there is a diagonal contribution, a $\boldsymbol{k}$-independent non-diagonal spin-orbit matrix,[2] and a term linear in $\boldsymbol{k}$. The $\boldsymbol{k}$-dependent effect of the spin-orbit interaction, carried on by the term $\boldsymbol{k} \cdot \boldsymbol{\vartheta}_{bb'}$, is usually much smaller than that of the term

[2] Sometimes it is desirable (see Sec. 2.2.2) to start the $\boldsymbol{k} \cdot \boldsymbol{p}$ method by assuming that we know

$\boldsymbol{k}\cdot\boldsymbol{p}_{bb'}$. Therefore, although not strictly necessary, in practice it is commonly neglected, and only the term $\boldsymbol{k}\cdot\boldsymbol{p}_{bb'}$ is retained.

Since the basis functions U_b are proportional to the Γ-point Bloch functions, their symmetry properties can be anticipated by making use of group theory. More specifically, they can be labeled by the irreducible representations of the crystal point group. This symmetry information results of utmost importance to identify the set of independent parameters in the matrix $H_{bb'}(\boldsymbol{k})$.

- The Hamiltonian matrix (2.20) is still of infinite dimension. However, at this point one realizes that in the majority of the studies on direct gap semiconductors, the energy range of interest locates around the fundamental band gap at the Γ-point of the band structure. Under these conditions, only the set of bands adjacent to that gap needs an explicit and accurate description, whereas the remaining bands, energetically remote, play a secondary role in the final configuration of the band structure around the gap. The $\boldsymbol{k}\cdot\boldsymbol{p}$ method implements formally these considerations as follows. First, the set of basis functions $\{U_b\}_b$ is divided into two subsets: The functions in subset A, $\{U_a\}_{a=1}^{N_A}$, correspond to the bands that we want to describe explicitly and accurately (bands A); the remaining basis functions form the subset R and are associated to the remote bands (bands R). Then, by means of the perturbation theory introduced by Löwdin,[96,99] the eigenvalue equation associated to (2.20) is approximated by a finite matrix problem:

$$\sum_{a'=1}^{N_A} \tilde{H}_{aa'}(\boldsymbol{k})\,\tilde{C}_{a'} = E\,\tilde{C}_a \quad (a,a'=1,\ldots,N_A) \quad , \tag{2.22}$$

with eigenvalues $E \to E_a(\boldsymbol{k})$ describing the approximate dispersion of the A bands around the Γ-point, and eigenvectors $\tilde{C}_{a'} \to \tilde{C}_{a\boldsymbol{k},a'}$ being the coeffi-

---

the solutions of the Γ-point problem including the spin-orbit interaction:

$$\left(H^{(0)} + H_{\rm so}\right)\,u_b(\boldsymbol{r}) = \left[\frac{\boldsymbol{p}^2}{2m_0} + V_0(\boldsymbol{r}) + H_{\rm so}\right]\,u_b(\boldsymbol{r}) = E_b\,u_b(\boldsymbol{r})\,, \tag{2.21}$$

leading to the Hamiltonian matrix:

$$H_{bb'}(\boldsymbol{k}) = \left(E_b + \frac{\hbar^2\boldsymbol{k}^2}{2m_0}\right)\,\delta_{bb'} + \frac{\hbar}{m_0}\,\boldsymbol{k}\cdot(\boldsymbol{p}_{bb'} + \boldsymbol{\vartheta}_{bb'}) \quad .$$

cients of the approximate expansion of the corresponding Bloch amplitude:

$$u_{a\boldsymbol{k}}(\boldsymbol{r}) \approx \sum_{a'=1}^{N_A} \tilde{C}_{a\boldsymbol{k},a'}\, u_{a'}(\boldsymbol{r}) \quad . \tag{2.23}$$

The new Hamiltonian matrix elements $\tilde{H}_{aa'}(\boldsymbol{k})$, which differ from those in (2.20) by a renormalization correction due to the influence of the functions of type R, can be conveniently expressed in terms of a reduced number of parameters.

It must be noticed, however, that the partition of $\{U_b\}_b$ between the subsets A y R is not unique, and depending on the way it is performed, the $\boldsymbol{k}\cdot\boldsymbol{p}$ method gives rise to different models, with different degrees of complexity and accuracy. Of course, the truncation leading to the approximation (2.22) entails a reduction in the $\boldsymbol{k}$-range of validity of the approximation that depends ultimately on the number of bands retained in the subset A.

In the simplest case, i.e., when we can focus on a well isolated band, then $N_A = 2$. If, in addition, the spin-orbit can be neglected, the corresponding two Bloch amplitudes can be taken as:

$$\{ \quad U_{a=1}(\boldsymbol{r}) = U(\boldsymbol{r})\ |\uparrow\rangle \quad , \quad U_{a=2}(\boldsymbol{r}) = U(\boldsymbol{r})\ |\downarrow\rangle \quad \} \quad ,$$

where $U(\boldsymbol{r})$ is here a scalar function. Then we have

$$u_{a\boldsymbol{k}}(\boldsymbol{r}) \simeq u_a(\boldsymbol{r}) = \sqrt{\Omega}\, U_a(\boldsymbol{r}) \quad a = 1, 2 \quad ,$$

and the energy band adopts a doubly degenerate parabolic dispersion relation,

$$E_a(\boldsymbol{k}) \simeq \tilde{H}_{a,a}(\boldsymbol{k}) = E^{(0)} + \frac{\hbar^2 \boldsymbol{k}^2}{2m^*} \quad a = 1, 2 \quad ,$$

where m^* is the effective mass parameter, which for simplicity here has been taken to be isotropic.

In Sec. 2.2.2 and 2.2.3 below (and in Appendix A) we detail the eight-band ($N_A = 8$) models that, in combination with the envelope function approximation (see Sec. 2.3), are used in this work to simulate the electronic structure of zincblende and wurtzite nanowires.

To take into account the effect of a uniform deformation of the crystal (represented by a constant strain tensor ε_{ij}) on its electronic structure, one usually adopts the method proposed by G. L. Bir and G. E. Pikus.[100–102] This method

shows that, in order to include the influence of small deformations, we must just add to the $\boldsymbol{k}\cdot\boldsymbol{p}$ Hamiltonian in (2.22) a new term that depends linearly with ε_{ij} (Bir-Pikus Hamiltonian): $\tilde{H}_{aa'} \to \tilde{H}_{aa'} + H^{\mathrm{BP}}_{aa'}(\varepsilon_{ij})$. The parameters that weigh the impact of each component of the strain on the electronic structure are the so-called (electronic) deformation potentials (see Appendix A).

2.2.2. Application to Zincblende Semiconductors

In the band structure of zincblende semiconductors the fundamental gap is direct and occurs at $\boldsymbol{k} = 0$ (Γ-point). Around that gap there are a doubly degenerate conduction band and three doubly degenerate valence bands. In the neighborhood of Γ, this set of bands is well separated from the remaining, lower and higher, bands. Therefore, the situation is favorable to treat the band structure with a $\boldsymbol{k}\cdot\boldsymbol{p}$ Hamiltonian in which the above mentioned bands are retained as A-bands (then $N_A = 8$), and the associated Γ-point Bloch amplitudes are taken as basis functions, $\{U_a\}_{a=1}^{8}$.

A more precise picture of the Bloch states around the gap can be obtained by taking advantage of the information provided by the tight-binding method. This method shows that, in the absence of spin-orbit interaction, the highest valence band states result essentially from the combination of the p-orbitals of the constituent atoms (both anion and cation). The corresponding (spinor) Bloch amplitudes will be schematically denoted:

$$\{|X\rangle|\uparrow\rangle, |X\rangle|\downarrow\rangle\} \quad , \quad \{|Y\rangle|\uparrow\rangle, |Y\rangle|\downarrow\rangle\} \quad , \quad \{|Z\rangle|\uparrow\rangle, |Z\rangle|\downarrow\rangle\} \quad ,$$

where $\langle \boldsymbol{r} \,|\, X\rangle$ is a normalized periodic function which behaves under the symmetry operations of the tetrahedral group as an atomic p_x function. Similar considerations apply to $\langle \boldsymbol{r} \,|\, Y\rangle$ and $\langle \boldsymbol{r} \,|\, Z\rangle$. Note that the coordinates (x, y, z) refer to the cubic crystallographic axes:

$$(x, X) \parallel [100] \quad , \quad (y, Y) \parallel [010] \quad , \quad (z, Z) \parallel [001] \quad ,$$

and $|\uparrow\rangle$ and $|\downarrow\rangle$ indicate basic spinors with the spin quantized along $Z \parallel [001]$. On the other hand, the conduction band states at Γ are formed from the s-orbitals of the constituent atoms. The corresponding (spinor) Bloch amplitudes will be schematically denoted:

$$\{|S\rangle|\uparrow\rangle, |S\rangle|\downarrow\rangle\} \quad ,$$

where $\langle \boldsymbol{r} \mid S \rangle$ is a normalized periodic function which behaves under the symmetry operations of the tetrahedral group in the same way as an atomic s function.

Let us consider now the matrix elements of the $\boldsymbol{k}\cdot\boldsymbol{p}$ Hamiltonian at $\boldsymbol{k} = 0$, $H^{(0)} + H_{\rm so}$, within the subspace generated by the above states. The spin-independent Hamiltonian matrix $H^{(0)}$ is diagonal with matrix elements:

$$\left\langle X \left| H^{(0)} \right| X \right\rangle = \left\langle Y \left| H^{(0)} \right| Y \right\rangle = \left\langle Z \left| H^{(0)} \right| Z \right\rangle =: E_v \quad ,$$

$$\left\langle S \left| H^{(0)} \right| S \right\rangle =: E_c \quad .$$

On the other hand, the spin-orbit matrix $\Delta_{aa'} = \langle U_a \left| H_{\rm so} \right| U_{a'} \rangle$ appearing in (2.20) is not diagonal in the basis introduced above. However, group theory considerations indicate that the non-zero matrix elements are all expressable in terms of a single parameter Δ_0:[102]

$$\langle X \left| H_{\rm so} \right| Y \rangle = \frac{1}{2} \frac{1}{m_0^2 c_0^2} \frac{\hbar}{2} \left\langle X \left| [\boldsymbol{\nabla} V_0(\boldsymbol{r}) \times \boldsymbol{p}]_z \right| Y \right\rangle =: -i \frac{1}{3} \Delta_0 \quad .$$

The fact that the $\boldsymbol{k} \cdot \boldsymbol{p}$ Hamiltonian at $\boldsymbol{k} = 0$, $H^{(0)} + H_{\rm so}$, is not diagonal is in itself not a critical issue, but in the case of zincblende crystals it is possible to construct, by exploiting the analogy in symmetry between the wave functions $|X\rangle$, $|Y\rangle$ and $|Z\rangle$ and the atomic orbitals p_x, p_y and p_z, an alternative basis in which $H^{(0)} + H_{\rm so}$ will be diagonal.[103] In a first step one transforms the original basis as follows:

$$\left\{ \begin{array}{l} |X\rangle \\ \\ |Y\rangle \\ \\ |Z\rangle \end{array} \right\} \Longrightarrow \left\{ \begin{array}{ll} -\dfrac{1}{\sqrt{2}} |X + iY\rangle & =: |l = 1, l_z = +1\rangle \\ \\ |Z\rangle & =: |l = 1, l_z = 0\rangle \\ \\ +\dfrac{1}{\sqrt{2}} |X - iY\rangle & =: |l = 1, l_z = -1\rangle \end{array} \right\} \quad . \tag{2.24}$$

Note that these states behave under the tetrahedral group symmetry operations in the same way as the spherical harmonics Y_{l,l_z} do, and therefore we assign to them the notation $\{|l, l_z\rangle |\uparrow\rangle, |l, l_z\rangle |\downarrow\rangle\}$. The spin-orbit interaction is not yet diagonal in this basis but, by following a standard procedure of atomic physics, one can construct from it another basis, denoted $\{|j, j_z\rangle\}$, as detailed in Table 2.1, in which $H^{(0)} + H_{\rm so}$ is diagonal.[104] The states $|j, j_z\rangle$ are eigenstates of the total angular momentum $\hat{\boldsymbol{j}} = \hat{\boldsymbol{l}} + \hat{\boldsymbol{s}}$ and its z projection $\hat{j}_z$.

The explicit form of the eight-band $\boldsymbol{k} \cdot \boldsymbol{p}$ Hamiltonian matrix in this basis is

given in Appendix A. This Hamiltonian was first introduced by E. O. Kane for the study of narrow gap semiconductors and is often called the Kane Hamiltonian.[105] The Hamiltonian at $\boldsymbol{k}=0$, $H^{(0)}+H_{\rm so}$, is diagonal in the basis $\{U_a\}$ of Table 2.1, with the following eigenvalues and eigenfunctions:

$$\begin{array}{lll} E_c(=E_v+E_g) & \rightarrow \{\,|U_1\rangle\,,|U_2\rangle\,\} & (\,\Gamma_6^{\rm c}\,) \\ E_v & \rightarrow \{\,|U_3\rangle\,,|U_6\rangle\,\}\,\{\,|U_4\rangle\,,|U_5\rangle\,\} & (\,\Gamma_8^{\rm v}\,) \\ E_v-\Delta_0 & \rightarrow \{\,|U_7\rangle\,,|U_8\rangle\,\} & (\,\Gamma_7^{\rm v}\,) \end{array} \quad , \tag{2.25}$$

where E_g is the fundamental gap of the material. In the language of group theory, the Γ Bloch states are basis states of the following irreducible representations of the double group associated to the zincblende point group: Γ_6 , Γ_8 and Γ_7. In (2.25) the auxiliary label $\lambda=c,v$ indicates whether the states correspond to the conduction or valence bands. As said above, to include the effect of strain on the band structure, we follow the formulation of Bir and Pikus,[102]. The eight-band zincblende Bir-Pikus Hamiltonian can also be found in Appendix A.

Zincblende [001]

	$\lvert U_a\rangle$		$\lvert\lambda,j,j_z\rangle$	$j_z(a)$
$\lvert{\rm c}\,+\rangle$	$\lvert U_1\rangle$	$\lvert iS\rangle\,\lvert\uparrow\rangle$	$\lvert{\rm c},\frac{1}{2},+\frac{1}{2}\rangle$	$+\frac{1}{2}$
$\lvert{\rm c}\,-\rangle$	$\lvert U_2\rangle$	$\lvert iS\rangle\,\lvert\downarrow\rangle$	$\lvert{\rm c},\frac{1}{2},-\frac{1}{2}\rangle$	$-\frac{1}{2}$
$\lvert{\rm hh}\,+\rangle$	$\lvert U_3\rangle$	$\lvert 1,+1\rangle\,\lvert\uparrow\rangle$	$\lvert{\rm v},\frac{3}{2},+\frac{3}{2}\rangle$	$+\frac{3}{2}$
$\lvert{\rm lh}\,+\rangle$	$\lvert U_4\rangle$	$\sqrt{\frac{1}{3}}\,\lvert 1,+1\rangle\,\lvert\downarrow\rangle+\sqrt{\frac{2}{3}}\,\lvert 1,0\rangle\,\lvert\uparrow\rangle$	$\lvert{\rm v},\frac{3}{2},+\frac{1}{2}\rangle$	$+\frac{1}{2}$
$\lvert{\rm lh}\,-\rangle$	$\lvert U_5\rangle$	$\sqrt{\frac{1}{3}}\,\lvert 1,-1\rangle\,\lvert\uparrow\rangle+\sqrt{\frac{2}{3}}\,\lvert 1,0\rangle\,\lvert\downarrow\rangle$	$\lvert{\rm v},\frac{3}{2},-\frac{1}{2}\rangle$	$-\frac{1}{2}$
$\lvert{\rm hh}\,-\rangle$	$\lvert U_6\rangle$	$\lvert 1,-1\rangle\,\lvert\downarrow\rangle$	$\lvert{\rm v},\frac{3}{2},-\frac{3}{2}\rangle$	$-\frac{3}{2}$
$\lvert{\rm so}\,+\rangle$	$\lvert U_7\rangle$	$+\sqrt{\frac{2}{3}}\,\lvert 1,+1\rangle\,\lvert\downarrow\rangle-\sqrt{\frac{1}{3}}\,\lvert 1,0\rangle\,\lvert\uparrow\rangle$	$\lvert{\rm v},\frac{1}{2},+\frac{1}{2}\rangle$	$+\frac{1}{2}$
$\lvert{\rm so}\,-\rangle$	$\lvert U_8\rangle$	$-\sqrt{\frac{2}{3}}\,\lvert 1,-1\rangle\,\lvert\uparrow\rangle+\sqrt{\frac{1}{3}}\,\lvert 1,0\rangle\,\lvert\downarrow\rangle$	$\lvert{\rm v},\frac{1}{2},-\frac{1}{2}\rangle$	$-\frac{1}{2}$

Table 2.1: Basis of Γ-point Bloch amplitudes to be used for the representation of the eight-band $\boldsymbol{k}\cdot\boldsymbol{p}$ Hamiltonian for zincblende semiconductors. Several alternative notations are provided. We have introduced the auxiliary label λ =c,v, depending on whether the state corresponds to the conduction band or valence band, respectively. In the last column we single out the *intrinsic* angular momentum projection $j_z(a)$ associated to each basis element U_a, $a=1,\ldots,8$.

Figures 2.1a and 2.1b show the band structures around the Γ-point for bulk InAs and GaAs, respectively, as calculated with the eight-band $\boldsymbol{k}\cdot\boldsymbol{p}$ Hamiltonian presented above. The material parameters used are available in Appendix E.1. The

fourfold degenerate valence band edge is split away of Γ into two doubly degenerate bands. The curvature of one of them is significantly larger (and is therefore called light-hole, lh, band) than the other (heavy-hole, hh, band). The lower (doubly degenerate) valence band is well separated due to spin-orbit interaction (and is therefore called the spin-orbit split-off, so, band) The doubly-degenerate conduction band is not purely parabolic (especially for InAs) due to the coupling between the conduction and valence bands included in the Kane Hamiltonian. When comparing the dispersion curves along the [0001] and [111] directions, it is observed that the dispersion is not symmetrical, as a consequence of the directions not being exactly equivalent. This can have some consequences on the behavior of the NW electronic structure for different NW orientations, as will be seen in Chapter 5.

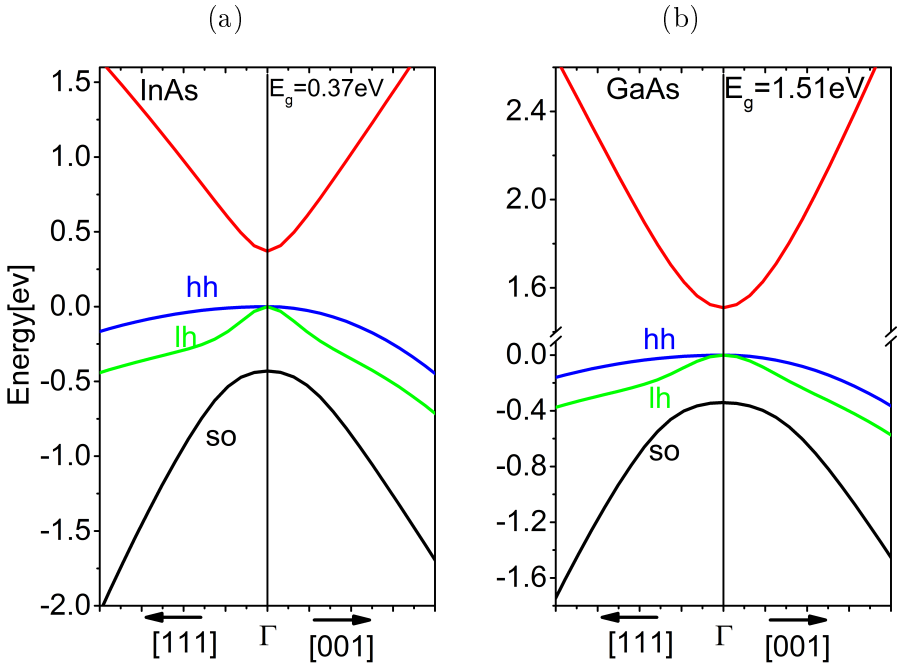

Figure 2.1: Band structure of (a) InAs and (b) GaAs around the Γ-point, along the [001] and [111] directions, as calculated with the eight-band $\boldsymbol{k} \cdot \boldsymbol{p}$ Hamiltonian.

2.2.3. Application to Wurtzite Semiconductors

The construction of the $\boldsymbol{k} \cdot \boldsymbol{p}$ Hamiltonian for wurtzite semiconductors follows a procedure analogous to the one presented for zincblende crystals. As in that case, a sufficient description of the bands around the Γ-point direct bandgap can be constructed from the bands formed by the linear combination of the anion and

cation s and p valence atomic functions. In the absence of spin-orbit interaction those Γ-point Bloch amplitudes are again denoted:

$$\{|S\rangle|\uparrow\rangle, |S\rangle|\downarrow\rangle, |X\rangle|\uparrow\rangle, |Y\rangle|\uparrow\rangle, |Z\rangle|\uparrow\rangle, |X\rangle|\downarrow\rangle\ |Y\rangle|\downarrow\rangle, |Z\rangle|\downarrow\rangle\} \quad .$$

Now, given the anisotropic crystalline structure, the spin-independent Hamiltonian matrix $H^{(0)}$ is diagonal with matrix elements:[101]

$$\left\langle X\left|H^{(0)}\right|X\right\rangle = \left\langle Y\left|H^{(0)}\right|Y\right\rangle =: E_v + \Delta_1 \quad , \quad \left\langle Z\left|H^{(0)}\right|Z\right\rangle =: E_v \quad ,$$

$$\left\langle S\left|H^{(0)}\right|S\right\rangle =: E_c \quad ,$$

and all the non-zero values of the nondiagonal spin-orbit matrix $\Delta_{aa'}$ can be expressed in terms of two parameters, Δ_2 and Δ_3:[101]

$$\langle X|H_{\rm so}|Y\rangle = \frac{1}{2}\frac{1}{m_0^2c_0^2}\frac{\hbar}{2}\langle X|[\boldsymbol{\nabla}V_0(\boldsymbol{r})\times\boldsymbol{p}]_z|Y\rangle =: -i\frac{1}{3}\Delta_2 \quad .$$

$$\langle Y|H_{\rm so}|Z\rangle = \frac{1}{2}\frac{1}{m_0^2c_0^2}\frac{\hbar}{2}\langle Y|[\boldsymbol{\nabla}V_0(\boldsymbol{r})\times\boldsymbol{p}]_x|Z\rangle =: -i\frac{1}{3}\Delta_3 \quad .$$

Unlike in the case of zincblende, in wurtzite materials it is not possible to find a material-independent form for the basis of eigenvectors of the Hamiltonian $H^{(0)} + H_{\rm so}$. Therefore, to study the nanowires whose crystal structure is of wurtzite type we have preferred to work out the $\boldsymbol{k}\cdot\boldsymbol{p}$ Hamiltonian in the basis representation$\{|l, l_z\rangle|\uparrow\rangle, |l, l_z\rangle|\downarrow\rangle\}$ introduced in (2.24), despite not rendering $H^{(0)} + H_{\rm so}$ to a diagonal form. The basis is detailed again in Table 2.2. Althought these basis functions do not have a well defined intrinsic angular momentum, as in the representation chosen for the zincblende, they still have a well defined projection, $j_z = l_z + s_z$, which is therefore a convenient quantum number. This fact has great importance for the modeling of the NW electronic structures, and will be discussed in depth in Chapter 4.

The $\boldsymbol{k}\cdot\boldsymbol{p}$ Hamiltonian for wurtzite semiconductors was originally derived in a series of articles by E. I.Rashba, V. I. Sheka and G. E. Pikus and hence is sometimed named the Rashba-Sheka-Pikus (RSP) Hamiltonian.[106] In a later work, S. L. Chuang and C. S. Chang[101] have repeated the derivation of the Hamiltonian, expressing it in an updated notation that is currently more widespread. We report it in the Appendix A. The energies of the band edges and corresponding eigenfunctions can be obtained by diagonalization of the $\boldsymbol{k}\cdot\boldsymbol{p}$ Hamiltonian at $\boldsymbol{k} = 0$,

Wurtzite [0001]

$\|U_a\rangle$		$\|\lambda, l_z, s_z\rangle$	$j_z(a)$
$\|U_1\rangle$	$\|iS\rangle \ \|\uparrow\rangle$	$\left\|\mathrm{c}, \ 0, +\frac{1}{2}\right\rangle$	$+\frac{1}{2}$
$\|U_2\rangle$	$\|iS\rangle \ \|\downarrow\rangle$	$\left\|\mathrm{c}, \ 0, -\frac{1}{2}\right\rangle$	$-\frac{1}{2}$
$\|U_3\rangle$	$\|1, +1\rangle \ \|\uparrow\rangle$	$\left\|\mathrm{v}, +1, +\frac{1}{2}\right\rangle$	$+\frac{3}{2}$
$\|U_4\rangle$	$\|1, -1\rangle \ \|\uparrow\rangle$	$\left\|\mathrm{v}, -1, +\frac{1}{2}\right\rangle$	$-\frac{1}{2}$
$\|U_5\rangle$	$\|1, \ 0\rangle \ \|\uparrow\rangle$	$\left\|\mathrm{v}, \ 0, +\frac{1}{2}\right\rangle$	$+\frac{1}{2}$
$\|U_6\rangle$	$\|1, +1\rangle \ \|\downarrow\rangle$	$\left\|\mathrm{v}, +1, -\frac{1}{2}\right\rangle$	$+\frac{1}{2}$
$\|U_7\rangle$	$\|1, -1\rangle \ \|\downarrow\rangle$	$\left\|\mathrm{v}, -1, -\frac{1}{2}\right\rangle$	$-\frac{3}{2}$
$\|U_8\rangle$	$\|1, \ 0\rangle \ \|\downarrow\rangle$	$\left\|\mathrm{v}, \ 0, -\frac{1}{2}\right\rangle$	$-\frac{1}{2}$

Table 2.2: Basis of Γ-point Bloch amplitudes to be used for the representation of the eight-band $\boldsymbol{k}\cdot\boldsymbol{p}$ Hamiltonian for wurtzite semiconductors. In the last column we single out the *intrinsic* angular momentum projection $j_z(a)$ associated to each basis element U_a, $a = 1, \ldots, 8$.

$H^{(0)} + H_{\mathrm{so}}$:[101]

$$\begin{aligned}
E_{\Gamma_7^{\mathrm{c}}} \quad &\rightarrow \{\, |U_1\rangle, |U_2\rangle \,\} && (\,\Gamma_7^{\mathrm{c}}\,) \\
E_{\Gamma_9^{\mathrm{v}}} \quad &\rightarrow \{\, |U_3\rangle, |U_6\rangle \,\} && (\,\Gamma_9^{\mathrm{v}}\,) \\
E_{\Gamma_{7,+}^{\mathrm{v}}} \quad &\rightarrow \{\, a\,|U_4\rangle + b\,|U_8\rangle, b\,|U_5\rangle + a\,|U_7\rangle \,\} && (\,\Gamma_{7,+}^{\mathrm{v}}\,) \\
E_{\Gamma_{7,-}^{\mathrm{v}}} \quad &\rightarrow \{\, b\,|U_4\rangle - a\,|U_8\rangle, -a\,|U_5\rangle + b\,|U_7\rangle \,\} && (\,\Gamma_{7,-}^{\mathrm{v}}\,)
\end{aligned} \quad , \tag{2.26}$$

where

$$\begin{aligned}
E_{\Gamma_7^{\mathrm{c}}} &\equiv E_c \\
E_{\Gamma_9^{\mathrm{v}}} &\equiv E_v + \Delta_1 + \Delta_2 \\
E_{\Gamma_{7,+}^{\mathrm{v}}} &\equiv E_v + \frac{\Delta_1 - \Delta_2}{2} + \sqrt{\left(\frac{\Delta_1 - \Delta_2}{2}\right)^2 + 2\Delta_3^2} \\
E_{\Gamma_{7,-}^{\mathrm{v}}} &\equiv E_v + \frac{\Delta_1 - \Delta_2}{2} - \sqrt{\left(\frac{\Delta_1 - \Delta_2}{2}\right)^2 + 2\Delta_3^2}
\end{aligned} \quad , \tag{2.27}$$

and

$$a = \frac{E_{\Gamma_{7,+}^{\mathrm{v}}}}{\sqrt{E_{\Gamma_{7,+}^{\mathrm{v}}}^2 + 2\Delta_3^2}}, \quad b = \frac{\sqrt{2}\Delta_3}{\sqrt{E_{\Gamma_{7,+}^{\mathrm{v}}}^2 + 2\Delta_3^2}}\,. \tag{2.28}$$

Note that the eigenvectors depend on the material through the parameters E_c, E_v,

Δ_1, Δ_2 and Δ_3. The eight-band wurtzite Bir-Pikus Hamiltonian can also be found in Appendix A.

Figures 2.2a and 2.2b show the band structures around the Γ-point for bulk InN and ZnO, respectively, as calculated with the eight-band $\boldsymbol{k} \cdot \boldsymbol{p}$ Hamiltonian presented above. The material parameters used are available in Appendix E.2. Note that now the bandstructure consists of a single conduction band and three separated valence bands. However, we see that the ordering of the symmetries of the valence band edges is again material-dependent. The corresponding group representations of valence bands for InN are $\Gamma_{7,+}$,Γ_9 and $\Gamma_{7,-}$ while for ZnO are Γ_9,$\Gamma_{7,+}$ and $\Gamma_{7,-}$. The topmost valence band edge in InN has dominant $|Z\rangle$-symmetry while in ZnO it has dominant $(|X\rangle, |Y\rangle)$-symmetry. We also notice that the dispersion of the valence bands is rather anisotropic.

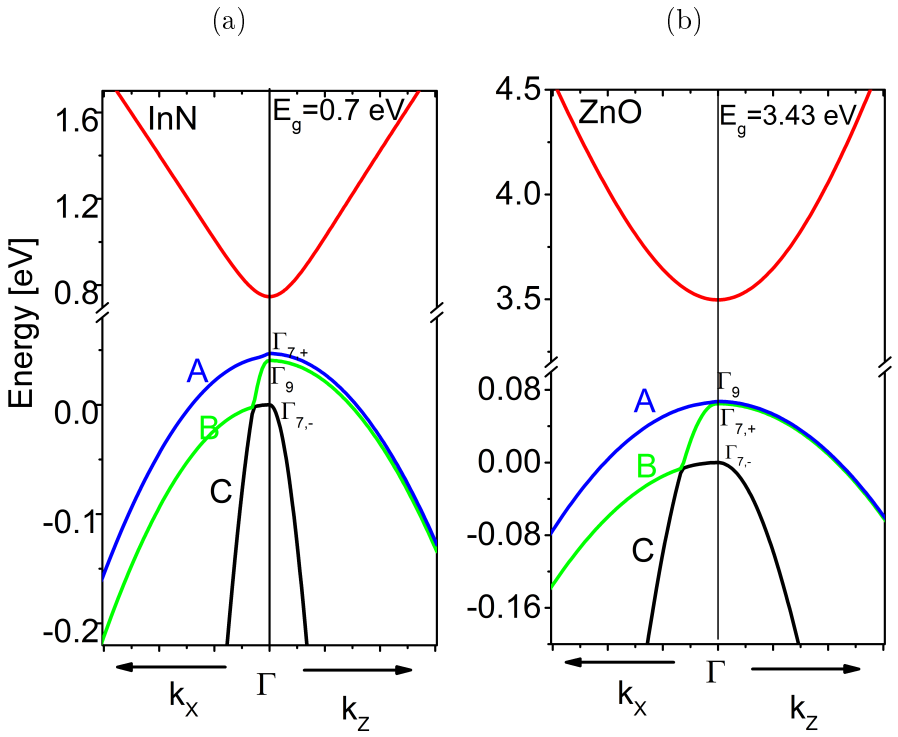

Figure 2.2: Band structure of (a) InN and (b) ZnO around the Γ-point, as calculated with the eight-band $\boldsymbol{k} \cdot \boldsymbol{p}$ Hamiltonian.

2.3. The Envelope Function Approximation

The envelope function approximation is a very useful theoretical tool for the study of the electronic structure of crystals perturbed by some kind of disturbance, e.g. the presence of a defect, an electric and/or magnetic field, etc... [107] Likewise, it has also proved useful in the study of the electronic structure of heterostructures in the quantum confinement regime.[108,109] In this work, we will use the envelope function approximation for studying the electronic structure of nanowires, including the effects of confinement, deformation and internal fields.

The first part of this section will cover the most fundamental aspects of the method and then we discuss its application to the heterostructure problem. Although the envelope function approximation has a long history and an extensive literature, we will follow here the works of M. G. Burt, which in our opinion present it in the most logical and rigorous way.[109–111]

2.3.1. General Formulation

When the crystalline Hamiltonian H introduced in Sec. 2.2.1 is disturbed by the presence of an additional potential $W(\boldsymbol{r})$, the Schrödinger-like equation to be solved becomes:

$$[H + W(\boldsymbol{r})]\,\Psi(\boldsymbol{r}) = E\Psi(\boldsymbol{r})\,. \tag{2.29}$$

M. G. Burt has approached this problem by first formally expanding the electron wave function $\Psi(\boldsymbol{r})$ in terms of a (yet unspecified) orthonormal basis of lattice-periodic (spinor) functions $\{\chi_h\}_h$ (as in Sec. 2.2.1) as follows:[109,110]

$$\Psi(\boldsymbol{r}) = \sum_h F_h(\boldsymbol{r})\,\chi_h(\boldsymbol{r}) \quad . \tag{2.30}$$

The expansion (2.30) is mathematically rigorous and unique provided that the functions $\{F_h(\boldsymbol{r})\}_h$ appearing as 'coefficients' have a spatial Fourier spectrum limited to the first BZ, i.e.,

$$F_h(\boldsymbol{r}) = \frac{1}{\mathcal{V}} \sum_{\boldsymbol{k}\in \mathrm{BZ}} F_{h,\boldsymbol{k}}\, e^{i\boldsymbol{k}\cdot\boldsymbol{r}} \quad .$$

It is due to the separation of scales between χ_h and F_h that the later are called the envelope functions. Burt has developed in a series of papers a mathematically rigorous and exact framework that allows to transform the eigenvalue problem (2.29) into an infinite system of coupled integro-differential equations for the set

of envelope functions $\{F_h\}$ (exact envelope function theory).[109–111] This system is in general rather complicated and, although in principle is amenable to (heavy) numerical solution, in practice nobody tries to follow this approach. It is more interesting to use the Burt envelope function theory instead as a starting point for the development of further approximations.

One way to further simplify the envelope function theory is to follow the same methodology as in the $\boldsymbol{k}\cdot\boldsymbol{p}$ approach sketched in Sec. 2.2.1. More specifically, one chooses as basis functions $\{\chi_h\}_h$ the restricted set of Γ-point Bloch amplitudes corresponding to the bands in the energy range of interest (A-bands),

$$\{\chi_h\}_h \quad \longrightarrow \quad \left\{U_a \equiv \frac{1}{\sqrt{\Omega}}\, u_a\right\}_{a=1}^{N_A} \quad .$$

The envelope functions are now denoted as $\{F_h\}_h \to \{F_a\}_{a=1}^{N_A}$, and the electron wave function becomes:[3]

$$\Psi(\boldsymbol{r}) = \sum_{a=1}^{N_A} F_a(\boldsymbol{r}) U_a(\boldsymbol{r}) \quad . \tag{2.31}$$

Note that, if we require the set of electron wavefunctions $\{\Psi_\lambda\}$ to be orthonormal:

$$\int_{\mathcal{V}} d\boldsymbol{r}\; \Psi^*_\lambda(\boldsymbol{r})\, \Psi_{\lambda'}(\boldsymbol{r}) = \delta_{\lambda\lambda'} \quad ,$$

the orthonormality of $\{U_a\}$ implies the following integral relation for the envelope functions:

$$\sum_a \int_{\mathcal{V}} d\boldsymbol{r}\; \frac{1}{\sqrt{\Omega}}\, F^*_{\lambda,a}(\boldsymbol{r})\, \frac{1}{\sqrt{\Omega}}\, F_{\lambda',a}(\boldsymbol{r}) = \delta_{\lambda\lambda'} \quad .$$

By using (2.31), it can be shown that, under certain reasonable requirements on the smoothness of the potential W and the envelope functions $\{F_a\}$, the later can be approximated by the solutions of the more manageable eigenvalue problem:[109]

$$\sum_{a'} \left[\tilde{H}_{aa'}(-i\boldsymbol{\nabla}) + W(\boldsymbol{r})\, \delta_{aa'}\right] F_{a'}(\boldsymbol{r}) = E F_a(\boldsymbol{r})\,. \tag{2.32}$$

[3] Sometimes written as a multicomponent wavefunction:

$$\Psi(\boldsymbol{r}) = \sum_{a=1}^{N_A} F_a(\boldsymbol{r})\, |U_a\rangle \quad .$$

The differential operators $\tilde{H}_{aa'}(-i\boldsymbol{\nabla})$ are obtained from the $\boldsymbol{k}\cdot\boldsymbol{p}$ Hamiltonian matrix elements $\tilde{H}_{aa'}(\boldsymbol{k})$ introduced in (2.22) simply by making the formal substitution $\boldsymbol{k}\to -i\boldsymbol{\nabla}$. Therefore, in (2.32) all the information about the underlying crystal is encoded in the parameters of the associated $\boldsymbol{k}\cdot\boldsymbol{p}$ Hamiltonian, and only the perturbing potential W appears explicitly. If, in addition, the crystal presents a state of inhomogeneous deformation, it has been shown that its influence can be accounted for within this framework by enlarging (2.32) with the corresponding Bir-Pikus Hamiltonian in terms of the associated strain field $\varepsilon_{ij}(\boldsymbol{r})$.[112,113]

This level of description of the electronic structure of the perturbed crystal can be called the multiband $(\boldsymbol{k}\cdot\boldsymbol{p})$ envelope function approximation.

Clearly, if $W=0$ one recovers the bulk results presented in Sec. 2.2.1:

$$F_{\lambda,a'} \quad\to\quad F_{a\boldsymbol{k},a'} = \frac{1}{\sqrt{N}}\, e^{i\boldsymbol{k}\cdot\boldsymbol{r}}\, \tilde{C}_{a\boldsymbol{k},a'}\,,$$

$$\Psi_\lambda(\boldsymbol{r}) \quad\to\quad \Psi_{a\boldsymbol{k}}(\boldsymbol{r}) = \frac{1}{\sqrt{N}}\, e^{i\boldsymbol{k}\cdot\boldsymbol{r}} \sum_{a'=1}^{N_A} \tilde{C}_{a\boldsymbol{k},a'}\, U_{a'}(\boldsymbol{r}) = \frac{1}{\sqrt{\mathcal{V}}}\, e^{i\boldsymbol{k}\cdot\boldsymbol{r}}\, u_{a\boldsymbol{k}}(\boldsymbol{r})\,,$$

$$E_\lambda \to E_a(\boldsymbol{k})\,.$$

In the simplest case, i.e., when we can focus on a well isolated band and the spin-orbit can be neglected, then $N_A=2$ and the Hamiltonian operator $\tilde{H}_{aa'}(-i\boldsymbol{\nabla})$ reduces to (see Sec. 2.2.1)

$$\tilde{H}_{a,a'}(-i\boldsymbol{\nabla}) = \left[E^{(0)} + \frac{\hbar^2}{2m^*}(-i\boldsymbol{\nabla})^2\right]\,\delta_{aa'}\,,$$

so that we have a doubly degenerate state,

$$\{\quad \Psi_{a=1}(\boldsymbol{r}) = F(\boldsymbol{r})\,U(\boldsymbol{r})\;|\uparrow\rangle \quad,\quad \Psi_{a=2}(\boldsymbol{r}) = F(\boldsymbol{r})\,U(\boldsymbol{r})\;|\downarrow\rangle \quad\}\quad,$$

where the unique scalar envelope function $F(\boldsymbol{r})$ is the solution of the eigenvalue problem:

$$\left[-\frac{\hbar^2\boldsymbol{\nabla}^2}{2m^*} + W(\boldsymbol{r})\right]\,F(\boldsymbol{r}) = \left(E - E^{(0)}\right)\,F(\boldsymbol{r})\,. \tag{2.33}$$

We recognize in this particular case the appealing picture that the dynamics of the envelope function is equivalent to that of an electron of effective mass m^* (which replaces the effect of the periodic potential $V_0(\boldsymbol{r})$ of the undisturbed crystal) evolving in empty space under the influence of the potential $E^{(0)}+W(\boldsymbol{r})$. This is why this single-band envelope function approximation is more widely known as

the effective mass approximation.[4]

2.3.2. Application to Heterostructures

In this section we show how the general envelope function approximation presented above can be adapted for the study of the electronic states of heterostructures and eventually of the nanowires that we are interested in.

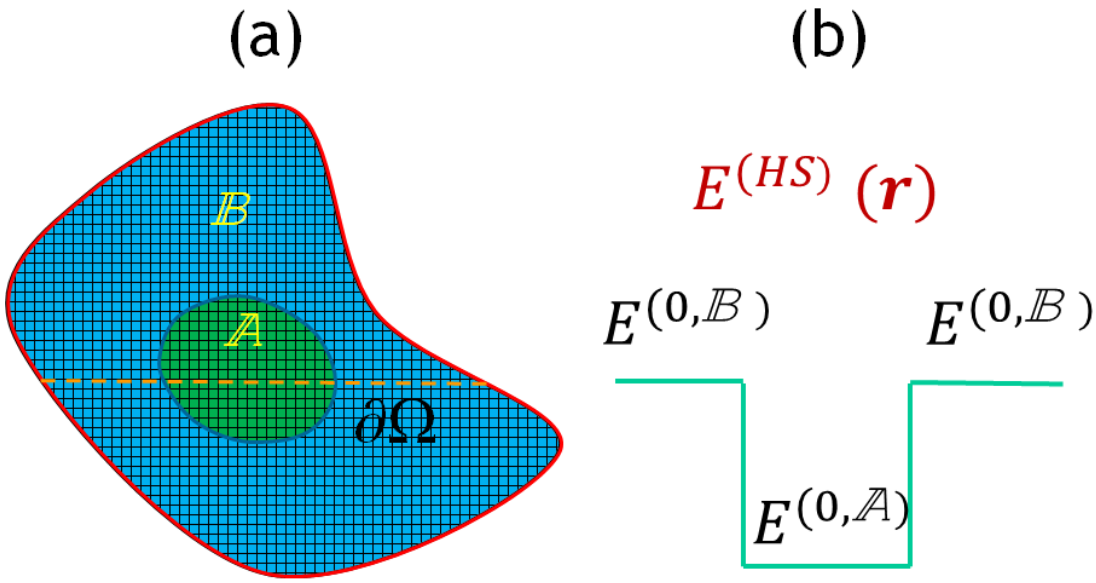

Figure 2.3: (a) Heterostructure consisting of two materials occupying domains $\mathbb{A}$ and $\mathbb{B}$, separated by the interface boundary $\partial\Omega$. The system is limited by the outer surface, outside of which we assume there is air/vacuum. (b) Heterostructure potential $E^{(\mathrm{HS})}(\boldsymbol{r})$, given by the discontinuity of the band-edge energies across the interface between the two materials.

Let us suppose first that we are interested in a heterostructure like that shown schematically in Fig. 2.3(a). The system is in general limited spatially by the external interface to air/vacuum, and composed of two domains occupied by different materials (here both domains and materials are denoted by the same label, $\mathbb{A}$ and $\mathbb{B}$) separated by an interface $\partial\Omega$ with an arbitrary geometry. Initially we do not consider any additional potential W imposed on the system. Even in the absence of W, the configuration shown in Fig. 2.3(a) implies discontinuous changes in the

[4]Many authors also use the name *effective mass approximation* when actually referring to the *multiband envelope function approximation* described above, eventhough the multiband approach requires more parameters than simply the effective masses.

lattice-periodic potential at the interfaces. This overall potential is expected to result in a perturbed electronic structure, as compared with that of the constituent materials. However, the exact specification of that potential is already a problem in itself, due to the presence of interfaces around which there are different atomic species whose positions differ from those of the constituent crystals, and must be obtained self-consistently. The exact study of the electronic structure of such a heterostructure can only be undertaken by *ab initio* methods but, as soon as the size of the system goes beyond a few nanometers, the task becomes extraordinarily complicated. An alternative is to attempt to take advantage of the envelope function theory. Although the mentioned potential discontinuity does not seem to fit well with the smoothness requirements of the envelope function approximation, Burt has shown how it is possible to systematically incorporate this situation into a very convenient envelope-function-like approximate calculation scheme.

We focus in the first place on the outer surface of the system. For most purposes it is sufficient to assume the air/vacuum as an impenetrable region, what simply amounts to restricting the domain of definition of the electron wave functions. The situation is less clear with respect to the treatment of the interfaces between different materials. It is in principle assumed that the interface is perfectly pseudomorphic. The effects of strain in lattice-mismatched heterostructures will be introduced later on. Lacking a precise microscopic description of the real potential at the interface, a rather reasonable assumption is to consider an *abrupt interface approximation*, in which the potential of the heterostructure (HS) is written as:

$$V^{(\mathrm{HS})}(\boldsymbol{r}) = V_0^{(\mathbb{A})}(\boldsymbol{r})\,\chi^{(\mathbb{A})}(\boldsymbol{r}) + V_0^{(\mathbb{B})}(\boldsymbol{r})\,\chi^{(\mathbb{B})}(\boldsymbol{r})\,,$$

where $V_0^{(\mathbb{A},\mathbb{B})}(\boldsymbol{r})$ are the bulk crystalline potential of materials $(\mathbb{A},\mathbb{B})$ and $\chi^{(\mathbb{A},\mathbb{B})}(\boldsymbol{r})$ are the characteristic functions of the domains occupied by materials $(\mathbb{A},\mathbb{B})$. This potential can then be inserted into (2.29) (with $W = 0$) in the place of V_0. According to Burt, if the Γ-point Bloch functions of the semiconductors making up the heterostructure are similar, the expansion of the wave function (2.31) can be tried with U_a chosen to be any one such set of zone-centre eigenfunctions or some linear combinations thereof.[109] Burt then shows in detail that, if one can further assume that the F_a will be slowly varying, the cumbersome nonlocal terms related to the interface are negligible and that the envelope functions of the states of the heterostructure can be approximated by the solutions of the following system of

equations:

$$\sum_{a'} \tilde{H}^{(\mathrm{HS})}_{aa'}\left(-i\boldsymbol{\nabla}\right)\, F_{a'}(\boldsymbol{r}) = \sum_{a'} \left[\tilde{T}^{(\mathrm{HS})}_{aa'}\left(-i\boldsymbol{\nabla}\right) + E^{(\mathrm{HS})}_{aa'}(\boldsymbol{r})\right] F_{a'}(\boldsymbol{r}) = E F_a(\boldsymbol{r})\,. \tag{2.34}$$

Equation (2.34) is to be solved in the restricted geometrical domain defined by the outer surface of the system. The operator $\tilde{H}^{(\mathrm{HS})}_{aa'}$ in the eigenvalue equation (2.34) has the structure of the $\boldsymbol{k}\cdot\boldsymbol{p}$ Hamiltonian introduced in Sec. 2.2.1, except for the substitution $\boldsymbol{k}\to -i\boldsymbol{\nabla}$ and the $\boldsymbol{r}$-dependence (piecewise-constant) of the parameters there appearing. It has been conveniently splitted into its $\boldsymbol{k}$-dependent ($\tilde{T}^{(\mathrm{HS})}_{aa'}$) and $\boldsymbol{k}$-independent ($E^{(\mathrm{HS})}_{aa'}$) parts. It then exhibits the standard structure consisting of a kinetic operator and a potential profile determined by the elements $E^{(\mathrm{HS})}_{aa'}(\boldsymbol{r})$ which reflect the spatial discontinuity of the band-edge energies and spin-orbit splitting parameters between the $\mathbb{A}$ and $\mathbb{B}$ materials:

$$E^{(\mathrm{HS})}_{aa'}(\boldsymbol{r}) = \left(E^{(0,\mathbb{A})}_{a}\,\delta_{aa'} + \Delta^{(\mathbb{A})}_{aa'}\right)\,\chi^{(\mathbb{A})}(\boldsymbol{r}) + \left(E^{(0,\mathbb{B})}_{a}\,\delta_{aa'} + \Delta^{(\mathbb{B})}_{aa'}\right)\,\chi^{(\mathbb{B})}(\boldsymbol{r})\,. \tag{2.35}$$

In Fig. 2.3(b) we have represented schematically the discontinuity of the band-edge energies across the interface between the two materials. The energy difference $E^{(0,\mathbb{B})}_{a} - E^{(0,\mathbb{A})}_{a}$ is called the *a-band-offset* and is a key parameter in determining the confinement effects in the system. It is typically determined experimentally or calculated by *ab initio* methods. Finally, if there were an additional potential $W(\boldsymbol{r})$ acting on the system, it could be easily incorporated by making the substitution $E^{(\mathrm{HS})}_{aa'}(\boldsymbol{r}) \to E^{(\mathrm{HS})}_{aa'}(\boldsymbol{r}) + W(\boldsymbol{r})\delta_{aa'}$. This theoretical framework, that was introduced in an heuristic/phenomenological manner before its rigouros justification by Burt,[114] has been used with extraordinary success in most of the studies of the electronic structure and optical properties of semiconductor heterostructures.

However, despite the attractiveness of this scheme, an important aspect remains to be clarified: The material parameters appearing in the kinetic matrix elements $\tilde{T}^{(\mathrm{HS})}_{aa'}$ are also space-dependent and the question arises as to their placement with respect to the differential operators. One necessary but not sufficient criterium is the Hermiticity of the operator. Among the allowed possibilities, one popular heuristic approach, used in the vast majority of published papers, requires the symmetrization of the differential operators as follows:

$$Q(\boldsymbol{r})\frac{\partial}{\partial x_i} \to \frac{1}{2}\left(Q(\boldsymbol{r})\frac{\partial}{\partial x_i} + \frac{\partial}{\partial x_i}Q(\boldsymbol{r})\right)\,, \tag{2.36}$$

$$Q(\boldsymbol{r})\frac{\partial}{\partial x_i}\frac{\partial}{\partial x_j} \to \frac{1}{2}\left(\frac{\partial}{\partial x_i}Q(\boldsymbol{r})\frac{\partial}{\partial x_j} + \frac{\partial}{\partial x_j}Q(\boldsymbol{r})\frac{\partial}{\partial x_i}\right)\,, \tag{2.37}$$

where $Q(\boldsymbol{r})$ generically represents a parameter or field depending on the position. Foreman has investigated this problem rigorously and arrived to the proper ordering rules, which appear to be dependent on the $\boldsymbol{k}\cdot\boldsymbol{p}$ model used and the orientation of the interface.[115] It is to be noted that, in some cases, the electronic states calculated with the Foreman rules differ significatively from those obtained using the above symmetrization rules.

Finally, we are going to particularize the above treatment to the class of so-called one-dimensional problems, where the system is lattice-periodic along one of the directions, say Z, and the perturbing potential (if any) is independent of the coordinate z, i.e. $W = W(x,y)$. This implies that the system is indefinite along Z, and can be equivalently treated as having a finite large length $\mathcal{L}$ supplemented with periodic boundary conditions. Clearly the nanowires (NWs) we are interested in belong to this class of problems. Within this framework, each NW electronic state (with wave vector k_z) is written as

$$F_a(\boldsymbol{r}) = \frac{1}{\sqrt{\mathcal{L}}}\, e^{ik_z z}\, F_a^{(k_z)}(x,y) \quad \rightarrow \quad \Psi^{(k_z)}(\boldsymbol{r}) = \frac{1}{\sqrt{\mathcal{L}}}\, e^{ik_z z} \sum_a F_a^{(k_z)}(x,y)\, U_a(\boldsymbol{r})\,.$$

$$\int_{\mathcal{V}} d\boldsymbol{r}\; \Psi_\lambda^{(k_z)*}(\boldsymbol{r})\, \Psi_{\lambda'}^{(k_z')}(\boldsymbol{r}) = \delta_{k_z k_z'}\delta_{\lambda\lambda'} \quad ,$$

$$\sum_a \int_{\mathcal{S}} dx\, dy\, \frac{1}{\sqrt{\Omega}}\, F_{\lambda,a}^{(k_z)*}(x,y)\, \frac{1}{\sqrt{\Omega}}\, F_{\lambda',a}^{(k_z)}(x,y) = \delta_{\lambda\lambda'} \quad .$$

The envelope function equation (2.34) adopts a reduced form for this class of problems: The electronic structure is determined, for each wavevector k_z, by the eigenvalue equation (by making (HS) $\rightarrow$ (NW)):

$$\sum_{a'} \left[\tilde{T}_{aa'}^{(\mathrm{NW})} \left(-i\frac{\partial}{\partial x}, -i\frac{\partial}{\partial y}, k_z \right) + E_{aa'}^{(\mathrm{NW})}(x,y) \right] F_{a'}^{(k_z)}(x,y) = E(k_z) F_a^{(k_z)}(x,y)\,. \tag{2.38}$$

The energy spectrum is organized in one-dimensional subbands $E(k_z)$. If there is an additional potential, it can be incorporated by making $E_{aa'}^{(\mathrm{NW})}(x,y) \rightarrow E_{aa'}^{(\mathrm{NW})}(x,y) + W(x,y)\delta_{aa'}$.

In this thesis we have implemented this scheme to study the electronic structure of nanowires. As we will see in Chapter 3, the nanowires can exhibit sometimes a nonuniform deformation. It will be taken into account by adding the corresponding Bir-Pikus Hamiltonian. In order to bypass the complications connected with the discontinuity in the material parameters at the interfaces, in this work we shall take the simplified approach of considering that the kinetic and deformation potential

parameters are uniform throughout the entire structure.

2.4. Radiation-Matter Interaction

To describe the basic optical properties of the nanowires we need to incorporate the radiation-matter interaction. The theory of quantum electrodynamics describes completely the interaction between an electromagnetic field and matter. However, in the context of solid state physics it is sufficient to work within the framework of a semi-classical description of the problem.[116] In the semi-classical approximation, the electronic structure of the matter is described by quantum mechanics and the electromagnetic field through classical electrodynamics.

In our case the material system is the single electron treated in a mean field approximation that we have considered in Sec. 2.2.1 and 2.3, and whose Hamiltonian can be written generically as:

$$\mathbb{H} = \frac{\boldsymbol{p}^2}{2m_0} + \mathbb{V}(\boldsymbol{r})\,, \tag{2.39}$$

where

$$\mathbb{V} = \begin{cases} V_0 & \text{for a bulk crystal (see Sec. 2.2.1)} \\ V_0 + W & \text{for a perturbed crystal (see Sec. 2.3.1)} \\ V_0^{(\mathrm{HS,NW})} & \text{for a heterostructure, nanowire (see Sec. 2.3.2)} \end{cases} .$$

Let us suppose that the electron in the solid is acted upon by an external electromagnetic field, here modeled by a monochromatic plane wave specified through its vector potential,

$$\boldsymbol{A}(\boldsymbol{r},t) = A_0 \cos\left(\boldsymbol{q}\cdot\boldsymbol{r} - \omega t\right)\,\hat{\boldsymbol{e}} = A_0\,\frac{1}{2}\left[\mathrm{e}^{+i(\boldsymbol{q}\cdot\boldsymbol{r}-\omega t)} + \mathrm{e}^{-i(\boldsymbol{q}\cdot\boldsymbol{r}-\omega t)}\right]\,\hat{\boldsymbol{e}}\,, \tag{2.40}$$

where A_0 is the amplitude and $\hat{\boldsymbol{e}}$ is the unit polarization vector transverse to the propagation wave vector $\boldsymbol{q}$, i.e., $\boldsymbol{q}\cdot\hat{\boldsymbol{e}} = 0$. The vector potential then satisfies the Coulomb gauge condition, $\boldsymbol{\nabla}\cdot\boldsymbol{A} = 0$. The wavevector $\boldsymbol{q}$ and angular frequency ω are related through the phase velocity, $\omega/|\boldsymbol{q}| = v_{\mathrm{ph}}$ which in turn is determined by the background refractive index, $v_{\mathrm{ph}}(\omega) = c_0/n(\omega)$. The electric and magnetic

fields of the wave are explicitly obtained through the following expressions:

$$\boldsymbol{E} = -\frac{\partial \boldsymbol{A}}{\partial t}\,, \tag{2.41a}$$

$$\boldsymbol{B} = \boldsymbol{\nabla} \times \boldsymbol{A}\,. \tag{2.41b}$$

Within this framework, the Hamiltonian operator of an electron in the solid (with charge $-e$) under the action of the electromagnetic field becomes, after some manipulations,[117]

$$\mathbb{H} + \underbrace{\frac{e}{m_0}\boldsymbol{A}(\boldsymbol{r},t)\cdot\boldsymbol{p}}_{\equiv H_{\text{r-m}}} \quad . \tag{2.42}$$

The effect of the electromagnetic field in (2.42) appears then as a perturbation to the problem of the electron in the solid. This additional term $H_{\text{r-m}}$ is called the radiation-matter interaction Hamiltonian or, in quantum language, the photon-electron interaction.[5]

2.4.1. Optical Absorption

The interaction Hamiltonian $H_{\text{r-m}}$ depends harmonically with time through the vector potential, and this dependence will be made explicit as follows:

$$H_{\text{r-m}} = H_{\text{r-m}}^{(-)}\,\mathrm{e}^{-i\,\omega t} + H_{\text{r-m}}^{(+)}\,\mathrm{e}^{+i\,\omega t} \quad ,$$

with

$$H_{\text{r-m}}^{(\pm)} = \frac{1}{2}\,\frac{e}{m_0}\,A_0\,\mathrm{e}^{\mp i\,\boldsymbol{q}\cdot\boldsymbol{r}}\;(\hat{\boldsymbol{e}}\cdot\boldsymbol{p}) \quad .$$

However, in this work we are not interested in the exact description of the time evolution of the system determined by the total Hamiltonian (2.42). As discussed below, the basic optical properties (reflexion, transmission, absorption) can be obtained from the transition probability per unit time between two electronic states induced by the field, and this probability can be conveniently calculated by means of time-dependent perturbation theory.[102] Thus, in first order in $H_{\text{r-m}}$, the probability per unit time of a transition between initial state i and final state f

[5] In the following, we shall loosely use the quantum term 'photon' here and there, but actually meaning a classical normal mode of the electromagnetic field. We emphasize, though, that throughout this work we are staying within the semiclasical theory of the radiation-matter interaction.

can be expressed as:[102]

$$W_{i\to f} = \frac{2\pi}{\hbar}\left|\langle\Psi_f|H^{(-)}_{\text{r-m}}|\Psi_i\rangle\right|^2\delta(E_f - E_i - \hbar\omega) + \frac{2\pi}{\hbar}\left|\langle\Psi_f|H^{(+)}_{\text{r-m}}|\Psi_i\rangle\right|^2\delta(E_f - E_i + \hbar\omega)\,. \quad (2.43)$$

The first term describes the absorption of a photon by excitation of an electron from i to f with $E_f = E_i + \hbar\omega$ while the second term corresponds to the (stimulated) emission of a photon with deexcitation of an electron from i to f with $E_f = E_i - \hbar\omega$. Therefore, the total probability per unit time of absorption of a photon of energy $\hbar\omega$ is:

$$R(\hbar\omega) = \frac{2\pi}{\hbar}\sum_f\sum_i\left|\langle\Psi_f|H^{(-)}_{\text{r-m}}|\Psi_i\rangle\right|^2\delta(E_f - E_i - \hbar\omega)\,. \quad (2.44)$$

Finally, we must link the microscopic description developed until now with the macroscopic optical properties observed experimentally. To do this we introduce the optical absorption coefficient α defined as the number of absorbed photons per unit volume and per unit of time with respect to the number of incident photons per unit area per unit time[102]. This quantity, that has dimensions of inverse length, can be related to the penetration length of the photon in the medium, l_{ph}, in the following manner:

$$\alpha = \frac{1}{l_{\text{ph}}} = \frac{1}{v_{\text{ph}}\tau_{\text{ph}}} = \frac{n}{c}\frac{1}{\tau_{\text{ph}}}\,, \quad (2.45)$$

where τ_{ph} is the lifetime of the photon in the material whose inverse coincides with the total probability per unit time of absorption of one photon $R(\hbar\omega)$. Finally, we get the expression:

$$\alpha(\hbar\omega) = \frac{n(\omega)}{c}\frac{2\pi}{\hbar}\sum_f\sum_i\left|\langle\Psi_f|H^{(-)}_{\text{r-m}}|\Psi_i\rangle\right|^2\delta(E_f - E_i - \hbar\omega)\,. \quad (2.46)$$

The shape of the spectral line associated to each absorption transition $i \to f$ is here represented by a Dirac delta function. In reality, there are different mechanisms (radiative decay, scattering by impurities and phonons, etc..) that broaden the spectral line. Therefore, in the practical computations presented in this work we have assumed a phenomenological Lorentzian shape function with broadening parameter Γ, without delving into the details of its origin, so that the absorption

spectrum is calculated by means of the expression:

$$\alpha(\hbar\omega) = \frac{n(\omega)}{c}\frac{2\pi}{\hbar}\sum_f\sum_i \left|\langle\Psi_f|H_{\text{r-m}}^{(-)}|\Psi_i\rangle\right|^2 \frac{1}{\pi}\frac{\Gamma/2}{(E_f - E_i - \hbar\omega)^2 + (\Gamma/2)^2}\,. \quad (2.47)$$

Until now the treatment has been rather general. Thinking in its application to nanowires, below we describe the calculation of $\langle\Psi_f|H_{\text{r-m}}^{(-)}|\Psi_i\rangle$, which we call the optical matrix element, in the framework of the envelope function approximation.

2.4.2. The Optical Matrix Element

The initial and final electron states of the optical transition in the solid will be described within the envelope function approximation introduced in Sec. 2.3 as:

$$\Psi_i(\boldsymbol{r}) = \sum_a F_{i,a}(\boldsymbol{r})\,U_a(\boldsymbol{r})\,, \quad (2.48a)$$

$$\Psi_f(\boldsymbol{r}) = \sum_a F_{f,a}(\boldsymbol{r})\,U_a(\boldsymbol{r})\,. \quad (2.48b)$$

In this work, we will study only optical transitions in which the dipole approximation is valid, i.e., the wavevector of the electromagnetic field is negligible, $\boldsymbol{q} \approx 0$. The matrix element then reduces to:

$$\langle\Psi_f|H_{\text{r-m}}^{(-)}|\Psi_i\rangle = \frac{1}{2}\frac{e}{m_0}A_0\int_{\mathcal{V}} d^3\boldsymbol{r}\,\Psi_f^*(\boldsymbol{r})\,(\hat{\boldsymbol{e}}\cdot\boldsymbol{p})\,\Psi_i(\boldsymbol{r})$$

$$= \frac{1}{2}\frac{e}{m_0}A_0\sum_{aa'}\int_{\mathcal{V}} d^3\boldsymbol{r}\,\left[U_a^*(\boldsymbol{r})\,(\hat{\boldsymbol{e}}\cdot\boldsymbol{p})\,U_{a'}(\boldsymbol{r})\right]\,F_{f,a}^*(\boldsymbol{r})\,F_{i,a'}(\boldsymbol{r})$$

$$+\frac{1}{2}\frac{e}{m_0}A_0\sum_{aa'}\int_{\mathcal{V}} d^3\boldsymbol{r}\,\left[U_a^*(\boldsymbol{r})\,U_{a'}(\boldsymbol{r})\right]\,F_{f,a}^*(\boldsymbol{r})\,(\hat{\boldsymbol{e}}\cdot\boldsymbol{p})\,F_{i,a'}(\boldsymbol{r})\,.$$

The range of integration comprises the entire system volume $\mathcal{V}$. By taking advantage of the lattice periodicity of U_a and the limitation in the Fourier spectrum of F_a, the matrix element can be rewritten as follows:[103]

$$\langle\Psi_f|H_{\text{r-m}}^{(-)}|\Psi_i\rangle = \frac{1}{2}\frac{e}{m_0}A_0\left[P_{fi}^{(\text{inter})}(\hat{\boldsymbol{e}}) + P_{fi}^{(\text{intra})}(\hat{\boldsymbol{e}})\right]\,, \quad (2.49)$$

with

$$P_{fi}^{(\text{inter})}(\hat{\boldsymbol{e}}) = \sum_{aa'}(\hat{\boldsymbol{e}}\cdot\boldsymbol{p}_{aa'})\int_{\mathcal{V}} d^3\boldsymbol{r}\,\frac{1}{\sqrt{\Omega}}F_{f,a}^*(\boldsymbol{r})\,\frac{1}{\sqrt{\Omega}}F_{i,a'}(\boldsymbol{r})\,, \quad (2.50)$$

$$P_{fi}^{(\mathrm{intra})}(\hat{\boldsymbol{e}}) = \sum_a \int_{\mathcal{V}} d^3\boldsymbol{r}\, \frac{1}{\sqrt{\Omega}}\, F_{f,a}^*(\boldsymbol{r})\, (\hat{\boldsymbol{e}}\cdot\boldsymbol{p})\, \frac{1}{\sqrt{\Omega}}\, F_{i,a}(\boldsymbol{r})\,, \tag{2.51}$$

where

$$\boldsymbol{p}_{aa'} = \langle U_a\, |\boldsymbol{p}|\, U_{a'}\rangle = \frac{1}{\Omega}\int_{\Omega} d^3\boldsymbol{r}\, u_a^*(\boldsymbol{r})\, \boldsymbol{p}\, u_{a'}(\boldsymbol{r})\,. \tag{2.52}$$

Interestingly, the matrix element (2.52) was already introduced in the course of the development of the $\boldsymbol{k}\cdot\boldsymbol{p}$ method, see Eq. (2.20). We thus see that $P_{fi}^{(\mathrm{inter})}(\hat{\boldsymbol{e}})$ is governed by the same parameters that appear in the $\boldsymbol{k}\cdot\boldsymbol{p}$ Hamiltonian. In the case of the zincblende and wurtzite semiconductors that we study in this paper these matrix elements are ultimately determined by the Kane parameter P defined in Eq. (A.4) and (A.10), respectively.

The optical matrix element (2.49) contains two contributions that have been denoted as *interband* and *intraband*. In general, both terms contribute to any transition $i \to f$, but the former dominates for transitions across the band gap where the states i and f have different dominant Bloch symmetry. In this work we will only retain the interband contribution $P_{fi}^{(\mathrm{inter})}(\hat{\boldsymbol{e}})$ in the calculations of the optical absorption around the fundamental energy gap. As we see, $P_{fi}^{(\mathrm{inter})}(\hat{\boldsymbol{e}})$ is governed by the overlaps of the envelope functions of the initial and final states, weighted by the factors $(\hat{\boldsymbol{e}}\cdot\boldsymbol{p}_{aa'})$. These polarization-dependent weighting factors are determined by the symmetries of the Γ-point Bloch amplitudes (see Appendix B). In turn, they determine to a great extent (as long as the corresponding envelope function overlaps are appreciable) the light polarization selection rules and the possible polarization-anisotropy properties of the optical absorption spectrum of the system.

We can now particularize the interband matrix element to the class of one-dimensional problems, in particular the nanowires (NWs) we are interested in. The initial and final NW electron states of the optical transition are given by:

$$\Psi_{\lambda_i}^{(k_z^{(i)})}(\boldsymbol{r}) = \frac{1}{\sqrt{\mathcal{L}}}\, e^{ik_z^{(i)}z} \sum_a F_{\lambda_i,a}^{(k_z^{(i)})}(x,y)\, U_a(\boldsymbol{r})\,, \tag{2.53a}$$

$$\Psi_{\lambda_f}^{(k_z^{(f)})}(\boldsymbol{r}) = \frac{1}{\sqrt{\mathcal{L}}}\, e^{ik_z^{(f)}z} \sum_a F_{\lambda_f,a}^{(k_z^{(f)})}(x,y)\, U_a(\boldsymbol{r})\,. \tag{2.53b}$$

The interband matrix element is then given by:

$$P_{fi}^{(\mathrm{inter})}(\hat{\boldsymbol{e}}) = \delta_{k_z^{(f)}k_z^{(i)}} \sum_{aa'} (\hat{\boldsymbol{e}}\cdot\boldsymbol{p}_{aa'}) \int_{\mathcal{S}} dx\, dy\, \frac{1}{\sqrt{\Omega}}\, F_{\lambda_f,a}^{(k_z^{(f)})*}(x,y)\, \frac{1}{\sqrt{\Omega}}\, F_{\lambda_i,a'}^{(k_z^{(i)})}(x,y)\,. \tag{2.54}$$

Chapter 3

Piezoelectric Properties of Nanowires

Some dielectric crystals have the following property: when deformed by the application of external stress, the electric dipoles in the crystal get oriented such that the crystal develops positive and negative charges on opposite faces, resulting in an electric field across the crystal. The associated potential difference has one polarity or the inverse depending on the character (tensile or compressive) of the applied stress. The electric field is found to be directly proportional to the applied stress. Jacques and Pierre Curie first observed this effect in quartz crystal in 1880 and called it the (direct) piezoelectric effect. Piezoelectric materials also exhibit the reverse property: When they are subjected to an external electric field, they develop asymmetric displacements of anions and cations that cause a net deformation of the crystal. In order to exhibit piezoelectricity, a crystal must be noncentrosymmetric.

Due to the intrinsic characteristics of piezoelectric materials, there are numerous applications of piezelectric semiconductors that benefit from their uses, e.g., in energy harvesting[118–120], sensors[121] and piezoelectric generators[82]. In previous studies,[122] it has been shown that the high surface-to-volume ratio at the nanoscale could dramatically enhance the surface effects and could ultimately lead to distinct elastic and piezoelectric properties that are significantly different from their macroscopic counterparts. Recently, piezoelectric nanowires have been used for energy harvesting[123,124] and sensing[125–127].

In this chapter we develop a theoretical model to treat fully-coupled piezoelectric problems in very long or infinite translationally invariant systems. Clearly, this model will be particularly useful for the study the piezoelectric properties of heterostructure core-shell nanowires. The formulation developed incorporates the

possibility to work with different material types, crystal structures, geometries, growth directions and multiple shells. The model also allows considering different types of applied loads. The chapter is organized as follows. We start by presenting the general piezoelectric problem in Sec. 3.1. The theoretical model developed by us is presented in Sec. 3.2. The numerical applications to different systems of heterostructure nanowires are presented in Sec. 3.3.

3.1. The Three-Dimensional Piezoelectric Problem

3.1.1. General Formulation

To fix the theoretical framework and the notation adopted, we summarize first the general formulation of a piezoelectric continuum problem. To specify the necessary tensors we shall use index notation throughout the thesis. The Latin indices $(i, j, k, l, m, n = 1, 2, 3)$ in the tensorial objects will label the components with respect to a Cartesian reference frame $O X_1 X_2 X_3$, with associated coordinates (x_1, x_2, x_3). Einstein summation convention applies unless the contrary is explicitly stated.

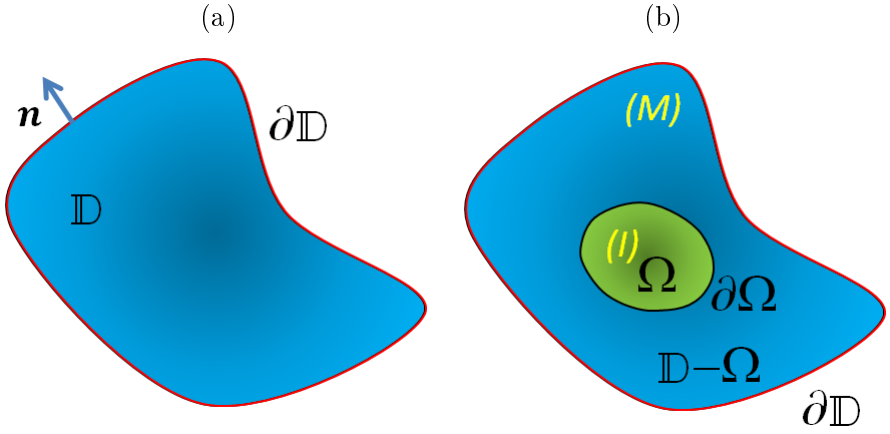

Figure 3.1: (a) 3D piezoelectric body. (b) Piezoelectric bimaterial system with domains $\mathbb{D} - \Omega$ (matrix (M)) and Ω (inclusion (I)), separated by the interface boundary $\partial\Omega$.

Let us consider a piezoelectric solid (see Fig. 3.1(a)) that occupies a 3D domain $\mathbb{D}$ delimited by the boundary $\partial\mathbb{D}$, containing the free volume charge density ρ and subjected to a body force per unit volume f_i. The goal is to find the distribution of the elastic displacement vector u_i and the piezoelectric potential ϕ over the solid. When assuming the small-deformation and electrostatic approximations, the above

quantities can be related to the strain tensor ε_{ij} and the piezoelectric field E_m by the expressions:

$$\varepsilon_{ij} = \frac{1}{2}\left(\frac{\partial u_i}{\partial x_j} + \frac{\partial u_j}{\partial x_i}\right) , \tag{3.1a}$$

$$E_m = -\frac{\partial \phi}{\partial x_m} . \tag{3.1b}$$

We restrict ourselves to the linear piezoelectric regime, which allows to express the stress tensor σ_{ij} and the piezoelectric displacement vector D_m in terms of ε_{ij} and E_m by means of the standard linear constitutive relations:[84,85]

$$\sigma_{ij} = C_{ijkl}\varepsilon_{kl} - e_{nij}E_n , \tag{3.2a}$$

$$D_m = e_{mkl}\varepsilon_{kl} + \epsilon_{mn}E_n , \tag{3.2b}$$

where C_{ijkl} is the elastic stiffness tensor, e_{nij} is the piezoelectric tensor, and ϵ_{mn} is the dielectric tensor.

The equilibrium configuration is determined by the following set of coupled differential equations:

$$\frac{\partial \sigma_{ij}}{\partial x_i} = -f_j , \tag{3.3a}$$

$$\frac{\partial D_m}{\partial x_m} = \rho . \tag{3.3b}$$

The first equation is the mechanical equilibrium equation, and the second is the electrostatic Poisson equation.

When dealing with specific problems, the tensors appearing in the general formulation of the piezoelectric problem are often transformed into a matrix form by means of the Voigt notation[128]. In Appendix D.1 we give the elastic, piezoelectric and dielectric matrices, C_{IK}, e_{nI} and ϵ_{mn} ($I, K = 1, \ldots, 6$, $m, n = 1, 2, 3$), for the crystalline materials belonging to the cubic system (crystal classes T and T_d).

Equations (3.1)-(3.3), together with appropriate boundary conditions specified at the surface $\partial\mathbb{D}$ (with outward normal vector n_i), constitute the complete mathematical description of the 3D fully-coupled piezoelectric problem. The most general setting of boundary conditions would allow to specify either the applied traction force $\bar{t}_j$ or a prescribed displacement $\bar{u}_j$, and the impressed surface charge

density $\bar{\varrho}$ or a fixed potential $\bar{\phi}$, in the following way:[1]

$$n_i \sigma_{ij} = \bar{t}_j \quad \text{on} \quad \partial\mathbb{D}_t \qquad \text{and} \qquad u_j = \bar{u}_j \quad \text{on} \quad \partial\mathbb{D}_u \,, \tag{3.4a}$$

$$-\, n_m D_m = \bar{\varrho} \quad \text{on} \quad \partial\mathbb{D}_\varrho \quad \text{and} \qquad \phi = \bar{\phi} \quad \text{on} \quad \partial\mathbb{D}_\phi \,, \tag{3.4b}$$

where $(\partial\mathbb{D}_t, \partial\mathbb{D}_u)$ and $(\partial\mathbb{D}_\varrho, \partial\mathbb{D}_\phi)$ represent two, in general different, partitions of the boundary $\partial\mathbb{D}$. The physical problems are usually modeled by a simpler situation, the simplest one being the uncharged free boundary (that would correspond to $\partial\mathbb{D}_t = \partial\mathbb{D}_\varrho = \partial\mathbb{D}$ with $\bar{t}_j = 0$ and $\bar{\varrho} = 0$).

The so-called semi-coupled approach to the piezoelectric problem consists of neglecting the piezoelectric contribution to the stress, by imposing $e_{nij} \to 0$ in Eq. (3.2a), and solving the resulting purely mechanical problem given by Eqs. (3.3a) and (3.4a). In a second decoupled step, the obtained strain ε_{ij} is inserted into Eq.(3.2b) and the electrostatic Poisson problem given by Eqs. (3.3b) and (3.4b) is solved to give the piezoelectric field E_n and the potential ϕ. Of course, in the case of a non-piezoelectric material the piezoelectric constants vanish exactly ($e_{nij} = 0$) in every expression, and one has to solve separately the uncoupled mechanical and electrostatic problems.

3.1.2. The Coherent Piezoelectric Inclusion Problem

One problem of particular interest is that of finding the elastic and electric fields induced in a coherent (or pseudomorphic) lattice-mismatched bimaterial system. Such a heterostructure consists of two domains, $\mathbb{D} - \Omega$ and Ω, occupied by two materials that have the same crystalline structure but differ in their lattice parameters (see Fig. 3.1(b)). Quite conventionally these domains are respectively called the *matrix* (associated quantities will be hereafter labeled with (M)) and the *inclusion* (label (I)). Their lattice parameters are denoted by $a_i^{(M)}$ and $a_i^{(I)}$, $i = 1, 2, 3$. The contact interface between both materials is assumed to be coherent, i.e., dislocation-free, despite the existing lattice mismatch. This requirement is the cause for the appearance of a certain strain and field distribution over the system, that we want to calculate.

For later reference it is convenient to introduce here the so-called *misfit* (or *mismatch*) *strain* derived from the nominal lattice mismatch between the matrix

[1] We ignore the electric field on the air/vacuum region surrounding the piezoelectric medium, which is a good approximation as long as the dielectric constant of the medium is much larger than the vacuum dielectric permittivity.

and inclusion materials:

$$\varepsilon_{ij}^{(\text{misfit})} = \varepsilon_i^{(\text{misfit})}\,\delta_{ij} = \frac{a_i^{(M)} - a_i^{(I)}}{a_i^{(I)}}\,\delta_{ij}\;. \tag{3.5}$$

Note that here, and in Eq. (3.8) below, the repeated index i is not summed.

The elastic constants of the heterostructure can be written as:

$$C_{ijkl}(\boldsymbol{r}) = C_{ijkl}^{(M)}\chi^{(M)}(\boldsymbol{r}) + C_{ijkl}^{(I)}\chi^{(I)}(\boldsymbol{r})\;, \tag{3.6}$$

where $\chi^{(I)}$ is the characteristic function of the inclusion defined as:

$$\chi^{(I)}(\boldsymbol{r}) = \begin{cases} 1 & \text{if } \boldsymbol{r} \in \Omega \\ 0 & \text{if } \boldsymbol{r} \in \mathbb{D} - \Omega \end{cases}\;, \tag{3.7}$$

and $\chi^{(M)} = 1 - \chi^{(I)}$ is the characteristic function of the matrix. Similar expressions to Eq. (3.6) can be written for the piezoelectric constants $e_{nij}(\boldsymbol{r})$ and dielectric constants $\epsilon_{mn}(\boldsymbol{r})$ of the heterostructure.

A generalization of the classical Eshelby inclusion method, well-known in the micromechanics literature,[129,130] provides a systematic procedure to obtain the strain and electric field in the above described system. It essentially amounts to a *gedanken* procedure in which the two material domains are first independently constrained to a common crystal lattice, characterized by reference lattice parameters $a_i^{(\text{ref})}$, by applying appropriate stresses and charges. For later use it is convenient to introduce here the notation:

$$\varepsilon_{ij}^{(0)}(\boldsymbol{r}) = \frac{a_i^{(\text{ref})} - a_i^{(M)}}{a_i^{(M)}}\,\delta_{ij}\,\chi^{(M)}(\boldsymbol{r}) + \frac{a_i^{(\text{ref})} - a_i^{(I)}}{a_i^{(I)}}\,\delta_{ij}\,\chi^{(I)}(\boldsymbol{r})\;. \tag{3.8}$$

Note that if we take $a_i^{(\text{ref})} = a_i^{(M)}$ then:

$$\varepsilon_{ij}^{(0)}(\boldsymbol{r}) = \varepsilon_{ij}^{(\text{misfit})}\,\chi^{(I)}(\boldsymbol{r})\;, \tag{3.9}$$

which is the usual choice when treating inclusions in an infinite matrix.

Following with the *gedanken* procedure, the now lattice-matched material domains are coherently joined, and left to relax to the final equilibrium configuration under applied stresses and charges opposite to the ones in the previous step, thereby removing any external action on the system. We summarize here the final results of this procedure:

- First, it has to be noticed that the Eshelby procedure gives the total strain with respect to the undeformed state of the local lattice as the sum of two terms:

$$\varepsilon_{ij}^{(T)}(\boldsymbol{r}) = \varepsilon_{ij}^{(0)}(\boldsymbol{r}) + \varepsilon_{ij}(\boldsymbol{r}) \,. \tag{3.10}$$

  In the context of the coherent inclusion problem, the unknown $\varepsilon_{ij}(\boldsymbol{r})$ describes the strain state attained after relaxation from the reference lattice configuration, and therefore is here called the *relaxation strain*. Associated to $\varepsilon_{ij}(\boldsymbol{r})$ we have a displacement field u_i as given by Eq. (3.1a) and constitutive relations as given by Eq. (3.2).

- The final equilibrium configuration for the relaxation strain $\varepsilon_{ij}(\boldsymbol{r})$ and the electric field $E_m(\boldsymbol{r})$ can be obtained by solving the following set of coupled partial differential equations:

$$\frac{\partial \sigma_{ij}}{\partial x_i} = -f_j^{(0)} \,, \tag{3.11a}$$

$$\frac{\partial D_m}{\partial x_m} = \rho^{(0)} \,, \tag{3.11b}$$

  where the lattice mismatch induced force $f_i^{(0)}$ and charge $\rho^{(0)}$ are given by:

$$f_j^{(0)} = \frac{\partial \sigma_{ij}^{(0)}}{\partial x_i} \quad \text{with} \quad \sigma_{ij}^{(0)}(\boldsymbol{r}) = C_{ijkl}(\boldsymbol{r})\, \varepsilon_{kl}^{(0)}(\boldsymbol{r}) \,, \tag{3.12a}$$

$$\rho^{(0)} = -\frac{\partial P_m^{(0)}}{\partial x_m} \quad \text{with} \quad P_m^{(0)}(\boldsymbol{r}) = e_{mkl}(\boldsymbol{r})\, \varepsilon_{kl}^{(0)}(\boldsymbol{r}) \,. \tag{3.12b}$$

  Note that, due to the presence of the step-like characteristic functions inside the derivatives in Eq. (3.12), $f_i^{(0)}$ and $\rho^{(0)}$ represent actually surface force and charge applied on the interface $\partial\Omega$ separating the inclusion and matrix.

- If the system is further loaded with force f_i and/or charge ρ, and/or subjected to arbitrary boundary conditions on the surface $\partial\mathbb{D}$, these effects can be easily added, by means of the superposition principle, to the inclusion problem represented by Eq. (3.11).

In conclusion, we have shown that the particular problem of a coherent piezoelectric inclusion can be mapped to a standard piezoelectric problem as described in Sec. 3.1.1 by a proper introduction of equivalent forces and charges. As long as $\varepsilon_{ij}^{(0)}$ is small, the results of the generalized Eshelby procedure will be rather insensitive to the specific choice of $a_i^{(\mathrm{ref})}$.

3.1.3. Weak Form of the 3D Piezoelectric Problem

In Sec. 3.1.1, the piezoelectric boundary value problem has been formulated directly in terms of the field equilibrium equations (3.3), as well as the boundary conditions according to Eqs. (3.4). Together these equations form the so-called *strong form* of the piezoelectric boundary value problem. The strong term means that, since the problem is defined by a system of partial differential equations, this approach poses high requirements on the differentiability of the field variables (the displacements u_i and potential ϕ in this case). Therefore, the functions used to approximate those field variables have to be differentiable up to the order of the partial differential equations. However, this problem can alternatively be represented in an integral form, in the manner to be detailed below. This formulation arrives at an integral condition that has to be fulfilled globally over the whole piezoelectric domain, which moreover involves lower order derivatives than the strong form. For these reasons, this formulation is commonly called the *weak form* of the piezoelectric problem. It should be mentioned however that strong and weak form are equivalent formulations as long as identical solution spaces are assumed and no discretization is performed yet. The great utility of the weak form is that, being able to accommodate approximate solutions with weaker continuity properties and fewer boundary constraints, it is a convenient starting point for the approximation of the problem by various discrete numerical methods.

In general various routes can be employed to arrive to the weak formulation of a problem. In the case of the piezoelectric problem, the most natural approach is to start from a physical variational principle, that will lead in the first instance to a set of variational integral equations (weak form of the problem), and eventually to a set of Euler differential equations (strong form of the problem).

Although we are ultimately interested in a stationary, time-independent problem, it is convenient to begin with the formulation of the variational principle for the general case of a dynamic, time-dependent problem. Then, it is necessary to introduce first the kinetic energy density:

$$\mathcal{K} = \frac{1}{2}\,\rho_m \frac{\partial u_i}{\partial t}\,\frac{\partial u_i}{\partial t} \quad ,$$

where ρ_m is the mass density. On the other hand, we remind that the internal energy density associated to the linear continuum piezoelectric problem contains mechanical and electrical contributions as follows:

$$\mathcal{U} = \frac{1}{2}\,\sigma_{ij}\,\varepsilon_{ij} + \frac{1}{2}\,D_m\,E_m \quad .$$

This state function $\mathcal{U}$ is the appropriate working choice when the system is to be described in terms of the variables ε_{ij} and D_m.[131] However, as seen in Sec. 3.1.1, we have taken as primary variables the mechanical displacement u_i (therefore ε_{ij}, see Eq. (3.1a)) and the electric potential ϕ (therefore E_m, see Eq. (3.1b)). In this approach, the relevant state function is the electric enthalpy density $\mathcal{H}$, which is formally obtained from $\mathcal{U}$ through the following Legendre transform:[131]

$$\begin{aligned}\mathcal{H} &= \mathcal{U} - D_m\, E_m = \frac{1}{2}\,\sigma_{ij}\,\varepsilon_{ij} - \frac{1}{2}\,D_m\,E_m \\ &= \frac{1}{2}\,C_{ijkl}\,\varepsilon_{ij}\,\varepsilon_{kl} - e_{mkl}\,E_m\,\varepsilon_{kl} - \frac{1}{2}\,\epsilon_{mn}\,E_m\,E_n \\ &= \frac{1}{2}\,C_{ijkl}\,\frac{\partial u_i}{\partial x_j}\,\frac{\partial u_k}{\partial x_l} + e_{mkl}\,\frac{\partial \phi}{\partial x_m}\,\frac{\partial u_k}{\partial x_l} - \frac{1}{2}\,\epsilon_{mn}\,\frac{\partial \phi}{\partial x_m}\,\frac{\partial \phi}{\partial x_n} \quad , \end{aligned} \tag{3.13}$$

where explicit use has been made of the constitutive equations (3.2) and kinematic equations (3.1).

The following step requires the definition of an associated Lagrangian density in terms of the electric enthalpy $\mathcal{H}$:

$$\mathcal{L}\left(\frac{\partial u_i}{\partial x_j}, \frac{\partial u_i}{\partial t}, \frac{\partial \phi}{\partial x_m}\right) = \mathcal{K}\left(\frac{\partial u_i}{\partial t}\right) - \mathcal{H}\left(\frac{\partial u_i}{\partial x_j}, \frac{\partial \phi}{\partial x_m}\right) \quad ,$$

and the introduction of the Lagrangian functional of the arbitrary functions u_i and ϕ,

$$L[u_i, \phi; t] = \int_{\mathbb{D}} d^3\boldsymbol{r}\, \mathcal{L}\left(\frac{\partial u_i}{\partial x_j}, \frac{\partial u_i}{\partial t}, \frac{\partial \phi}{\partial x_j}\right) \quad ,$$

where $\mathbb{D}$ is the domain occupied by the piezoelectric body. The corresponding action functional, associated to the time interval $[t_1, t_2]$, is given by:

$$S[u_i, \phi] = \int_{t_1}^{t_2} dt\, L[u_i, \phi; t] \quad .$$

The Hamilton's principle (or principle of least action) now states that the physical solutions for the evolution of displacement and potential fields between times t_1 and t_2, $u_i(\boldsymbol{r}, t)$ and $\phi(\boldsymbol{r}, t)$, are determined by the condition of stationarity of the action:

$$\delta S[u_i, \phi] = \int_{t_1}^{t_2} dt\, \delta L[u_i, \phi; t] = 0 \quad ,$$

or, more explicitly,

$$\int_{t_1}^{t_2} dt \int_{\mathbb{D}} d^3\boldsymbol{r} \left\{ \delta\mathcal{K}\left(\frac{\partial u_i}{\partial t}\right) - \delta\mathcal{H}\left(\frac{\partial u_i}{\partial x_j}, \frac{\partial \phi}{\partial x_j}\right) \right\} = 0 \quad ,$$

under arbitrary admissible virtual infinitesimal variations around the physical solutions, δu_i and $\delta\phi$.

If the system is acted upon by external forces/charges, the Hamilton's principle can be generalized simply reformulating it as follows:

$$\delta S[u_i, \phi] + \int_{t_1}^{t_2} dt\, \delta W_{\text{ext}} = \int_{t_1}^{t_2} dt\, \{\delta L[u_i, \phi; t] + \delta W_{\text{ext}}\} = 0 \quad ,$$

where δW_{ext} is the instantaneous external virtual work done by the external agents when virtual variations δu_i and $\delta\phi$ are taken.

Although the further development of the general dynamic problem poses no major problem, we proceed hereafter with the stationary case. In this case, no time dependence arises at any point, so that we can trivially eliminate $\delta\mathcal{K}$ from $\delta\mathcal{L}$ and ignore the integrals $\int_{t_1}^{t_2} dt$. The principle then states that the physical solutions for the displacement and potential fields, $u_i(\boldsymbol{r})$ and $\phi(\boldsymbol{r})$, are determined by the variational condition:

$$-\int_{\mathbb{D}} d^3\boldsymbol{r}\, \delta\mathcal{H}\left(\frac{\partial u_i}{\partial x_j}, \frac{\partial \phi}{\partial x_j}\right) + \delta W_{\text{ext}} = 0 \quad ,$$

or, by using (3.13):

$$\begin{aligned} &-\int_{\mathbb{D}} d^3\boldsymbol{r} \left\{ \sigma_{ij} \frac{\partial \delta u_j}{\partial x_i} + D_m \frac{\partial \delta\phi}{\partial x_m} \right\} + \delta W_{\text{ext}} \\ &= -\int_{\mathbb{D}} d^3\boldsymbol{r}\, \{\sigma_{ij}\, \delta\varepsilon_{ij} - D_m\, \delta E_m\} + \delta W_{\text{ext}} = 0 \quad , \end{aligned} \tag{3.14}$$

under admissible virtual variations around the physical solutions, δu_i and $\delta\phi$. We recognize here the so-called principle of virtual work as generalized to a piezoelectric problem. This principle asserts that, in the equilibrium state, the sum of the external virtual work and the virtual work from internal stresses σ_{ij} and electric displacements D_m during an (admissible) virtual displacement δu_i and potential variation $\delta\phi$ is zero. More specifically, as proposed in Sec. 3.1.1, in our case the external work is due to applied body force f_j and surface traction $\bar{t}_j$ (on $\partial\mathbb{D}_t$) and applied charge density ρ and surface charge $\bar{\varrho}$ (on $\partial\mathbb{D}_\varrho$), and therefore is to be

written as:

$$\delta W_{\text{ext}} = \int_{\mathbb{D}} d^3\boldsymbol{r}\ (f_j\,\delta u_j - \rho\,\delta\phi) + \int_{\partial\mathbb{D}_t} dS\,\bar{t}_j\,\delta u_j - \int_{\partial\mathbb{D}_\varrho} dS\,\bar{\varrho}\,\delta\phi \quad . \tag{3.15}$$

The above equations (3.14) and (3.15) represent the so-called weak formulation of the piezoelectric problem. As said above, they are formulated as a global integral condition that moreover implies weaker requirements on the field variables (only derivatives of u_i ϕ are in principle involved). However, the formal mathematical solution of the above variational equation (weak form of the problem) under the same conditions of continuity and differentiability as the strong problem, is equivalent to the enforcement of the equilibrium equations (3.3) and the boundary conditions 3.4 (strong form of the problem). Indeed, after standard manipulations, the variational principle (3.14) takes the form:[131]

$$\int_{\mathbb{D}} d^3\boldsymbol{r}\,\left\{\frac{\partial\sigma_{ij}}{\partial x_i} + f_k\right\}\,\delta u_j + \int_{\mathbb{D}} d^3\boldsymbol{r}\,\left\{\frac{\partial D_m}{\partial x_m} - \rho\right\}\,\delta\phi$$

$$- \int_{\partial\mathbb{D}_t} dS\,\left\{n_i\sigma_{ij} - \bar{t}_k\right\}\,\delta u_j + \int_{\partial\mathbb{D}_\varrho} dS\,\left\{n_m D_m + \bar{\varrho}\right\}\,\delta\phi = 0 \quad , \tag{3.16}$$

which can be divided into a *body term*:

$$\int_{\mathbb{D}} d^3\boldsymbol{r}\,\left\{\frac{\partial\sigma_{ij}}{\partial x_i} + f_k\right\}\,\delta u_j + \int_{\mathbb{D}} d^3\boldsymbol{r}\,\left\{\frac{\partial D_m}{\partial x_m} - \rho\right\}\,\delta\phi = 0 \quad , \tag{3.17}$$

and a *surface term*:

$$- \int_{\partial\mathbb{D}_t} dS\,\left\{n_i\sigma_{ij} - \bar{t}_k\right\}\,\delta u_j + \int_{\partial\mathbb{D}_\varrho} dS\,\left\{n_m D_m + \bar{\varrho}\right\}\,\delta\phi = 0 \quad . \tag{3.18}$$

When enforced under arbitrary variations, δu_i and $\delta\phi$, compatible with the essential boundary conditions (i.e., $\delta u_i = 0$ on $\partial\mathbb{D}_u$ and $\delta\phi = 0$ on $\partial\mathbb{D}_\phi$), the variational equations (3.17) and (3.18) lead to the differential equations (3.3) and boundary conditions (3.4) characterising the strong form of the problem.

Analytical solutions to the strong form equations are rare and only for geometrically simple problems. On the other hand, semi-analytic or fully numerical approximations are always possible, but again the type of problems that can be treated efficiently is limited. However, the integral formulation in Eqs. (3.14) and (3.15) can be used as a starting point to generate practical and flexible numerical approximation methods. The usual procedure consists in (i) first, choosing a set of explicit and flexible enough trial functions to expand the solutions and its

virtual variations, (ii) then substituting them into (3.14), and (iii) after some algebra one obtains a set of discretized system equations that (iv) when finally solved give much more stable and accurate results, especially for problems of complex geometry. One very popular approach pertaining to this philosophy is the finite element method (FEM). The method consists of dividing the continuum domain $\mathbb{D}$ into subdomains called finite elements. These elements are interconnected at a finite number of points, where unknowns are defined. Within each finite element, unknowns are uniquely defined by the values they assume at the element nodes, by using interpolation functions, usually named shape functions. The introduction of this ansatz into the integral equations leads to a set of well behaved algebraic system equations, which can be efficiently solved for arbitrarily complex geometries and general boundary conditions and applied loads/charges. In this thesis we have adopted the finite element method to derive the numerical solution for various piezoelectric problems. In particular, we have used the commercial implementation offered by the piezoelectric module of the COMSOL Multiphysics software platform.[132]

3.1.4. Application: Bending of a GaN Nanowire

Recently, a new approach for converting nanoscale mechanical energy into electric energy has been demonstrated using piezoelectric NWs.[123,133,134] The typical setup of a piezoelectric nanowire nanogenerator is shown in Fig. 3.2a. The theoretical basis of the nanogenerator and the field of nanopiezotronics arises from the voltage drop created across the cross section of the NW when it is laterally deflected. The surface of the compressed side of the NW will exhibit a negative potential, while the surface of the stretched side will present a positive potential. The piezoelectric potential is created by the polarization of anions and cations inside the NW and will remain as long as the NW is maintained in a deformed configuration, because the polarization charges cannot freely move.

In the previous sections we have presented the theoretical formulation of the general 3D piezoelectric problem. Here we will apply this approach by means of a finite element method (FEM) implementation to model the bending of a GaN nanowire by an AFM tip. This exercise will serve to illustrate the computational cost in directly solving a 3D piezoelectric problem. We investigate the piezoelectric properties in a cylindrical GaN NW using direct 3D finite element calculations. The NW has wurtzite structure and is oriented along the [0001] crystallographic direction. The NW modeled has radius of R =20 nm and length of 200 nm. We assume that the bottom end of the NW is fixed and grounded. An important

detail of our simulation is the mechanism used to apply the force responsible of the NW bending. Experimentally the NW is bent by an AFM tip (See 3.2a). Since it is difficult to realistically model this interaction in our simulation, we have employed a simpler method and used a point force as shown schematically in Fig. 3.2b. Finally, the problem is solved by means of the finite element method as implemented in the software COMSOL Multiphysics. Figure 3.3a illustrates the piezoelectric potential created in the bent GaN NW, which shows highest/lowest values of the in-plane potential of $\pm$ 0.63V. The cross-section is taken at the center of the GaN NW along the axial direction. In Fig. 3.3b we present the piezoelectric potential ϕ as a function of the bending force F_y. As expected, the piezoelectric potential increases with the applied bending force.

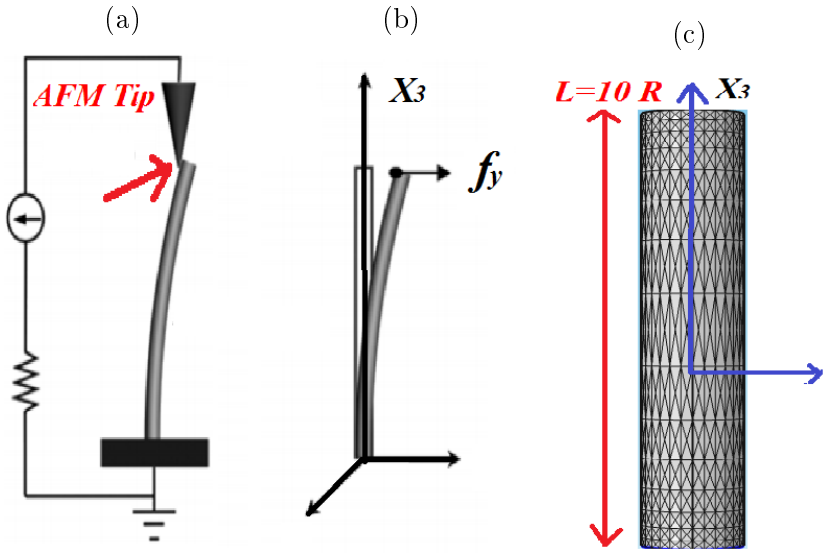

Figure 3.2: (a) Sketch of the experimental set-up of a nanogenerator: A conductive AFM tip scans over a GaN NW, resulting in mechanical deflection and piezoelectric polarization in the NW. (b) Simplified model of the AFM tip action for the FEM simulations. (c) Geometry of the GaN nanowire investigated with details about the mesh employed.

The meshes used in the 3D FEM calculations are created by using quadrilateral mesh with maximum element size 5 nm (See Fig. 3.2c). The number of degrees of freedom is 295956 and it took 5 minutes to solve the problem on personal computer, which required 5GB of memory. If one wants to perform repeated calculations by parametric changes of, say, the force or the geometrical parameters, the computational cost scales up rapidly. We can see then that direct 3D simulation of Eq. 3.2 is computationally expensive, especially when repeated calculations are necessary, e.g. to explore the space of parameters of the problem. In the following section we

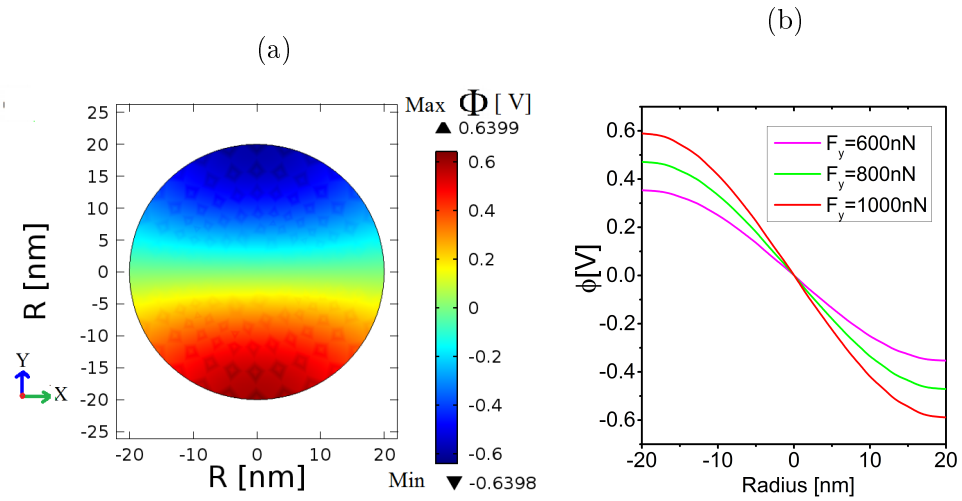

Figure 3.3: (a) Potential distribution across the transverse section of a GaN NW with radius 20 nm and length 200 nm under a lateral bending force of F_y=1000 nN, as obtained by using direct 3D finite element calculations. (b) Linescan of the piezoelectric potential ϕ along the Y-axis for various values of the bending force F_y.

will develop an alternative, computationally efficient, two-dimensional approach to solve the fully-coupled equations Eq. 3.2 for general wire-like systems.

3.2. The Generalized Plane Piezoelectric (GPP) Problem

As we have see in the previous section, the direct simulation of fully-coupled 3D piezoelectric problems is costly in terms of the required computing time and resources. One possibility to overcome these difficulties for a broad class of problems is to approximate the original fully-coupled 3D piezoelectric problem into a 2D piezoelectric problem, as will be explained in detail in this section.

3.2.1. Motivation and Hypothesis

Many 2D approaches to original 3D piezoelectric problems rely on the so-called plane strain (and field) approximation[135–137] This approximation is applied typically to elongated systems (e.g., along the X_3 axis) and assumes that $u_3 = 0$ and $E_3 = 0$, and that the remaining components depend only on the in-plane coordinates (x_1, x_2). We shall use here the term *plane piezoelectric* problem or approximation to refer to this situation. However, this approximation has limitations: there

are many piezoelectric problems involving specific crystal structures, orientations and loading conditions, where the medium develops out-of-plane axial (ε_{33}) and/or shear (ε_{13} and ε_{23}) strain components and/or axial electric field component (E_3), resulting in more general deformation and field states that cannot be captured by the plane piezoelectric approach. To overcome such limitations we propose in this work a more general 2D approach, which is called here the *generalized plane piezoelectric (GPP)* problem.

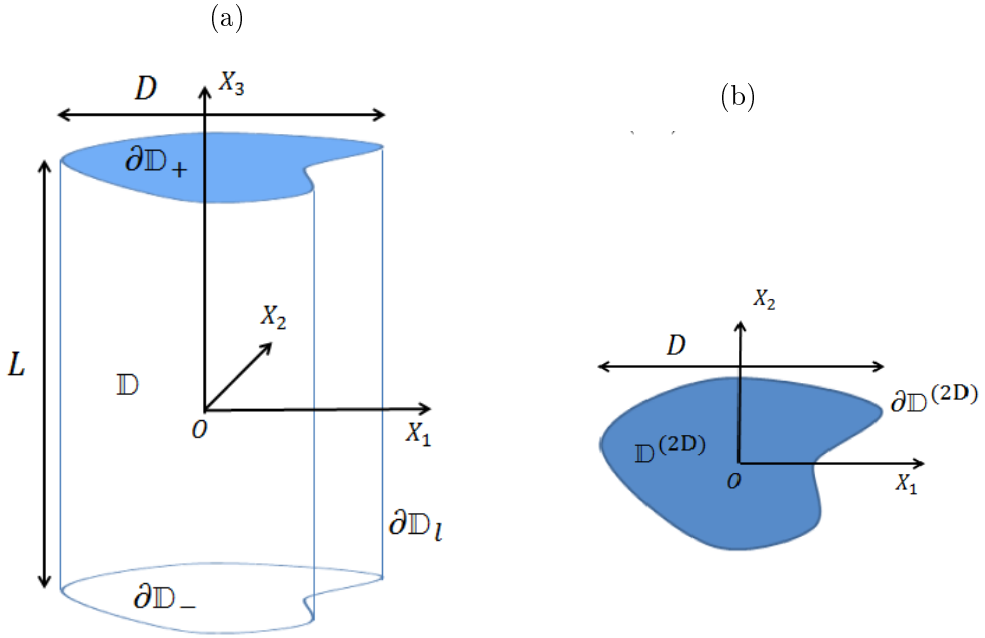

Figure 3.4: Sketch of the geometry of the generalized plane piezoelectric problem: (a) 3D geometry and (b) 2D cross section.

More specifically, the class of problems adapted to the GPP approach to be developed below correspond to the situation sketched in Fig. 3.4(a): The geometry of the general piezoelectric body of Fig. 3.1 is further restricted here by assuming a right cylindrical shape, oriented along the X_3 axis (hereafter referred as the longitudinal axis), and with constant cross section. The axial length of the system is in principle finite with magnitude L. In this geometry, the boundary delimiting $\mathbb{D}$ can be naturally decomposed as $\partial\mathbb{D} = \partial\mathbb{D}_l \bigcup \partial\mathbb{D}_+ \bigcup \partial\mathbb{D}_-$, where $\partial\mathbb{D}_l$ is the lateral surface of the cylinder, and $\partial\mathbb{D}_\pm$ are the two extreme sections of the body, at $x_3 = \pm\frac{L}{2}$. The transversal section of $\mathbb{D}$ determines a 2D domain $\mathbb{D}^{(2D)}$, its boundary $\partial\mathbb{D}^{(2D)}$ being determined by the transversal section of $\partial\mathbb{D}_l$ (see Fig. 3.4(b)). In addition, we assume that the material constants are independent of the axial coordinate x_3. The system may be subjected to body or boundary loads and/or displacement restrictions, as well as impressed charges and/or applied potentials,

as explained in Sec. 3.1.1, but we assume that the quantities representing these actions are also independent of the x_3 coordinate.

Even after all these assumptions, due to the end effects, the problem is still 3D, i.e., ε_{ij} and E_m depend on (x_1, x_2, x_3). If we are interested in the exact solution (particularly, the behavior near the ends of the system), there is no option but to solve the genuine 3D problem. However, in many cases the system has a high aspect ratio, i.e., $L \gg D$ (say $L/D \gtrsim 2-3$), where D is the largest dimension of the cross section $\mathbb{D}^{(2D)}$ (see Fig. 3.4(b)). For such a system, the Saint-Venant's principle of linear elasticity suggests that, far from the end sections $\partial\mathbb{D}_{\pm}$, *it is expected* that all the cross sections along the longitudinal axis can be considered to be at identical conditions.[138,139] Hence, the strain and electric field distribution at the central part of the body can be described as invariant along the longitudinal X_3 direction and dependent at most on the in-plane coordinates (x_1, x_2)[85,140]:

$$\varepsilon_{ij} = \varepsilon_{ij}(x_1, x_2)\,, \tag{3.19a}$$

$$E_m = E_m(x_1, x_2)\,. \tag{3.19b}$$

Note that here it is not required a priori that any strain and/or electric field component vanishes, in contrast to the assumptions of the standard plane piezoelectric approximation. In the following, we examine in detail the consequences of the ansatz (3.19).

In the first place, by carefully integrating the kinematical relations (3.1) with respect to x_3, under the constraint (3.19), the following general expressions of the displacement field and the electric potential are obtained:

$$u_1(x_1, x_2, x_3) = U_1(x_1, x_2) - \frac{1}{2}\frac{1}{R_1}{x_3}^2 + \theta x_2 x_3\,, \tag{3.20a}$$

$$u_2(x_1, x_2, x_3) = U_2(x_1, x_2) - \frac{1}{2}\frac{1}{R_2}{x_3}^2 - \theta x_1 x_3\,, \tag{3.20b}$$

$$u_3(x_1, x_2, x_3) = U_3(x_1, x_2) + \varepsilon_{\parallel} x_3 + \frac{1}{R_1} x_1 x_3 + \frac{1}{R_2} x_2 x_3\,, \tag{3.20c}$$

$$\phi(x_1, x_2, x_3) = \Phi(x_1, x_2) - E_{\parallel} x_3\,, \tag{3.21}$$

where $\varepsilon_{\parallel}$, R_1, R_2, θ, and $E_{\parallel}$ are constants, and $U_i(x_1, x_2)$ $(i = 1, 2, 3)$ and $\Phi(x_1, x_2)$ are mathematically 2D fields. As shown below, all of these quantities will have to be determined ultimately from the equilibrium equations subjected to the boundary conditions. By introducing the expressions (3.20) and (3.21) into Eq. (3.1), we can

also obtain the general form of the strain tensor:

$$\varepsilon_{ij}(x_1,x_2) = \varepsilon_{ij}^{(U)}(x_1,x_2) + \varepsilon_{ij}^{(\bullet)}(x_1,x_2)\,, \tag{3.22a}$$

$$\varepsilon_{ij}^{(U)}(x_1,x_2) \leftrightarrow \begin{pmatrix} \frac{\partial U_1}{\partial x_1} & \frac{1}{2}(\frac{\partial U_1}{\partial x_2} + \frac{\partial U_2}{\partial x_1}) & \frac{1}{2}\frac{\partial U_3}{\partial x_1} \\ \times & \frac{\partial U_2}{\partial x_2} & \frac{1}{2}\frac{\partial U_3}{\partial x_2} \\ \times & \times & 0 \end{pmatrix}, \tag{3.22b}$$

$$\varepsilon_{ij}^{(\bullet)}(x_1,x_2) \leftrightarrow \begin{pmatrix} 0 & 0 & +\frac{1}{2}\theta x_2 \\ 0 & 0 & -\frac{1}{2}\theta x_1 \\ \times & \times & \varepsilon_\parallel + \frac{1}{R_1}x_1 + \frac{1}{R_2}x_2 \end{pmatrix}, \tag{3.22c}$$

and the electric field:

$$\boldsymbol{E}(x_1,x_2) = \begin{pmatrix} -\frac{\partial \Phi}{\partial x_1} \\ -\frac{\partial \Phi}{\partial x_2} \\ 0 \end{pmatrix} + \begin{pmatrix} 0 \\ 0 \\ E_\parallel \end{pmatrix} \equiv \boldsymbol{E}^{(\Phi)}(x_1,x_2) + E_\parallel \boldsymbol{u}_3\,. \tag{3.23}$$

The symbol $\times$ in Eqs. (3.22b) and (3.22c) means that the corresponding matrix elements are obtained from the symmetry of the strain tensor. Moreover, the inspection of (3.22) and (3.23) provides a clear interpretation of the different constants and fields introduced in Eqs. (3.20) and (3.21). Thus, the vector field (U_1, U_2, U_3) represents the part of the displacement which is invariant along the X_3 axis. The out-of-plane displacement U_3 is commonly called the warping function. Further, Φ is the part of the potential leading to the in-plane projection of the field. It will be called hereafter the in-plane piezoelectric potential. The constants $\varepsilon_\parallel$, R_1, R_2, θ, and $E_\parallel$ have the following meaning:

- $\varepsilon_\parallel$ is the axial strain describing the relative elongation of the of the system along the X_3 axis.
- R_1 (R_2) is the curvature radius associated to the bending of the body in the X_1X_3 (X_2X_3) plane.
- θ is the twist per unit length associated to the torsion of the body about the X_3 axis.
- $E_\parallel$ is the electric field along the X_3 axis.

The general form of the stress tensor and electric displacement field compatible with the ansatz (3.19) are obtained by combining Eqs. (3.22) and (3.23) with the

constitutive relations (3.2) to obtain:

$$\sigma_{ij}(x_1, x_2) = \sigma_{ij}^{(U\Phi)}(x_1, x_2) + \sigma_{ij}^{(\bullet)}(x_1, x_2)\,, \tag{3.24a}$$

$$\sigma_{ij}^{(U\Phi)}(x_1, x_2) = C_{ijkl}\,\varepsilon_{kl}^{(U)}(x_1, x_2) - e_{nij}\,E_n^{(\Phi)}(x_1, x_2)\,, \tag{3.24b}$$

$$\sigma_{ij}^{(\bullet)}(x_1, x_2) = C_{ijkl}\,\varepsilon_{kl}^{(\bullet)}(x_1, x_2) - e_{nij}\,E_{\|}\delta_{n3}\,. \tag{3.24c}$$

$$D_m(x_1, x_2) = D_m^{(U\Phi)}(x_1, x_2) + D_m^{(\bullet)}(x_1, x_2)\,, \tag{3.25a}$$

$$D_m^{(U\Phi)}(x_1, x_2) = e_{mkl}\,\varepsilon_{kl}^{(U)}(x_1, x_2) + \epsilon_{mn}\,E_n^{(\Phi)}(x_1, x_2)\,, \tag{3.25b}$$

$$D_m^{(\bullet)}(x_1, x_2) = e_{mkl}\,\varepsilon_{kl}^{(\bullet)}(x_1, x_2) + \epsilon_{mn}\,E_{\|}\delta_{n3}\,. \tag{3.25c}$$

To sum up, the condition (3.19) has been shown to determine the most general form of the various fields as expressed in detail by Eqs. (3.20)-(3.25). The piezoelectric problem that complies with that condition and the consequent field pattern is here called a *generalized plane piezoelectric (GPP)* problem. If the materials involved are not piezoelectric (i.e., $e_{nij} = 0$) we would encounter uncoupled *generalized plane strain (GPS)* and *generalized plane electrostatic* problems. Note that in a GPP problem the strain and electric field are independent of x_3, but the mechanical displacement and electric potential can depend on x_3 as well as on (x_1, x_2). If one further requires that $\frac{\partial u_i}{\partial x_3} = 0 = \frac{\partial \phi}{\partial x_3}$, then the standard plane piezoelectric problem is recovered. It is worth mentioning that other authors have used the *generalized plane* qualification for problems with a more restricted scope than our defining condition (3.19) (see Ref.[140–143]). Those problems can always be treated as particular cases of the general situation described in this paper.

3.2.2. Equilibrium Equations

So far, we have specified the structure of the fields for the GPP problem. It is necessary now to establish the corresponding form of the equilibrium equations.

First, we introduce the GPP form of the stress (3.24) and electric displacement (3.25) into the general 3D equilibrium equations (3.3) to obtain:

$$\frac{\partial \sigma_{\alpha j}^{(U\Phi)}}{\partial x_\alpha} + \frac{\partial \sigma_{\alpha j}^{(\bullet)}}{\partial x_\alpha} = -f_j(x_1, x_2)\,, \tag{3.26a}$$

$$\frac{\partial D_\alpha^{(U\Phi)}}{\partial x_\alpha} + \frac{\partial D_\alpha^{(\bullet)}}{\partial x_\alpha} = \rho(x_1, x_2)\,. \tag{3.26b}$$

Hereafter, the Latin indices continue to run over all spatial directions, i.e., i, j, k, l, $m, n = 1, 2, 3$, whereas Greek indices will run only over in-plane directions, i.e., $\alpha, \beta = 1, 2$. Note that σ_{33} and D_3 do not appear in the equilibrium equations, since they are determined by the remaining components, as can be shown by making use of the inverse constitutive equations relating ε_{33} and E_3 to σ_{ij} and D_m.

Finally, after inserting Eqs. (3.22) and (3.23) into Eqs. (3.24) and (3.25), one gets expressions for the stress tensor and electric displacement vector in terms of the fields U_i and Φ. These expressions can be entered into Eq. (3.26) to produce the GPP problem equilibrium equations, that read in a compact matrix form as:

$$\begin{pmatrix} \hat{L}_{11} & \hat{L}_{12} & \hat{L}_{13} & \hat{L}_{14} \\ \hat{L}_{21} & \hat{L}_{22} & \hat{L}_{23} & \hat{L}_{24} \\ \hat{L}_{31} & \hat{L}_{32} & \hat{L}_{33} & \hat{L}_{34} \\ \hat{L}_{41} & \hat{L}_{42} & \hat{L}_{43} & \hat{L}_{44} \end{pmatrix} \begin{pmatrix} U_1 \\ U_2 \\ U_3 \\ \Phi \end{pmatrix} = \begin{pmatrix} -f_1^{(\bullet)} \\ -f_2^{(\bullet)} \\ -f_3^{(\bullet)} \\ \rho^{(\bullet)} \end{pmatrix} \quad , \tag{3.27}$$

where the matrix elements $\hat{L}_{jk}$ are linear differential operators defined as:

$$\begin{aligned} \hat{L}_{jk} &= \frac{\partial}{\partial x_\alpha}\, C_{\alpha j \beta k}\, \frac{\partial}{\partial x_\beta} \quad , \\ \hat{L}_{j4} &= \frac{\partial}{\partial x_\alpha}\, e_{\beta,\alpha j}\, \frac{\partial}{\partial x_\beta} \quad , \\ \hat{L}_{4k} &= \frac{\partial}{\partial x_\alpha}\, e_{\alpha,\beta k}\, \frac{\partial}{\partial x_\beta} \quad , \\ \hat{L}_{44} &= -\frac{\partial}{\partial x_\alpha}\, \epsilon_{\alpha\beta}\, \frac{\partial}{\partial x_\beta} \quad , \end{aligned} \tag{3.28}$$

the inhomogeneous terms $f_j^{(\bullet)}$ are modified body forces given by

$$f_j^{(\bullet)} = f_j + \frac{\partial \sigma_{\alpha j}^{(\bullet)}}{\partial x_\alpha} \quad , \tag{3.29}$$

and $\rho^{(\bullet)}$ is a modified charge density given by

$$\rho^{(\bullet)} = \rho - \frac{\partial D_\alpha^{(\bullet)}}{\partial x_\alpha} \quad . \tag{3.30}$$

The above equations can be applied for inhomogeneous material properties, but remember that in the context of the GPP problem they may depend at most on

the in-plane coordinates, i.e., $C_{ijkl}(x_1, x_2)$, $e_{nij}(x_1, x_2)$ and $\epsilon_{mn}(x_1, x_2)$.

For general anisotropic piezoelectric materials, the out-of-plane displacement (warping function) U_3 is coupled to the in-plane displacements U_α and potential Φ. However, in the case of materials for which $C_{I4} = 0 = C_{I5}$ (for $I = 1, 2, 6$) and $e_{\beta 4} = 0 = e_{\beta 5}$ (for $\beta = 1, 2$), one gets that $\hat{L}_{\alpha 3} = 0 = \hat{L}_{3\alpha}$ ($\alpha = 1, 2$) and $\hat{L}_{43} = 0 = \hat{L}_{34}$, and therefore the equilibrium equations simplify as follows:

$$\begin{pmatrix} \hat{L}_{11} & \hat{L}_{12} & 0 & \hat{L}_{14} \\ \hat{L}_{21} & \hat{L}_{22} & 0 & \hat{L}_{24} \\ 0 & 0 & \hat{L}_{33} & 0 \\ \hat{L}_{41} & \hat{L}_{42} & 0 & \hat{L}_{44} \end{pmatrix} \begin{pmatrix} U_1 \\ U_2 \\ U_3 \\ \Phi \end{pmatrix} = \begin{pmatrix} -f_1^{(\bullet)} \\ -f_2^{(\bullet)} \\ -f_3^{(\bullet)} \\ \rho^{(\bullet)} \end{pmatrix} \quad , \tag{3.31}$$

the differential equation related to the warping function U_3 being decoupled from the in-plane problem associated to (U_1, U_2, Φ). The above requirements on the material constants hold for specific situations of interest, such as the case of diamond- and zincblende-based systems with their longitudinal axis along the [001] direction (see Appendix D.2) and wurtzite-type systems along the [0001] direction. There are other interesting cases, such as the diamond- and zincblende-based systems with axis along the [111] direction, that do not comply with the above material symmetry requirements (see Appendix D.2) and they exhibit a warping function fully-coupled into the piezoelectric problem as illustrated by the numerical results in Sec.3.3.

As commented at the end of Sec. 3.2.1, in the case of general non-piezoelectric materials with $e_{nij} = 0$, one has to deal separately with the uncoupled 2D electrostatic and elastic problems. The electrostatic problem amounts to solve the 2D Poisson equation. In the absence of body and surface charges or potentials, though, one is left only with a purely elastic *generalized plane strain* (*GPS*) problem[144]:

$$\begin{pmatrix} \hat{L}_{11} & \hat{L}_{12} & \hat{L}_{13} \\ \hat{L}_{21} & \hat{L}_{22} & \hat{L}_{23} \\ \hat{L}_{31} & \hat{L}_{32} & \hat{L}_{33} \end{pmatrix} \begin{pmatrix} U_1 \\ U_2 \\ U_3 \end{pmatrix} \equiv \begin{pmatrix} -f_1^{(\bullet)} \\ -f_2^{(\bullet)} \\ -f_3^{(\bullet)} \end{pmatrix} . \tag{3.32}$$

As before, there exists, in general, the coupling between (U_1, U_2) and U_3. Only for materials with $C_{I4} = 0 = C_{I5}$ (for $I = 1, 2, 6$), the equilibrium equations become uncoupled and simplify as:

$$\begin{pmatrix} \hat{L}_{11} & \hat{L}_{12} & 0 \\ \hat{L}_{21} & \hat{L}_{22} & 0 \\ 0 & 0 & \hat{L}_{33} \end{pmatrix} \begin{pmatrix} U_1 \\ U_2 \\ U_3 \end{pmatrix} \equiv \begin{pmatrix} -f_1^{(\bullet)} \\ -f_2^{(\bullet)} \\ -f_3^{(\bullet)} \end{pmatrix} . \tag{3.33}$$

3.2.3. Boundary Conditions

In this section we define appropriate boundary conditions for the GPP problem. Given the special geometry displayed in Fig. 3.4, we must distinguish between those conditions that must be satisfied at the lateral surface $\partial\mathbb{D}_l$ from those at the end surfaces $\partial\mathbb{D}_\pm$ of the piezoelectric body.

Although more general settings are possible, we examine here the boundary conditions corresponding to fixing the tractions and charges at the surfaces (Neumann−type boundary conditions).

Lateral Surface Boundary Conditions

It is assumed here that the problem requires the specification on the lateral surface of the applied traction force $\bar{t}_i$ and impressed surface charge density $\bar{\varrho}$. When working on the 2D cross section of the problem, this implies the following requirements:

$$n_\alpha \sigma_{\alpha j} = \bar{t}_j \,, \tag{3.34a}$$

$$-n_\alpha D_\alpha = \bar{\varrho} \,, \tag{3.34b}$$

to be satisfied on the boundary $\partial\mathbb{D}^{(2D)}$.

End Surface Boundary Conditions

According to the Saint-Venant's principle, originally stated for an elastic problem,[139] the point-wise specification of the imposed tractions at the end surfaces of a finite but long body is only necessary if the adjacent regions are to be studied. Far from those extreme sections, at the central region of the body, *it is expected* that the influence of the detailed distribution of end tractions becomes negligible and the solution of the problem is only affected by the total force and torque.[85] Therefore, to specify completely the GPP problem it should be enough to prescribe the resulting force $\boldsymbol{F} = (F_1, F_2, F_3)$ and torque $\boldsymbol{M} = (M_1, M_2, M_3)$, as well as the net charge Q, on the end surfaces:

$$\int_{\mathbb{D}^{(2D)}} dx_1 dx_2 \, \sigma_{3j}(x_1, x_2) = F_j \,, \tag{3.35a}$$

$$\int_{\mathbb{D}^{(2D)}} dx_1 dx_2 \, \eta_{j\beta k} \, x_\beta \, \sigma_{3k}(x_1, x_2) = M_j \,, \tag{3.35b}$$

$$-\int_{\mathbb{D}^{(2D)}} dx_1 dx_2\, D_3(x_1, x_2) = Q\,, \tag{3.35c}$$

where η_{jlk} is the completely antisymmetric tensor. Note that within the GPP problem the same boundary conditions must apply at both extreme surfaces, and indeed to every transverse section of the system, as expressed by (3.35).

3.2.4. Overview

The theoretical framework defined by the set of equations Eq. (3.20)- (3.30), together with boundary conditions (3.34) and (3.35), constitutes the mathematically 2D *generalized plane piezoelectric (GPP)* problem. Since $f_i^{(\bullet)}$ and $\rho^{(\bullet)}$ depend implicitly on $\varepsilon_{\|}$, R_1, R_2, θ, and $E_{\|}$, the non-homogeneous system of coupled partial differential equations (3.27) must be solved under appropriate boundary conditions, in a self-consistent manner, for the unknown in-plane fields $U_i(x_1, x_2)$ and $\Phi(x_1, x_2)$ and constants $(\varepsilon_{\|}, R_1, R_2, \theta, E_{\|})$. We note that, although not carried further on here, the solutions of the homogeneous version of system (3.27) can be conveniently studied by using the Stroh formalism[84].

The GPP problem has been introduced as a good *approximation*, in the sense of the Saint-Venant's principle, for the central region of 3D finite (length L) but *high aspect-ratio* systems, whose transverse section, material properties, loads (forces and charges) and boundary (and interface) conditions are translationally invariant along their longitudinal direction. Alternatively, if the limit $L \to \infty$ is taken, the above approximation becomes an exact picture for the whole system, and therefore the GPP can also be viewed as an *exact representation* for an *idealized infinite system* with homogeneous physics along the longitudinal direction.

3.2.5. Weak Form of the GPP Problem

In this section we are going to particularize the weak formalism of Sec. 3.1.3 taking into account the specific features of the GPP problem. By taking into account the particular form of u_i and ϕ within the GPP problem, their variations adopt the form:

$$\delta u_1 = \delta U_1(x_1, x_2) - \frac{1}{2}\delta\left(\frac{1}{R_1}\right) {x_3}^2 + \delta\theta x_2 x_3\,, \tag{3.36a}$$

$$\delta u_2 = \delta U_2(x_1, x_2) - \frac{1}{2}\delta\left(\frac{1}{R_2}\right) {x_3}^2 - \delta\theta x_1 x_3\,, \tag{3.36b}$$

$$\delta u_3 = \delta U_3(x_1, x_2) + \delta\varepsilon_{\|} x_3 + \delta\left(\frac{1}{R_1}\right) x_1 x_3 + \delta\left(\frac{1}{R_2}\right) x_2 x_3\,, \tag{3.36c}$$

$$\delta\phi = \delta\Phi(x_1, x_2) - \delta E_{\|} x_3\,. \tag{3.37}$$

There are associated variations of the strain field:

$$\delta\varepsilon_{ij}(x_1, x_2) = \delta\varepsilon_{ij}^{(U)}(x_1, x_2) + \delta\varepsilon_{ij}^{(\bullet)}(x_1, x_2)\,, \tag{3.38}$$

and the electric field:

$$\delta E_m(x_1, x_2) = -\delta\frac{\partial\Phi(x_1, x_2)}{\partial x_m} + \delta_{m,3}\,\delta E_{\|}\,. \tag{3.39}$$

Now we analyze the variational equations of the piezoelectric problem under the variations compatible with the GPP problem. On one hand, when taking into account the variations (3.36) and (3.37), and the special form of the stress and electric diplacement fields within the GPP problem, the body term (3.17) immediately leads to the equilibrium equations (3.26). We turn now to the surface term (3.18). As said before, we only treat here the case of pure natural (Neumann) boundary conditions, and therefore, in the expression (3.18) we can make

$$\partial\mathbb{D}_t \to \partial\mathbb{D} \quad \text{and} \quad \partial\mathbb{D}_\varrho \to \partial\mathbb{D} \quad ,$$

and the virtual variations δu_i and $\delta\phi$ are unrestricted. Moreover, according to the geometry described in Fig. 3.4(a), the surfaces are as:

$$\partial\mathbb{D} = \partial\mathbb{D}_l \cup \partial\mathbb{D}_- \cup \partial\mathbb{D}_+ \quad ,$$

which leads to a corresponding separation of the variational equation (3.18) into three associated equations. The enforcement of the variational equation on the lateral surface $\partial\mathbb{D}_l$ also leads to the boundary conditions (3.34).

The variational equations on the end surfaces $\partial\mathbb{D}_-$ (i.e., at $x_3 = -\frac{L}{2}$) and $\partial\mathbb{D}_+$ (i.e., at $x_3 = +\frac{L}{2}$) require a more careful treatment. Let us in principle assume that there is a distribution of tractions $\bar{t}_j^{(\pm)}(x_1, x_2)$ and surface charge density $\bar{\varrho}^{(\pm)}(x_1, x_2)$ applied on the surface $\partial\mathbb{D}_\pm$. The enforcement of the variational equations on $\partial\mathbb{D}_\pm$ with respect to variations δU_i and $\delta\Phi$ leads immediately to the condition:

$$\bar{t}_j^{(-)}(x_1, x_2) = -\bar{t}_j^{(+)}(x_1, x_2) \quad \text{and} \quad \bar{\varrho}^{(-)}(x_1, x_2) = -\bar{\varrho}^{(+)}(x_1, x_2) \quad ,$$

which restricts the types of applied end loads/charges compatible with the GPP problem. Now, the analysis of the variational equation on $\partial\mathbb{D}_{\pm}$ with respect to variations $\delta\left(\frac{1}{R_1}\right)$, $\delta\left(\frac{1}{R_2}\right)$, $\delta\theta$, $\delta\varepsilon_{\|}$ and $\delta E_{\|}$ gives:[2]

$$\left\{\int_{\mathbb{D}^{(2D)}} dx_1\, dx_2\, x_1\, \sigma_{33}(x_1,x_2) - (-M_2)\right\}\delta\left(\frac{1}{R_1}\right) = 0\,, \quad (3.40a)$$

$$\left\{\int_{\mathbb{D}^{(2D)}} dx_1\, dx_2\, \sigma_{31}(x_1,x_2) - F_1\right\}\delta\left(\frac{1}{R_1}\right) = 0\,, \quad (3.40b)$$

$$\left\{\int_{\mathbb{D}^{(2D)}} dx_1\, dx_2\, x_2\, \sigma_{33}(x_1,x_2) - (+M_1)\right\}\delta\left(\frac{1}{R_2}\right) = 0\,, \quad (3.40c)$$

$$\left\{\int_{\mathbb{D}^{(2D)}} dx_1\, dx_2\, \sigma_{32}(x_1,x_2) - F_2\right\}\delta\left(\frac{1}{R_2}\right) = 0\,, \quad (3.40d)$$

$$\left\{\int_{\mathbb{D}^{(2D)}} dx_1\, dx_2\, \left[x_2\, \sigma_{31}(x_1,x_2) - x_1\, \sigma_{32}(x_1,x_2)\right] - (-M_3)\right\}\delta\theta = 0\,, \quad (3.40e)$$

$$\left\{\int_{\mathbb{D}^{(2D)}} dx_1\, dx_2\, \sigma_{33}(x_1,x_2) - F_3\right\}\delta\varepsilon_{\|} = 0\,, \quad (3.40f)$$

$$\left\{-\int_{\mathbb{D}^{(2D)}} dx_1\, dx_2\, D_3(x_1,x_2) - Q\right\}\delta E_{\|} = 0\,, \quad (3.40g)$$

where

$$F_j = \int_{\partial\mathbb{D}_+} dx_1 dx_2\, \bar{t}_j^{(+)}(x_1,x_2)$$

is the total force applied on $\partial\mathbb{D}_+$,

$$M_j = \int_{\partial\mathbb{D}_+} dx_1 dx_2\, \eta_{j\beta k}\, x_\beta\, \bar{t}_k^{(+)}(x_1,x_2) \quad ,$$

with η_{jlk} the completely antisymmetric tensor, is the total torque applied on the system, and

$$Q = \int_{\partial\mathbb{D}_+} dx_1 dx_2\, \bar{\varrho}^{(+)}(x_1,x_2)$$

is the total surface charge on $\partial\mathbb{D}_+$.

The enforcement of Eqs. (3.40) leads to the boundary conditions (3.35) and this shows that, in agreement with the Saint-Venant principle, in order to fully specify the GPP problem it is not necessary to specify in detail the distributions $\bar{t}_j^{(+)}(x_1,x_2)$ and $\bar{\varrho}^{(+)}(x_1,x_2)$ but it suffices to give the global values F_j, M_j and Q.

[2] We take into account here that $\partial\mathbb{D}_+ = \mathbb{D}^{(2D)}$.

This closes the weak formulation of the GPP problem. In the calculations shown below we have employed a finite element method based on that formulation as implemented in the COMSOL Multiphysics software platform.[132] However, the 2D modules of this platform only provide the plane piezoelectric approximation. Therefore, with the help of the presented theoretical formalism we have adapted the software to include the solution for the warping field $U_3(x_1, x_2)$ and the parameters $\left(\varepsilon_\parallel, \frac{1}{R_1}, \frac{1}{R_2}, \theta, E_\parallel\right)$.

3.3. Application to Core-Shell Nanowires

To illustrate the use and utility of the generalized plane (GPS and GPP) approaches, we present in this section numerical results of the strain and electric field distributions in a lattice-mismatched core-shell nanowire (CSNW), a system which has been studied extensively in recent years[145–151].

In this work we have opted to solve numerically for the strain and electric fields by using the finite element method (FEM), as implemented in the COMSOL Multiphysics software platform.[132,152,153] We will first study the purely elastic problem as manifested in Ge/Si(111) and Si/Ge(111) core-shell nanowires.[149,154–156] Further applications of the developed model are illustrated by studying the In-concentration dependence of the strain distribution in WZ [0001] InN/$\mathrm{In}_x\mathrm{GaN}_{1-x}$ CSNWs and the thermoelastic properties of Ge/Si(111) CSNWs. Finally, we will consider a system that exhibits reasonably strong piezoelectric effects, namely the zincblende InN/GaN(111) and GaN/InN(111) core-shell nanowires, which have also been studied recently.[157–161]

We have performed 2D generalized plane calculations according to the framework introduced in Sec. 3.2 for a nanowire of radius R_{NW} (to be precisely specified below). In addition, in order to test the quality of our GPS/GPP approaches, in both cases we have also performed fully 3D computations for a finite but long nanowire. The nanowire length L is chosen such that the system has a high aspect ratio, i.e., $L/(2R_{\mathrm{NW}}) \gg 1$. The later calculations (more precisely, the results at the central cross section) are then compared with those obtained from the 2D GPS/GPP approaches. From the comparison, we can ascertain under what circumstances the generalized plane approaches represent a good approximation to the central part of 3D systems, thereby quantifying their accuracy and limitations.

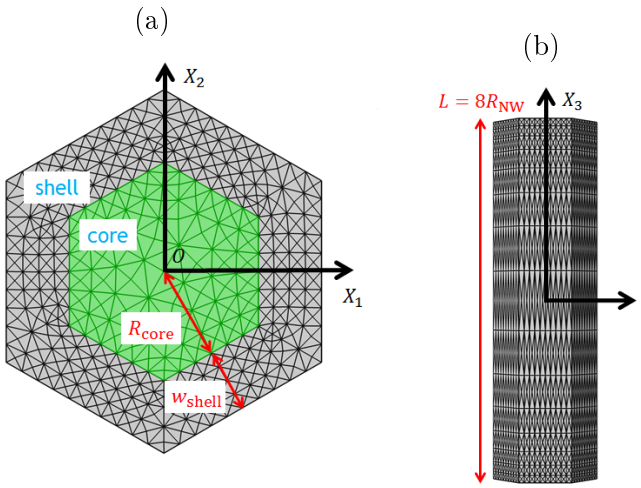

Figure 3.5: Geometry of the core-shell nanowire investigated, with the meshes employed in the FEM calculations. (a) The hexagonal cross section is characterized by the values of the core radius R_{core} and the width of the shell w_{shell}. The total radius of the nanowire is then $R_{\text{NW}} = R_{\text{core}} + w_{\text{shell}}$. (b) Lateral view of the finite nanowire considered for the 3D simulations. The length used is $L = 8R_{\text{NW}}$.

3.3.1. Elasticity Problem in Core-Shell Nanowires

Ge/Si Core-Shell Nanowires

First, we will apply the GPS approach to study a purely elastic problem corresponding to a Ge/Si(111) core-shell nanowire. The core is made of Ge and the shell is made of Si. The geometry of the nanowire is shown in Fig. 3.5. The cross section is assumed to be hexagonal and it is characterized by the values of the core radius R_{core} and the width of the shell w_{shell}. The total radius of the nanowire is then $R_{\text{NW}} = R_{\text{core}} + w_{\text{shell}}$. Within the linear elastic continuum theory the distribution of the strain fields does not depend on the absolute dimensions but on their relative size, in this case on $w_{\text{shell}}/R_{\text{core}}$.

Ge and Si have diamond crystalline structure and therefore exhibit macroscopic cubic O_h symmetry, which is fully taken into account in the following calculations. We have chosen the longitudinal axis $\hat{X}_3 \equiv Z$ of the nanowire to be along the [111] crystallographic direction, whereas the axes $\hat{X}_1 \equiv X$ and $\hat{X}_2 \equiv Y$ are taken along $[10\bar{1}]$ and $[\bar{1}2\bar{1}]$ directions, respectively. The matrix of elastic constants $\hat{C}_{IK}$ corresponding to the above axes can be found in Appendix D.2. It is apparent there that, since $\hat{C}_{14}, \hat{C}_{24}(= -\hat{C}_{14}) \neq 0$, it is not possible the decoupling leading to Eq. 3.33, and it is expected a nonvanishing warping function U_3 coupled to the in-plane deformation (U_1, U_2).

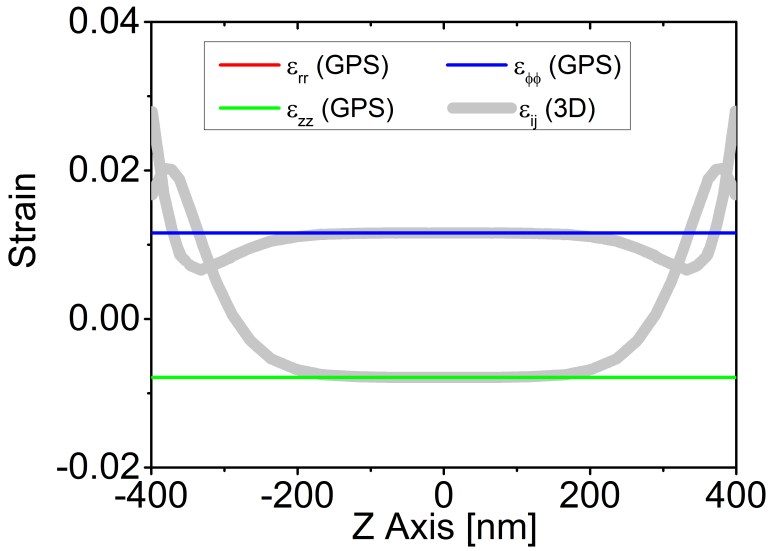

Figure 3.6: Linescans of the strain components ε_{rr}, $\varepsilon_{\phi\phi}$ and ε_{zz} along the axis of a finite Ge/Si(111) nanowire, as obtained from the 3D calculations. Note that $\varepsilon_{rr} = \varepsilon_{\phi\phi}$ along the nanowire axis. For comparison the results corresponding to an infinite nanowire as obtained by means of the GPS approach are also displayed.

We assume that the nanowire is free from external traction and body forces (i.e., $\bar{t}_j, F_j, M_j, f_j = 0$), so that the strain is solely induced by the internal lattice mismatch between the core (inclusion, I) and shell (matrix, M) regions, through the body force $f_i^{(0)}$ given by Eq. (3.12a). The lattice parameters and elastic constants used in the calculations can be found in Appendix E. For cubic materials there is only one lattice parameter, $a_i \to a_0$, and therefore the misfit strain is diagonal, with magnitude $\varepsilon^{(\text{misfit})} = -0.039$ (3.9 %). The negative sign indicates that the strain is compressive.

We have taken the following numerical values for the geometry parameters (see Fig. 3.5): $R_{\text{core}} = 60$ nm, w_{shell} 40 nm, so that $R_{\text{NW}} = R_{\text{core}} + w_{\text{shell}} = 100$ nm. Therefore, we have $w_{\text{shell}}/R_{\text{core}} = 2/3$. For the 3D calculations we have taken $L = 8R_{\text{NW}}$, so that the aspect ratio is $L/(2R_{\text{NW}}) = 4$, which will be shown to represent well the limiting case $L/(2R_{\text{NW}}) \gg 1$. Note that the output of our numerical calculations is the displacement associated to the relaxation strain ε_{ij} with respect to the reference lattice $a_0^{(\text{ref})}$ (see discussion in Sec. 3.1.2). In the numerical calculations below we have taken as reference lattice that specified by $a_0^{(\text{ref})} = (a_0^{(M)} + a_0^{(I)})/2$. In the 3D-2D comparisons of Figs. 3.6 and 3.7 it has been represented the relaxation strain ε_{ij} because it is the direct output from the FEM calculations. We note that, although the concrete numerical values obtained for ε_{ij} depend on the choice of $a_0^{(\text{ref})}$, the relevant total local strain $\varepsilon_{ij}^{(T)}$ can be recovered eventually by adding the strain associated to the reference lattice $\varepsilon_{ij}^{(0)}$, as shown in

Eq. (3.10).

The strain components to be analyzed below are referred to the system of axes $O\,\hat{X}_1\hat{X}_2\hat{X}_3$ presented in Fig. 3.5, although for the discussion below it is preferable to express them in cylindrical coordinates (r, ϕ, z) rather than in Cartesian ones (see Appendix D.3).

In the first place, we display in Fig. 3.6 the linescans of the relaxation strain components ε_{rr}, $\varepsilon_{\phi\phi}$ and ε_{zz} along the Z axis of the finite nanowire, as obtained with the 3D calculations. For comparison, the values obtained by means of the 2D GPS calculations at the center of the NW cross section are also indicated as horizontal lines. The GPS approach gives an axial strain $\varepsilon_{\parallel} = -0.00787$ and no bending (the calculated maximum bending strains are $|R_{\rm NW}/R_1|, |R_{\rm NW}/R_2| < 10^{-8}$, which can be considered zero within the numerical error), so that $\varepsilon_{zz} = \varepsilon_{\parallel}$. The calculated maximum torsion strain $(\theta R_{\rm NW})/2 = 2.3 \times 10^{-8}$ is also zero within the numerical error. The absence of bending in this particular case is due to the concentric nature of the core-shell system. The first conclusion we want to draw from Fig. 3.6 is that the 3D calculation for the long nanowire studied here presents two well differentiated regions. There is the region $|z| \leq 150$ nm around the center of the nanowire (otherwise stated, at distances away from the end surfaces larger than $250\,\text{nm} = 1.25(2R_{\rm NW})$), where the strain is essentially independent of z, with no strain component deviating by more than 4 % from the central values at $z = 0$. On the contrary, in the region within a distance of $\sim 1.25(2R_{\rm NW})$ from the end surfaces the strains are rather inhomogeneous. Moreover, the agreement between the results for the central cross section of the finite model and those of an infinite nanowire is better than 99.8 %. The above picture already indicates that our finite nanowire has sufficient length so that the strain field at its central portion corresponds to that of the infinite model modeled by our GPS approach, thus giving a numerical confirmation of the Saint-Venant's principle,[92]. In Fig. 3.7, scans of the various relaxation strain components are shown now along two different directions on the nanowire cross section. The linescans for the strain calculated by means of the GPS approach show again an excellent agreement with the 3D results at the central cross section of the finite wire.

Since the above analysis confirms the 2D GPS approach as a very reliable tool to model long nanowires, we use it in the following for a detailed description and understanding of the strain distribution in the nanowire cross section. In Fig. 3.8 we show the contour plots of the total strain components $\varepsilon_{ij}^{(T)}$ in the XY plane as provided by the GPS approach. We will try to elucidate the obtained anisotropic strain distribution with the following comments, that show that the overall features can be traced back to the initial lattice mismatch and the geometry.

(a)

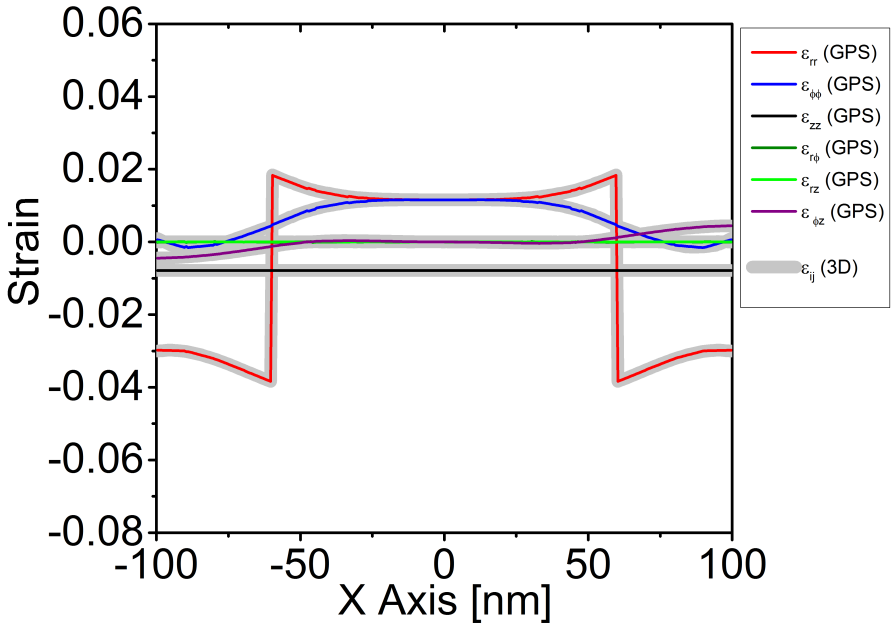

(b)

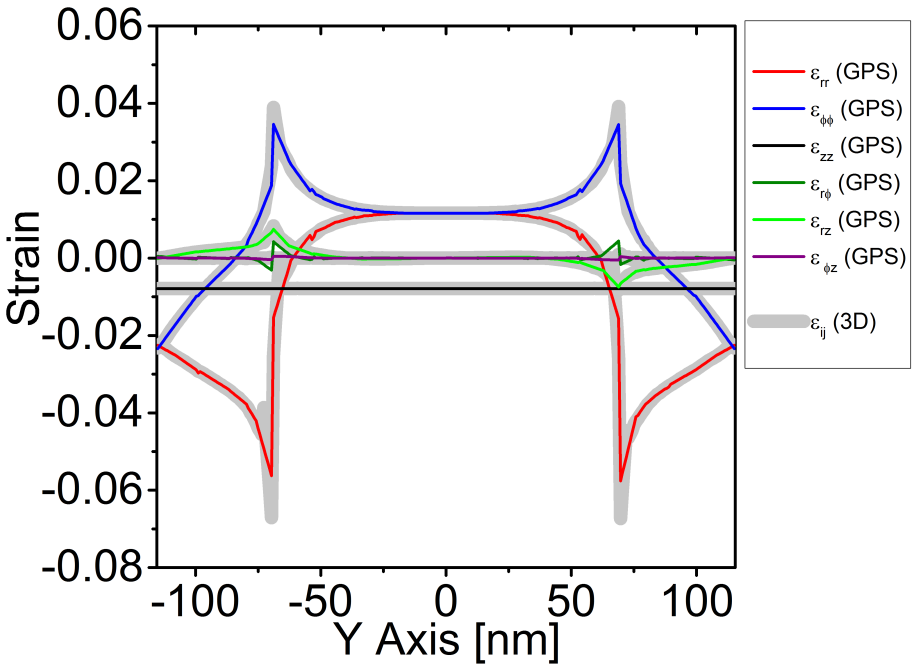

Figure 3.7: Linescan of various relaxation strain components for a Ge/Si(111) CSNW along the (a) X-axis (b) Y-axis sketched in Fig. 3.5. The 3D results are obtained by scanning the cross section at the middle of the nanowire.

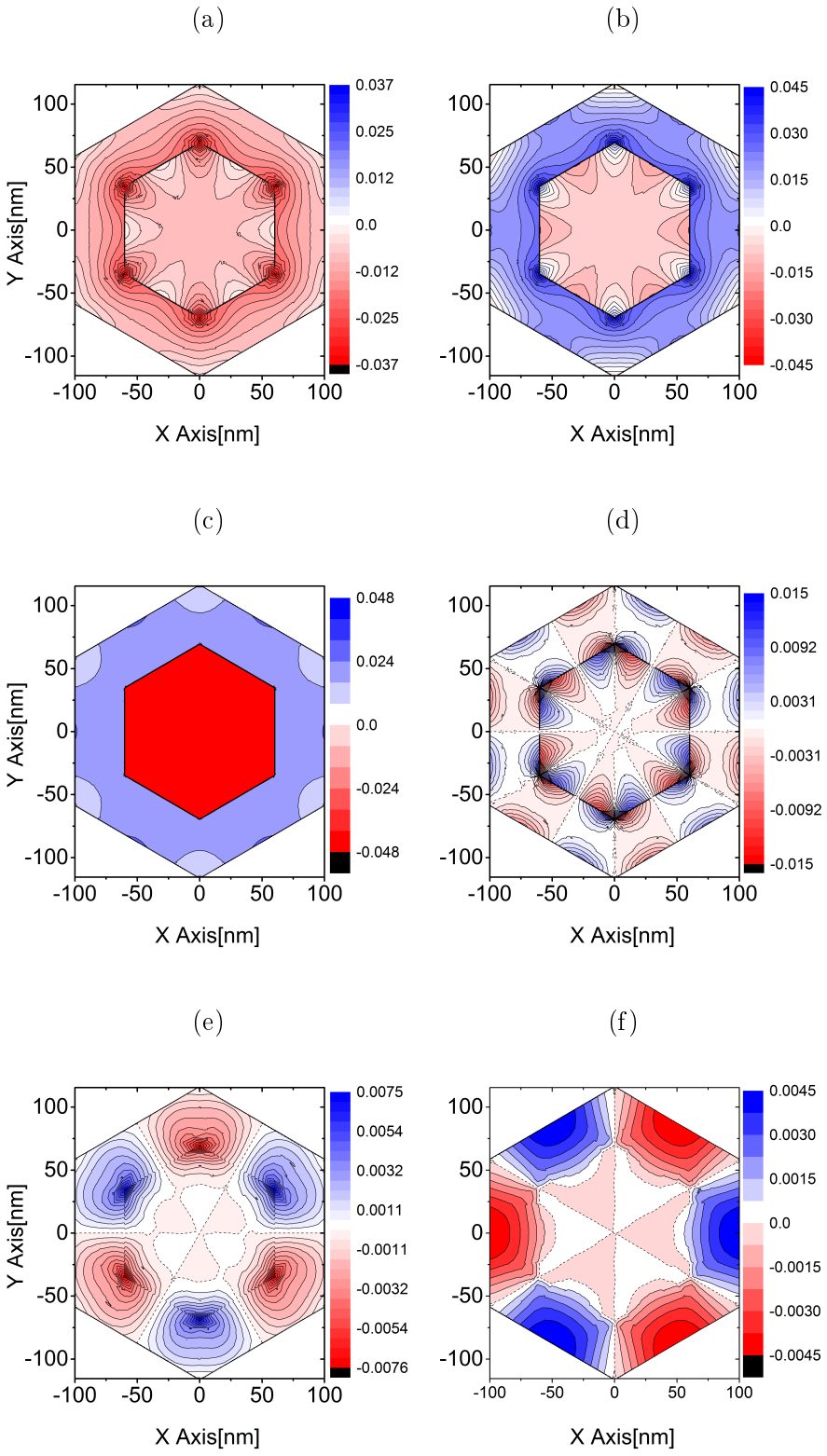

Figure 3.8: In-plane distribution of the total strain in an infinite Ge/Si(111) CSNW as calculated by the GPS approach. Plots (a)-(c) show the strain components $\varepsilon_{rr}^{(T)}$, $\varepsilon_{\phi\phi}^{(T)}$, $\varepsilon_{\text{hydro}}^{(T)} = \varepsilon_{rr}^{(T)} + \varepsilon_{\phi\phi}^{(T)} + \varepsilon_{zz}^{(T)}$, and plots (d)-(f) show the shear strains $\varepsilon_{r\phi}^{(T)}$, $\varepsilon_{rz}^{(T)}$ and $\varepsilon_{\phi z}^{(T)}$, respectively.

- The axial strain component $\varepsilon_{zz}^{(T)}$ (not shown in the figure) exhibits a simple step-like profile, whose values can be obtained easily from the calculated $\varepsilon_{\|}$ and the initial strain $\varepsilon_{ij}^{(0)}$: a compressive strain in the core $\varepsilon_{zz}^{(T)}(\text{core}) = -0.0275$ and tensile strain in the shell $\varepsilon_{zz}^{(T)}(\text{shell}) = +0.0126$ are so obtained. These values are consistent with the lattice mismatch. The core material (Ge) has a larger lattice constant than the shell material (Si), and the energetically most favorable configuration in the deformed core-shell system corresponds to a common axial lattice constant of value $a_z = 5.497$ Å in between those of bulk Ge and bulk Si .

- Now we focus on the core-shell interface. If one looks in particular at the central part of that interface, one sees a difference in sign between the values of the tangential component $\varepsilon_{\phi\phi}$ at the core and shell sides of the interface, the shell material being expanded ($\varepsilon_{\phi\phi}(\text{shell}) > 0$) whereas the core material is compressed ($\varepsilon_{\phi\phi}(\text{core}) < 0$), much in the same way as ε_{zz}, and for the same reasons. Concerning the radial strain ε_{rr} in the shell material, the compressive character of ε_{zz} and $\varepsilon_{\phi\phi}$, and the freedom at the outer surface of the shell determines that $\varepsilon_{rr}(\text{shell}) < 0$, i.e., that the shell is radially compressed. Although the same rationale would imply that the ε_{rr} of the core would tend to be positive, the fact that the core is constrained by the shell makes that response impossible to attain and the radial strain is eventually slightly compressive, $\varepsilon_{rr}(\text{shell}) < 0$.

- The measure of the local volume deformation, the hydrostatic strain $\varepsilon_{\text{hydro}}^{(T)} = \varepsilon_{rr}^{(T)} + \varepsilon_{\phi\phi}^{(T)} + \varepsilon_{zz}^{(T)}$, is depicted in Fig. 3.8c. In contrast to the individual strain components, which have a complicated inhomogeneous space distribution, the hydrostatic strain has a very simple behavior: The volume of the shell (core) is expanded (compressed) in almost an uniform manner.

- In general, the values of the strain components change smoothly when moving from the core-shell interface towards the nanowire center (in the core) and towards the surface (in the shell). However, when moving towards the corners they experience a stronger variation. This behavior can also be seen in the linescans of Fig. 3.9b. The corner geometry allows for some partial stress relief, as manifested by the increased importance of the shear strain $\varepsilon_{r\phi}$.

- The small but nonvanishing values for the out-of-plane shear strain components ε_{rz} and $\varepsilon_{\phi z}$ displayed in Figs. 3.8e and 3.8f are a direct consequence of $U_3(x_1, x_2) \neq 0$, and correspond to the fact that a cross section in the XY plane is warped into a non-flat surface in the strained wire (warping effect).

In other words, when the core pushes outwards on the shell, it is energetically favorable for the system to respond by not only becoming deformed in the plane, but also by warping out of the XY plane. One important aspect of our 2D GPS calculation is that it is able to fully capture that warping effect, which is impossible to obtain by working under the standard plane strain approximation that forces the warping function U_3 to vanish.

Si/Ge Core-Shell Nanowire

In the previous subsection we have studied within the GPS approach the elasticity problem in a Ge/Si [111] CSNW where the misfit strain inside the core is compressive (negative). For completeness, we show here the strain distribution in a Si/Ge [111] CSNW, so that the misfit strain of the core with respect to the shell is tensile (positive) $\varepsilon^{(0)} = 0.041$ (4.1 %). We have taken the same geometry and size as used previously for the study of the Ge/Si [111] system.

In Fig. 3.9 we present the X and Y-axis linescans of the relaxation strain components while the corresponding total strain distributions are displayed in Fig. 3.10. One important figure is the axial strain of the system, which in this case adopts the value $\varepsilon_{\parallel}$ =0.0033. In general, the results are essentially reciprocal (i.e., with a change of sign in all strain components) to those of the Ge/Si system.

3.3.2. Wurtzite InN/InGaN Core-Shell Nanowires: Influence of the Ga Concentration

In this section we study the strain distribution as a function of In concentration in wurtzite [0001] InN/In_xGaN_{1-x} CSNW which has been recently grown by catalyst-free plasma-assisted MBE [162]. The CSNW has hexagonal geometry (See Fig. 3.5a) and is composed of InN core, R_{core}= 50 nm, and In_xGaN_{1-x} shell, w_{shell}=10 nm. We assumed the NWs are free from forces and thus the strains induced in the core-shell system are caused by In concentration dependence misfit strain between the core and shell materials. The lattice and elastic constants of the alloy In_xGaN_{1-x} are calculated from the parameters of InN and GaN using Vegard's law.[163]. The material parameters used in the calculations are available at Appendix E.2. Finally, the In concentration dependent strain distribution inside InN/In_xGaN_{1-x} core-shell nanowire is obtained by solving Eq. (3.2a) using GPS problem approach.

The general trend of the strain distributions inside the WZ InN/In_xGaN_{1-x} [0001] NWs are similar to the Ge/Si NWs due to the similarity in the sign of

(a)

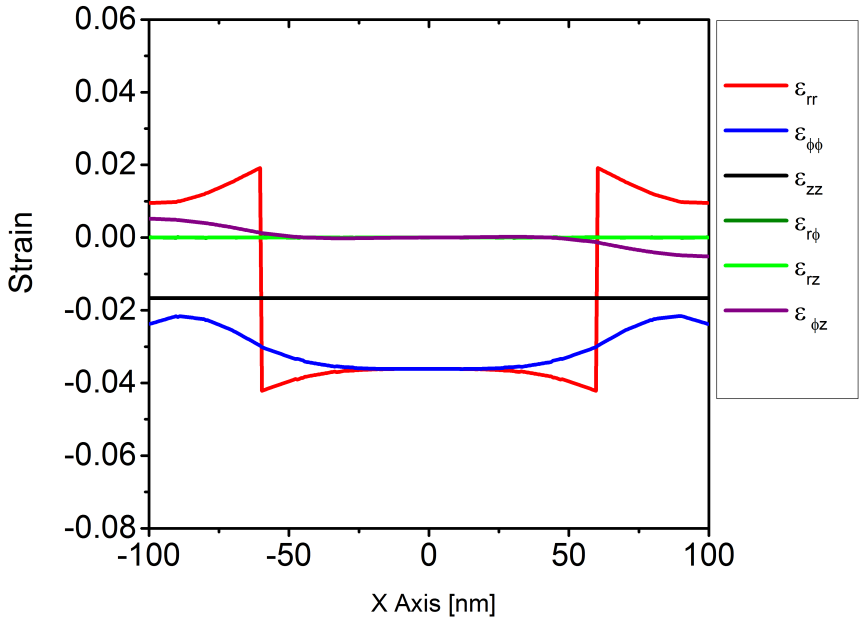

(b)

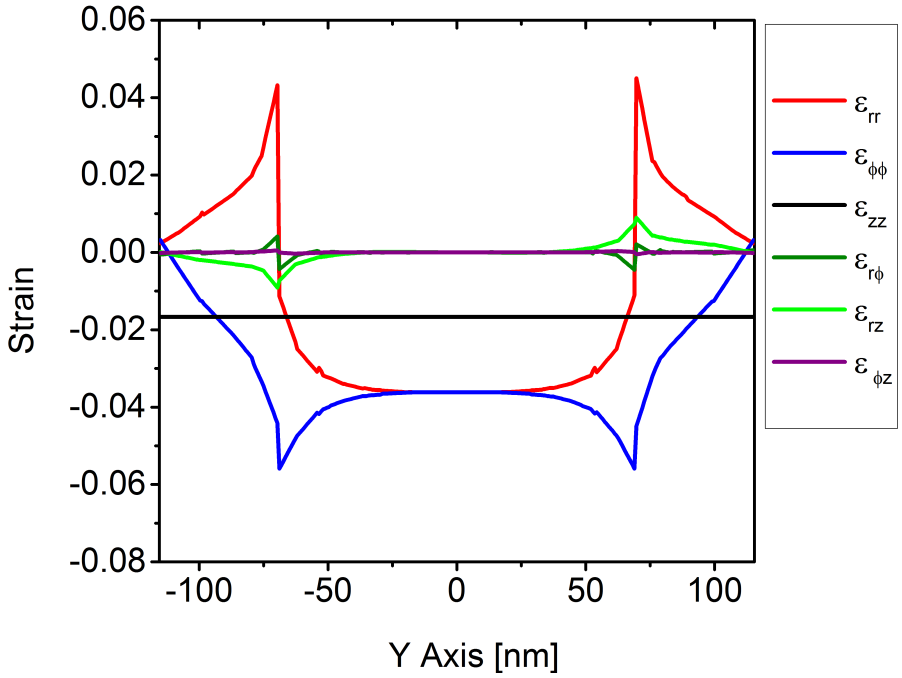

Figure 3.9: Linescan of various relaxation strain components for a Si/Ge(111) CSNW along the (a) X-axis (b) Y-axis sketched in Fig. 3.5.

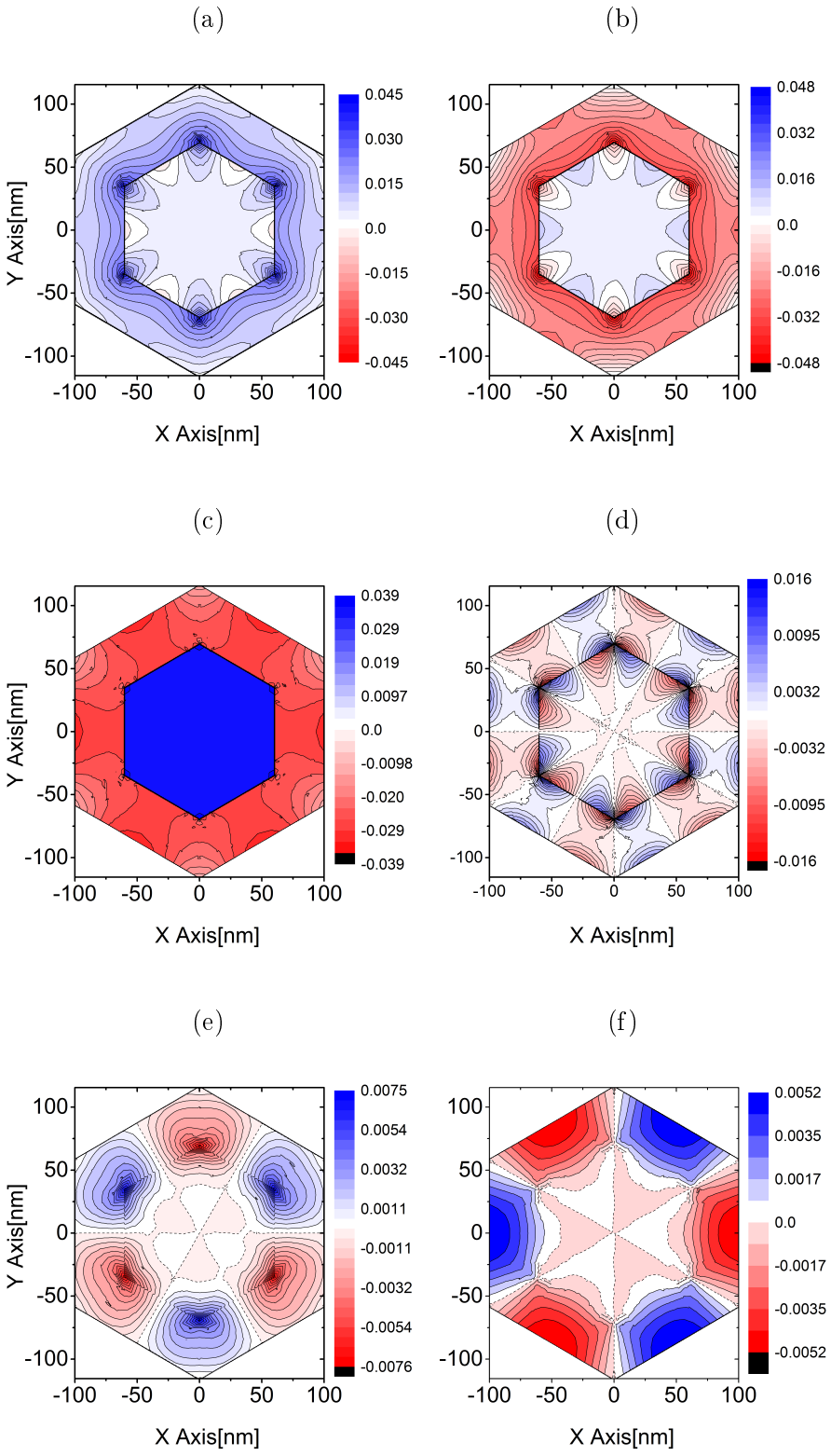

Figure 3.10: In-plane distribution of the total strain in an infinite Si/Ge(111) CSNW as calculated by the GPS approach. Plots (a)-(c) show the strain components $\varepsilon_{rr}^{(T)}$, $\varepsilon_{\phi\phi}^{(T)}$, $\varepsilon_{\text{hydro}}^{(T)} = \varepsilon_{rr}^{(T)} + \varepsilon_{\phi\phi}^{(T)} + \varepsilon_{zz}^{(T)}$, and plots (d)-(f) show the shear strains $\varepsilon_{r\phi}^{(T)}$, $\varepsilon_{rz}^{(T)}$ and $\varepsilon_{\phi z}^{(T)}$, respectively.

(a)

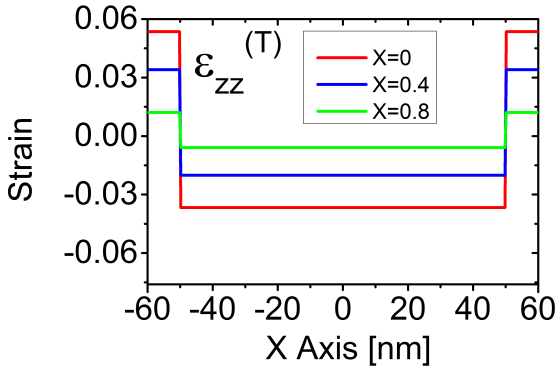

(b)

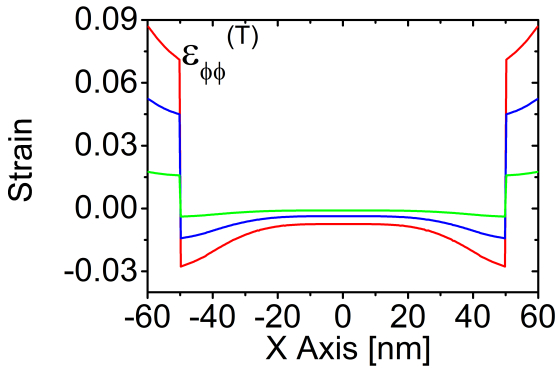

(c)

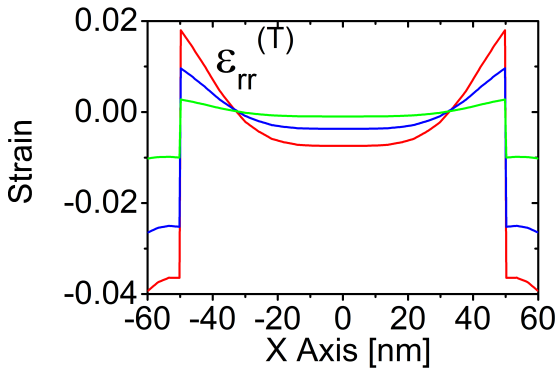

Figure 3.11: The X-Axis linescan of total strain components in an infinite InN/In_xGaN_{1-x} CSNW obtained by GPS problem. Plots (a)-(c) show $\varepsilon_{zz}^{(T)}$, $\varepsilon_{\phi\phi}^{(T)}$, and $\varepsilon_{rr}^{(T)}$ respectively.

the misfit strain. Thus, in Fig. 3.11 we present the effect of In concentration inside the shell on the strain distribution of the entire InN/In_xGaN_{1-x} CSNW. The linescans are taken along the X-axis. We comment first the case of x =0. In the axial direction the core-shell system undergoes stepwise compression $\varepsilon_{zz}^{(T)}$(core) = -0.037 inside InN and extension $\varepsilon_{zz}^{(T)}$(shell) = 0.053 inside GaN. In the angular direction the core InN is contracted while the shell GaN is relaxed. The amount of contraction inside the core InN decreases away from the core-shell interface while the relaxation inside the shell GaN increases as we go into the surface of the CSNW. In the radial direction the center of the core and the shell are under compressive strain while the part of the core near the core-shell interface becomes relaxed. Unlike the case of the non-piezoelectric problem in ZB [111] Ge/Si CSNW, here the warping of the cross section disappears i.e. zero out-off-plane shear strains, $\varepsilon_{rz}^{(T)} = \varepsilon_{\phi z}^{(T)} = 0$.

Turning into the In concentration dependence strain distribution,

- In the axial direction, increase of In concentration forces the shell to relax less as shown in Fig. 3.11a. Increase of In concentration by 80 % changes the axial relaxation from $\varepsilon_{zz}^{(T)}$(shell) = 0.053 to $\varepsilon_{zz}^{(T)}$(shell) = 0.012. To the contrast, the core has to contract less with increase of In concentration inside the shell In_xGaN_{1-x} as the space left for it increased after the decrease in the relaxation of the shell. Increase of In concentration by 80 % decreased the contraction from $\varepsilon_{zz}^{(T)}$(core) = -0.037 to $\varepsilon_{zz}^{(T)}$(core) = -0.006. These changes are direct result of the decrease in the misfit strain between the core and shell with increase of In concentration inside the shell In_xGaN_{1-x}. The axial strain inside the shell and core goes to unstrained state ($\varepsilon_{zz}^{(T)} \rightarrow 0$) as the concentration of In approaches 100 %.

- In the angular direction, the effects of In concentration are similar to the axial strain. Increase of In concentration from x =0 to x =0.8 resulted in decrease of compressive strain at the center of the core InN from $\varepsilon_{\phi\phi}^{(T)}$ =-0.0185 to $\varepsilon_{\phi\phi}^{(T)}$ =-0.00226 while the relaxation at the middle of the shell In_xGaN_{1-x} is forced to decrease from $\varepsilon_{\phi\phi}^{(T)}$ =0.077 to $\varepsilon_{\phi\phi}^{(T)}$ =0.016 (See Fig. 3.11b).

- The strain in radial direction $\varepsilon_{rr}^{(T)}$ (See Fig. 3.11c) is under contraction inside both the center of the core and shell. Particularly, at the center of the core InN the compressive strain decreases from $\varepsilon_{rr}^{(T)}$ =-0.007 to $\varepsilon_{rr}^{(T)}$ =-0.001 as the concentration of In increases from x =0 to x = 0.8. The same increase of In concentration changes the contraction inside the shell from $\varepsilon_{rr}^{(T)}$ =-0.037

to $\varepsilon_{rr}^{(T)}$ =-0.1. The relaxation strain at the part of the core near the core-shell interface also decreases with increase of In inside the shell.

Unlike the other CSNWs discussed above, where we have taken the sizes of the NWs for theoretical study, the same core-shell nanowire considered in this section has been grown recently by plasma-assisted molecular beam epitaxy [162]. Moreover, the results of the calculation performed here has been used in Ref. [162] to study the strain induced phonon frequency change in $In_xGa_{1-x}N$ core-shell nanowire which is given by $\Delta\omega_\lambda = a_\lambda(\varepsilon_{11} + \varepsilon_{22}) + b_\lambda(\varepsilon_{33})$, where a_λ and b_λ are phonon deformation potentials[164].

The frequencies of the A_1(LO) phonon along the radius of the core-shell NW with and without the strain fields in the NW are shown in figure 3.12. The concentration of Ga inside the core and shell are taken as $X^{(\text{core})}{}_{Ga} = 4\,\%$, and $X^{(\text{shell})}{}_{Ga} = 30\,\%$. Under these conditions, the core becomes compressed while the shell is under tensile strain. It was found that, these strain fields cause a nearly constant 7 cm $^{-1}$ phonon blue-shift in the core region and a variation between 15 and 5 cm^{-1} for the shell of the NW. The strain-corrected theoretical predictions compare very well with the two contributions, centered a 597 and 625 cm $^{-1}$.

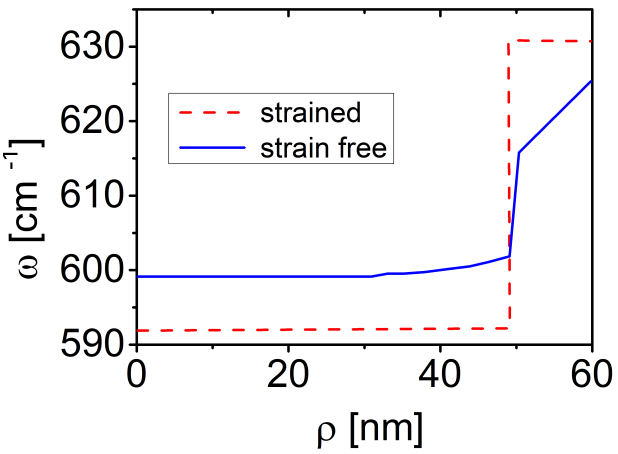

Figure 3.12: Calculated frequency of A_1(LO) phonon along the radius of a core-shell NW with (solid line) and with out (dashed line) the inclusion of strain corrections taken from Ref. [162]. The characteristic of the core-shell NW are $X^{(\text{core})}{}_{Ga} = 4\,\%$, R_{core} =50 nm, $X^{(\text{shell})}{}_{Ga} = 30\,\%$ and w_{shell} =10 nm. Reproduced from Ref. [162].

3.3.3. Elasticity Problem in Non-Concentric Core-Shell Nanowires

In all the elasticity problem in CSNWs discussed above, we have assumed the geometric center of the core and shell to coincide. Thus the terms to related bending strain (R_{NW}/R_1 and R_{NW}/R_2) given in Eq. 3.20 were numerically very small as all the out of plane stress components cancel out each other due to the symmetry. Here, we want to investigate the bending behaviour of the CSNW as a result of non-concentric core and shell inclusion i.e. by assuming that the geometric center of the core and shell do not coincide. For demonstration, we have considered the ZB [111] Ge/Si CSNW discussed in Sec. 3.3.1. We have kept the same core and shell radii but moved the center of the Ge core along the X-Axis by a distance d =1-10 nm as shown in Fig. 3.13. This is a situation found sometimes in actually grown samples where specific experimental conditions can lead to a 'shadow effect' that inhibit the shell growth on some facets with respect to others.

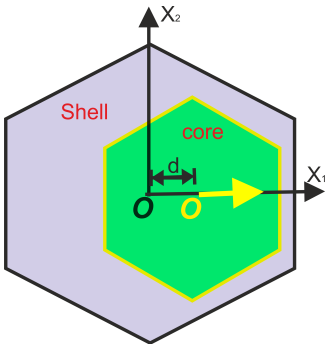

Figure 3.13: Displacement of the center of the Ge core with respect to the center of the Si domain along the X_1 direction by distance d. The radius of the core and NW are taken as, R_{core} =60 nm and R_{NW} =100 nm.

When the center of the core is moved along X_1 direction with respect to the center of the shell, the symmetry between the core and shell will be lost. As a result, the total out of plane shear stress component along X_1 direction will become non-zero. There fore, the core-shell nanowire will experience out of plane bending along the $X_1 - X_3$ plane even though no bending moment is applied. When we compare the results with the concentric inclusion, now R_{NW}/R_1 is different from zero but R_{NW}/R_2 and Θ still equal to zero. In Fig. 3.14a we present the bending strain along the $X_1 - X_3$ plane as function of distance d. We can see that the bending strain increases as the center of the core moves away from the center of the shell creating bending without external force. The profile of other strain components showed similar trends as the case of concentric core-shell inclusion in the range of distances d explored. The change in the minimum and maximum of all strain

components as a result of largest displacement d =10 nm, when compared with the concentric inclusion, was found to be in the order of $\times 10^{-3}$. In Fig. 3.14b we show how the NW is bent as a result of the out-of plane bending strains given in Fig. 3.14a. Here we have taken the length of the NW as L =200 nm. We clearly see that the more the center of the core-is moved the more the NW bends.

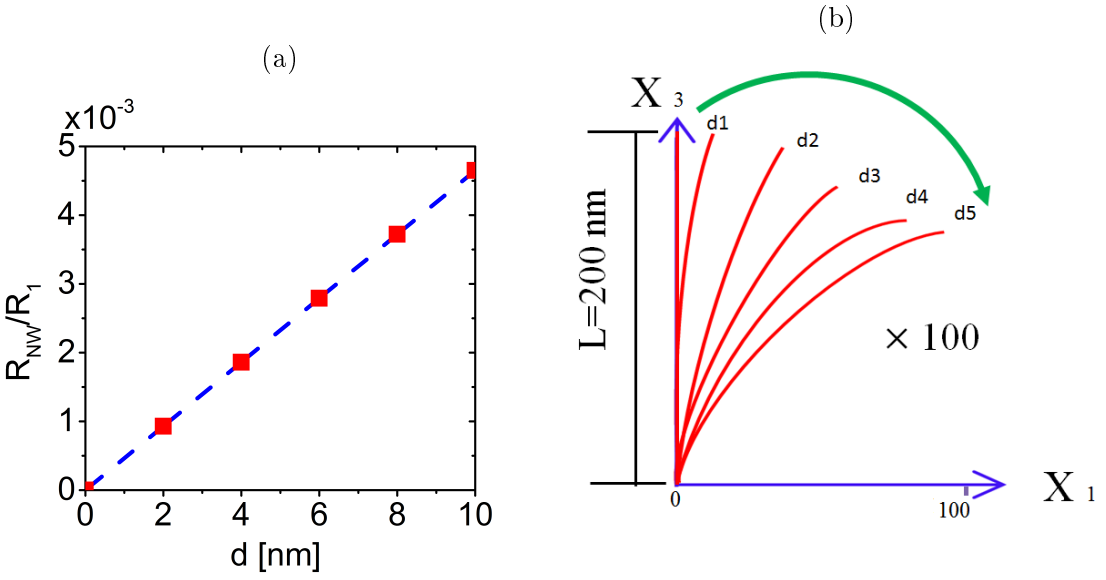

Figure 3.14: (a) Bending strain component in non-concentric ZB Ge/Si [111] CSNWs created by displacing the center of the core with respect to the center of the shell along the X-axis. (b) Shows the bending of the NW with L =200 nm as a result of out-of plane bending strain. The labels d_1,..., d_5 correspond to displacement of the center of the core by 2,4,6,8, and 10 nm respectively as shown in Fig. 3.13.

3.3.4. Thermo-Elastic Properties in Core-Shell Nanowires

In the Sec. 3.3.1 we have seen that the GPS problem approach is computationally cheap and able to describe the strain distributions at the central region of an long CSNWs. In this section we will extend the GPS problem to study the elastic properties of CSNW under thermal loading.

Generally, the constitutive equation for thermoelastic material with an initial lattice constant $a_i^{(0)}$, at temperature temperature T_0 which is then heated or cooled to a final temperature T, can be extended from the pure elasticity problem given in Eq. (3.2a) by including the proportionality of deformation as a result of temperature change using Duhamel-Neumann Law[165] as:

$$\sigma_{ij} = C_{ijkl}\varepsilon_{kl} - \beta_{ij}\Theta \tag{3.41}$$

Where the temperature change $\Theta = T - T_0$, T_0 is a reference temperature usually taken at room temperature, i.e., T_0=300 K, β_{ij} is the coefficient of linear thermal expansion. Note that no shear strains are induced by the thermal effect and as a result the material will retain its shape. Then the equilibrium equation of the thermo-elastic problem can be given by,

$$\frac{\partial \sigma_{ij}}{\partial x_j} = -f_i^{(0)} + f_i^{(T)} \tag{3.42}$$

Where $f_i^{(0)}$ is the lattice-mismatch induced body force defined in Eq. 3.12a and the thermal induced body force $f_i^{(T)}$ is given by,

$$f_i^{(T)} = f_i^{(M)}\chi^{(M)} + f_i^{(I)}\chi^{(I)} \tag{3.43}$$

where $\chi^{(M)}(\boldsymbol{r})$ and $\chi^{(I)}(\boldsymbol{r})$ are the characteristic function of the inclusion defined at 3.7. $f_i^{(S)}$ and $f_i^{(C)}$ are thermal induced body forces inside the shell and core respectively and are given as:

$$f_i^{(I)} = \frac{\partial}{\partial x_i}\left[\beta_{ij}^{(I)}(r)\Theta\right] \tag{3.44a}$$

$$f_i^{(M)} = \frac{\partial}{\partial x_i}\left[\beta_{ij}^{(M)}(r)\Theta\right], \tag{3.44b}$$

where $\beta_{ij}^{(I)}$ and $\beta_{ij}^{(M)}$ are the thermal expansion coefficients of the core and shell respectively.

As demonstration of the model presented, we will study the thermoelastic properties of the ZB [111] Ge/Si CSNW discussed in Sec. 3.3.1 and also studied recently in Ref.[166]. The thermal expansion coefficients of Si and Ge are taken as $\beta_{ij}^{(Si)} = 2.6\times 0^{-6}/K$ and $\beta_{ij}^{(Ge)} = 5.9\times 10^{-6}/K$ respectively. The temperature change varies as $0\leq \Theta \leq$900 K. We assume that the temperature change accompanying the deformation does not result in essential variations of material parameters[90]. Thus, we assumed that these coefficients are independent of temperature (T) and we consider geometrically linear thermoelasticity. Moreover, we assume that the nanowire is free from external forces, so that the strain is solely induced by the internal lattice-mismatch induced body force $f_i^{(0)}$ and thermal induced body force $f_i^{(T)}$ (see Eq. 3.42). Finally, the temperature dependent strain distribution inside

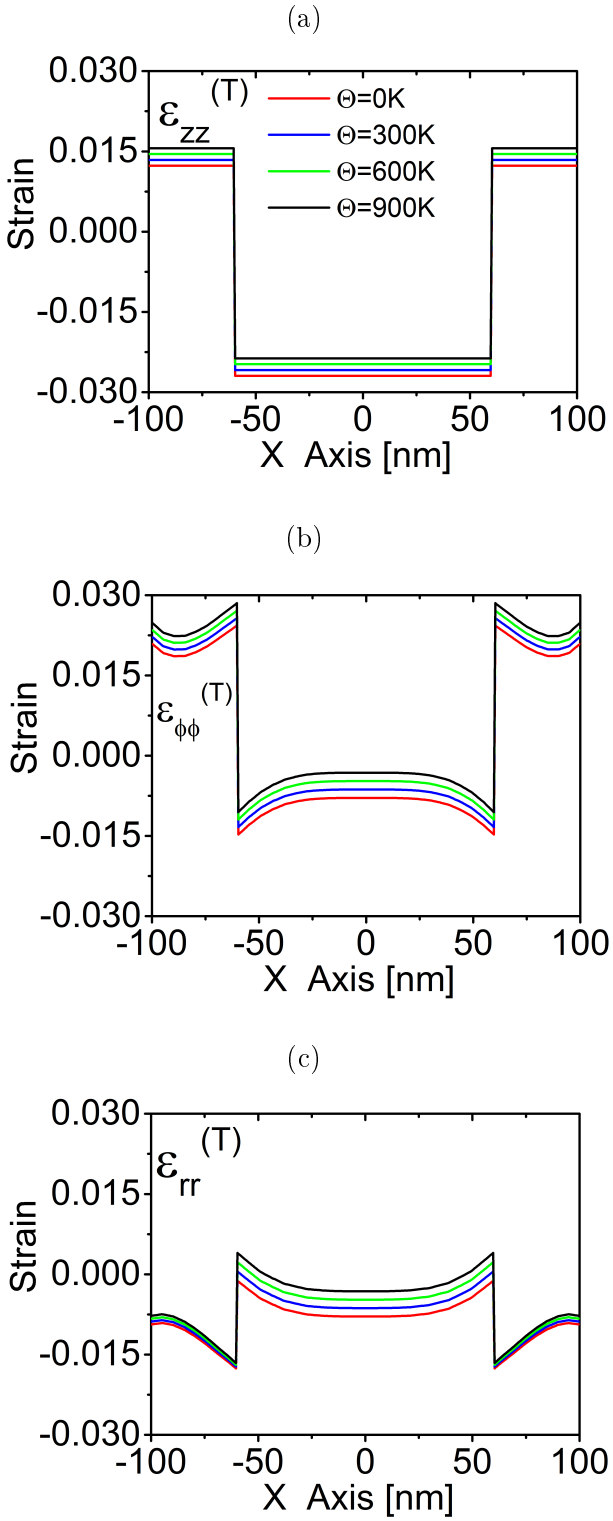

Figure 3.15: The X-Axis linescan of total strain components in ZB [111] Ge/Si CSNW under thermal loading as obtained by the GPS problem. Plots (a)-(c) show $\varepsilon_{zz}^{(T)}$, $\varepsilon_{\phi\phi}^{(T)}$ and $\varepsilon_{rr}^{(T)}$ respectively. The temperature varies as Θ =0-900 K. The radius of the core R_1 =60 nm and shell w_{shell} =40 nm.

the CSNW is obtained by solving Eq. (3.11a) using the GPS problem approach. In Fig. 3.15 we detail the effects of the change in temperature on the elastic properties of the CSNW by presenting X-axis linescans of strain components.

- In the axial direction, the Si shell becomes more relaxed with increase of temperature as shown in Fig. 3.15a. The rise of temperature from Θ =0 K to Θ =900 K changes the relaxation from ε_{zz}^{T}(shell) =0.0123 to ε_{zz}^{T}(shell) =0.0156. To the contrary, the contraction inside Ge core decreases with increase of temperature even though it has smaller space left after the relaxation of the Si shell. The contraction becomes $\varepsilon_{zz}^{(T)}$(core) =-0.0267 at 0 K and $\varepsilon_{zz}^{(T)}$(core) =-0.0237 at 900 K.

- In the angular direction, the core becomes less contracted with increase of temperature while the shell becomes more relaxed as the CSNW becomes hotter as shown in Fig. 3.15b. The values at the center of the core becomes $\varepsilon_{\phi\phi}^{(T)}$ = -0.0079 at Θ =0 K and $\varepsilon_{\phi\phi}^{(T)}$ = -0.0032 at Θ =900 K. At the middle of the shell, the relaxation has increased from $\varepsilon_{\phi\phi}^{(T)}$ = 0.020 at Θ =0 K to 0.024 at Θ =900 K.

- In the radial direction, the rise of temperature resulted in decrease of compression inside both the Ge core and Si shell as shown in Fig. 3.15c. Particularly, the compression inside the Ge core decreased by a larger amount than inside the Si shell which is due to the large thermal expansion coefficient of Ge as compared to that in Si. At the center of the Ge core the values of the radial strains are $\varepsilon_{rr}^{(T)}$ =-0.0079 at Θ =0 K and $\varepsilon_{rr}^{(T)}$ = -0.0032 at Θ =900 K. We also note that the core-shell interface in the side of the core Ge becomes fully relaxed ($\varepsilon_{rr}^{(T)} > 0$) at higher temperatures (Θ >300 K).

3.3.5. Piezoelectric Problem in Core-Shell Nanowires

InN/GaN Core-Shell Nanowires

Next, we will present the GPP results for a fully-coupled piezoelectric problem. The problem corresponds to a zincblende core-shell nanowire oriented along the [111] direction. The core is made of InN and the shell is made of GaN. The geometry of the nanowire is the same shown in Fig. 3.5. The elastic, piezoelectric and dielectric tensors of zincblende materials exhibit cubic T_d symmetry, which is fully taken into account in the calculations. The Voigt matrices in the reference frame associated to the nanowire, $\hat{C}_{IK}$, $\hat{e}_{nI}$ and $\hat{\varepsilon}_{mn}$, can be found in Appendix

D.2. Now, besides the nonvanishing elastic constants $\hat{C}_{14}, \hat{C}_{24}(=-\hat{C}_{14}) \neq 0$, there appear nonvanishing piezoelectric constants $\hat{e}_{15}, \hat{e}_{24}(=\hat{e}_{15}) \neq 0$, so the system will exhibit a nonvanishing warping function U_3, coupled to both (U_1, U_2) and Φ.

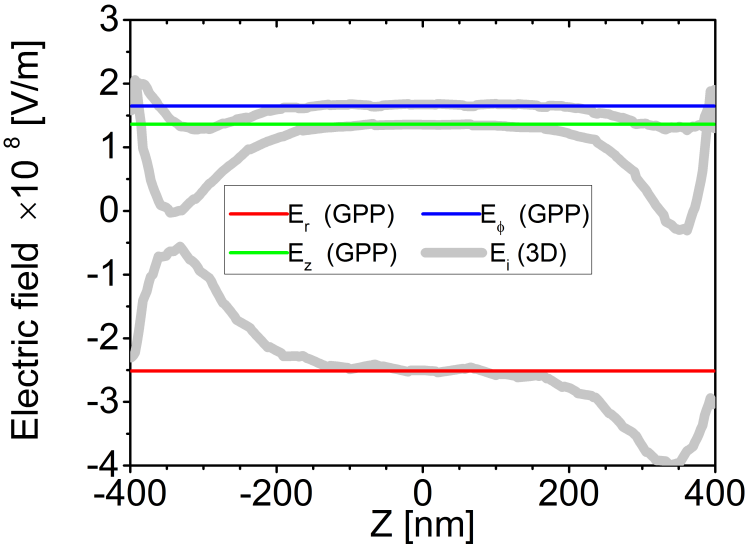

Figure 3.16: The gray thick curves represent the linescans of the electric field components E_r, E_ϕ and E_z along the longitudinal axis of the finite nanowire passing through $(x = 0.5R_{\rm NW}, y = 0.5R_{\rm NW})$ as obtained from the 3D calculations. For comparison, the results corresponding to an infinite nanowire as obtained by means of the GPP approach are also displayed as horizontal lines.

We assume again that the nanowire is free from external traction and body forces (i.e., $\bar{t}_j, F_j, M_j, f_j = 0$), as well as from external charges (i.e., $\bar{\varrho}, Q, \rho = 0$), so that the only cause for the deformation and potential fields is the lattice mismatch, through the body force $f_i^{(0)}$ and the charge density $\rho^{(0)}$ given in Eqs. (3.12). The lattice parameters and material constants used can be found in Table E.3. In this case, the diagonal misfit strain between the core (inclusion, I) and shell (matrix, M) is $\varepsilon^{(\rm misfit)} = -0.0964$ (9.64 %). For the following calculations we have taken the same cross section geometry and length as in Sec. 3.3.1. As before, the relaxation strain is calculated starting from a reference lattice with $a_0^{(\rm ref)} = (a_0^{(M)} + a_0^{(I)})/2$, and the strain and electric fields will be expressed in cylindrical coordinates (see Appendix D.3).

Since the sign of the misfit strain is the same, the strain fields in this case follow a pattern qualitatively similar to that for the non-piezoelectric nanowire in Sec. 3.3.1. Consequently, we focus here on the piezoelectric field and potential. In the first place, we will analyze the linescans of the field along a longitudinal axis of the finite nanowire. Due to symmetry reasons, $E_r, E_\phi = 0$ along the Z axis, so we have chosen to display in Fig. 3.16 a linescan of the field components, as

(a)

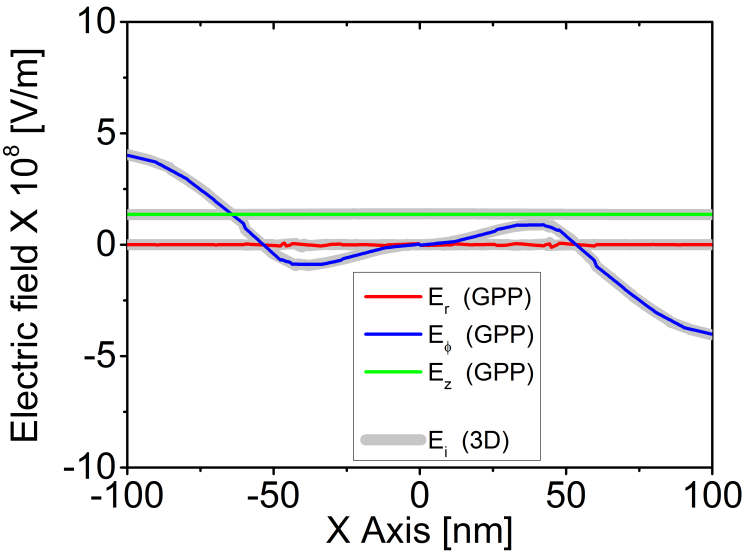

(b)

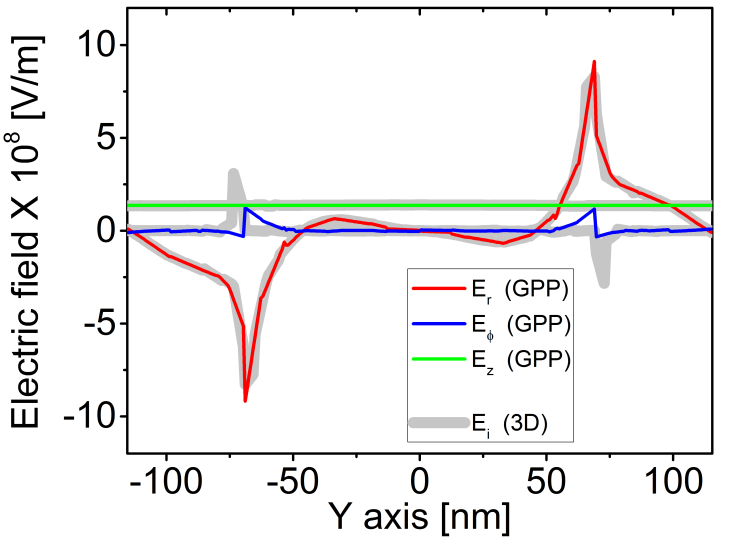

Figure 3.17: Linescan of the field components for a InN/GaN(111) CSNW along the (a) X-axis (b) Y-axis sketched in Fig. 3.5, as obtained with the 3D calculations at the central cross section of the finite nanowire (thick gray lines) and by means of the 2D GPP calculations (thin coloured lines).

(a)

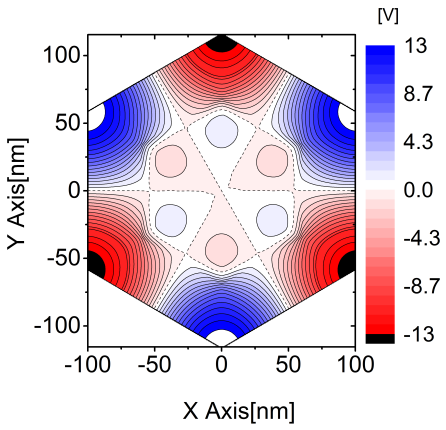

(b)

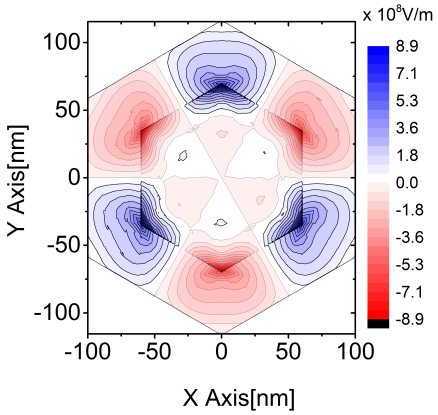

(c)

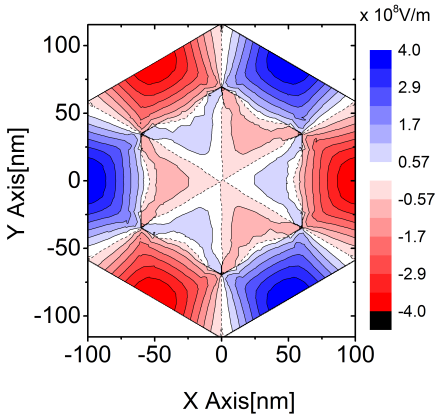

Figure 3.18: In-plane distribution of: (a) the potential Φ , and field components (b) E_r and (c) E_ϕ in an infinite InN/GaN(111) CSNW as calculated by the GPP approach.

obtained from the full 3D calculation, along a longitudinal off-center axis crossing the transverse section through coordinates ($x = 0.5R_{\mathrm{NW}}, y = 0.5R_{\mathrm{NW}}$). For comparison, the corresponding values obtained by means of the GPP approach are also indicated as horizontal lines. In particular, the GPP approach gives an axial field $E_z = E_{\parallel} = 1.36 \times 10^8$ V/m, which is uniform throughout the transverse section. As for the strain, we distinguish also in the field profile two regions. In the central region, for distances away from the end surfaces larger than $1.25(2R_{\mathrm{NW}})$ (i.e., $|z| < 150$ nm), the field is rather uniform along the axis (e.g., E_z does not deviate by more than 5 % from the value at $z = 0$). On the other hand, within a distance of $1.25(2R_{\mathrm{NW}})$ from the end surfaces, the field varies considerably, mainly as a consequence of the over relaxation effect in the strain components. The results for the central cross section of the finite model are again very well approximated by those of an infinite nanowire as calculated by means of the 2D GPP approach (the agreement at $z = 0$ being better than 99.3 % for E_z and better than 98 % for E_r and E_ϕ). These results represent a numerical confirmation that the Saint-Venant's principle works well also for the fully-coupled piezoelectric nanowire problem.

In Fig. 3.17 the various field components are shown along two different directions on the nanowire cross section. The field linescans calculated by means of the GPP approach show again a remarkable agreement with the 3D results at the central cross section of the finite wire, thus confirming the reliability of the GPP approach to simulate the central region of high aspect-ratio piezoelectric problems.

Finally, we illustrate in Fig. 3.18 the distribution of the in-plane piezoelectric potential profile $\Phi(x_1, x_2)$ and electric field components across the XY plane for an infinite wire modeled using the GPP model. Remember that E_z is uniform and equal to 1.36×10^8 V/m. It is apparent in Fig. 3.18a that the highest/lowest value of piezoelectric potential ($\pm 13.6V$) locate in an alternated manner at the external corners of the GaN shell, while the InN core is mostly at zero potential. The associated in-plane field distribution is shown in Figs. 3.18b and 3.18c. The maximum values of the radial component of the in-plane field $E_{r,\max} = 8.95 \times 10^8$ V/m are confined at the corners of the core-shell interface. On the other hand, $E_{\phi,\max} = 3.97 \times 10^8$ V/m is located at the outer surface of the shell, between the corners.

GaN/InN Core-Shell Nanowires

In the previous subsection we have studied within the GPP approach the piezoelectric problem in a ZB [111] InN/GaN CSNW where the misfit strain inside the core is compressive (negative). For completeness, we show here the strain dis-

tribution in the reciprocal GaN/InN CSNW, where the misfit strain of the core with respect to the shell is now tensile $\varepsilon^{(\text{misfit})} = 0.107$. We have taken the same geometry and size as used previously for the study of the InN/GaN system.

In Fig. 3.19 we present the X and Y-axis linescans of the electric field components whereas the corresponding 2D potential and field distributions are given in Fig. 3.20. The piezoelectric potential $\Phi(x_1, x_2)$ is displayed in Fig. 3.20a: The highest/lowest value of piezoelectric potential developed is localized inside the InN shell and corresponds to ± 27.2 V, which is higher than found in the InN/GaN configuration. The electric field components in the radial E_r and angular directions E_ϕ are shown in Figs. 3.20b and 3.20c, respectively. The maximum radial electric field is $E_{r,\max} = 1.059 \times 10^9$ V/m and is confined at the corners of the core-shell interface. On the other hand, the maximum electric field in the angular direction is $E_{\phi,\max} = 7.44 \times 10^8$ V/m and is localized inside the shell. The axial electric field is uniform of value $E_z = 2.40 \times 10^8$ V/m. The results are sign-reversed as compared to those of the InN/GaN system, although we see that the GaN/InN configuration exhibits larger values of the potential and electric fields.

(a)

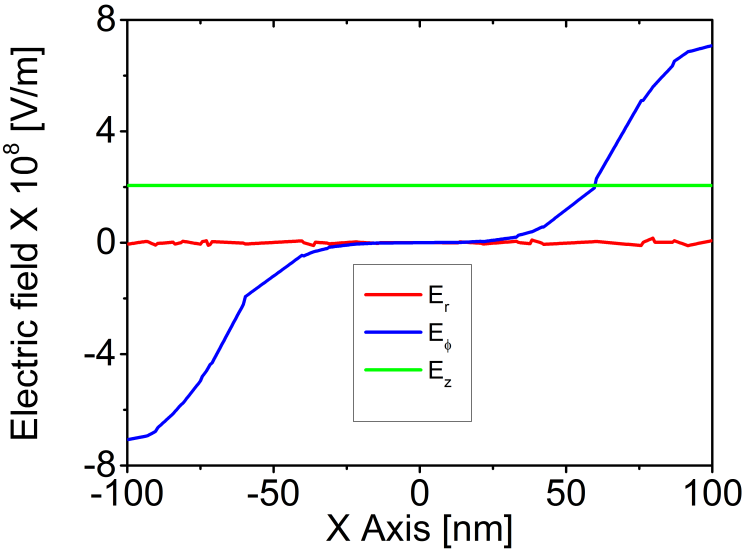

(b)

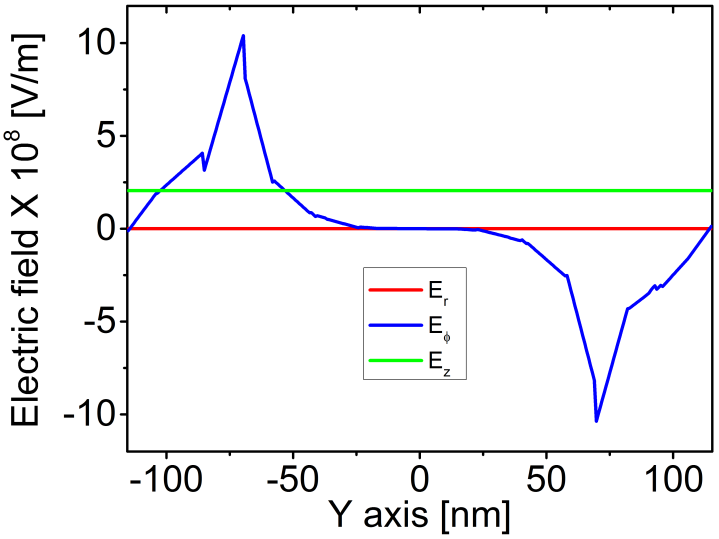

Figure 3.19: Linescan of the field components for a GaN/InN(111) CSNW along the (a) X-axis (b) Y-axis sketched in Fig. 3.5, as obtained with the 2D GPP calculations.

(a)

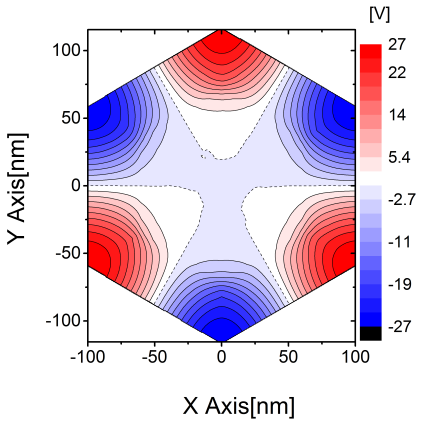

(b)

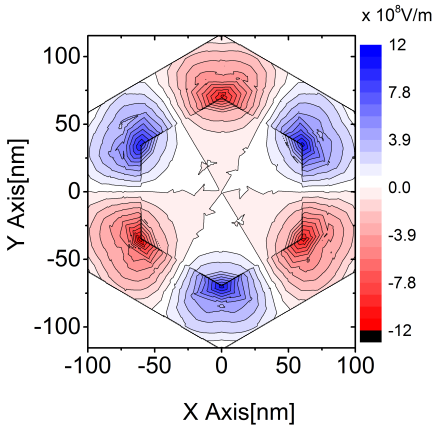

(c)

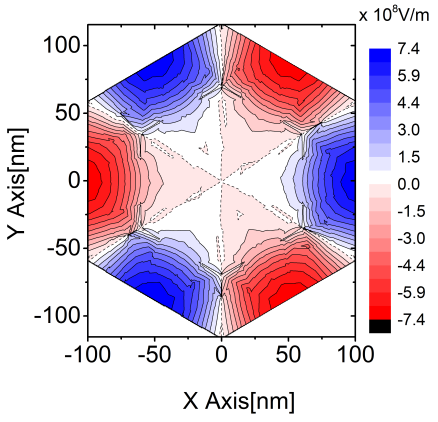

Figure 3.20: In-plane distribution of: (a) the potential Φ, and field components (b) E_r and (c) E_ϕ in an infinite GaN/InN(111) CSNW as calculated by the GPP approach.

Chapter 4

Envelope Function Model for the Nanowire Electronic Structure

In this chapter we will explain the methodology employed for the calculation of the electronic structure and optical absorption in model nanowires. We have chosen as theoretical framework the multiband ($\boldsymbol{k} \cdot \boldsymbol{p}$) envelope function approximation introduced in Sec. 2.3. For ease of presentation, the technical details of the computational approach will be first introduced within the single band envelope function approximation (or effective mass approximation) in Sec.4.1. Within this simplifed model, one needs to solve only a single Schrödinger-like equation and the results obtained are easy to interpret. Although the picture offered by this model is sound and very popular, it is insufficient to describe realistically the electronic structure of many types of nanowires. It can only be considered as the crudest approximation to the problem, and we analyse it first only because it will allow us to gain an insight into the problem of electronic confinement that will be of great help in the discussion of the results that will be obtained when we treat multiband models in Sec. 4.2. Indeed, in Sec. 4.2, we will introduce the necessary generalizations to be taken into account when working within the multiband approach that will be finally used in the calculations presented in Chapters 5 and 6.

4.1. Single Band Model

In this section we will use a single band model to describe the nanowire in the framework of the envelope function approximation explained in Sec. 2.3. In this simplest situation, where one focus on a well isolated band ($N_A = 2$) and neglects

the spin-orbit interaction, the doubly degenerate NW states have the form

$$\{ \quad \Psi_{a=1}(\boldsymbol{r}) = F(\boldsymbol{r})\, U(\boldsymbol{r})\, |\uparrow\rangle \quad , \quad \Psi_{a=2}(\boldsymbol{r}) = F(\boldsymbol{r})\, U(\boldsymbol{r})\, |\downarrow\rangle \quad \} \quad ,$$

where $U(\boldsymbol{r})$ is the $\boldsymbol{k} = 0$ scalar Bloch amplitude of the band under study and $F(\boldsymbol{r})$ is the scalar envelope function. This shows that, although in principle the envelope function is an spinor, when the problem is spin-independent the NW states are doubly degenerate in spin and the single band model refers to a scalar envelope function. Eventually, this treatment can be done separately for the conduction band and valence band.

In the coming subsections, we will introduce the formulation of the single band problem and describe the numerical method used for its resolution.

4.1.1. Formulation of the Single Band Envelope Function Equation

As explained in Sec. 2.3.2, the envelope function for a 1D system adopts the form

$$F(\boldsymbol{r}) \to F^{(k_z)}(\boldsymbol{r}) = \frac{1}{\sqrt{\mathcal{L}}}\, e^{ik_z z}\, F^{(k_z)}(x,y) \quad , \tag{4.1}$$

and the effective mass equation describing the nanowire electronic structure for fixed k_z can be written in cartesian coordinates as follows:

$$H^{(\mathrm{NW})} F^{(k_z)}(x,y) = E(k_z) F^{(k_z)}(x,y)\,, \tag{4.2}$$

where $E(k_z)$ is the energy, and

$$H^{(\mathrm{NW})} \equiv \left[\underbrace{-\frac{\hbar^2}{2m_x^*}\frac{\partial^2}{\partial x^2} - \frac{\hbar^2}{2m_y^*}\frac{\partial^2}{\partial y^2}}_{=:T_\perp} + \frac{\hbar^2 k_z^2}{2m_z^*} + V^{(\mathrm{NW})}(x,y) \right] ,$$

where an anisotropic effective mass of the band has been introduced, and it is considered uniform across the NW cross section. The potential term $V^{(\mathrm{NW})}(x,y)$ is given by the discontinuity of the energy band edge $E^{(0)}$ between regions $\mathbb{A}$ and $\mathbb{B}$ of the NW cross section:

$$V^{(\mathrm{NW})}(x,y) = E^{(0,\mathbb{A})}\, \chi^{(\mathbb{A})}(x,y) + E^{(0,\mathbb{B})}\, \chi^{(\mathbb{B})}(x,y)\,. \tag{4.3}$$

Note that an additional perturbing potential $W(x,y)$, as originated, e.g., from space charge or from piezoelectric charges, could be easily added here. It has to be remembered here that, for bounded systems limited by an external interface to air/vacuum, as the nanowires, it is common to assume that outside that surface the potential is infinitely high, and therefore the domain of definition of the electron wavefunctions is restricted to the cross section of the material system.

Now we introduce a strong assumption and suppose that the geometry and whatever other ingredients that contribute to $V^{(\mathrm{NW})}$ are axially symmetric, i.e., by working on cylindrical coordinates:

$$(x,y) \to (\rho,\phi) \Longrightarrow V^{(\mathrm{NW})}(x,y) = V^{(\mathrm{NW})}(\rho) \quad .$$

We will also need to assume that the underlying band structure is such that the effective mass is transversely isotropic:

$$m_x^* = m_y^* =: m_\perp^* \quad .$$

With all these considerations, we can express Eq. (4.2) in cylindrical coordinates (ρ,ϕ) as:[1]

$$H^{(\mathrm{NW})}F^{(k_z)}(\rho,\phi) \equiv \left[T_\perp + \frac{\hbar^2 k_z^2}{2m_z^*} + V^{(\mathrm{NW})}(\rho)\right] F^{(k_z)}(\rho,\phi) = E(k_z)F^{(k_z)}(\rho,\phi)\,, \tag{4.4}$$

where now

$$T_\perp = -\frac{\hbar^2}{2m_\perp^*}\left(\frac{1}{\rho}\frac{\partial}{\partial\rho}\,\rho\,\frac{\partial}{\partial\rho} - \frac{1}{\rho^2}\,\frac{1}{\hbar^2}\,\hat{L}_z^2\right). \tag{4.5}$$

$\hat{L}_z$ is the z component of the angular momentum associated with the envelope function given by,

$$\hat{L}_z = x\,\hat{p}_y - y\,\hat{p}_x = x\left(-i\hbar\frac{\partial}{\partial y}\right) - y\left(-i\hbar\frac{\partial}{\partial x}\right) = -i\hbar\frac{\partial}{\partial\phi}\,. \tag{4.6}$$

Whenever the above assumptions are met, the Hamiltonian H commutes with $\hat{L}_z$. Therefore, its eigenvalue m (in units of $\hbar$) is a good quantum number, and we classify the states of the system according to it. As long as $[H,\hat{L}_z] = 0$, the

[1] Do not confuse the cylindrical coordinates (ρ,ϕ) with the same notation used for the charge density and piezoelectric potential in Chapter 3.

eigenfunctions of the Eq. (4.4) can be written as:

$$F^{(k_z,m)}(\rho,\phi) = \frac{1}{\sqrt{2\pi}}\, e^{i\,m\phi}\mathcal{F}^{(k_z,m)}(\rho) \quad , \quad m = 0, \pm 1, \pm 2, \ldots \,. \tag{4.7}$$

Substituting (4.7) in (4.4) we get a series of problems with independent energy subbands for each value of m.

$$\left[T_\rho^{(m)} + \frac{\hbar^2 k_z^2}{2m_z^*} + V^{(\mathrm{NW})}(\rho)\right] \mathcal{F}_\lambda^{(k_z,m)}(\rho) = E_{m,\lambda}(k_z)\mathcal{F}_\lambda^{(k_z,m)}(\rho)\,, \tag{4.8}$$

where the kinetic operator has been rewritten as:

$$T_\perp \rightarrow T_\rho^{(m)} = -\frac{\hbar^2}{2m_\perp^*}\left(\frac{1}{\rho}\frac{\partial}{\partial\rho}\,\rho\,\frac{\partial}{\partial\rho} - \frac{m^2}{\rho^2}\right). \tag{4.9}$$

and λ represents other quantum numbers necessary to label the energy eigenstates. Besides the spin degeneracy we find that the states with $\pm m$ are also degenerate.

4.1.2. Resolution of the Problem

In general, it is not possible to solve the equation (4.8) analytically for an arbitrary potential. In this work, to solve the nanowire problem, we have chosen a method in which we first expand the envelope function in a series of orthogonal basis functions with coefficients to be determined. Introducing such expansion in (4.8), the resolution of the differential equation reduces to a matrix eigenvalue problem, which can be solved numerically to give the energies of the nanowire. Once the eigenvectors are obtained we can reconstruct the envelope functions. This method was successfully implemented in a similar problem by J. Y. Marzin and G. Bastard[167]. A more general formulation and a thorough discussion on the justification and validity can be found in the work of G. A. Baraff and D. Gershoni[168]. This strategy offers a versatile solution method requiring moderate computing resources. Other methods commonly employed for solving the Schrödinger equation are, for example, the transfer matrix formalism[169], and those where space is discretized (finite difference[170], finite element[171] and boundary element[172] methods).

To implement the solution method it is necessary to first choose a set of basis functions that fits with the geometry of the problem. We have chosen as basis states the eigensolutions for a cylindrical cavity with the same radius R as the NW and with infinity potential barriers, so that the assumed boundary conditions at the

external surface of the nanowire are immediately fulfilled. The basis functions and the energy eigenvalues of that auxiliar problem are then given, for m fixed, by:

$$\xi_\alpha^{(m)}(\rho,\phi) = \frac{1}{\sqrt{2\pi}} e^{im\phi} \mathcal{N}_\alpha^{(m)} J_m(k_\alpha^{(m)}\varrho)\,, \tag{4.10}$$

$$\epsilon_\alpha^{(m)} = \frac{\hbar^2}{2m_\perp^*}\left(\frac{k_\alpha^{(m)}}{R}\right)^2 + \frac{\hbar^2 k_z^2}{2m_z^*}\,, \tag{4.11}$$

where $\varrho = \rho/R$, J_m is the Bessel function of order m and $k_\alpha^{(m)}$ is its αth zero ($\alpha = 1, 2, \dots$). The normalization constant is defined as:

$$\mathcal{N}_\alpha^{(m)} = \frac{\sqrt{2}}{R\left|J_{m+1}\left(k_\alpha^{(m)}\right)\right|}\,, \tag{4.12}$$

so that the basis functions are orthonormal

$$\langle \xi_{\alpha'}^{(m')} | \xi_\alpha^{(m)} \rangle = \int_{\mathcal{S}_{\mathrm{NW}}} d^2\boldsymbol{r}\; \xi_{\alpha'}^{(m')*}(\rho,\phi)\, \xi_\alpha^{(m)}(\rho,\phi) = \delta_{m,m'}\delta_{\alpha,\alpha'}\,. \tag{4.13}$$

Now, to solve Eq. (4.8) we express the envelope function of the electron in the potential $V^{(\mathrm{NW})}(\rho)$ as a finite linear combination of basis functions $\xi_\alpha^{(m)}(\rho,\phi)$:

$$\frac{1}{\sqrt{\Omega}} F_\lambda^{(k_z,m)}(\rho,\phi) = \sum_{\beta=1}^{N_R} [A_\lambda^{(k_z,m)}]_\beta\, \xi_\beta^{(m)}(\rho,\phi)\,, \tag{4.14}$$

where $[A_\lambda^{(k_z,m)}]_\beta$ are the coefficients to be determined. The number of basis functions N_R is a parameter of the numerical method, and it must be chosen large enough so as to guarantee the convergence of the solutions to the eigenvalue problem. Now, by substituting (4.14) in (4.8), multiplying both sides of the equation by $\xi_\alpha^{(m)*}(\rho,\phi)$ and integrating over the cross section of the nanowire, $\mathcal{S}_{\mathrm{NW}}$, we obtain the following matrix problem, for fixed k_z and m:

$$\sum_{\beta=1}^{N_R} \left\langle \xi_\alpha^{(m)} \left| H^{(\mathrm{NW})} \right| \xi_\beta^{(m)} \right\rangle [A_\lambda^{(k_z,m)}]_\beta = E_{m,\lambda}(k_z)\,[A_\lambda^{(k_z,m)}]\,, \tag{4.15}$$

where

$$\left\langle \xi_\alpha^{(m)} \left| H^{(\mathrm{NW})} \right| \xi_\beta^{(m)} \right\rangle = \int_{\mathcal{S}_{\mathrm{NW}}} d^2\boldsymbol{r}\; \xi_\alpha^{(m)*}(\rho,\phi) H^{(\mathrm{NW})} \xi_\beta^{(m)}(\rho,\phi)\,. \tag{4.16}$$

With this procedure, we have transformed the differential equations into a matrix eigenvalue problem. The expressions for the matrix elements can be found in Appendix C. The Hamiltonian matrices so obtained for fixed k_z and m can be efficiently diagonalized to give a sequence of eigenvalues $\{E_{m,\lambda}(k_z)\}_\lambda$ and associated eigenvectors.

4.2. Multiband Model

In the single band model introduced in Section 4.1, we considered that all the information of the band structure could be represented by the effective mass parameters. Although the picture offered by this model has been used to successfully explain many properties of semiconductor heterostructures,[173] it is also well known that a realistic description of the NW electronic structure needs to go beyond that simplified model. In this section, we will extend the theoretical framework by considering a larger number of coupled Bloch functions in the description of the electron wave function. For this task, we used in its full capacity the multiband ($\boldsymbol{k}\cdot\boldsymbol{p}$) envelope function approximation developed in Sec. 2.3. This procedure will allow us to define multiband models for studying the electronic structure of NWs and give a more accurate description of the properties of these nanostructures.

4.2.1. Formulation of the Multiband Envelope Function Equation

In the first place, following the procedure presented in Sec. 2.3, we first select the underlying $\boldsymbol{k}\cdot\boldsymbol{p}$ model on which the multiband envelope function methodology is going to be built up. This implies identifying a set of A-bands (number N_A) for which the Γ-point Bloch amplitudes $\{U_a\}$ and energy matrices $\{E^{(0)}\,\delta_{aa'}+\Delta_{aa'}\}$ are known for the materials composing the NW. The Bloch amplitudes $\{U_a\}$ are assumed to be similar for all materials so any of them or a linear combination thereof can be used in the envelope function expansion of the nanowire electronic wavefunction:

$$\Psi^{(k_z)}(\boldsymbol{r}) = \sum_a F_a^{(k_z)}(\boldsymbol{r})\, U_a(\boldsymbol{r})\,, \tag{4.17}$$

where $F_a^{(k_z)}(\boldsymbol{r})$ can be written as:

$$F_a^{(k_z)}(\boldsymbol{r}) = \frac{1}{\sqrt{\mathcal{L}}}\, e^{ik_z z}\, F_a^{(k_z)}(x,y) \quad . \tag{4.18}$$

The equation determining these wave functions and energies for fixed k_z was introduced in Eq. (2.38) and we reproduce it here:

$$\sum_{a'} H^{(\mathrm{NW})}_{aa'} F^{(k_z)}_{a'}(x,y) = E(k_z) F^{(k_z)}_{a}(x,y)\,, \tag{4.19}$$

where $E(k_z)$ is the energy, and

$$H^{(\mathrm{NW})}_{aa'} \equiv \left[\tilde{T}^{(\mathrm{NW})}_{aa'}\left(-i\frac{\partial}{\partial x}, -i\frac{\partial}{\partial y}, k_z\right) + E^{(\mathrm{NW})}_{aa'}(x,y)\right]\,.$$

In the applications that we will undertake in this work, the multiband model considered is the 8×8 $\boldsymbol{k}\cdot\boldsymbol{p}$ method. The specific form of the differential matrix operator $\tilde{T}^{(\mathrm{NW})}_{aa'}$ $(a,a'=1,\ldots 8)$ is obtained by taking the $\boldsymbol{k}\cdot\boldsymbol{p}$ Hamiltonian of Eq. (A.3) and (A.9) and making the substitution $k_\alpha \to -i\hbar\frac{\partial}{\partial x_\alpha}$, for $x_\alpha = x, y$, in the kinetic part. The Bloch amplitudes U_a at the center of the Brillouin zone are listed in Table 2.1 for zincblende materials and in Table 2.2 for wurtzite materials. If there were deformation in the system, we should incorporate to the equation (4.19) the contribution of Bir-Pikus Hamiltonian, $H^{(\mathrm{NW})}_{aa'} \to H^{(\mathrm{NW})}_{aa'} + H^{\mathrm{BP}}_{aa'}(\,\varepsilon_{ij}(x,y)\,)$ (see (A.8) and (A.17)). This Hamiltonian has a dependence with position through the components of the strain tensor $\varepsilon_{ij}(x,y)$. The parameters of $\tilde{T}^{(\mathrm{NW})}$ and H^{BP} (kinetic Luttinger parameters, deformation potentials, etc ...) will be considered independent of position, i.e. constant throughout the NW cross section as discussed in Sec. 2.3.2. On the other hand, the potential term which appears in (4.19) is determined by the position dependence of the energy parameters used in the definition of the $\boldsymbol{k}=0$ band edges in the model:

$$E^{(\mathrm{NW})}_{aa'}(x,y) = \left(E^{(0,\mathbb{A})}_{a}\,\delta_{aa'} + \Delta^{(\mathbb{A})}_{aa'}\right)\,\chi^{(\mathbb{A})}(x,y) + \left(E^{(0,\mathbb{B})}_{a}\,\delta_{aa'} + \Delta^{(\mathbb{B})}_{aa'}\right)\,\chi^{(\mathbb{B})}(x,y)\,. \tag{4.20}$$

As before, for the nanowires we assume that outside their external surface the potential is infinitely high, and the domain of definition of the electron wavefunctions is limited to the cross section of the material system. An additional potential W could be easily taken into account by making $E^{(\mathrm{NW})}_{aa'}(x,y) \to E^{(\mathrm{NW})}_{aa'}(x,y) + W(x,y)\,\delta_{aa'}$.

Now there come the assumptions specific to our nanowire model. As in the single band model, we assume that we are focusing on a system with an axially symmetric potential, so that:

$$E^{(\mathrm{NW})}_{aa'}(x,y) = E^{(\mathrm{NW})}_{aa'}(\rho) \quad .$$

In Section (4.1), we presented a single band model which allowed to express the electron wave function as an eigenfunction of the envelope angular momentum projection $\hat{L}_z$. This greatly helped to simplify the problem. In the multiband approach the problem turns out to be more complicated because the function $\Psi(\boldsymbol{r})$ is a multiband object involving simultaneously N_A scalar envelope functions that have to obey the system of differential equations (4.19). It is however possible under some circumstances to use symmetry arguments to also simplify this problem. The formalism we have implemented in this work takes advantage of the symmetry properties of the nanowire even in the presence of multiband coupling.[174,175] Below we will briefly review the main elements of this procedure.

According to K. J. Vahala and P. C. Sercel, the space of the multiband envelope functions can be formally endowed with a generalized total angular momentum defined as $\hat{\boldsymbol{J}} = \hat{\boldsymbol{L}} + \hat{\boldsymbol{j}}$, where $\hat{\boldsymbol{L}}$ is the envelope orbital angular momentum operator acting on the space of envelope functions F_a and $\boldsymbol{j}$ is the intrinsic (Bloch) angular momentum associated to the symmetries under rotations of the (spinor) Bloch amplitudes U_a. The corresponding z-projection of the angular momentum operator is: $\hat{J}_z = \hat{L}_z + \hat{j}_z$.

Due to the axial symmetry of the nanowire, it seems reasonable to express the envelope function in terms of functions with well defined z component of the orbital angular momentum as follows:

$$F_a^{(k_z)}(\rho,\phi) = \sum_m \frac{1}{\sqrt{2\pi}}\, e^{i\,m\phi} \mathcal{F}_a^{(k_z,m)}(\rho)$$

$$\longrightarrow \quad \Psi^{(k_z)}(\boldsymbol{r}) = \frac{1}{\sqrt{\mathcal{L}}}\, e^{ik_z z} \sum_a \sum_m \frac{1}{\sqrt{2\pi}}\, e^{i\,m\phi} \mathcal{F}_a^{(k_z,m)}(\rho)\, U_a(\boldsymbol{r})\,, \tag{4.21}$$

where, for each a, we have included a sum over m since this is the most general form that the solution can adopt. As explained in Secs. 2.2.2 and 2.2.3, the Bloch amplitudes U_a have a well defined z component of the intrinsic angular momentum operator, $\hat{j}_z = \hat{l}_z + \hat{s}_z \to j_z(a)$, as can be easily checked in Tables 2.1 and 2.2. Therefore, each separate term in (4.21) would have an associated total angular momentum projection: $m + j_z(a)$.

If $[H^{\mathrm{NW}}, \hat{J}_z] = 0$, then it would be possible to work with simultaneous eigenfunctions of H^{NW} and $\hat{J}_z$, and therefore the eigenvalue of $\hat{J}_z \to M$ could be used to label the energy eigenstates. However, in general the commutator $[H^{\mathrm{NW}}, \hat{J}_z]$ is nonzero. This is because the rotational symmetry around the NW axis (Z-axis) of the underlying bulk $\boldsymbol{k}\cdot\boldsymbol{p}$ Hamiltonian is smaller than the rotation group C_∞. Although it can be shown that in the case of wurtzite with $Z \parallel [0001]$ we have

$[H^{\mathrm{NW}}, \hat{J}_z] = 0$, the most general zincblende Hamiltonian contains a number of terms that spoil the desired in-plane isotropy. To overcome this difficulty one can increase the symmetry of the Hamiltonian by introducing the axial approximation.[176] This approximation is based on the fact that $(\gamma_2 - \gamma_3)/2$ is very small when compared with $(\gamma_2 + \gamma_3)/2$ and therefore is expected to have a negligible impact on the elements of the $\boldsymbol{k}\cdot\boldsymbol{p}$ Hamiltonian where both terms appear (see Ec. (A.3)). Finally, if there is strain in the system, as induced, e. g., by some lattice mismatch or by external loads, its effect must be accounted for through the incorporation of $H^{\mathrm{BP}}(\varepsilon_{ij})$, and it is necessary to investigate also $[H^{\mathrm{BP}}, \hat{J}_z]$. In order for this commutator to vanish, one must require in the first place that the strain be axially symmetric (this necessitates making some isotropic approximations on the material constants in zincblende materials). Moreover, it must be required that the terms containing $(D_u - D'_u)/2$ in the Bir-Pikus Hamiltonian be neglected (see Ec. (A.8)). With all these approximations it is achieved that $[H^{\mathrm{NW}} + H^{\mathrm{BP}}, J_z] = 0$, and the energy eigenfunctions of $H^{\mathrm{NW}} + H^{\mathrm{BP}}$ can be chosen with defined angular momentum M:

$$\Psi^{(k_z,M)}(\boldsymbol{r}) = \frac{1}{\sqrt{\mathcal{L}}}\, e^{ik_z z} \sum_a F_a^{(k_z,M)}(\rho,\phi)\, U_a(\boldsymbol{r})$$

$$= \frac{1}{\sqrt{\mathcal{L}}}\, e^{ik_z z} \sum_a \left[\frac{1}{\sqrt{2\pi}}\, e^{i\, m_a \phi} \mathcal{F}_a^{(k_z,m_a)}(\rho)\right] U_a(\boldsymbol{r})\,, \tag{4.22}$$

where now the summation over m in (4.21) has been removed, since for each basis function U_a, the orbital angular momentum of the envelope function is uniquely determined by

$$m_a \equiv M - j_z(a) \quad .$$

In Table 4.1 we show, for different values of M, the corresponding envelope angular momenta m_a for both [001] zincblende and [0001] wurtzite materials.

Therefore, the Schrödinger (4.19) becomes:

$$\sum_{a'} H_{aa'}^{(\mathrm{NW})}\, F_{\lambda,a'}^{(k_z,M)}(\rho,\phi) = E_{M,\lambda}(k_z) F_{\lambda,a}^{(k_z,M)}(\rho,\phi)\,, \tag{4.23}$$

and, for fixed values of k_z and M, we have a family of independent states labeled by λ. Given the symmetry of the problem, the $\pm M$ solutions of (4.23) are Kramers doubly degenerate.[177]

		Zincblende [001]								Wurtzite [0001]							
	a	1	2	3	4	5	6	7	8	1	2	3	4	5	6	7	8
M	$j_z(a)$	$\frac{1}{2}$	$-\frac{1}{2}$	$\frac{3}{2}$	$\frac{1}{2}$	$-\frac{1}{2}$	$-\frac{3}{2}$	$\frac{1}{2}$	$-\frac{1}{2}$	$\frac{1}{2}$	$-\frac{1}{2}$	$\frac{3}{2}$	$-\frac{1}{2}$	$\frac{1}{2}$	$-\frac{3}{2}$	$\frac{1}{2}$	$-\frac{1}{2}$
$\frac{1}{2}$	m_a	0	1	-1	0	1	2	0	1	0	1	-1	1	0	2	0	1
$-\frac{1}{2}$	m_a	-1	0	-2	-1	0	1	-1	0	-1	0	-2	0	-1	1	-1	0
$\frac{3}{2}$	m_a	1	2	0	1	2	3	1	2	1	2	0	2	1	3	1	2
$-\frac{3}{2}$	m_a	-2	-1	-3	-2	-1	0	-2	-1	-2	-1	-3	-1	-2	0	-2	-1
$\frac{5}{2}$	m_a	2	3	1	2	3	4	2	3	2	3	1	3	2	4	2	3
$-\frac{5}{2}$	m_a	-3	-2	-4	-3	-2	-1	-3	-2	-3	-2	-4	-2	-3	-1	-3	-2
$\frac{7}{2}$	m_a	3	4	2	3	4	5	3	4	3	4	2	4	3	5	3	4
$-\frac{7}{2}$	m_a	-4	-3	-5	-4	-3	-2	-4	-3	-4	-3	-5	-3	-4	-2	-4	-3

Table 4.1: Pattern of values of the envelope angular momenta m_a for various values of M.

4.2.2. Resolution of the Problem

We will address the resolution of the equation (4.23) with the same numerical method used in the single band model and described in Sec. 4.1.2. First, we expand each envelope function appearing in (4.23) in terms of the basis functions (4.11):[2]

$$\frac{1}{\sqrt{\Omega}} F_{\lambda,a}^{(k_z,M)}(\rho,\phi) = \sum_{\alpha=1}^{N_R} [A_{\lambda,a}^{(k_z,M)}]_\alpha \, \xi_\alpha^{(m_a)}(\rho,\phi), \tag{4.24}$$

where $[A_{\lambda,a}^{(k_z,M)}]_\alpha$ are the coefficients to be determined. These expansions are introduced into (4.23) which is then transformed into the matrix eigenvalue problem:

$$\sum_{a'} \sum_{\alpha'=1}^{N_R} \left\langle \xi_\alpha^{(m_a)} \left| H_{aa'}^{(\mathrm{NW})} \right| \xi_{\alpha'}^{(m_{a'})} \right\rangle [A_{\lambda,a'}^{(k_z,M)}]_{\alpha'} = E_{M,\lambda}(k_z) \, [A_{\lambda,a}^{(k_z,M)}]_\alpha \, . \tag{4.25}$$

This problem of dimension $(8N_R \times 8N_R)$ can be solved by standard diagonalization techniques. Appendix C shows the details of the calculation of the matrix elements.

4.2.3. Optical Absorption

The initial and final NW electron states of the optical transition are given by:

$$i \equiv \left(k_z^{(i)}, M_i, \lambda_i\right) \Longrightarrow \Psi_{\lambda_i}^{(k_z^{(i)},M_i)}(\boldsymbol{r}) = \frac{1}{\sqrt{\mathcal{L}}} \, e^{ik_z^{(i)} z} \sum_a F_{\lambda_i,a}^{(k_z^{(i)},M_i)}(\rho,\phi) \, U_a(\boldsymbol{r}) \, , \tag{4.26a}$$

[2] The maximum number of basis functions used in our calculations has been $N_R = 30$.

$$f \equiv \left(k_z^{(f)}, M_f, \lambda_f\right) \Longrightarrow \Psi_{\lambda_f}^{(k_z^{(f)}, M_f)}(\boldsymbol{r}) = \frac{1}{\sqrt{\mathcal{L}}}\, e^{ik_z^{(f)} z} \sum_a F_{\lambda_f, a}^{(k_z^{(f)}, M_f)}(\rho, \phi)\, U_a(\boldsymbol{r})\,. \tag{4.26b}$$

The optical absorption spectrum is given by ($k_z^{(f)} = k_z^{(i)} =: k_z$):

$$\alpha(\hbar\omega) = \mathcal{C} \sum_{k_z} \sum_{M_f, \lambda_f} \sum_{M_i, \lambda_i} \left| P_{fi}^{(\mathrm{inter})}(\hat{\boldsymbol{e}}) \right|^2 \frac{1}{\pi} \frac{\Gamma/2}{(E_{M_f,\lambda_f}(k_z) - E_{M_i,\lambda_i}(k_z) - \hbar\omega)^2 + (\Gamma/2)^2}\,, \tag{4.27}$$

with

$$\mathcal{C} = \frac{n(\omega)}{c} \frac{2\pi}{\hbar} \left(\frac{1}{2} \frac{e}{m_0}\right)^2 |\, A_0\,|^2 \quad ,$$

and the interband matrix element is given here by:

$$P_{fi}^{(\mathrm{inter})}(\hat{\boldsymbol{e}}) = \sum_{aa'} (\hat{\boldsymbol{e}} \cdot \boldsymbol{p}_{aa'})\, \delta_{m_a, m_{a'}} \sum_{\alpha=1}^{N_R} \left[A_{\lambda_f, a}^{(k_z, M_f)}\right]_\alpha^* \left[A_{\lambda_i, a'}^{(k_z, M_i)}\right]_\alpha . \tag{4.28}$$

where $m_a = M_f - j_z(a)$ and $m_{a'} = M_i - j_z(a')$.

It is interesting to investigate whether there is any selection rule associated to the angular momentum number M. This is achieved by recalling the expressions (B.1) and (B.2), which show that the momentum matrix element has the property:

$$\hat{\boldsymbol{e}}_\pm \cdot \boldsymbol{p}_{aa'} \propto \delta_{j_z(a), j_z(a') \pm 1}\,, \tag{4.29a}$$

$$\hat{\boldsymbol{e}}_z \cdot \boldsymbol{p}_{aa'} \propto \delta_{j_z(a), j_z(a')}\,, \tag{4.29b}$$

where

$$\boldsymbol{e}_\pm = \frac{1}{\sqrt{2}}\, (\boldsymbol{e}_x \pm i\, \boldsymbol{e}_y) \quad .$$

By incorporating this result into (4.28) we obtain the following property of the interband matrix element:

$$P_{fi}^{(\mathrm{inter})}(\hat{\boldsymbol{e}}_\pm) \propto \delta_{M_f, M_i \pm 1}\,,$$
$$P_{fi}^{(\mathrm{inter})}(\hat{\boldsymbol{e}}_z) \propto \delta_{M_f, M_i}\,.$$

Consequently, we obtain the following selection rules:

- For a radiation field polarized in the XY plane ($\hat{\boldsymbol{e}}_\pm$) the z component of the total angular momentum of the initial and final states of the optical

transitions will differ in one unit: $M_f = M_i \pm 1$.

- For the case of polarization parallel to the NW orientation the value of M should be conserved: $M_f = M_f$.

In order to analyze the electronic structure and the optical absorption spectra obtained within this sophisticated multiband framework, it is interesting to have a characterization of the symmetry of the electronic states. We quantify it here by the projections of the wavefunction over Bloch (spinor) amplitudes of specified symmetry, generically denoted $|\ell\rangle$,

$$w_\ell = \int dx\, dy \left| \sum_a \langle \ell \, | U_a \rangle \; F_a(x,y) \right|^2 . \tag{4.30}$$

In the discussion of the symmetry of the electronic states of zincblende NWs that we present below we have decided to use the projections over the bulk Γ Bloch amplitudes:

$$\begin{aligned} w_S &= w_{S\uparrow} + w_{S\downarrow} \\ w_{hh} &= w_{hh+} + w_{hh-} \\ w_{lh} &= w_{lh+} + w_{lh-} \\ w_{so} &= w_{so+} + w_{so-} \end{aligned} \quad .$$

These symmetry weights satisfy

$$w_S + w_{hh} + w_{lh} + w_{so} = 1 \, .$$

On the other hand, in the case of wurtzite NWs we will use the projections:

$$\begin{aligned} w_S &= w_{S\uparrow} + w_{S\downarrow} \\ w_X &= w_{X\uparrow} + w_{X\downarrow} \\ w_Y &= w_{Y\uparrow} + w_{Y\downarrow} \\ w_Z &= w_{Z\uparrow} + w_{Z\downarrow} \end{aligned} \quad .$$

It is convenient to introduce also the notation $w_\perp = w_X + w_Y$. These symmetry weights satisfy

$$w_S + w_\perp + w_Z = 1 \, .$$

In analyzing the symmetry weights of the calculated electronic states it is often found that one of these weights is significantly larger than the rest (say $w_\ell > 0.5$), and then we say that the state has dominant ℓ-character or ℓ-symmetry . The

numbers w_ℓ themselves will be referred as symmetry weights, symmetry characters or simply characters.

Chapter 5

Electronic Structure and Optical Absorption of Zincblende Nanowires

In this chapter we will study the electronic structure and optical absorption of free-standing and core-shell nanowires having zincblende crystal structure. We use the term *free-standing* to refer to nanowires (NWs) made of a single material as opposed to heterostructure systems such as the core-shell nanowires. To calculate the electronic and optical properties, we will use the model developed in Chapter 4.

The chapter is organized as follows. Initially, in Sec. 5.1 we present the results on the size dependence of the electronic and optical properties of free-standing InAs and GaAs NWs. We have considered NWs grown along [001] and [111] crystallographic directions. Then, in Sec. 5.2 we focus on the study of lattice-matched [111] $Al_xGa_{1-x}A$/GaAs core-shell nanowires (CSNWs), which allows to discuss the purely geometrical effects induced by the new geometry. Finally, in Sec. 5.3 we present the results of the electronic and optical properties of lattice-mismatched [001] GaAs/InAs CSNWs, which allows to investigate the interplay of the geometry and the built-in strain fields.

Before the exposition of the results, it is convenient to fix some notation and methodology that will be followed during the discussions in Chapters 5 and 6. Obviously, the NW electronic structure is conveniently divided into the energy ranges corresponding to the bulk conduction band (CB) and valence bands (VB). The energy spectrum of the NWs is organized into a manifold of one-dimensional subbands, whose dispersion can be quite involved, specially in the VB region. It is therefore convenient to first focus on the $k_z = 0$ (Γ) states, hereafter referred simply as CB and VB states. In the coming discussions, these states will be labeled as follows: For a given nanowire, we will denote the CB (VB) states as $c_1, c_2, c_3, \ldots$

$(v_1, v_2, v_3, \dots)$ in order of increasing energy separation from the bulk CB (VB) edge. If necessary, each of these states can be more precisely described by giving its angular momentum $|M|$ and its dominant character ℓ (see (4.30)), e.g. $c_1(|M| = 1/2, S)$.[1] The lowest CB state is c_1 and the highest VB state is v_1, and their energy difference determines the NW fundamental gap energy $E_g^{(\mathrm{NW})} = E_{c_1} - E_{v_1}$. The material parameters used in the calculations are collected in Appendix E.1.

5.1. Free-Standing InAs and GaAs Nanowires

In this section we analyze first the free-standing NWs with zincblende structure. We investigate in detail the size dependence of the electronic and optical properties of both InAs and GaAs nanowires. We have considered NWs having radius $R = 1 - 120$ nm which covers the range of sizes in recently grown NWs.[36,178,179] This will give an idea of the effect of the confinement imposed by the NW geometry. Furthermore, we will explore in parallel the dependence on the nanowire orientation, by considering NWs grown along [001] and [111] crystallographic directions. We have chosen these orientations because they are compatible with the cylindrical symmetry of the bulk electronic structure, as explained in Sec. 4.2.1.

In the literature, the electronic and optical properties of both InAs and GaAs nanowires grown along the [001] and [111] crystallographic directions have been studied. Recently, the eight-band $\boldsymbol{k} \cdot \boldsymbol{p}$ model was implemented to study the electronic properties of InAs NWs grown along [001] and [111] directions [180]. Kishore et.al [95] also used the eight-band $\boldsymbol{k} \cdot \boldsymbol{p}$ model to study the electronic and optical properties of [001] InAs NWs. Redinski and Peeters have calculated the band structure of GaAs nanowires oriented in the [111] direction using the six-band $\boldsymbol{k} \cdot \boldsymbol{p}$ model.[18] However, these studies lack a detailed analysis of the size dependence of the electronic and optical properties of the nanowires. Particularly, they miss the analysis of the characters of the lowest CB and highest VB states, which play a very important role in understanding the optical absorption of nanowires.

5.1.1. InAs Nanowires

Electronic Structure

In order to study the effects of confinement and direction of growth on the electronic structure of the InAs NW, here we start with the analysis of the CB and

[1] Remember that each state c_i or v_i exhibits double ($\pm M$) degeneracy, and therefore only $|M|$ needs to be specified.

VB states as a function of size. We start by investigating the dependence on the NW radius R of the CB states at the Γ-point ($k_z = 0$). The R-dependence of the confinement energies of the five lowest CB states, denoted $c_1, \ldots, c_5$, is presented in Fig. 5.1. Note that, as explained in Chapter 4, due to the inclusion of the spin-orbit interaction, the spin up-down degeneracy does not apply here and it only remains the time-reversal (Kramers) degeneracy, which in this system is assimilated with the twofold degeneracy $\pm M$. Therefore, the CB states (c_2, c_3) and (c_4, c_5) are no longer degenerate, although the corresponding splittings $(E_{c_3} - E_{c_2})$ and $(E_{c_5} - E_{c_4})$ are very small (< 1 meV). The energies of the CB states show a monotonous increase with decreasing NW radius as a result of the lateral confinement effect, without any level crossing or anti-crossing. Moreover, the confinement effect is larger for [001] orientation as compared to the [111] one: the confinement energy of the state c_1 for $R = 1$ nm is 0.77 eV for the [001] InAs NW and 0.65 eV for the [111] InAs NW. This difference in the strength of CB confinement energies is mainly due to lighter in-plane heavy hole mass of [001] InAs NW (0.521 m_0) than [111] (0.596 m_0).

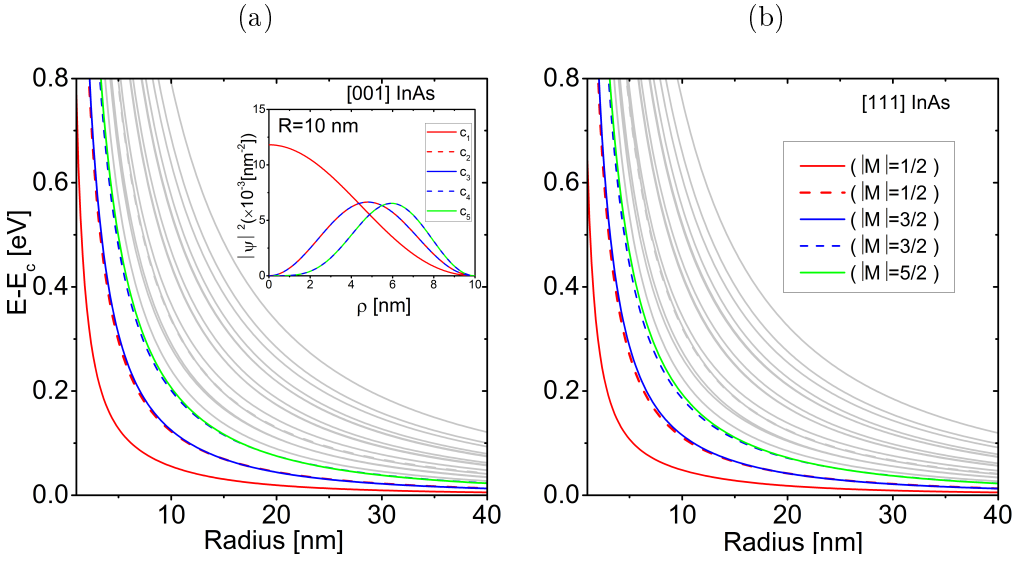

Figure 5.1: Confinement energies of the lowest CB states as a function of the NW radius for (a) [001] and (b) [111] InAs NWs. E_c denotes the bulk CB edge. The squared wave function of the states for $R = 10$ nm are given in the inset.

To investigate the dependence of the energy E_{c_1} with R, it has been fitted to the function:

$$E_{c_1}(R) - E_c = \frac{C}{R^\beta}\,, \tag{5.1}$$

and the following values are obtained: $C = 0.79$, $\beta = 1.16$ for [001] InAs NWs

and $C = 0.66$, $\beta = 1.15$ for [111] InAs NWs. Therefore, the dependence given in Eq. (5.1) deviates significantly from the relation $\sim 1/R^2$ predicted by the single-band effective mass approximation (EMA), which evidences the necessity of the multiband approach that we have used.

It is also interesting to study the symmetry of the CB states. In Figs. 5.2a and 5.2b we present the symmetry weights of the wavefunction for the state c_1 of InAs NWs grown along [001] and [111] directions, respectively. The results are again similar in both orientations. The S-character has the largest contribution ($w_S > 92\,\%$) for all NW sizes considered, whereas the remaining characters have contributions below 5 %. This admixture of VB symmetry within the CB state is induced by the enhancement of the CB-VB coupling due to the lateral confinement. As the NWs become wider (R >100 nm), the character w_S of the state c_1 tends to $\simeq 100\,\%$, in accordance with the pure S-symmetry of the CB edge in the bulk InAs crystal.

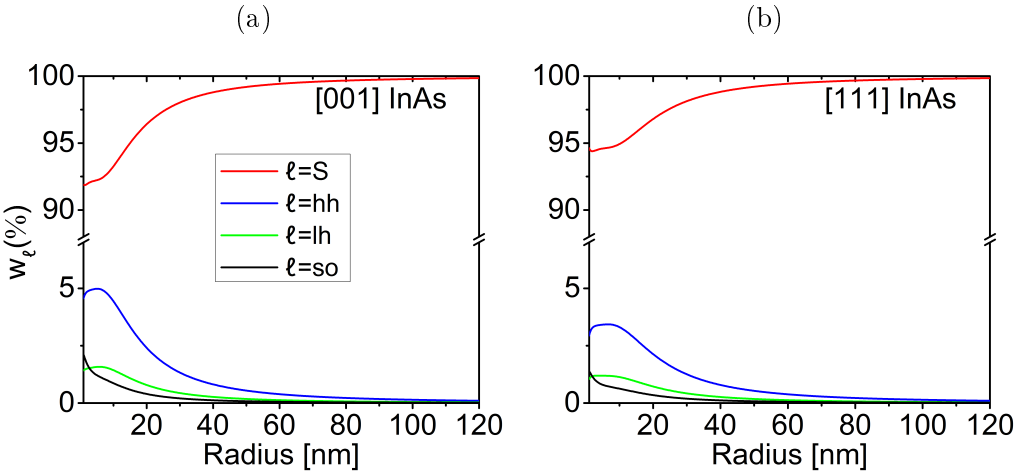

Figure 5.2: Symmetry weights of the wavefunction corresponding to the state c_1 in (a) [001] and (b) [111] InAs NWs, as a function of the radius.

Let us now see how the VB states behave for different sizes. Figures 5.3a and 5.3b show the confinement energies of the five highest VB states at the Γ-point for [001] and [111] InAs NWs as a function of size. In the smallest [001] InAs NW (R =1 nm), the confinement energies of the five highest VB states span a range of 1.7 eV, with $E_{v_1} - E_v$ being 0.73 eV. In the case of [111] InAs NWs, the confinement energies are slightly smaller: The five highest VB states span a range of 1.23 eV with $E_{v_1} - E_v$ corresponding to 0.35 eV. In both [001] and [111] InAs NWs the confinement energies decrease with increasing radius and become very small (<13 meV) in larger (R >15 nm) InAs NWs. The confinement energies of the two highest

states, v_1 and v_2 (that have the same angular momentum $|M| = 1/2$ but different dominant character) show a crossing for both orientations. In [001] InAs NWs, the size dispersion of v_1 and v_2 cross each other at a critical radius R_c ∼4.6 nm. For NWs with $R \leq 4.6$ nm v_1 and v_2 have dominant $lh(+)$ and $lh(-)$-characters, respectively, whereas for radius $R > 4.6$ nm they exchange those characters. This finding is contrary to results reported in Ref.[94,181] where the character of the VB states remain similar for different InAs nanowire sizes. The VB state v_3 and v_4 are dominantly composed of $lh(+)$ and $lh(-)$-characters, respectively. The size dispersion of v_3 and v_4 do not show any crossing in all the considered range. When we look at the [111] InAs NWs, we find the crossing radius is decreased to $R_c \sim 3.2$ nm. Unlike the case of [001] InAs NWs, the size dispersions of v_3 and v_4 also cross each other at around the same critical radius $R_c \sim 3.2$ nm. For [111] InAs NWs with radius $R \leq 3.2$ nm, v_3 and v_4 have $lh(-)$ and $lh(+)$-characters, respectively. This change in the symmetry of the topmost VB state can have influence on both the electronic and optical properties of the nanowires as will be discussed below.

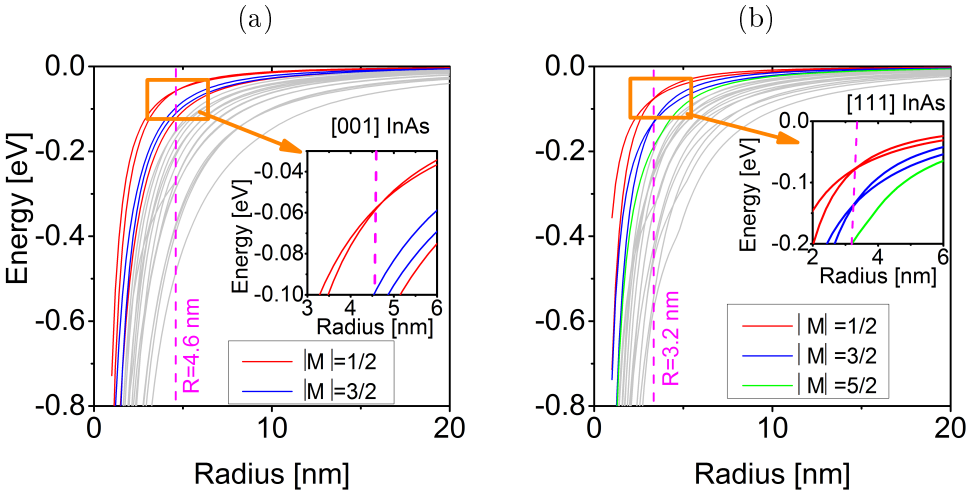

Figure 5.3: Size dependence of the confinement energies $E - E_v$ of the top five Γ-point VB states of (a) [001] and (b) [111] InAs NWs. The vertical dashed lines show the radius at which the energies cross each other. The states are labeled by their angular momentum $|M|$.

We extend our investigation to the study of the symmetry of the VB states. First we investigate the size dependent spinor distribution of v_1. In Fig. 5.4a we present the contribution of each symmetry to v_1 for [001] InAs as a function of the NW radius. For NWs with $R < 2$ nm the hh-character is dominant while for NWs with $R \geq 2$ nm the lh-character becomes more dominant. For larger ($R > 5$ nm) InAs NWs, the percentage contributions of both lh and hh becomes uniform at $w_{lh} \sim 74$ % and w_{hh} ∼26 %. Unlike the case of [001] InAs NWs, the

lh-character is dominant (w_{lh} >80 %) at all sizes for [111] InAs NWs as it can be seen in Fig. 5.4b. It has its smallest contribution ($w_{lh} \sim 80\,\%$) for $R \cong 1$ nm and reaches its maximum value ($w_{lh} \sim 91\,\%$) for $R \cong 5$ nm. That contribution slightly decreases as the NWs become larger ($R > 5$ nm) and almost becomes uniform at ($w_{hh} \sim 87\,\%$). The hh-character has a significant role in the composition of v_1 only for larger [111] InAs NWs. For both orientations of InAs NWs, the so-character has significant contribution in very small NWs. The S-character has no influence for all the NW sizes explored.

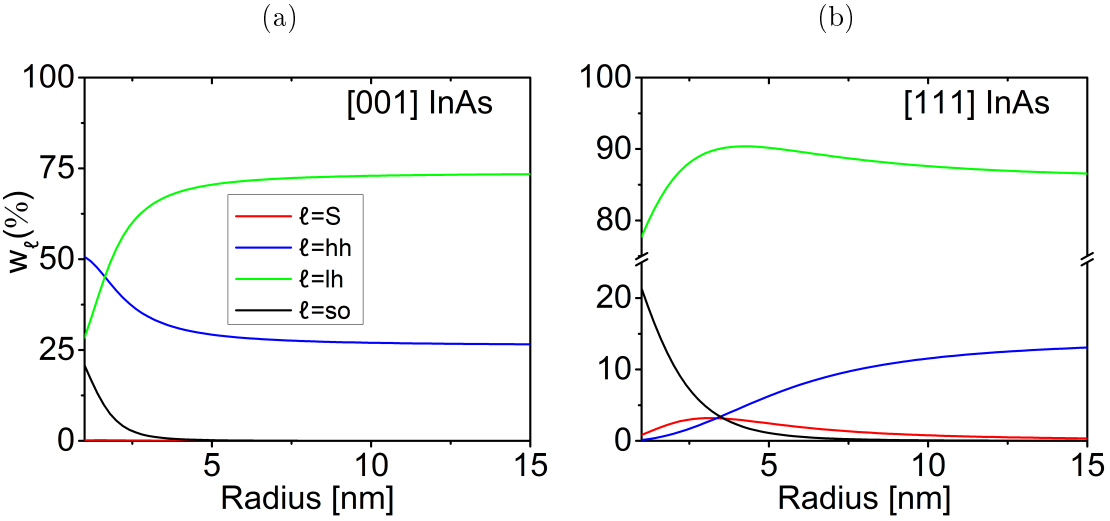

Figure 5.4: Symmetry weights of the spinors corresponding to the Γ-point VB v_1 for (a) [001] and (b) [111] InAs NWs as a function of the NW radius from 1 to 15 nm.

Next we present the size dependence of the fundamental band gap of [001] and [111] InAs NWs, $E_g^{\mathrm{NW}} = E_{c1} - E_{v1}$, which play an important role to understand the electronic and optical properties. In Figs. 5.5a and 5.5b we illustrate the confinement effect by representing the change of the NW band gap with respect to that of bulk InAs crystal band gap $\Delta\, E_g\,(R) = E_g^{\mathrm{NW}}(\mathrm{R}) - E_g^{\mathrm{bulk}}$ (where E_g^{bulk} =0.37 eV) as a function of size for InAs NWs oriented along [001] and [111]. For the smallest radius considered, R =1 nm, the band gaps are increased by 1.5 eV and 1 eV, respectively in [001] and [111] InAs NWs. However, as the radius increases the effect of confinement on the band gap monotonously decreases for both orientations and becomes very small (< 2 meV) for very large size nanowires with $R > 20$ nm. The nanowire band gap dependence with the radius can be compared with that predicted by the single band effective mass approximation (EMA). According to the single band EMA, the band gap change of the NW (ΔE_g) should follow the relation $\Delta E_g(R) \sim \hbar^2 R^2/2m$. We fitted our results to the function $\Delta E_g(R) = a/R^b$

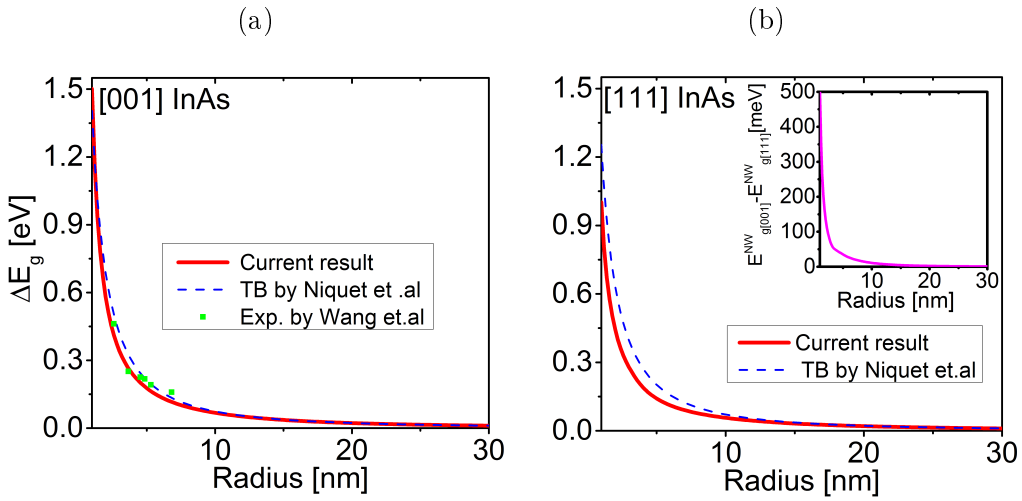

Figure 5.5: Change in the fundamental band gap energy ΔE_g of InAs NWs with respect to the band gap of bulk InAs crystal E_g =0.37 eV for (a) [001] and (b) [111] InAs NWs as a function of their size. The solid red lines are the results from our eight-band $\boldsymbol{k}\cdot\boldsymbol{p}$ Hamiltonian. Blue dashed lines correspond to TB calculations from Ref.[182]. Green dots in (a) are experimental results from Ref. [183]. The inset in (b) shows the band gap difference $E^{\mathrm{NW}}_{g[001]}$-$E^{\mathrm{NW}}_{g[111]}$ of InAs NWs.

where a and b are constants to be fitted. We obtain the values: a =1.54 and b =1.50 for [001] InAs NWs while we obtain relatively smaller a = 1.03 and b = 1.25 values for the [111] InAs NWs. These significant deviations from the relation predicted by the EMA again show the inadequacy of the single-band EMA and the necessity of the multiband model which is implemented in this work. Similar deviations are reported in different previous works.[19,93,183–185] When we compare our results with other theoretical and experimental works, we find that our result for small [001] InAs NWs (solid lines) fits well with both tight binding (TB) results from Ref. [182] (blue dashed lines) and experimental results from Ref. [183] (green squares). For larger [001] InAs NWs, particularly with radius R >7 nm, our results and TB results from Ref. [182] become indistinguishable. For the case of [111] InAs NWs, our band gap prediction fits well with TB results from Ref. [182] even though we observe small difference for smaller sizes. In the inset of Fig. 5.5b, we present the band gap difference ($E^{\mathrm{NW}}_{g[001]}$-$E^{NW}_{g[111]}$) between the [001] and [111] InAs NWs. The [001] InAs NWs have relatively larger band gap in small NWs. For example at R =1 nm the difference amounts to $\sim$ 500 meV. However, that difference becomes very small ($\leq$4 meV) as the NWs become larger ($R >$ 15 nm).

In Fig. 5.6 we present the band structures of InAs NWs with radius R =2.5, 10 and 20 nm. The zero of the energy is taken at the VB maximum of the corresponding bulk material. The conduction subbands in InAs NWs are not parabolic

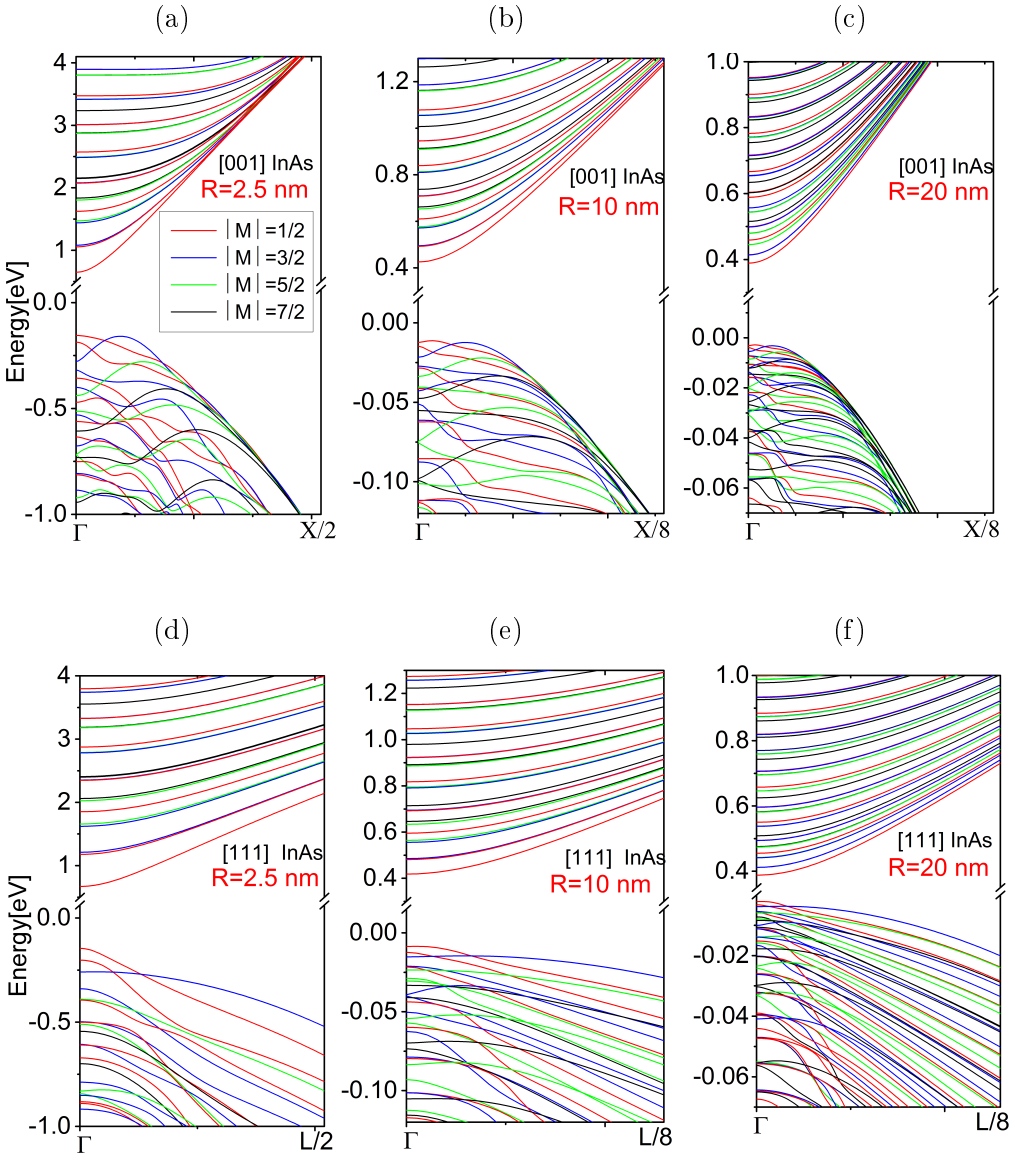

Figure 5.6: Band structure of [001] [Plots (a)-(c)] and [111] [Plots (d)-(f)] InAs NWs. For each orientation the results corresponding to R=2.5, R=10 and R=20 nm are shown. All the bands are labeled based on their angular momentum $|M|$.

around the Γ-point due to the CB-VB coupling. The highest VB states in both types of NWs have a camel back structure which results in a negative effective mass for some subbands. The camel back structure is more visible in the smaller NW while it disappears as the size of the NW is increased which is in agreement with the results from Ref.[18]. We also see in Fig. 5.6 that the VB dispersion of larger NWs become more complicated due to weaker confinement.

Optical Absorption

In Fig. 5.7 we show the calculated optical absorption for InAs NWs, following the theoretical model presented in Sec. 4.2.3. We have separately calculated the spectra for light polarizations $\hat{\boldsymbol{e}}_+$ (hereafter denoted $\hat{\boldsymbol{e}}_\perp$[2]) and $\hat{\boldsymbol{e}}_z$. In all the calculations in this thesis, the optical absorption spectra are obtained by introducing a Lorentzian broadening of $\Gamma = 5$ meV. We will particularly focus on the range of small radii ($R = 1 - 10$ nm) where we have found changes in the character of the highest VB states as the size is varied around a critical radius R_c. Remember that the values of R_c corresponding to [001] and [111] InAs NWs are 4.6 nm and 3.2 nm respectively. The spinor wavefunctions are labeled by the total angular momentum, $|M|$, which determines the *a priori* possible transitions according to the selection rules detailed in Sec. 4.2.3. But it is also of interest to identify the dominant character (or Bloch amplitude) in each spinor, and the associated envelope symmetry, according to the Table 4.1. To facilitate the analysis of the optical spectra, the properties of selected CB and VB states are summarized in Tables 5.1a and 5.1b for [001] and [111] InAs NWs, respectively.

In both [001] and [111] NWs, the lowest CB state c_1 has $S(\uparrow)$-character and s-type ($m = 0$) envelope function symmetry independently of the size. On the other hand, for NWs with radius $R \leq R_c$, the topmost VB state v_1 is composed of mainly $lh(+)$-character and has s-type ($m = 0$) envelope function symmetry. As a result, the oscillator strength of the transition $v_1(lh) \rightarrow c_1$ is non-zero for both polarizations. Due to this, the fundamental optical gap (defined as the lowest transition energy with appreciable oscillator strength) is exactly coincident with the NW band gap. This can be seen in the optical absorption of [001] and [111] InAs NWs with radius R =2.5 nm shown in Figs. 5.7a and 5.7c respectively. However, for [001] and [111] InAs NWs with radius $R > R_c$, the oscillator strength for the transition $v_1(lh) \rightarrow c_1$ is zero. However, the second VB state v_2 is composed of $lh(+)$-character and has s-type envelope function symmetry. Thus the oscillator

[2]In the axially symmetric NWs under study, the spectra for $\hat{\boldsymbol{e}}_+$ and $\hat{\boldsymbol{e}}_-$ are found to be identical so we refer to them generally by the notation $\hat{\boldsymbol{e}}_\perp$.

(a)

Size (nm)	State	Envelope symmetry	Dominant character	Optical transition
$R \leq 4.6$	c_1	s	S($\uparrow$)	
	v_1	s	$lh(+)$	bright
	v_2	p	$lh(-)$	dark
	v_3	p	$lh(+)$	dark
	v_4	d	$lh(-)$	dark
$R > 4.6$	c_1	s	S($\uparrow$)	-
	v_1	p	$lh(-)$	dark
	v_2	s	$lh(+)$	bright
	v_3	p	$lh(+)$	dark
	v_4	d	$lh(-)$	dark

(b)

Size (nm)	State	Envelope symmetry	Dominant character	Optical transition
$R \leq 3.2$	c_1	s	S($\uparrow$)	
	v_1	s	$lh(+)$	bright
	v_2	p	$lh(-)$	dark
	v_3	d	$lh(-)$	dark
	v_4	p	$lh(+)$	dark
$R > 3.2$	c_1	s	S($\uparrow$)	-
	v_1	p	$lh(-)$	dark
	v_2	s	$lh(+)$	bright
	v_3	p	$lh(+)$	dark
	v_4	d	$lh(-)$	dark

Table 5.1: Electronic and optical properties of the lowest CB and highest VB states for (a) [001] and (b) [111] InAs NWs as a function of size. Note that we have considered only the states with positive angular momentum: The states c_1, v_1, and v_2 have $M = +1/2$, and v_3 and v_4 have $M = +3/2$. The counterpart states with negative angular momentum are degenerate and have opposite spin projections. For each VB state, it is also annotated the dark or bright nature of the optical transition towards c_1, depending whether the full oscillator strength is zero/negligible or not.

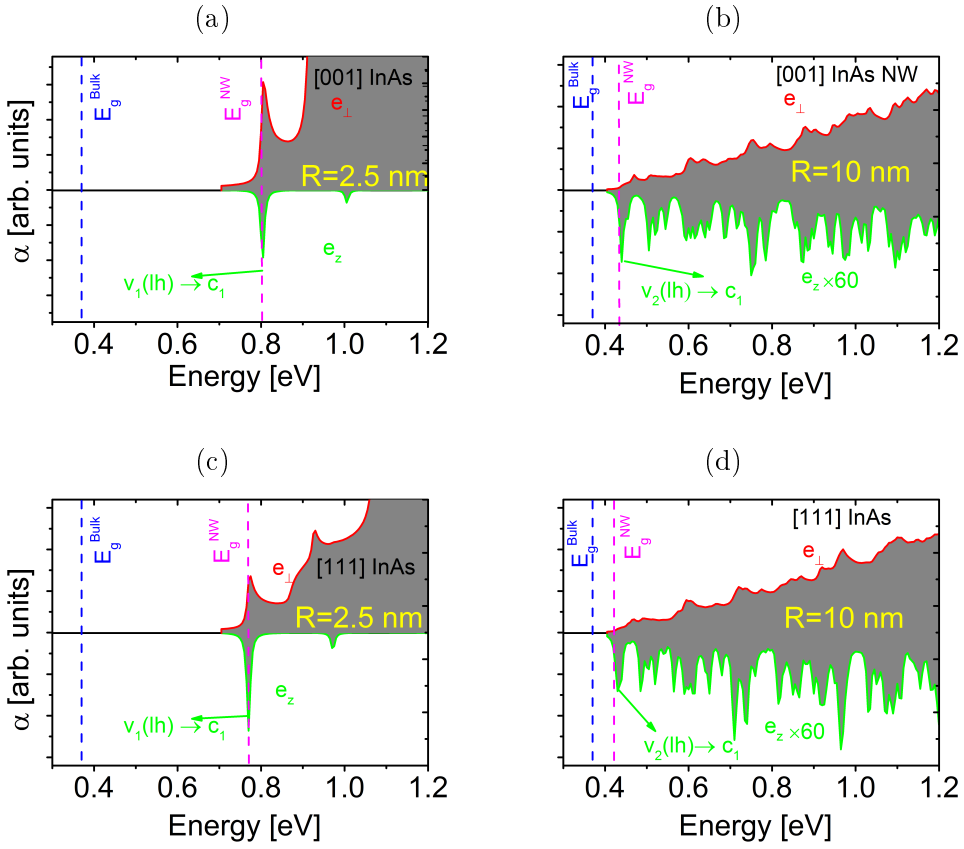

Figure 5.7: Plots (a) and (b) show the optical absorption of [001] InAs NWs with radius R=2.5 nm and R=10 nm respectively. Plots (c) and (d) show corresponding results for [111] InAs NWs. The purple and blue dashed vertical lines show the fundamental gaps of the InAs NW and bulk InAs crystal, respectively.

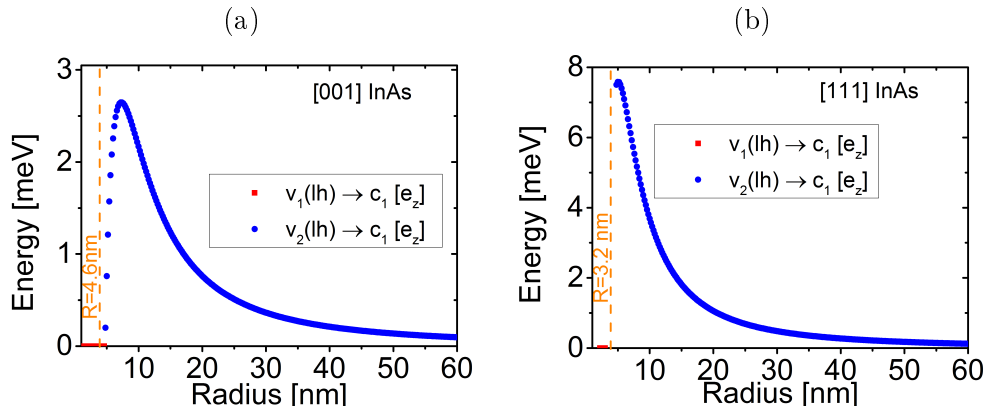

Figure 5.8: Plots (a) and (b) show the blueshift of the fundamental optical gap as as a function of size for [001] and [111] InAs NWs respectively.

strength of the transition $v_2(lh) \rightarrow c_1$ becomes non-zero. As a result, the onset of the optical absorption for [001] and [111] InAs NWs with radius $R > R_c$ is not placed at the band gap of the NWs. For [001] and [111] InAs NWs with radius R =10 nm (See Figs. 5.7b and 5.7d), the fundamental optical gaps lay respectively 2.1 and 3.7 meV higher in energy than the band gap of the corresponding NWs.

In the discussions above we have seen that the crossing in the size dispersion of the topmost VB states results in a blueshift of the fundamental optical gap with respect to the NW band gap of the in both [001] and [111] InAs NWs. Here we investigate the effect of size on this blueshift of the optical gap. In Fig. 5.8a we present the amount of blueshift in the fundamental optical gap of the optical absorption in [001] InAs NW. As discussed above, v_1 for [001] InAs NWs with radius $R \leq$4.6 nm is a bright state. As a result, the blueshift in this range of radius is zero. However, for NWs with radius $R >$4.6 nm, the blueshift increases with increase of size of the NW up to radius of $R \cong$ 7.2 nm where it reaches a maximum value of 2.65 meV. To the contrary, for NWs with radius $R >$ 7.2 nm the blueshift starts to decrease with increase of size of the NW and becomes below 2.4 meV as the confinement effects become weaker for large NWs ($R >$ 20 nm). Finally, when we compare the two orientations of InAs NWs, we can clearly see that the blueshift for the [111] orientation is almost two times larger than for the [001] one. This is due to relatively smaller confinement in the case of [111] direction as compared to [001] InAs NWs.

5.1.2. GaAs Nanowires

In the previous subsection we have explored in detail the size and orientation dependence of the electronic and optical properties of InAs NWs. Thus, in this subsection, devoted to the same calculations on GaAs NWs, we will mainly focus on the differences between the two types of NWs.

Electronic Structure

We start our discussion by investigating the effect of the NW size on the CB energy spectrum of the [001] and [111] GaAs NWs: In Figs. 5.9a and 5.9b we present the variation with the NW size of the confinement energy of the first five CB states. The behavior obtained is qualitatively similar to the one found for InAs NWs. The confinement of the lowest CB state at R =1 nm corresponds to 0.47 eV for [001] GaAs NW while for [111] GaAs NW it becomes only 0.38 eV. These values are smaller than values obtained for InAs NW of same size discussed in

Sec. 5.1.1. The differences arise mainly as a result of the larger conduction band effective mass of GaAs than InAs.

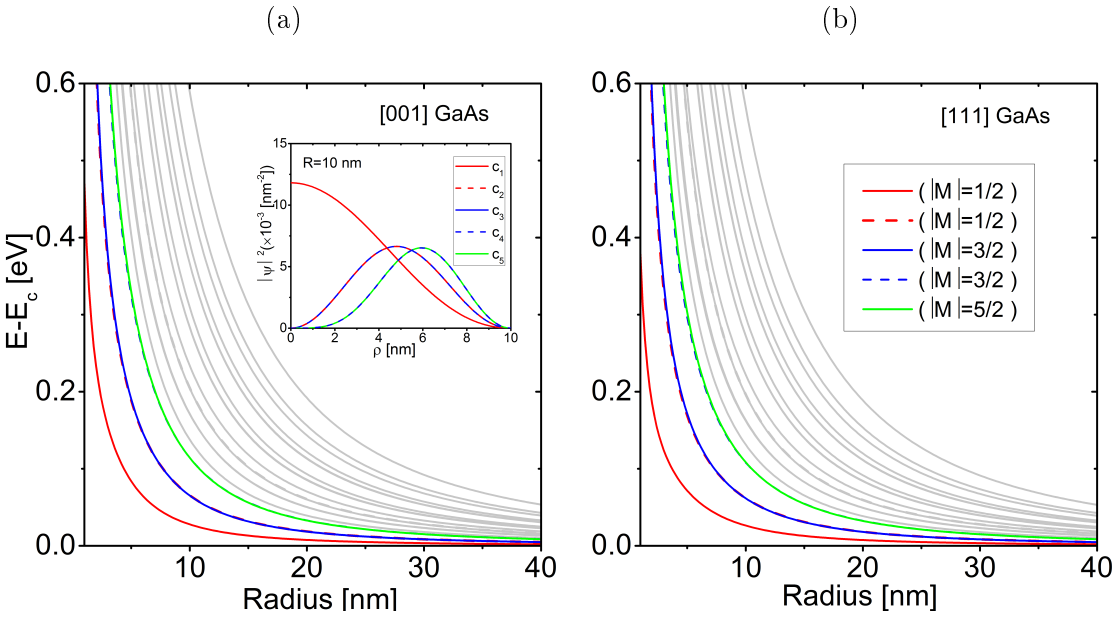

Figure 5.9: Confinement energies of the lowest CB states as a function of the NW radius for (a) [001] and (b) [111] GaAs NWs. E_c denotes the bulk CB edge. The squared wave function of the states for $R = 10$ nm are given in the inset.

As for InAs NWs, we have fitted the confinement energy $E_{c_1} - E_c$ to the function (5.1) and obtained the following values: C= 0.50 and $\beta = 1.18$ for [001] GaAs NWs and $C = 0.40$ and β =1.15 for [111] GaAs NW. Here again the dependence given deviates from the prediction given by single band EMA and confirms the need for a multiband approach.

In Section 5.1.1 we have seen the impact of of the VB-CB coupling in the symmetry weights of the CB wavefunctions in narrow gap InAs NWs. We repeat here the analysis for the wider band gap GaAs NWs: The symmetry weights of the wavefunction for the lowest CB state c_1 of GaAs NWs grown along [001] and [111] directions are given in Figs. 5.10a and 5.10b respectively. Here the S-character is very dominant (w_S >97 %) at all sizes considered. This is in contrast to the case of InAs NWs where w_{hh} can reach values of 5 % for small sizes ($R \leq 10$ nm). This difference is a direct result of the larger band gap of GaAs than InAs. Thus, the six-band $\boldsymbol{k}\cdot\boldsymbol{p}$ Hamiltonian model has been used by some authors for exploring the properties of the GaAs NWs[18].

Turning our attention to the VB states, we investigate the confinement energies of VB states as a function of size as we did in the previous section for InAs NWs.

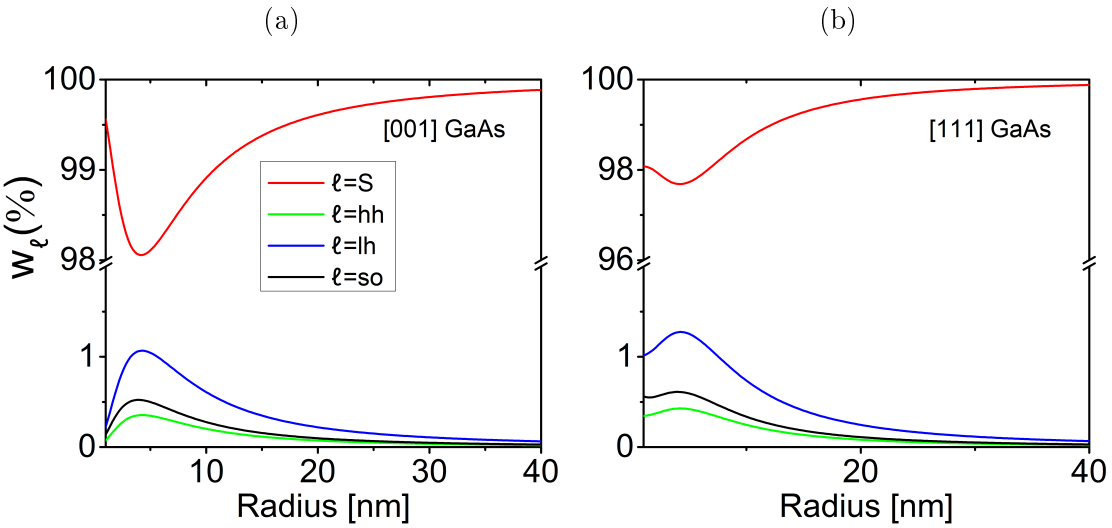

Figure 5.10: Symmetry weights of the wavefunction corresponding to the state c_1 in (a) [001] and (b) [111] GaAs NWs, as a function of the radius.

In Figs. 5.11a and 5.11b we present the confinement energies of the five highest VB states at the Γ-point for [001] and [111] GaAs NWs, respectively. The five states span an energy range of 1.42 (1.1) eV with the VB confinement energy of the smallest NWs considered R =1 nm being 0.6 (0.32) eV for [001] ([111]) GaAs NW. The VB states v_1 and v_2 in both [001] and [111] GaAs have dominant $lh(+)$ and $lh(-)$-characters respectively for all sizes of the NWs considered without any crossing, unlike the case of InAs NWs discussed in the previous section.

In Figure 5.12 we present the symmetry weights for v_1 of [001] and [111] GaAs NWs as a function of NW size. The results obtained for both orientations are similar. The character lh is the most dominant ($w_{lh} > 78$ %) at all NW sizes considered. However, for GaAs NWs with radius R <3 nm NWs, the *so*-symmetry also has significant contribution. Unlike the case of InAs NWs, the lh-character has no important influence on the v_1 spinor of v_1 for all the GaAs NW sizes explored.

Optical Absorption

For all sizes considered, the state c_1 of the [001] and [111] GaAs NWs is dominantly composed of $S(\uparrow)$-character and has s-type envelope function symmetry. Moreover, the size dispersions of v_1 and v_2 of both [001] and [111] GaAs NWs do not cross each other unlike the case of InAs NWs discussed in Sec. 5.1.1. As a result, we expect the same polarization properties of the optical absorption at all sizes of GaAs NWs (See Fig. 5.13(a) and Fig. 5.13(b)). Moreover, the fundamental

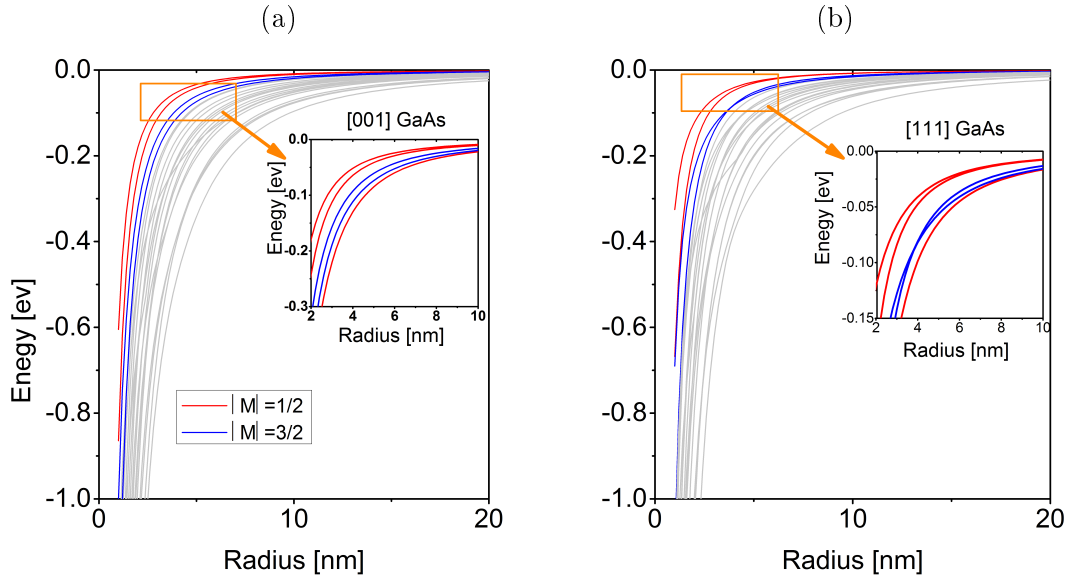

Figure 5.11: Confinement energy $E - E_v$ of the five highest Γ-point VB states of (a) [001] and (b) [111] GaAs NWs versus NW size. The states are distinguished by its angular momentum $|M|$.

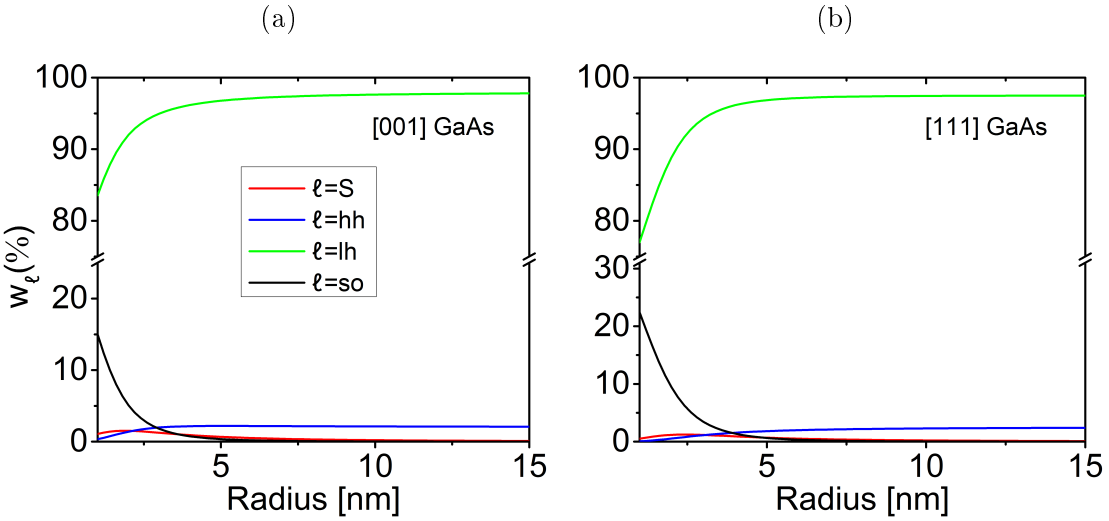

Figure 5.12: Symmetry weights of the spinor corresponding to the Γ-point VB v_1 for (a) [001] and (b) [111] GaAs NWs as a function of the NW radius from 1 to 15 nm.

optical gap is exactly located at the band gaps irrespective of the size of the GaAs NWs. As an illustration, the optical absorption of [001] and [111] GaAs NWs with radius $R = 2.5$ nm are shown in Fig. 5.13.

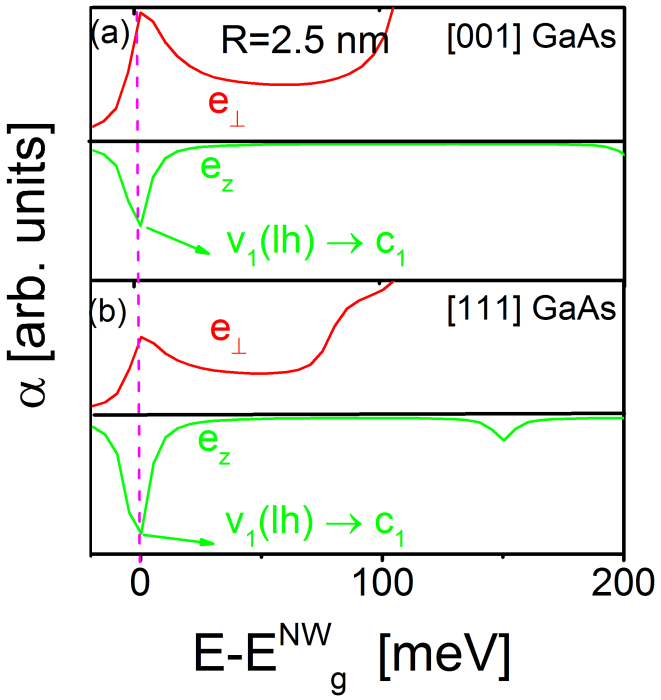

Figure 5.13: Polarization-dependent optical absorption of (a) [001] and (b) [111] GaAs NWs with radius R =2.5 nm. In each case it has been represented separately, in the positive and negative vertical axis, the spectra corresponding to $\boldsymbol{e}_\perp$ and $\boldsymbol{e}_z$ polarization, respectively.

5.2. AlGaAs/GaAs Core-Shell Nanowires

In Sec. 5.1 we have studied the electronic and optical properties of free-standing InAs and GaAs NWs. In particular, we have reported how the electronic and optical properties depend on the geometry (size and orientation) of the NWs. In this section we extend our investigation to core-shell nanowires (CSNWs). As explained in detail in Chapter 3, the presence of two lattice-mismatched materials leads to the appearance of a built-in strain distribution whose effects on the electronic structure superpose to those coming from the pure geometry. In order to disentangle both influences, we first discuss a system where it is a reasonable approximation to neglect strain effects in a first approximation, namely the core-shell nanowires made of GaAs and $Al_xGa_{1-x}As$/GaAs. The lattice constant of GaAs and AlAs

correspond to 5.65 Å and 5.66 Å respectively,[186] and the misfit strain between both materials is below 0.2 %. As a result, these materials and their alloys can be easily grown epitaxially on top of each other without accumulating significative elastic deformation. The geometry of our cylindrical model for the core-shell system is presented in Fig. 5.14a, and it can be specified by the radius of core R_{core} and the thickness of the shell w_{shell}. The core-shell nanowire is a heterostructure and hence the inclusion of the band offsets is essential to define the confinement potentials appearing in the diagonal terms of the Hamiltonian. The offsets between the valence and conduction band edges at the $Al_xGa_{1-x}As$-GaAs interface are taken as $\Delta E_v = 0.57x$ eV and $\Delta E_c = 0.87x$ eV, respectively.[187] The resulting band alignments between $Al_xGa_{1-x}As$ and GaAs are shown in Fig. 5.14b. For a given combination of materials, in this case GaAs and $Al_xGa_{1-x}As$, there are two possible configurations of the CSNW: Either the lower gap material (in this case, GaAs) is in the core or it is in the shell. The electronic structure and optical absorption of [001] $Al_xGa_{1-x}As$/GaAs and GaAs/$Al_xGa_{1-x}As$ CSNWs have been studied recently by using the six-band $\boldsymbol{k}\cdot\boldsymbol{p}$ Hamiltonian for the valence band and a parabolic energy spectrum for the conduction band.[94] It is there confirmed that the electronic structure of unstrained CSNWs can differ significantly from the corresponding single material nanowires. Here we focus on a [111] $Al_xGa_{1-x}As$/GaAs CSNW, where the carriers are expected to be confined in the shell forming a ring-like charge distribution, and use the eight-band $\boldsymbol{k}\cdot\boldsymbol{p}$ envelope function formalism developed in Chapter 4 to investigate the effects of the core-shell geometry on the electronic and optical properties. The material parameters for $Al_xGa_{1-x}As$ used in the calculations are taken from the material parameters of GaAs and AlAs using linear interpolation.[163] They are available in Appendix E.1. Since we are here interested in investigating the geometry effects we consider for all the calculations a fixed Al concentration x =0.4, and from here on the term AlGaAs will be used to abbreviate $Al_{0.4}Ga_{0.6}As$.

Electronic Structure

In order to study the effect of confinement on the electronic structure of CSNWs we will examine the influence of increasing the shell thickness w_{shell} for fixed core radius R_{core}. The total nanowire radius is therefore $R = R_{\text{core}} + w_{\text{shell}}$. In Fig. 5.15a we present the five lowest CB states as a function of shell thickness for $R_{\text{core}} = 10$ nm. In this case it will be instructive to consider simultaneously the distribution of the CB electron in the cross section of the CSNW: In Fig. 5.15b we present the probability density of the lowest CB state c_1 for various values of w_{shell}. As expected, for $w_{\text{shell}} = 0$, i.e., for a free-standing AlGaAs NW of radius 10 nm,

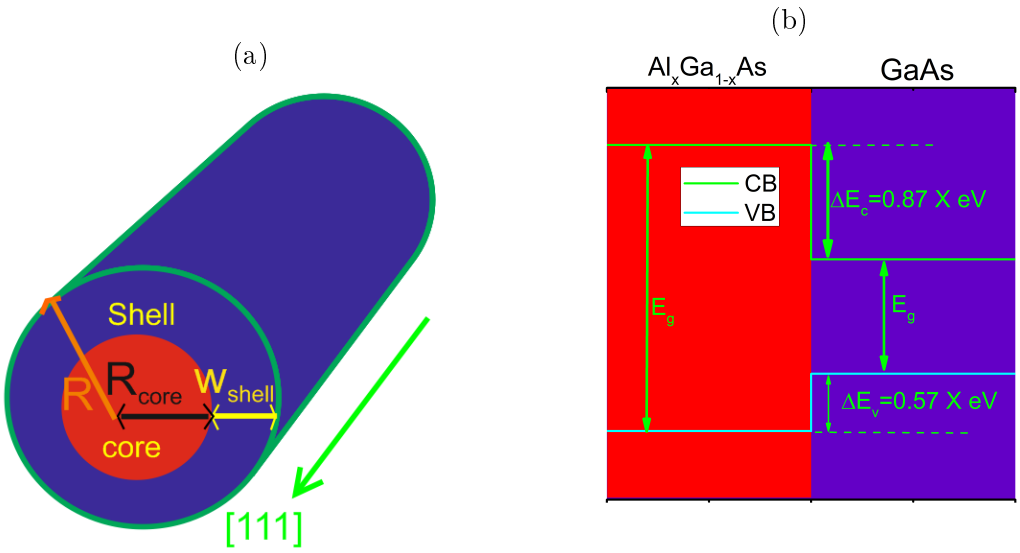

Figure 5.14: (a) Cylindrical core-shell nanowire with radius of the core R_{core} and thickness of the shell w_{shell}. The nanowire is oriented along the [111] direction, which is taken as the Z axis. (b) Band alignments between $Al_xGa_{1-x}As$ and GaAs.

the lowest five CB states locate above the CB bulk AlGaAs band edge, spanning an energy range of around 0.54 eV, with the lowest one exhibiting a confinement energy of ~ 0.43 eV. The corresponding c_1 wavefunction is localized on the center of the NW. For thin shells, e.g. $w_{\text{shell}} < 2$ nm, the energies show a slight decrease, but keep themselves above E_c(AlGaAs), and the wavefunctions stays localized near the center of the core. However, at $w_{\text{shell}} \sim 2$ nm, a rather abrupt change of behavior can be identified: the CB energies start to decrease more steeply with increase of shell thickness moving below E_c(AlGaAs). This behavior reflects the transition to a confinement within the lower energy shell region, as can be clearly visualized by the probability density for $w_{\text{shell}} = 2$ nm, which shows the electron *transiting* from the core to the shell. As the shell becomes thicker, the energies decrease further and the electron is being increasingly localized on the shell in a ring-like configuration. For very large w_{shell}, the energy levels cluster above E_c(GaAs) spanning a range from 47 to 60 meV. The whole evolution proceeds without any level crossing or anti-crossing, and therefore without changes in the symmetry of the states.

Now we turn to the VB states. In the VB confinement (See Fig. 5.16a), the five highest VB states cover an energy range of ~ 0.26 eV with the highest one showing a confinement energy of ~ 0.24 eV, whereas for the largest shell thickness the confinement energy spans a range from 5 to 10 meV. When we compare, we can clearly see that the the CB states pushed downward with increase of shell thickness than the VB states.

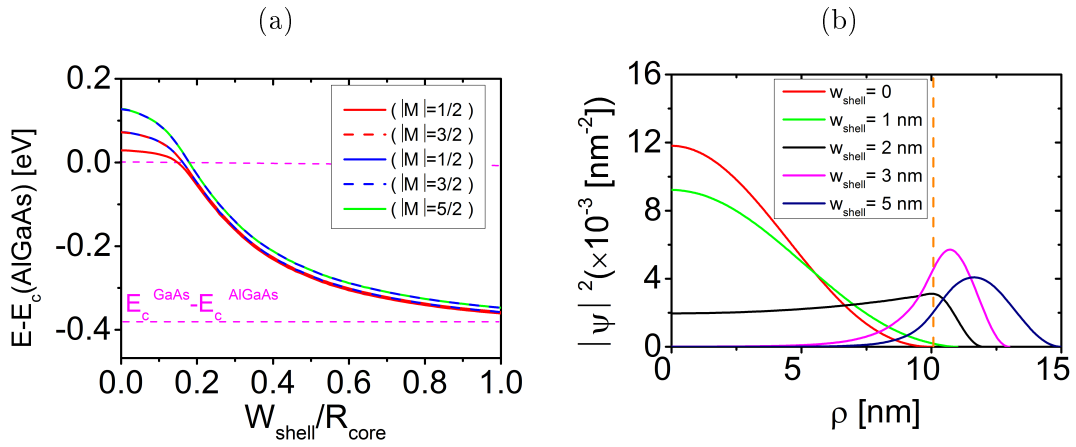

Figure 5.15: (a) Energies of the five lowest CB states in a [111] AlGaAs/GaAs CSNW as a function of the shell width. The radius of the core is $R_{\text{core}} = 10$ nm and the shell thickness is let to vary from 0 to 10 nm. The energies are referred to the CB edge of bulk AlGaAs, E_c(AlGaAs). For illustration purposes, both CB edges of AlGaAs and GaAs are indicated as horizontal dashed lines. (b) Probability density for the lowest CB state c_1 for various values of the shell thickness.

Finally, we are interested in investigating the localization of electron and hole inside the $Al_{0.4}Ga_{0.6}As$/GaAs CSNW as function of shell thickness. In Figs. 5.15b and 5.16b we present the shell thickness dependence probability density of c_1 and v_1 respectively at the Γ-point for $Al_{0.4}Ga_{0.6}As$/GaAs CSNWs with R_{core} =10 nm. For the case of free-standing (w_{shell}=0) $Al_{0.4}Ga_{0.6}As$ NW, both the electron and hole are populated at the center of the NW. For w_{shell} = 1 nm, the electron is still confined inside the core but become pushed away from the center of the NW. This explains the reason why we didn't see significant change in the band gap for very small shell thickness as shown in Fig. 5.17. For w_{shell}=2 nm, the electron becomes strongly pushed away from the center of the core and appears partially inside the shell as a result the band gap starts to become sensitive to the change in the thickness of the shell. Increase of shell thickness further leads to the shift in the position of the electron from the core to the shell. This can be seen in the case of w_{shell} =3 nm where there is high chance of getting the electron inside the shell GaAs than the core. When we look at the hole, for all shell thickness $w_{\text{shell}} \geq$1 nm, is already confined entirely inside the shell unlike the case of the electron.

The band gaps of AlGaAs/GaAs CSNWs as function of shell thickness w_{shell} and radius of the core R_{core} are given in Fig. 5.17. For reference, the band gap of bulk AlGaAs and GaAs are also shown with horizontal dashed lines. Generally, the band gap of AlGaAs/GaAs CSNW CSNWs with smaller core size have larger band gaps while the band gap converge as both the core and shell become larger in size. We can also see that the increase of Al concentration inside the core increases the

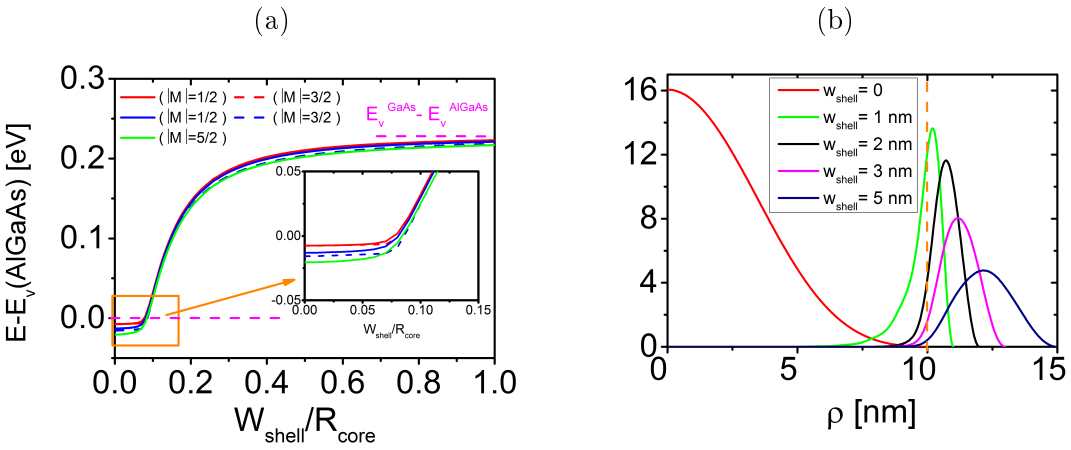

Figure 5.16: (a) Energies of the five highest VB states in a [111] AlGaAs/GaAs CSNW with $R_{\text{core}} = 10$ nm as a function of the shell width. The energies are referred to the VB edge of bulk AlGaAs, E_v(AlGaAs). Both VB edges of AlGaAs and GaAs are indicated as horizontal dashed lines. (b) Probability density for the lowest VB state v_1 for various values of the shell thickness.

confinement inside the shell GaAs due to the increase in the band offsets. However, the band gaps decrease monotonously with increase of shell thickness. We also note that for very small thickness ($w_{\text{shell}}/R_{\text{core}} \to 0$) the change in the band gap with increase of shell thickness becomes very small (below 1 meV). This is due to the thin shell which forces the electron to be confined inside the core. As a result the electron will not be sensitive to a change in thickness of the shell. When both the core and shell becomes larger, the band gap approaches band gap of bulk GaAs crystal.

Optical Absorption

In this section we present the polarization dependent optical absorption of [111] AlGaAs/GaAs CSNW as function shell thickness. For all sizes of shell thickness, c_1 has s-type envelope function symmetry and is composed of $S(\uparrow)$-character. For free standing AlGaAs ($w_{\text{shell}} = 0$), c_1 and v_1 at the Γ-point have s-type envelope function symmetry and are dominantly composed of $S(\uparrow)$ and $lh(+)$-characters respectively. Thus the first strong transition at the Γ-point comes from the transition $v_{1,lh} \to c_1$. As a result, the optical absorption is polarized along the [111] direction. Moreover, the fundamental optical gap is exactly placed at the band gap of the NW as shown in Fig. 5.18(a). For shell thickness $w_{\text{shell}} \geq 1$nm, the dominant character of v_1 at the Γ-point changes into $lh(-)$. As a result and cannot couple with c_1. This change in the character can be seen qualitatively in the wave functions presented in Fig. 5.16. However the optical absorption remained polarized

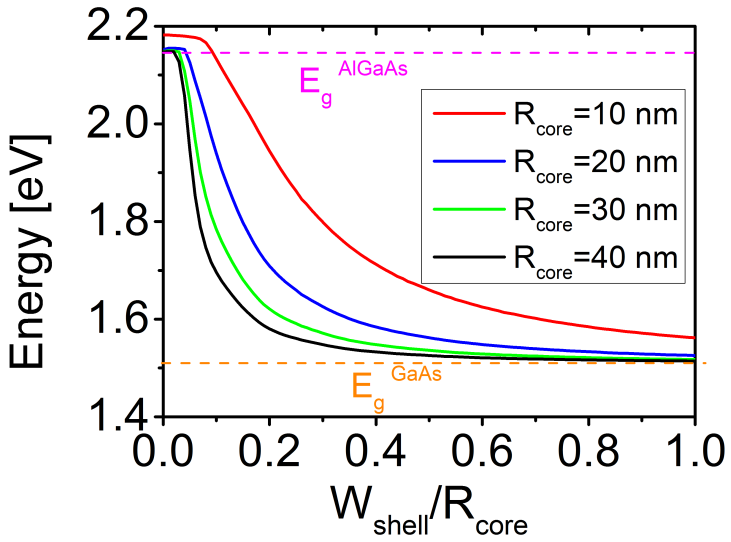

Figure 5.17: Band gap E_g of AlGaAs/GaAs CSNWs as function of shell thickness radius core w_{shell} . The CSNWs are grown along [111] direction. The purple and orange dashed lines correspond receptively to the band gaps of bulk AlGaAs and GaAs.

along the axis of the NW (See Figs. 5.18(b)-(d)) but blueshifted due to v_2 which has dominant $lh(+)$-character at the Γ-point.

5.3. GaAs/InAs Core-Shell Nanowires

The properties of heterostructure nanowires depend first on their chemical composition and crystalline structure. These properties can be further manipulated by varying the geometrical parameters[94,95] or by doping[188–190]. Recently, the tailoring of the electronic properties of nanowires by an external mechanical strain has also been considered.[191–197] Besides external strains, the strain induced by a lattice-mismatch is also known to modify the electronic and optical properties of core-shell nanowires.[78,198–209] In this section we investigate the effects of the built-in strain on the electronic structure and optical absorption of lattice-mismatched [001] GaAs/InAs CSNWs, see Fig. 5.19a. The unstrained band alignment is shown in Fig. 5.19b. We will make the analysis as a function of the shell thickness to understand the change in the confinement imposed both by the geometry and strain.

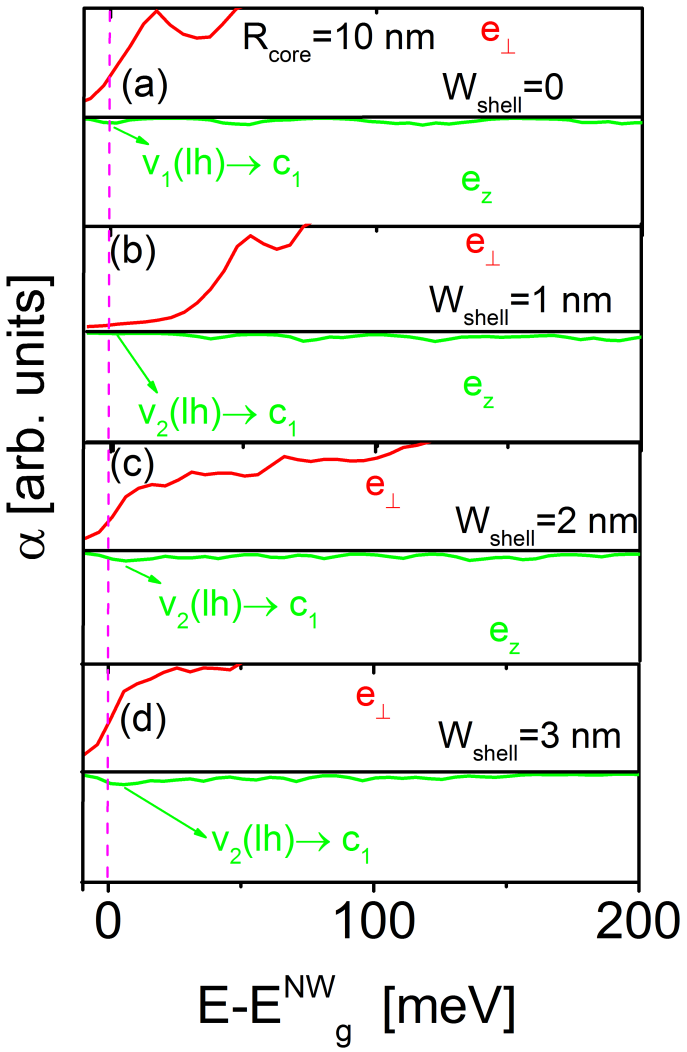

Figure 5.18: Polarization dependent optical absorption of AlGaAs/GaAs core-shell nanowires as function f shell thickness. Plots (a)-(d) correspond to results for shell thickness w_{shell} =0, 1, 2 and 3 nm respectively. The CSNWs are grown along [111] direction with radius R_{core} = 10 nm. In each case it has been represented separately, in the positive and negative vertical axes, the spectra corresponding to $\vec{e}_{\perp}$ and $\vec{e}_z$ polarization, respectively.

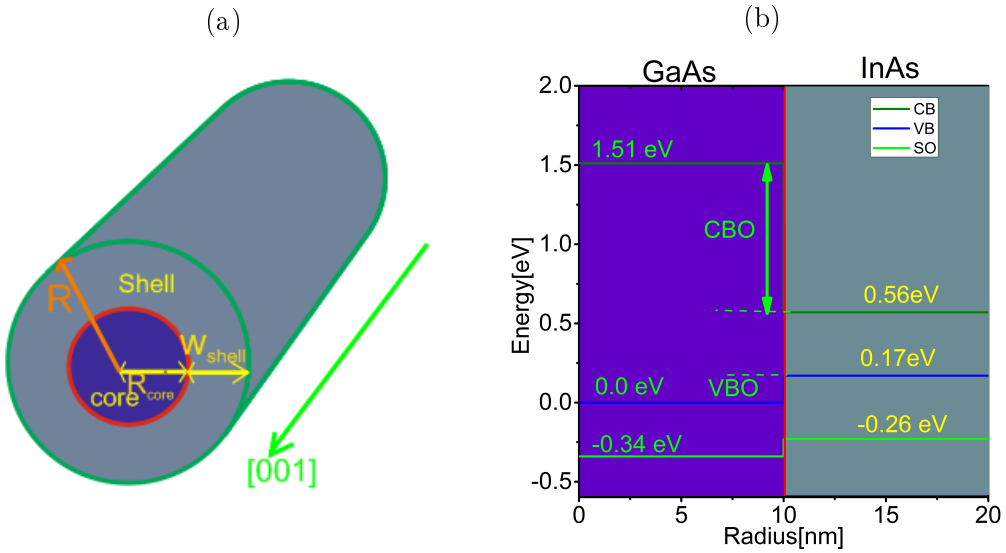

Figure 5.19: (a) Cylindrical core-shell nanowire with radius of core R_{core} and thickness of shell w_{shell}. The nanowire is oriented along the [001] direction, which is taken as Z axis. (b) Band alignments between GaAs and InAs.

Strain Distribution

Before examining the electronic and optical properties of strained GaAs/InAs CSNWs, we start with the investigation of strain profiles inside the CSNW. The radius of the core is fixed to $R_{\text{core}} = 10$ nm and the thickness of the shell varies as $2 \leq w_{\text{shell}} \leq 10$ nm. The lattice constant of InAs and GaAs are $a_{\text{InAs}} = 6.033$ Å and a_{GaAs} =5.645 Å respectively. Thus the misfit strain inside the core with reference to the shell is $\varepsilon_{\parallel} = 6.87\,\%$. For each value of the shell thickness, the elastic problem is solved by using the GPS approach discussed in Sec. 3.2. Here we will discuss only the strain components, $\varepsilon_h = \varepsilon_{xx}^{(T)} + \varepsilon_{yy}^{(T)} + \varepsilon_{zz}^{(T)}$, $\hat{\varepsilon} = \varepsilon_{xx}^{(T)} - \varepsilon_{yy}^{(T)}$ and $\tilde{\varepsilon} = -2\varepsilon_{zz}^{(T)} + \varepsilon_{xx}^{(T)} + \varepsilon_{yy}^{(T)}$, that appear at the Pikus-Bir Hamiltonian for zincblende structures (See (A.8)). Below we will discuss the main features of the strain profile in the core-shell system:

- The hydrostatic strain ε_h is displayed in Fig. 5.20a. We can see that the strain inside the GaAs is uniform and of tensile character as a result of having a smaller lattice constant than InAs. The strain increases with increase of shell thickness. In contrast, the shell is dominated by uniform compressive strain which decreases with increase of shell thickness and approaches the unstrained state.

- The strain component $\hat{\varepsilon}$ is shown in Fig. 5.20b. Its value inside the core

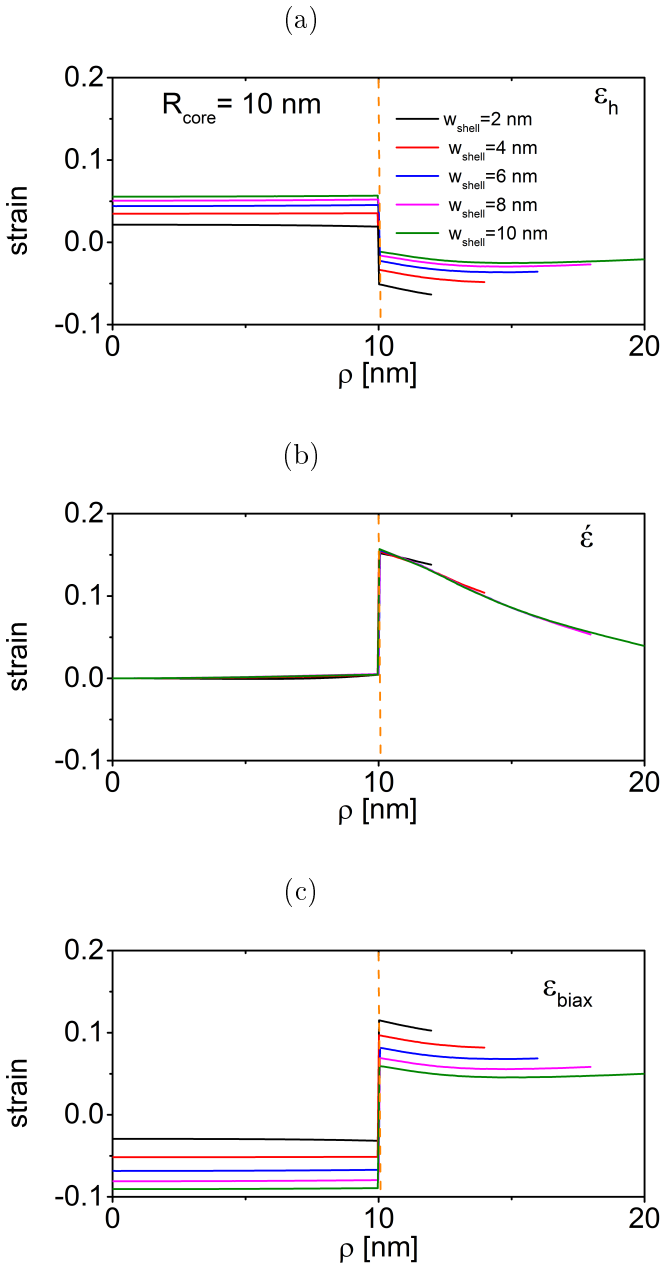

Figure 5.20: The X-Axis line scan of strain components for (a) ε_h,(b) ε_{biax} and (c) $\hat{\varepsilon}$ inside the core and shell of GaAs/InAs CSNW. The radius of the core is fixed at $R_{\text{core}} = 10$ nm and thickness of the shell varies as $2 \leq w_{\text{shell}} \leq 10$ nm. The vertical dashed lines show the core-shell interface.

is zero but manifests as tensile strain inside the shell and decreases as one moves towards the surface of the CSNW.

- The biaxial stain (See Fig. 5.20c) inside the core GaAs is compressive and increases with increase of shell thickness. Inside the shell GaAs, the strain is tensile and rather inhomogeneous. It has the larger values near the core but decreases slowly when moving in the direction of the InAs surface.

Electronic Structure

In this section we investigate the electronic properties of strained GaAs/InAs CSNW. The valence band off set is taken as VBO = 0.17 eV.[210] We have fixed the radius of the core to R_{core} =10 nm and made the study as a function of the shell thickness in the range 1≤ w_{shell} ≤10 nm. In Figs. 5.21a and 5.21b we present the energies (referred to the bulk GaAs CB and VB edges) of the five lowest CB ($E_{c_1}, \ldots, E_{c_5}$) and five highest VB states ($E_{v_1}, \ldots, E_{v_5}$) for the strained GaAs/InAs CSNWs. We found out that the energy of the CB states decreases with the increase of the shell thickness. The energy of the lowest CB state decreases by ∼ 0.74 eV as the thickness of the shell increases to 10 nm. In contrast, the energies of the VB states are pushed upwards as the GaAs shell becomes thicker. The changes in the VB states are more abrupt for small shell thickness. When the shell becomes very thick (w_{shell}/R >0.3) the energy of the VB states almost remains constant.

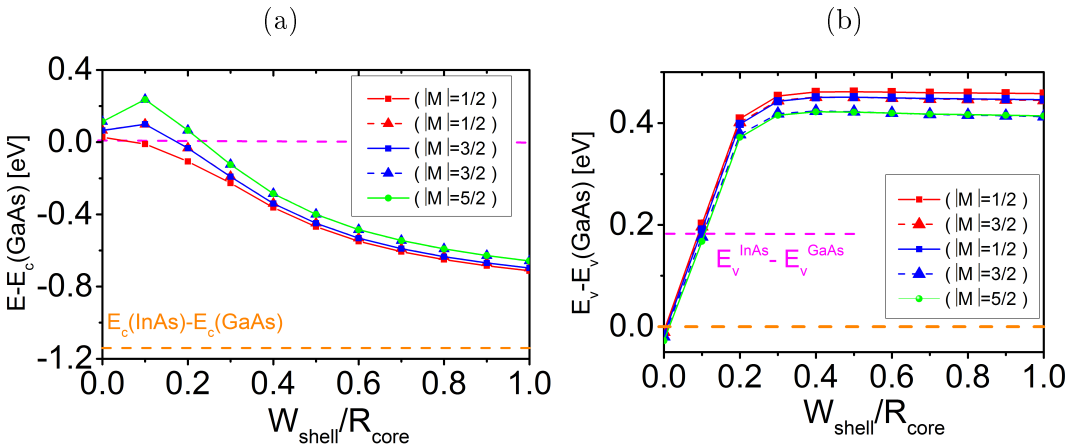

Figure 5.21: Confinement energies of the (a) five lowest CB states and (b) five highest VB states of [001] GaAs/GaAs CSNW with core radius R_{core} = 10 nm as a function of the shell thickness. The energies of the CB and VB states are referred to the bulk GaAs CB and VB nband edges.

In Fig. 5.22 we present the band gaps of strain-free and strained GaAs/InAs CSNWs. The first feature we note is that the change in the thickness alone, without including the mismatch-induced strain, has an impact in changing the band gap: The band gap has higher values for thinner shell and decreases as the shell becomes thicker. For example, the band gap for the smallest shell thickness considered, w_{shell} =1 nm, is E_g^{NW} =1.58e eV while it decreases to 0.512 eV for w_{shell} =10 nm. When we look at the band gap of strained GaAs/InAs CSNWs, we observe a qualitatively similar trend However, the hydrostatic strain results in a decrease of the band gap when compared with the strain-free case. The band gap is decreased from E_g^{NW} =1.3 eV for w_{shell} =1 nm to 0.338 eV at w_{shell} =10 nm. Thus, the band gap decreases with increase of the shell thickness as a combined effect of the geometry and the strain. We also note that the band gap change in the strained CSNW is mainly due to the decrease in energy of the CB states as shown in Fig. 5.21.

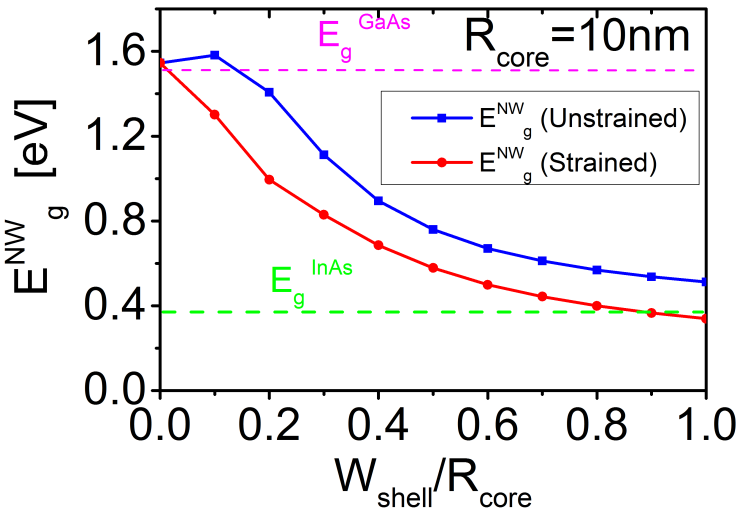

Figure 5.22: Band gaps of GaAs/InAs CSNWs with and with out strain. The radius of the core is fixed at R_{core} = 10 nm and thickness of the shell varies as $1 \leq w_{\text{shell}} \leq 10$.

To investigate the effects of the confinement and strain on the localization of the CB and VB wavefunctions, we present in Figs. 5.23a and 5.23b the probability densities associated to states c_1 and v_1, respectively, as a function of shell thickness again for the core radius fixed to R_{core} =10 nm. In the case of free-standing GaAs (w_{shell} =0), the probability density of the CB state is concentrated at the center of the NW while that of the VB state is confined at the middle ($\rho \cong 5$ nm) of the NW. For w_{shell} = 2 nm, we see that the CB state density is still mainly concentrated inside the core but when the shell becomes thicker ($w_{\text{shell}} > 2$ nm) it becomes pushed away from the center of the NW and starts to appear inside

the shell GaAs. The VB state density has become confined entirely inside the shell GaAs for w_{shell} >2 nm.

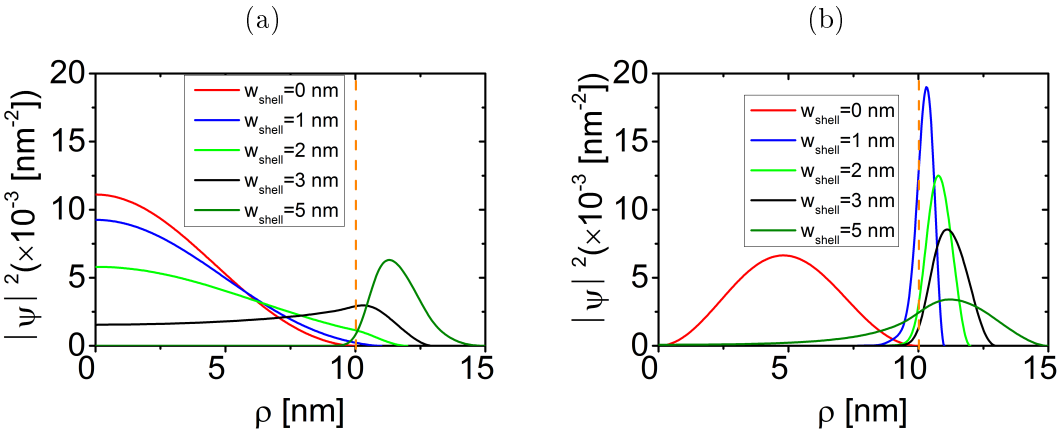

Figure 5.23: Probability densities for states (a) c_1 and (b) v_1 of GaAs/InAs CSNWs of different shell thicknesses. The core radius is R_{core} =10 nm. The vertical dashed line shows the core-shell interface.

Optical Absorption

In this section we examine the optical absorption of strained GaAs/InAs CSNWs. In Fig. 5.24 we present the optical absorption for various shell thicknesses for fixed core radius R_{core} =10 nm. For w_{shell} =0, which corresponds to a pure GaAs NW, the oscillator strength of the transition $v_1(lh) \rightarrow c_1$ is non zero as seen in Sec. 5.1.2. Thus the polarization for the optical absorption is along the [001] direction and the fundamental optical gap coincides with the band gap of the NW as shown in Fig. 5.24(a). In contrast, the oscillator strength for the transition $v_1(lh) \rightarrow c_1$ in the strained GaAs/InAs CSNW (w_{shell} >0) becomes optically dark. However, the polarization for the optical absorption remains along the NW axis due to the transition $v_2(lh) \rightarrow c_1$ which has non-zero oscillator strength. Thus, the fundamental absorption edge becomes blueshifted by the energy $E_{v_1} - E_{v_2}$ as shown in Fig. 5.24(b)-(d) for $w_{\text{shell}} \geq$1 nm.

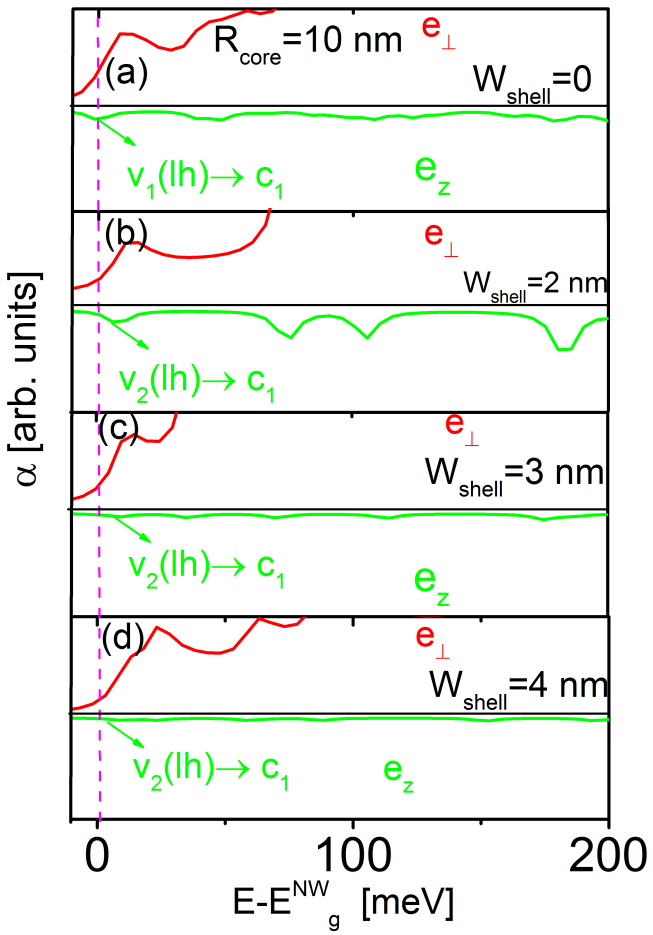

Figure 5.24: Optical absorption spectra of strained GaAs/InAs CSNW with core radius R_{core} =10 nm and shell thickness w_{shell} = 0-4 nm.

Chapter 6

Electronic Structure and Optical Absorption of Wurtzite Nanowires

In this chapter we present a study of the size dependence of the electronic and optical properties of free-standing InN and ZnO NWs having the wurtzite crystal structure and oriented along the [0001] crystallographic direction. In the case of ZnO NWs, we have also studied the effects of an applied uniaxial stress. The electronic structure is calculated by means of the model discussed in chapter 4 with the eight-band Hamiltonian presented in Appendix A. Since the analysis is parallel to that of the zincblende NWs presented in Chapter 5, here we will make emphasis only on the differences. The material parameters used in the calculations are collected in Appendix E.2

6.1. InN Nanowires

Electronic Structure

The variation of the confinement energies of the five lowest CB states, $c_1, \ldots, c_5$ with the NW radius R is presented in Fig. 6.1. In the inset of Fig. 6.1 we present the corresponding squared wave function of the CB states of an InN NW with radius $R = 10$ nm. The state c_1 is localized at the center of the NW while c_2 is concentrated at a radial distance $\rho \simeq 5$ nm. As for the ZB NWs, we have fitted the confinement energy $E_{c_1} - E_c$ to the function (5.1) and obtained the values, $C = 0.468$ and $\beta = 1.252$. This behavior deviates significantly from the relation $\sim 1/R^2$ predicted by the EMA which again shows the inadequacy of the single-band EMA as also seen in Chapter 5 for the case of ZB NWs.

We continue our study by exploring the symmetry of the lowest CB state c_1. In Fig. 6.2 we present the contribution of the symmetry weights w_ℓ for the state c_1 as a function of NW radius. We found out that for all the sizes considered the S-symmetry is dominant ($w_S > 95\,\%$), the remaining contribution being of $\perp$-symmetry (i.e., of X- or Y- symmetry). The maximum mixing of $\perp$-symmetry ($\sim 4\,\%$) occurs for NWs with radius $R < 10$ nm and it is therefore a consequence of the increased lateral confinement.

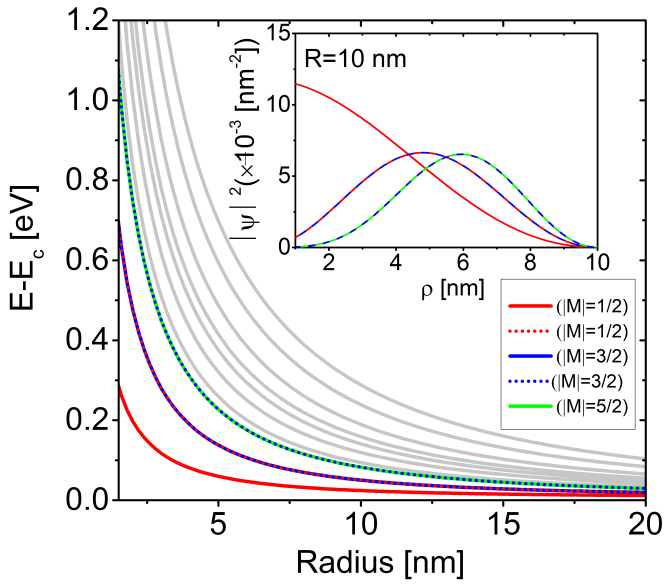

Figure 6.1: Confinement energies of the lowest CB states as a function of the radius of the InN NWs. E_c denotes the bulk CB edge. The squared wave function of the states for $R = 10$ nm are given in the inset.

Focusing on the VB states, in Fig. 6.3 we present the confinement energies $E - E_{\Gamma_{7+}^{v}}$ (with respect to the bulk VB edge $E_{\Gamma_{7+}^{v}}$) of the five highest Γ-point VB states for NWs of size R =1-15 nm. For the largest NW analyzed, these states cover an energy range of around 1.6 meV with the topmost one showing a confinement energy of around 1 meV, whereas for the smallest NW considered the confinement energy spans a range from 180 to 550 meV. Whereas the NW VB energies approach monotonically the VB edge of bulk InN $E_{\Gamma_{7+}^{v}}$ as R increases, for small radii the size dependence of the VB states is more involved. The size at which the dispersion of v_1 and v_2 undergo a change in their dominant character is shown with vertical dashed line. In the inset of Figure 6.3 we present the character of the four highest VB states as function of radius. For InN NWs with $R \leq 2$ nm the VB states v_1 and v_2 are dominantly composed of Z and $\perp$-characters, respectively. However, for

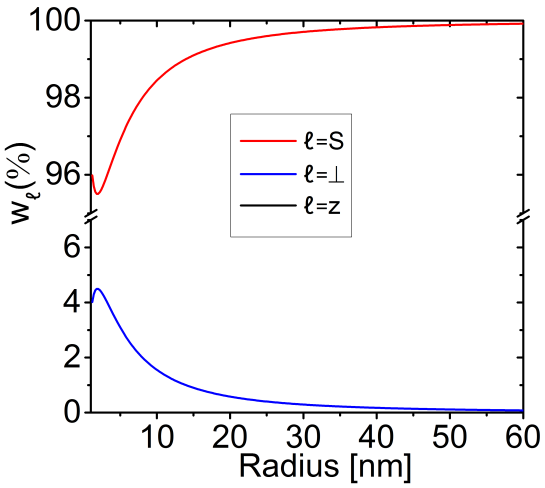

Figure 6.2: Symmetry weights of the wavefunction corresponding to the state c_1 in InN NWs, as a function of the radius.

InN NWs with radius $R > 2$ nm the dominant character of v_1 changes from Z to $\perp$. For v_2, we found out two size ranges where it has different dominant characters: For InN NWs with $2 < R \leq 3$, the Z-character is dominant while the $\perp$-character become more dominant for InN NWs with radius $R > 3$ nm. The third and fourth VB states (v_3 and v_4) have $|M| = 3/2$. Their size dispersion crosses at the same critical radius $R_c \sim 2$ nm: Thus, Z and $\perp$-characters are respectively dominant in v_3 and v_4 for InN NWs with $R \leq 2$ nm while they exchange their dominant characters for larger InN NWs with $R > 2$ nm.

In Figure 6.4 we present the change of the NW band gap $\Delta E_g = E_g^{\rm NW} - E_g^{\rm bulk}$, with respect to that of bulk InN crystal band gap $E_g^{\rm bulk} = 0.7$ eV. The change of the band gap is higher for small InN NWs. The band gap at $R = 1$ nm is increased by ~ 0.65 eV. However, thes effect monotonously decreases with increasing the size and becomes below 4.2 meV for InN NWs with large radius ($R >$30 nm).

In Fig. 6.5 we present the band structure of InN NWs with R =2, 2.5 and 10 nm. We can clearly see that the VB dispersions are highly non-parabolic due to band mixing effects. The lowest CB and highest VB states have the same angular momentum $\mid M \mid = 1/2$ so that transitions between them can only be induced by light linearly polarized along the axis of the NWs, which will be illustrated later. The conduction subbands all exhibit a similar curvature, because they come from the same bulk conduction band. Moreover, the subbands do not cross each other. In the case of the largest NW with radius R=10 nm (See Fig. 6.5c) we see a large number of subbands due to the weaker confinement effect. The valence subbands show a different picture. The different bands experience multiple crossings and anti-crossings. In the band structure of the small NW, we observe the coexistence

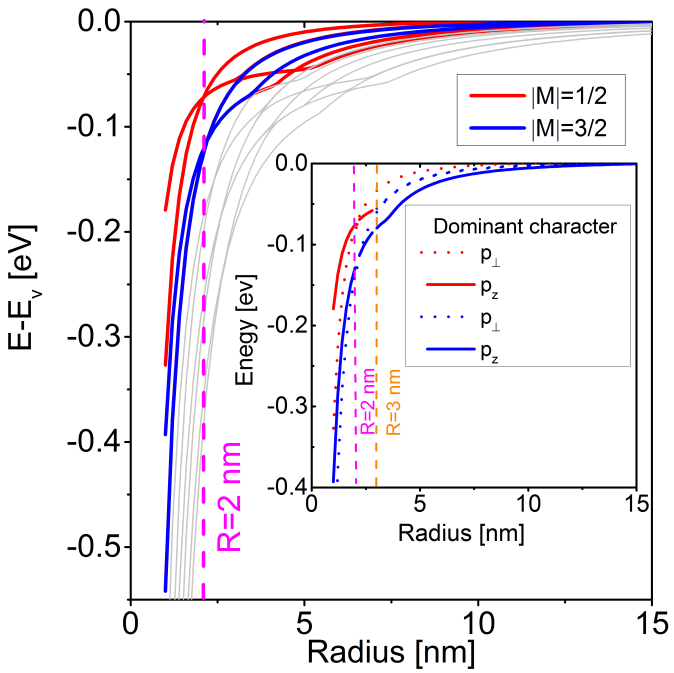

Figure 6.3: Confinement energy of the five highest Γ-point VB states of an InN NW versus radius. The states are distinguished by its angular momentum $|M|$. The inset show the dominant character of the VB states for different size ranges.

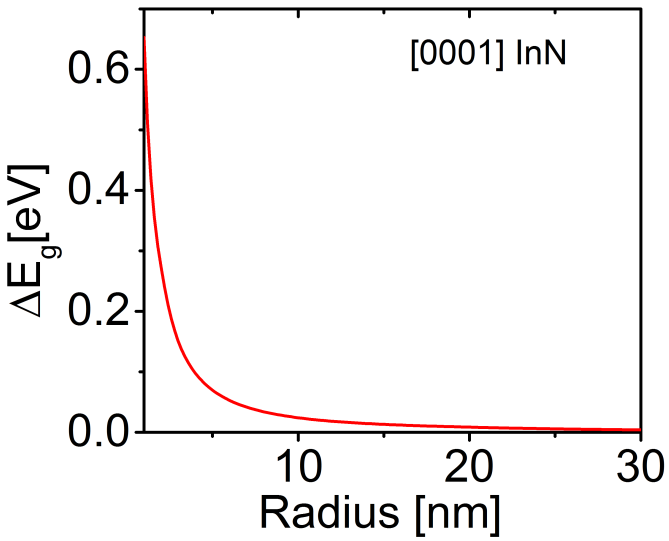

Figure 6.4: Change in the fundamental band gap energy ΔE_g of InN NWs, with respect to the InN bulk band gap $E_g^{\text{bulk}} = 0.7$ eV, as a function of size.

of subbands of very different curvature: the 'flatter' bands have $w_\perp \simeq 100\,\%$ while the bands with more pronounced curvature have $w_Z \simeq 100\,\%$. Note that in the largest NW the highest valence subbands are all 'flat' bands with dominant $\perp$-symmetry. On the other hand, in smaller NWs, the highest valence band structure is dominated by subbands with more pronounced curvature. The VB dispersion for the largest NW (Fig. 6.5c) is more involved as a result of the weaker confinement. Here, there is a larger number of flatter bands, all with dominant $w_\perp$-characters.

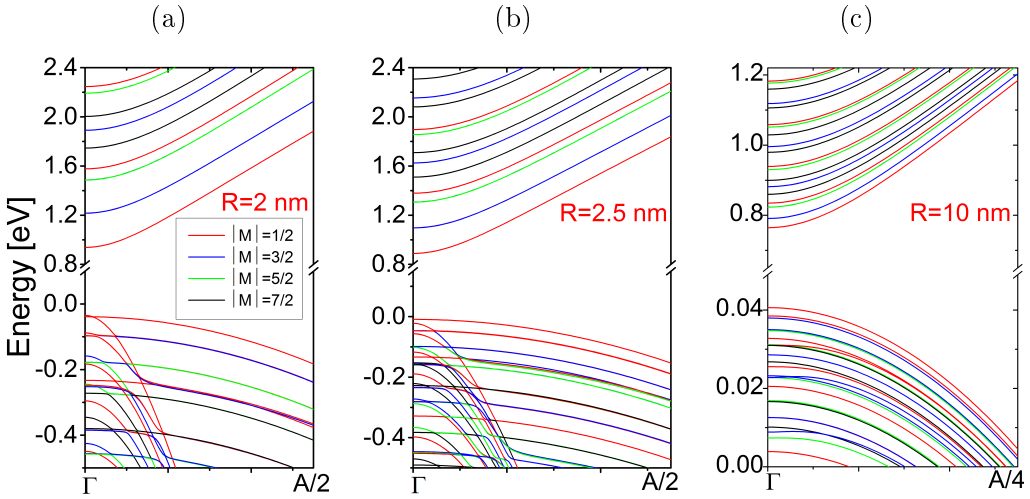

Figure 6.5: Plots (a)-(c) show the band structure of InN NWs with R=2 nm, 2.5 nm and 10 nm respectively.

Finally, in Fig. 6.6 we display the symmetry weights of the lowest CB state as a function of k_z for a NW with radius $R = 10$ nm. It is found out that the S contribution decreases to levels close to $\sim 80\,\%$, whereas the Z contribution reaches values of the order of $\sim 15\,\%$. The $\perp$-symmetry contribution remains very small in the whole range of k_z examined. The symmetry weights of the topmost VB state (not shown here) as a function of k_z, reveals that the $\perp$-character is dominant ($w_\perp \sim 100$ %) in the whole range of k_z examined.

Optical Absorption

In this section we will study in detail the polarization dependent optical absorption of InN NWs. The optical absorptions $\alpha(\hbar\omega)$ of InN NWs considering all the possible transitions from the valence-to-conduction band states are displayed in figure Fig. E.12. A 5 meV Lorentzian broadening function is used in the optical absorption calculations. Since we will focus on the investigation of the effects of the above described crossing of the topmost VB states, we have chosen to present

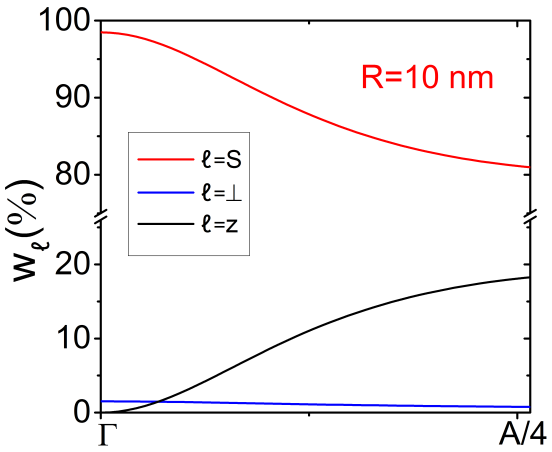

Figure 6.6: Dependence with k_z of the symmetry weights w_ℓ of the ground state (c_1) subband for a NW with radius R =10 nm.

the spectra for three InN NWs radii R =2, 2.5 and 10 nm, whose band structures are given in Fig. 6.5. In Table 6.1 we have summarized the electronic and optical properties of the lowest CB and highest VB states for different size of InN NWs. Generally, the optical spectra of $\hat{\boldsymbol{e}}_\perp$-polarized absorptions present a more complex profile while the spectra $\hat{\boldsymbol{e}}_z$-polarized absorptions are composed by single peaks well separated from each other. This is due to the large number of states with $\perp$-character than states with Z-character. Thus, for all the InN NW sizes considered, in the circular polarized spectra we recognize a structure composed by group of peaks of similar energies, where several transitions participate. In the case of the $\hat{\boldsymbol{e}}_z$-polarized spectra, the structure is simpler, and exhibits the mentioned single-peak profile.

For InN NWs with $R \leq$2 nm the optical absorption is polarized along the axis of the NW. Moreover, the fundamental optical gap is exactly located at the NW band gap as it can bee seen in the case of InN NW with R = 2 nm in Fig. 6.7a. This is due to the first VB state v_1 having s-type envelope function symmetry. This state has a non-zero oscillator strength in the transition $v_1(Z) \rightarrow c_1$ for the $\boldsymbol{e}_z$ polarized absorption since it is mainly composed of Z-character. Thus the state v_1 is a bright state. On the contrary, the $\hat{\boldsymbol{e}}_\perp$-polarized optical absorption has its first observable peaks from the transition $v_4(\perp) \rightarrow c_1$. This is because v_4 is composed of $\perp$-character and has s-type envelope function symmetry. Thus the $\hat{\boldsymbol{e}}_\perp$-polarized optical absorption is blueshifted with respect to the band gap by an amount equal to the energy separation $E_{v_1} - E_{v_4}$. In the case of InN with R = 2 nm the blueshift amounts to $\sim$ 53 meV. For InN NW with radius 2 $< R \leq$ 3 nm, transition from $v_1 \rightarrow c_1$ for $\hat{\boldsymbol{e}}_z$ has zero oscillator strength for both polarizations because of its

Size (nm)	Direction of polarization	State	Envelope symmetry	Dominant character	Optical state
R≤ 2.0	$\boldsymbol{e}_z$	c_1	s	S	-
		v_1	s	Z	bright
		v_2	p	$\perp$	dark
		v_3	p	Z	dark
		v_4	s,d	$\perp$	bright
2<R≤ 3.0	$\boldsymbol{e}_z$	c_1	s	S	-
		v_1	p	$\perp$	dark
		v_2	s	Z	bright
		v_3	s,d	$\perp$	bright
		v_4	p	Z	dark
R>3	$\boldsymbol{e}_\perp$	c_1	s	S	-
		v_1	p	$\perp$	dark
		v_2	s,d	$\perp$	bright
		v_3	s,d	$\perp$	bright
		v_4	p	Z	dark

Table 6.1: Electronic and optical properties of lowest CB and highest VB states at Γ-point of InN NW with different size.

dominant p-envelope symmetry, different from that of the c_1 state: State v_1 is then a dark state. However, v_2 in this window of radii is composed of dominantly Z-character and has s-type envelope function symmetry. As a result, the transition $v_2(Z) \rightarrow c_1$ has non-zero oscillator strength for the $\hat{\boldsymbol{e}}_z$ polarized absorption. So for InN NWs in this radius range, optical absorption is polarized along the c-axis but the fundamental optical edge is shifted by the energy difference of $E_{v_1} - E_{v_2}$. For InN with radius $R = 2.5$ nm the blueshift amounts to 13 meV (See Fig. 6.7b). When we look at larger ($R >$3 nm) InN NWs the first transition $v_1 \rightarrow c_1$ remains dark and the v_2 state, which has dominant $\perp$-character and a mixture of S- and d- envelope symmetries, can couple through $\hat{\boldsymbol{e}}_\perp$ light with the CB state c_1. As a result, the optical absorption becomes polarized into the in-plane direction. This is clearly visible in InN with radius $R = 10$ nm as shown in Fig. 6.7c. Thus, from the above discussion we see that the crossing between the size dispersion of the topmost VB states not only resulted in blueshift of the fundamental optical gap like the case of InAs NWs discussed in Sec. 5.1.1 but also a change in the direction of polarization.

In Fig. 6.8 we present the blueshift of the first strong VB to CB transition as a function of NW size. As seen above in very small InN NWs ($R \leq$2 nm) the fundamental absorption edge is located at the band gaps. Thus the blueshift of the on-axis polarized absorbtion is zero. However, for $2 < R \leq$3 nm, the on-axis optical

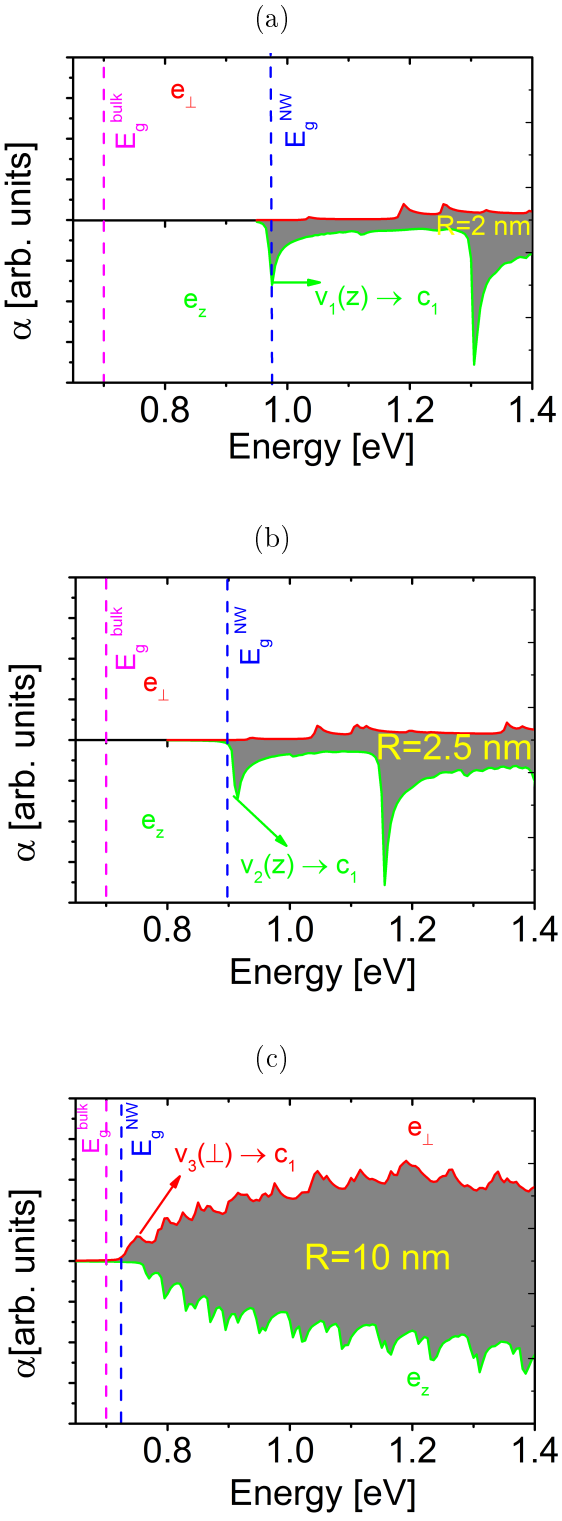

Figure 6.7: Polarization-dependent optical absorption spectra of InN NWs with radii (a) R=2 nm, (b)R=2.5 nm and (c) R=10 nm. In each case it has been represented separately, in the positive and negative vertical axes, the spectra corresponding to $\boldsymbol{e}_\perp$ and $\boldsymbol{e}_z$ polarization, respectively. The vertical blue and purple dashed lines shows the band gap of corresponding InN NW and bulk InN crystal respectively.

absorption is blueshifted by 4.2 meV at R=2.2 nm and increases with increase of radius and becomes 22.1 meV at R=3 nm. For very large InN NWs (R >3 nm), the blueshift for the in-plane polarized optical absorption reaches a maximum value of 23.4 meV at radius R =3.2 nm but decreases monotonously and becomes negligible as the NW becomes very large (R >20 nm).

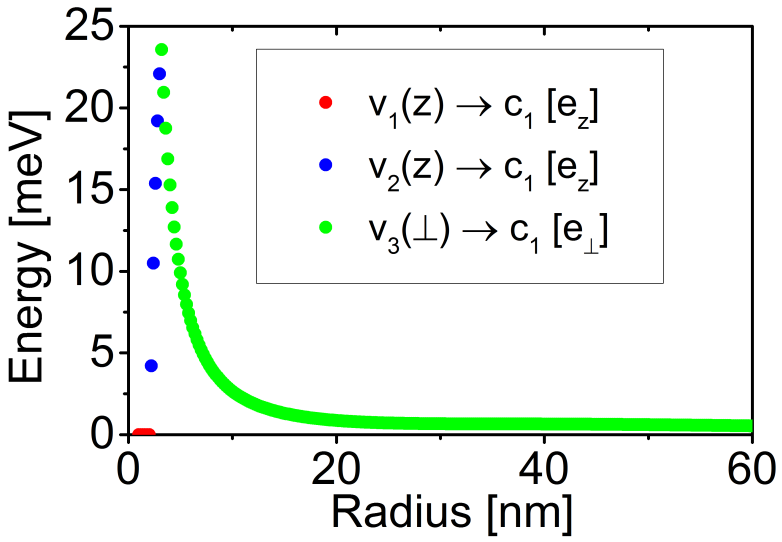

Figure 6.8: Blueshift of the optical absorption edges of the on-axis and in-plane polarized optical absorption in InN NWs. The red, blue and green dots show the first strong transitions of $v_{1,z} \rightarrow c_1$, $v_{2,z} \rightarrow c_1$ and $v_{3,\perp} \rightarrow c_1$ respectively.

6.2. ZnO Nanowires under Uniaxial Stress

In this section we consider cylindrical ZnO NW under uniaxial stress. We will make the analysis as function of radius and applied stress. The electronic structure of ZnO NW under uniaxial strain has been addressed recently by many authors. DFT calculations suggest that the band gap has nonlinear relationship with the applied uniaxial strain[193–197]. However, experimentally, it is shown that the band gap and the applied uniaxial strains have linear relationships[211,212]. It is also shown that the band gap reduction curve caused by applying uniaxial tensile strain exhibit a two-step linear feature for ZnO NW with diameters less than 300 nm[213]. The optical absorptions under axial strain have also been studied in Ref.[194]. However, in this work only the optical absorption along the axis of the nanowire is investigated and the effect of the applied stress on the absorption edges is not clear as the prediction of the band gaps is underestimated by DFT calculations. In addition, the size of the ZnO NWs considered is very small.

Here we want to clarify the ambiguities on the relationship between the applied uniaxial stress and the band gap. Moreover, we want to investigate the effects of compressive and tensile stress on the polarization dependent optical absorption.

Elastic Properties

In this section we start by investigating the elastic properties of ZnO NWs under uniaxial stress. The material constants used in our calculations can be found in Appendix. E.2. The geometry and mesh used in this work is shown in Fig. 6.9(a). The pure stretching and compressing homogeneous uniaxial stress are applied on both top and bottom surfaces of ZnO NW along the c-axis as shown in Fig. 6.9 (b) and (c). The boundary condition assumed is that the bottom and top ends of the NW are free. To model the infinite length ZnO NW with radius R, we consider cylindrical ZnO NW with a finite length L but having large aspect ratio ($L/R >> 1$) so that by Saint-Venant principle[7,140] the strain fields at its central portion correspond to that of the infinite length ZnO NW. This approach to model infinite length NWs has been used recently in piezoelectric problems of core-shell nanowires[92,152,153]. Then we solved the governing elastic problem 3.3a by finite element method to obtain the strain distributions. Note that the strain distributions do not depend on the size of the nanowires as long as the applied uniaxial stress is the same.

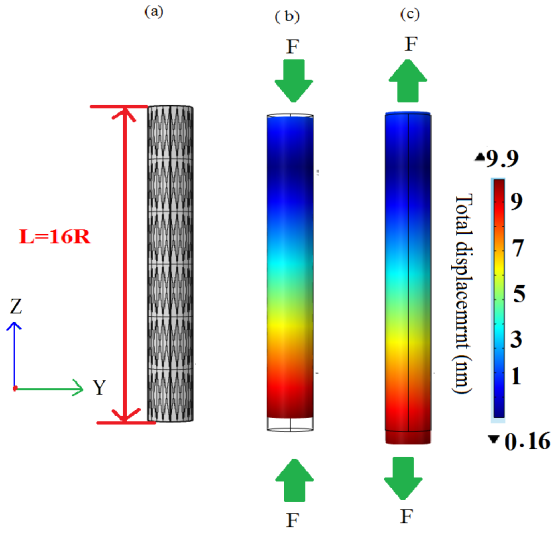

Figure 6.9: (a) Geometry of the unstrained ZnO nanowire investigated, with the meshes employed in the FEM calculations. The NW is grown along c-axis and the geometry is characterized by radius R and length L=16R. (b) and (c) The total displacement by compressing and stretching stress of F =20 GPa respectively.

In Figure 6.9 we present the total displacement of ZnO NW with radius R =5 nm under compressing and stretching uniaxial stress of F =-20 and F =20 GPa respectively. In both stretching or compressing, the total displacement continuously drops from one side of the nanowire to the other. As a representative of elastic deformation behavior of ZnO NWs, we present the resulting axial (ε_{zz}) and in-plane ($\varepsilon_{\perp} = \varepsilon_{xx}+\varepsilon_{yy}$) strain distributions in ZnO NWs under compressing and stretching stress are shown in Fig 6.10. Here we show only the strain components that will be included in the Pikus-Bir Hamiltonian and are presented in Cartesian coordinates. We can see that the stretching (compressing) stress resulted in surface-shrinking (tensile) strain along the in-plane directions and tensile (surface-shrinking) strain along the c-axis direction. As expected, the magnitude of the in-plane strains is much smaller than the axial strains. Moreover, we found out that both the in-plane $\varepsilon_{\perp}$ and out-off plane ε_{zz} strains have linear relationships with the applied stress. Note that the applied axial forces are homogenous and do not create shear deformations i.e $\varepsilon_{xy} = \varepsilon_{xz} = \varepsilon_{yz}$ =0.

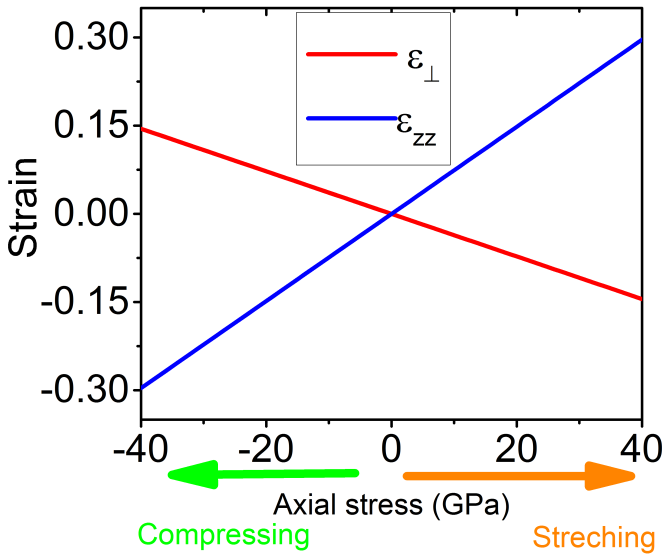

Figure 6.10: In-plane ($\varepsilon_{\perp}$) and out-off plane strain (ε_z) distributions in ZnO NW as a result of compressing and stretching axial stress applied on both top and bottom surfaces. The uniaxial stress varies from F =-40 GPa to 40 GPa.

Electronic Structure

Band gap plays an important role in the optical absorption, electron-hole pair recombination, and off-state leakage in semiconductor electronic devices, and so on. Band gap is altered by the strain as a result of strain-shifted conduction and

valence bands. If strain is introduced by applied external stress, the band gap can even be continuously tuned.

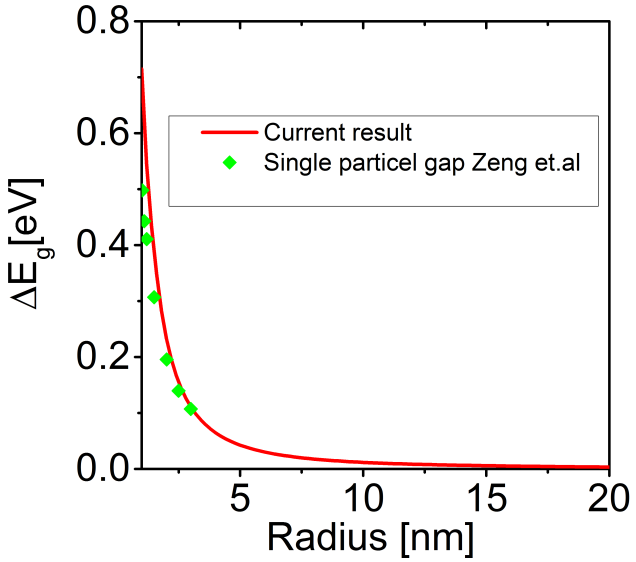

Figure 6.11: Size dependence change in the fundamental band gap energy ΔE_g of ZnO NWs with respect to the band gap of bulk ZnO crystal E_g =3.43 eV. The solid red lines are the results from our eight-band $\boldsymbol{k}\cdot\boldsymbol{p}$ Hamiltonian. The green squares corresponds to single particle calculations from Ref. [184].

Before going into the electronic properties of stressed ZnO NWs, in figure 6.11 we present the band gap change $\Delta\ E_g\ (R)= E_g^{\mathrm{NW}}(\mathrm{R})\text{-}E_g^{Bulk}$ of the stress free ZnO NW with respect to the band gap of bulk ZnO crystal E_g^{Bulk} =3.43 eV. For the smallest radius of NW considered $R = 1$ nm, the band gap of ZnO NW is increased by 0.72 eV because of high quantum confinement effect. However, as the radius increases (R >20 nm) the band gap monotonously decreases and becomes below 3.3 meV. To validate the eight-band $\boldsymbol{k}\cdot\boldsymbol{p}$ predicted band gaps, we compare our results with single particle band gaps from Ref. [184] (green squares). As it can been seen from Fig. 6.11, we got a very good agreement.

Focusing on the ZnO NWs under uniaxial stress, the strain distributions taken are included into the electronic structure calculations through Pikus-Bir Hamiltonian discussed in Sec. 2.2.3 and given in Appendix A. Finally, the electronic structures of stressed ZnO NWs are obtained by solving the total strain dependent Hamiltonian. In figure 6.12a we present the band gaps of ZnO NWs with radius R =1.5 to 10 nm under uniaxial stress of F =-40 GPa to F =40 GPa. Clearly, the electronic properties of ZnO NWs are affected significantly by the applied stress. We can clearly see that the compressive uniaxial stress widened the energy gap

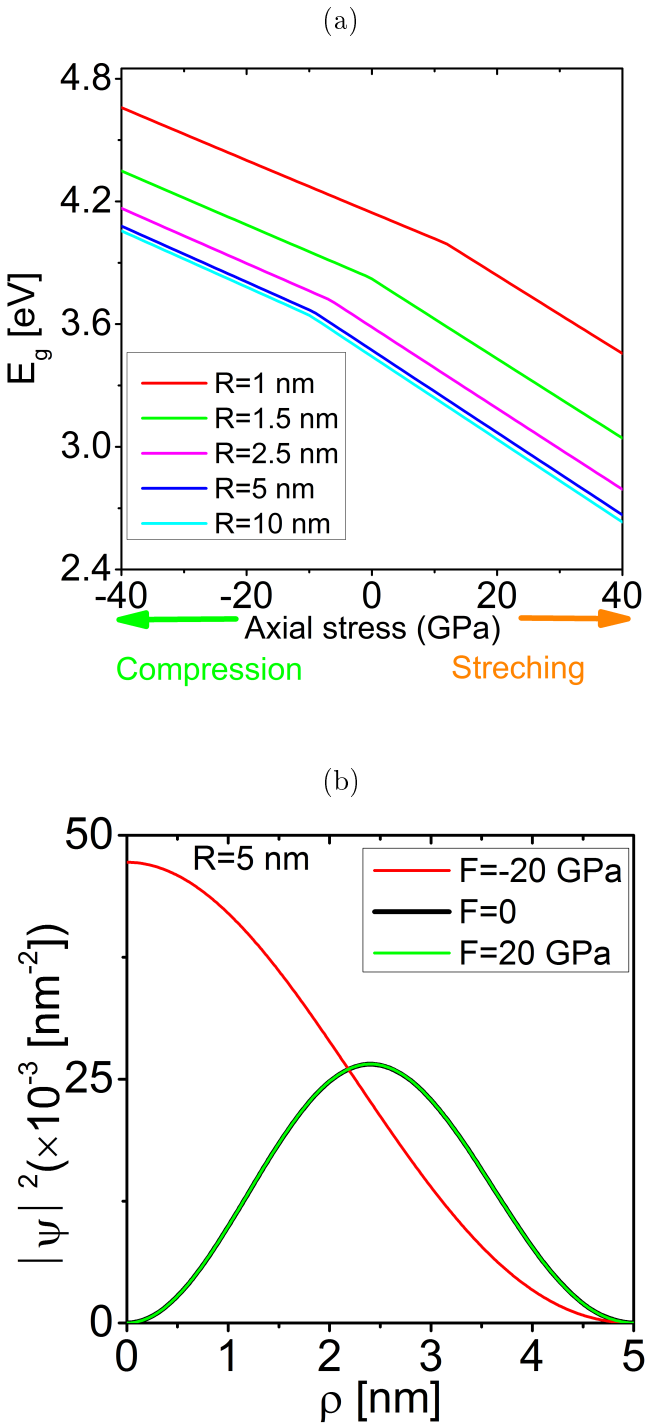

Figure 6.12: (a) Band gaps of ZnO NWs with R =1.5 to 10 nm under axial compressive and stretching stress. (b) Show the probability density of the highest VB states at Γ-point for ZnO NW with radius $R = 5$ nm under uniaxial stress of F =-20,0,20 GPa respectively.

while the stretching uniaxial stress diminished the band gap. Moreover, we see that the band gaps of thinner ZnO NWs are more sensitive to the applied stress than thicker ZnO NWs. We see that the relationship between the band gap of ZnO NWs with different size is linear with the applied stress which is consistent with the experimental results in[211,212]. To study the effect of applied compressive and stretching stress on the radial localization of hole, in Fig. 6.12b we present the probability densities of the highest VB states at Γ-point for ZnO NW with radius R =5 nm. We can clearly see that the holes are concentrated around the middle of the NW, r =2.5 nm, in the strain free and stretched ZnO NW. To the contrast the holes become confined at the center of the compressed ZnO NW.

To understand the effects of the uniaxial stress on the electronic structure of ZnO NW, in Fig. 6.13 we present the band structures of ZnO NW with R =5 nm under uniaxial stress of F =-20 to F =20 GPa. The compressing (stretching) uniaxial stress pushed the VB states downwards (lifted up ward) while the conduction band states are lifted upward (pushed down ward) by stretching (compressing) uniaxial strain. Moreover, by doing detail analysis on the valence bands we found out that bands which are almost flat have $w_{\perp} \sim 100$ % character while those bands with more pronounced curvature have $w_Z \sim 100$ % character.

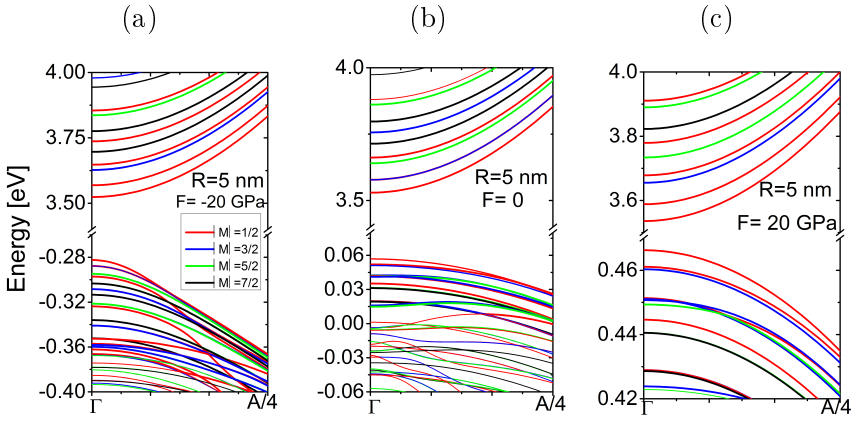

Figure 6.13: Band structure of ZnO NW with radius R=5 nm and under uniaxial stress of (a) $F = -20$ GPa, (b) $F = 0$ GPa, and (c) $F = 20$ GPa.

The size dependent electronic properties of the topmost VB states of strain free ZnO NWs at Γ-point is qualitatively similar to the case of free-standing InN NWs discussed in Sec. 6.1. In all sizes of ZnO NWs, v_1 and v_2 have s-type envelope function symmetry while v_3 has p-type envelope function symmetry. In small ZnO with radius $R \leq 1.4$ nm, v_1 and v_2 are composed of Z and $\perp$-characters respectively. In ZnO NWs with radius range of $1.4 < R \leq 2$ nm, v_1 and v_2 are composed of $\perp$

and Z-characters respectively. To the contrast, in very large ZnO NWs with radius R >2 nm, both v_1 and v_2 have $\perp$-dominant character. The third VB state v_3 is composed of $\perp$-character for ZnO NWs with radius R >2 nm.

In the discussion above, we have seen that the uniaxial stress changed the dominant character of the topmost VB of ZnO NWs. In Fig. 6.14 we present the minimum amount of critical stress F_c that creates a change in the dominant character of the topmost VB state as a function of size of the ZnO NWs.

- Tensile uniaxial stresses $F \geq F_c$ changes the dominant character of v_1,v_2 and v_3 at Γ-point into $\perp$ for ZnO NWs with radius $R \leq$2 nm as shown in Fig. 6.14a. The minimum amount of the tensile stresses corresponds to F_c ∼30 GPa for the smallest ZnO NW considered R = 1 nm while it is becomes F_c ∼2 GPa for ZnO NW with R =2 nm.

- Compressive stress $F \leq F_c$ changes the character of v_1,v_2 and v_3 at Γ-point into Z for ZnO NWs with radius R >2 nm. The amount of the critical stress is around F_c ∼ -6 GPa for ZnO NWs with R ∼2.1 nm but increases with increase of size of the NW to F_c ∼-10 GPa for NW with R =4.5 nm. However, for large ZnO NWs radius range 4.5 < R ≤14 nm and R >14 the critical stress becomes uniform at F_c ∼-10 and F_c ∼-11 GPa respectively as show in Fig. 6.14b.

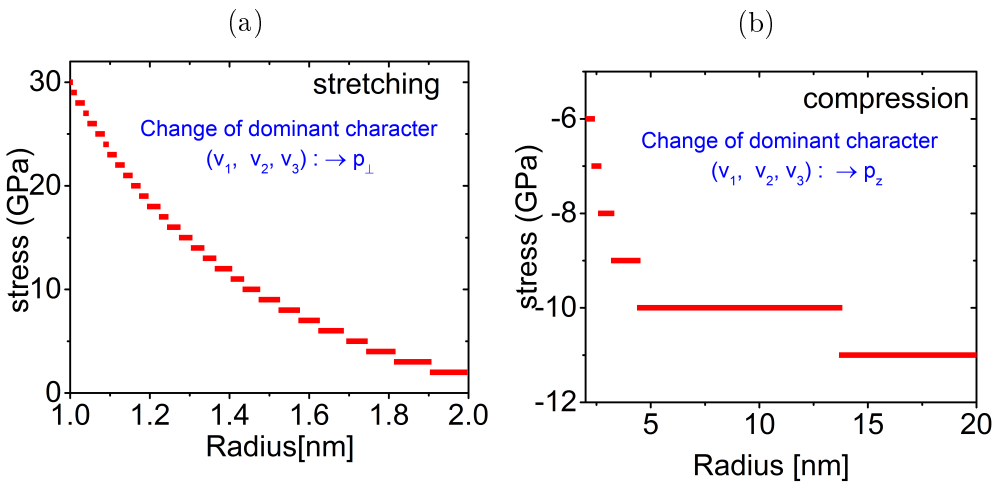

Figure 6.14: The minimum critical amount of uniaxial stress required to have a change in the dominant characteristic of the three highest VB states at Γ-point for the ZnO NWs with radius (a) $R \leq$2 and (b) $R >$ 2 nm.

From the discussion above we have seen that the dominant character of the top most VB states at the Γ-point can be changed from $\perp$ to Z and vice versa by applying uniaxial stress depending on the size of the NW. This gives the opportunity to tune the direction of the polarization for the optical absorption which will be discussed in the next section.

Optical Absorption

The size dependent optical properties of strain free ZnO NWs are qualitatively similar to the free-standing InN NWs discussed in Sec.6.1. For ZnO NWs with radius $R \leq 2$ nm, the optical absorbtion is polarized along the axis of the NW (See Fig. 6.15(a) for ZnO NW with radius R =1.4 nm). However, the fundamental optical gap concedes with the band gap of the NW only for NW with $R \leq$1.4 nm while it become blueshifted by separation energy of $v_2 - v_1$ for range of radius 1.4< $R \leq$2 nm. The direction of polarization changes in to the plane perpendicular to the axis of the NW for ZnO NWs with $R >$3 nm (See Fig. 6.15(c) for ZnO NW with radius R =5 nm).

Focusing on the optical properties of stressed ZnO NWs, in the discussion above we have seen that applying a uniaxial stress beyond a certain critical value changes the dominant characteristic of the topmost VB states at Γ-point of ZnO NWs and the values of the critical stress highly depend on the size of the NW. For small ZnO NWs ($R \leq$ 2 nm) stretched by a uniaxial stress of $F \geq F_c$, v_1 and v_2 have s-type envelope function and are dominantly composed of $\perp$-character. However, the transition from these states are not visible. The third VB has p-type envelope function symmetry and is composed of mainly $\perp$-character. Thus, the transition $v_{3,\perp} \rightarrow c_1$ has non-zero oscillator strength. As a result, the optical absorption becomes polarized into the in-plane direction. This can be seen in the case of ZnO NW with radius R =1.4 nm under a stretching stress of F =20 GPa as shown in Fig. 6.15(b).

In the case of lager ZnO NWs ($R >$2 nm) compressed by a uniaxial stress of $F \leq F_c$, the situation is different from the unstrained and stretched ZnO NWs. In this case, the top VB state v_1 at k_z =0 has Z-character and the value of the oscillator strength for the transition $v_1(Z) \rightarrow c_1$ becomes non-zero. Therefore, the optical absorption in the compressed ZnO NW becomes polarized along the c-axis and the fundamental absorption optical gap coincides with the band gap energy of the NW. This can been clearly seen in Fig. 6.15(d) for ZnO NWs with radius R = 5 nm under a compression stress of F =-20 GPa. In Table 6.2 we have summarized

the electronic and optical properties of of selected lowest CB and highest VB states in ZnO NW under uniaxial stress.

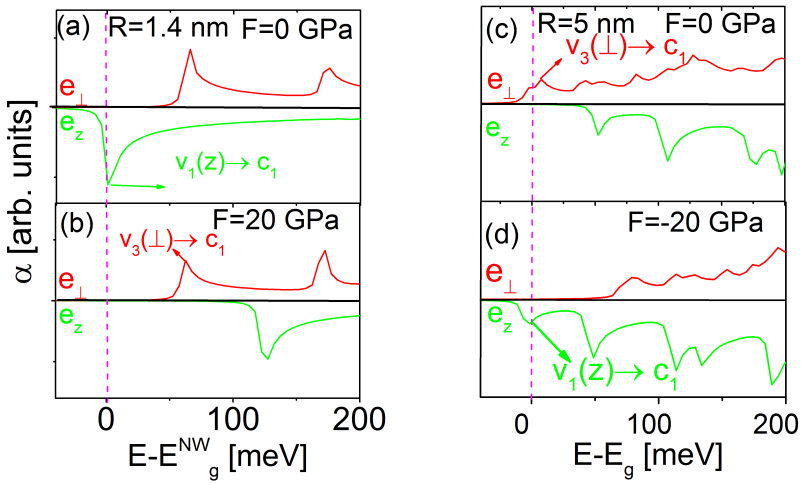

Figure 6.15: Polarization dependent optical absorption spectra of ZnO NWs nm under a uniaxial stress of (a) $F = 0$ GPa and (b) $F = 20$ GPa for radius $R = 1.4$ nm, and (c) $F = 0$ GPa, (b) $F = -20$ GPa for ZnO NW with radius $R = 5$ nm. In each case it has been represented separately, in the positive and negative vertical axes, the spectra corresponding to $\boldsymbol{e}_\perp$ and $\boldsymbol{e}_z$ polarization, respectively.

Applied Stress	Direction of of polarization	State	Envelope symmetry	Dominant character (ℓ)	Optical state
stretching (F> F_c)	$\boldsymbol{e}_\perp$	c_1	s	S	-
		v_1	s	$\perp$	dark
		v_2	s	$\perp$	dark
		v_3	p	$\perp$	bright
compressing (F$\leq$ F_c)	$\boldsymbol{e}_z$	c_1	s	S	-
		v_1	s	Z	bright
		v_2	s	Z	dark
		v_3	p	Z	dark

Table 6.2: Electronic and optical properties of lowest CB and highest VB states at Γ-point of ZnO NWs under uniaxial compressive and tensile stress.

Chapter 7

Summary and Conclusions

In this PhD thesis we have successfully developed theoretical models to study piezoelectric, electronic and optical properties of nanowires. The calculations for the piezoelectric properties are performed based on linear continuum mechanics theory while envelope function approach is used for the electronic structure study. We have considered both free standing and core-shell nanowires having wurtzite and zincblende crystal structures. The electronic subband structure and optical absorption spectrum are calculated as a function of the nanowire size.

Comprehensive introduction for the various growth techniques and the possible applications of selected nanowires is given in Chapter 1. In Chapter 2 the $\boldsymbol{k} \cdot \boldsymbol{p}$ method used in the calculation of electronic structure is discussed in detail for zincblende and wurtzite structures. The Pikus-Bir Hamiltonian to include strain effects for both zincblende and wurtzite structures is also discussed.

In Chapter 3 we developed computationally cheap and fast two dimensional approach (GPP problem), which is able to solve fully-coupled piezoelectric problems in wire-like three dimensional systems. In the case of non-piezoelectric problems, the model developed reduces to the purely elastic GPS problem. The model developed is able to accommodate different geometric cross sections and crystal structures with different axial orientations. Moreover, it allows to incorporate externally applied stresses and imposed surface charges. The developed models have been illustrated by studying indefinite lattice-mismatched core-shell nanowires along [111] direction made of diamond Ge/Si and zincblende piezoelectric InN/GaN materials. The 3D-2D comparisons show that for these systems, the behavior of the 3D solutions (strain and electric fields) at distance $\gtrsim 1.25D$ (where D is the largest dimension of the cross section) from the end surfaces is very well approximated by the predictions of the 2D GPP approach, in both non-piezoelectric and piezoelec-

tric problems. In other words, it has been numerically confirmed the validity of the Saint-Venant's principle also for the 3D fully-coupled piezoelectric problems. The superiority of the GPP approach is clearly manifested in the core-shell nanowire simulations where warping effects, completely absent in the standard 2D plane piezoelectric approximation, are perfectly taken into account. Further application of the developed 2D model was presented by studying thermoelastic properties of ZB [111] Ge/Si CSNW. Thus, the GPP approach provides a versatile procedure to study accurately and with moderate computing resources the details of the strain and electric field distribution in elongated piezoelectric systems. Furthermore, the developed models are expected to be important for analyzing and understanding the properties of epitaxially grown core-shell nanowires and their applications in nanowire electronics, optoelectronic and sensing.

The formulations of the eight-band $\boldsymbol{k}\cdot\boldsymbol{p}$ method using envelope function method for studying electronic structure of nanowires are given in Chapter 4. In Chapter 5, we use this model to investigate electronic structure and optical absorption of zinc-blende nanowires grown along [001] and [111] directions. In InAs NWs, we found out that the narrow band gap resulted in strong coupling between the conduction and valence bands. To the contrast, the wide band gap of GaAs created weaker coupling between the conduction and valence bands. The dependence of the lowest conduction band state with with the size of the NWs obtained for both InAs and GaAs NWs was found significantly deviated from the relation predicted by the EMA which showed the inadequacy of the single-band approach and the need for the multiband method. In the valence band of both [001] and [111] InAs NW, the size dispersions of the topmost two states having the same angular momentum $\mid M = 1/2 \mid$ but different dominant character types cross each other at a critical radius R_c. The values of R_c correspond to 4.6 and 3.2 nm respectively for [001] and [111] InAs NWs. As a result, the optical phenomena around the band gap become strongly dependent on the size of the NW. We found out that the optical absorptions for both [001] and [111] InAs NWs are polarized along the axis of the NWs. However, the fundamental optical gaps coincide with the band gap of the NW only for [001] and [111] InAs NWs with $R \leq R_c$. For both [001] and [111] InAs NWs with $R > R_c$, the optical the optical gaps are blue-shifted by separation energy of $v_1 - v_2$ with respect to the band gaps of the NWs. To the contrast, the size dispersion of top most two VB states in both [001] and [111] GaAs NWs do not cross each other. Thus, the optical absorptions in both [001] and [111] GaAs NWs are polarized along the axis of the NWs and the fundamental optical gaps coincide with the band gaps of the NW independent of size. We believe that the results presented here will provide important information about the

electronic structures and optical absorption of the [001] and [111]-oriented InAs and GaAs nanowires and useful guidance for the use of these nanowires in novel nanoelectronic, optoelectronic and quantum devices.

We have also studied the electronic and optical properties of zincblende core-shell nanowires. In the lattice-matched ZB [111] AlGaAs/GaAs CSNW, we found that the presence of Al concentration increased the band gap due to the increase in the band offsets. Particularly, the change in the gap is higher for thinner core and shell. In the optical absorption, the presence of Al concentration created optically inactive states in the top most valence band state at Γ-point which resulted in the blue shift of the axially polarized optical absorption. Next we studied lattice-mismatched [001] GaAs/InAs CSNW. The lattice-mismatch induced strain distributions inside the CSNW are obtained by using GPS approach and their effects of the strain on the electronic structure are included by using the Pikus-Bir hamiltonian. In both strain free and strained GaAs/InAs CSNW, we found out that the band gaps decrease with increase of shell thickness for fixed radius of core. The band gap in the strained GaAs/InAs CSNWs are decreased as a result of the strain when compared with the strain free case. In the optical calculations, we found out that the optical absorptions are polarized along the [001] direction but blue-shifted due to the presence of dark states at the Γ-point of topmost VB state.

The electronic structure and optical absorption of wurtzite NWs are also investigated in Chapter 6. In InN NW, we found out that the CB states exhibit monotonously decreasing energy with increasing NW radius. On the other hand, the size dispersion of the valence band states show various crossing and anticrossing effects due to the interplay between the confinement and band mixing effects. The crossing between the size dispersion of topmost valence band states not only resulted in blueshift of fundamental optical gap, like the case of InAs NW, but also a complete change in the direction of polarization for the optical absorption. For InN NWs with $R \leq 3$ nm, the optical absorption is polarized along the axis of the NW while for InN NWs with $R > 3$ nm the optical absorption was found to be polarized along the in-plane direction. Moreover, the spectra of the smaller nanowires display a distinguishable sequence of peaks reflecting the one-dimensional density-of-states. The absorption peaks become denser for larger nanowires, and for radii larger than 10 nm the spectrum starts to resemble that of bulk InN.

Finally, we studied electronic and optical properties of ZnO NW under uniaxial stress. The band gaps follow a linear relationship with the applied stress. Compressive stress widened the band gap while the tensile stress narrows the gap. In the optical absorption, we found out a minimize critical uniaxial stress where the

direction of polarization can be be tuned depending on the size of the NW due to the change in the dominant character of top most valence band states at Γ-point. Thus, we found out that applying tensile stress beyond the critical values changes the direction of polarization for ZnO NWs with $R \leq 2$ nm from the axis of the NW into the in-plane direction. To the contrast, for ZnO NW with $R > 2$ nm, applying a compressive stress beyond a critical value changes the direction of polarization from the in-plane into the axis of the NW. The results obtained here contribute significantly to the understanding of the optoelectronic properties of ZnO nanowire and its device applications.

Appendix A

Hamiltonian Matrix for Zincblende and Wurtzite Structures

In this appendix we present the explicit form of the $\boldsymbol{k}\cdot\boldsymbol{p}$ Hamiltonians that have been discussed in Sec. 2.2 and used in Chapters 5 and 6 for the calculation of the zincblende and wurtzite nanowire electronic structures. In writing the Hamiltonian matrices we have used the following auxiliary notation:

$$k_\pm = k_x \pm i\, k_y, \tag{A.1a}$$
$$k_\perp^2 = k_x^2 + k_y^2 \quad (= k_+\, k_- = k_-\, k_+), \tag{A.1b}$$
$$k^2 = k_\perp^2 + k_z^2, \tag{A.1c}$$

$$\varepsilon_\perp = \varepsilon_{xx} + \varepsilon_{yy}, \tag{A.2a}$$
$$\mathrm{Tr}(\varepsilon) \equiv \varepsilon_h = \varepsilon_\perp + \varepsilon_{zz}, \tag{A.2b}$$
$$\tilde{\varepsilon} \equiv \varepsilon_{\mathrm{biax}} = \varepsilon_\perp - 2\,\varepsilon_{zz}, \tag{A.2c}$$
$$\hat{\varepsilon} = \varepsilon_{xx} - \varepsilon_{yy}, \tag{A.2d}$$
$$\varepsilon_{\pm\pm} = \hat{\varepsilon} \pm 2\, i\, \varepsilon_{xy}, \tag{A.2e}$$
$$\varepsilon_\pm = \varepsilon_{xz} \pm i\varepsilon_{yz}. \tag{A.2f}$$

A.1. Zincblende Structure

A.1.1. $\boldsymbol{k} \cdot \boldsymbol{p}$ Hamiltonian Matrix

Here we present the explicit form of the $\boldsymbol{k} \cdot \boldsymbol{p}$ Hamiltonian matrix for the zincblende structure discussed in Sec. 2.2.2.

$\left\vert c,\frac{1}{2},+\frac{\mathbf{1}}{\mathbf{2}}\right\rangle$	$\left\vert c,\frac{1}{2},-\frac{\mathbf{1}}{\mathbf{2}}\right\rangle$	$\left\vert v,\frac{3}{2},+\frac{\mathbf{3}}{\mathbf{2}}\right\rangle$	$\left\vert v,\frac{3}{2},+\frac{\mathbf{1}}{\mathbf{2}}\right\rangle$	$\left\vert v,\frac{3}{2},-\frac{\mathbf{1}}{\mathbf{2}}\right\rangle$	$\left\vert v,\frac{3}{2},-\frac{\mathbf{3}}{\mathbf{2}}\right\rangle$	$\left\vert v,\frac{1}{2},+\frac{\mathbf{1}}{\mathbf{2}}\right\rangle$	$\left\vert v,\frac{1}{2},-\frac{\mathbf{1}}{\mathbf{2}}\right\rangle$
$E_c+\frac{\hbar^2k^2}{2m'}$	0	$-\frac{1}{\sqrt{2}}Pk_+$	$\sqrt{\frac{2}{3}}Pk_z$	$\frac{1}{\sqrt{6}}Pk_-$	0	$-\frac{1}{\sqrt{3}}Pk_z$	$-\frac{1}{\sqrt{3}}Pk_-$
0	$E_c+\frac{\hbar^2k^2}{2m'}$	0	$-\frac{1}{\sqrt{6}}Pk_+$	$\sqrt{\frac{2}{3}}Pk_z$	$\frac{1}{\sqrt{2}}Pk_-$	$-\frac{1}{\sqrt{3}}Pk_+$	$\frac{1}{\sqrt{3}}Pk_z$
$-\frac{1}{\sqrt{2}}Pk_-$	0	$E_v-\frac{\hbar^2}{2m_0}(\gamma_1'+\gamma_2')k_\perp^2$ $-\frac{\hbar^2}{2m_0}(\gamma_1'-2\gamma_2')k_z^2$	$2\sqrt{3}\frac{\hbar^2}{2m_0}\gamma_3'k_-k_z$	$\sqrt{3}\frac{\hbar^2}{2m_0}\left[\left(\frac{\gamma_2'+\gamma_3'}{2}\right)k_-^2 +\left(\frac{\gamma_2'-\gamma_3'}{2}\right)k_+^2\right]$	0	$-\sqrt{6}\frac{\hbar^2}{2m_0}\gamma_3'k_-k_z$	$\sqrt{6}\frac{\hbar^2}{2m_0}\left[\left(\frac{\gamma_2'+\gamma_3'}{2}\right)k_-^2 +\left(\frac{\gamma_2'-\gamma_3'}{2}\right)k_+^2\right]$
$\sqrt{\frac{2}{3}}Pk_z$	$-\frac{1}{\sqrt{6}}Pk_+$	$2\sqrt{3}\frac{\hbar^2}{2m_0}\gamma_3'k_+k_z$	$E_v-\frac{\hbar^2}{2m_0}(\gamma_1'-\gamma_2')k_\perp^2$ $-\frac{\hbar^2}{2m_0}(\gamma_1'+2\gamma_2')k_z^2$	0	$\sqrt{3}\frac{\hbar^2}{2m_0}\left[\left(\frac{\gamma_2'+\gamma_3'}{2}\right)k_-^2 +\left(\frac{\gamma_2'-\gamma_3'}{2}\right)k_+^2\right]$	$-\sqrt{2}\frac{\hbar^2}{2m_0}\gamma_2'$ $\times\left(k_\perp^2-2k_z^2\right)$	$3\sqrt{2}\frac{\hbar^2}{2m_0}\gamma_3'k_-k_z$
$\frac{1}{\sqrt{6}}Pk_-$	$\sqrt{\frac{2}{3}}Pk_z$	$\sqrt{3}\frac{\hbar^2}{2m_0}\left[\left(\frac{\gamma_2'+\gamma_3'}{2}\right)k_+^2 +\left(\frac{\gamma_2'-\gamma_3'}{2}\right)k_-^2\right]$	0	$E_v-\frac{\hbar^2}{2m_0}(\gamma_1'-\gamma_2')k_\perp^2$ $-\frac{\hbar^2}{2m_0}(\gamma_1'+2\gamma_2')k_z^2$	$-2\sqrt{3}\frac{\hbar^2}{2m_0}\gamma_3'k_-k_z$	$3\sqrt{2}\frac{\hbar^2}{2m_0}\gamma_3'k_+k_z$	$\sqrt{2}\frac{\hbar^2}{2m_0}\gamma_2'$ $\times\left(k_\perp^2-2k_z^2\right)$
0	$\frac{1}{\sqrt{2}}Pk_+$	0	$\sqrt{3}\frac{\hbar^2}{2m_0}\left[\left(\frac{\gamma_2'+\gamma_3'}{2}\right)k_+^2 +\left(\frac{\gamma_2'-\gamma_3'}{2}\right)k_-^2\right]$	$-2\sqrt{3}\frac{\hbar^2}{2m_0}\gamma_3'k_+k_z$	$E_v-\frac{\hbar^2}{2m_0}(\gamma_1'+\gamma_2')k_\perp^2$ $-\frac{\hbar^2}{2m_0}(\gamma_1'-2\gamma_2')k_z^2$	$\sqrt{6}\frac{\hbar^2}{2m_0}\left[\left(\frac{\gamma_2'+\gamma_3'}{2}\right)k_+^2 +\left(\frac{\gamma_2'-\gamma_3'}{2}\right)k_-^2\right]$	$-\sqrt{6}\frac{\hbar^2}{2m_0}\gamma_3'k_+k_z$
$-\frac{1}{\sqrt{3}}Pk_z$	$-\frac{1}{\sqrt{3}}Pk_-$	$-\sqrt{6}\frac{\hbar^2}{2m_0}\gamma_3'k_+k_z$	$-\sqrt{2}\frac{\hbar^2}{2m_0}\gamma_2'$ $\times\left(k_\perp^2-2k_z^2\right)$	$3\sqrt{2}\frac{\hbar^2}{2m_0}\gamma_3'k_-k_z$	$\sqrt{6}\frac{\hbar^2}{2m_0}\left[\left(\frac{\gamma_2'+\gamma_3'}{2}\right)k_-^2 +\left(\frac{\gamma_2'-\gamma_3'}{2}\right)k_+^2\right]$	$E_v-\Delta_0$ $-\frac{\hbar^2}{2m_0}\gamma_1'k^2$	0
$-\frac{1}{\sqrt{3}}Pk_+$	$\frac{1}{\sqrt{3}}Pk_z$	$-\sqrt{6}\frac{\hbar^2}{2m_0}\left[\left(\frac{\gamma_2'+\gamma_3'}{2}\right)k_+^2 +\left(\frac{\gamma_2'-\gamma_3'}{2}\right)k_-^2\right]$	$3\sqrt{2}\frac{\hbar^2}{2m_0}\gamma_3'k_+k_z$	$\sqrt{2}\frac{\hbar^2}{2m_0}\gamma_2'$ $\times\left(k_\perp^2-2k_z^2\right)$	$-\sqrt{6}\frac{\hbar^2}{2m_0}\gamma_3'k_-k_z$	0	$E_v-\Delta_0$ $-\frac{\hbar^2}{2m_0}\gamma_1'k^2$

(A.3)

We remind that in the above Hamiltonian, the coordinates and wavectors are referred to the cubic crystallographic axes: ($X \parallel [100]$, $Y \parallel [010]$, $Z \parallel [010]$), and $|\uparrow\rangle$ and $|\downarrow\rangle$ indicate basic spinors with the spin quantized along $Z \parallel [001]$. To obtain the Hamiltonians referred to axes:

$$(X' \parallel [10\bar{1}] , \; Y' \parallel [\bar{1}2\bar{1}] , \; Z' \parallel [111]) \quad ,$$

that are used in the modeling of nanowires oriented along [111], we have followed the rotation procedure sketched in Ref.[180].

Below we will give the definition of the parameters appearing in the Hamiltonian matrix (A.3).

- The Kane parameter P is the parameter controlling the coupling strength between the conduction and valence bands, and is proportional to the momentum matrix element,

$$P = \frac{\hbar}{m_0}\langle S|p_x|X\rangle = \frac{\hbar}{m_0}\langle S|p_y|Y\rangle = \frac{\hbar}{m_0}\langle S|p_z|Z\rangle \, . \tag{A.4}$$

  With this definition P is purely imaginary, $P = -i|P|$, with $|P|$ being a positive number.[105] The Kane energy E_p is defined as:

$$E_p = \frac{2m_0}{\hbar^2}|P|^2. \tag{A.5}$$

- $(\gamma_1', \gamma_2', \gamma_3')$ are the reduced Luttinger parameters to be used in the 8×8 Hamiltonian. They are defined in terms of $(\gamma_1, \gamma_2, \gamma_3)$, introduced originally by Luttinger,[103] by the following relations,[214]

$$\gamma_1' = \gamma_1 - \frac{1}{3}\frac{E_p}{E_g}, \tag{A.6a}$$

$$\gamma_2' = \gamma_2 - \frac{1}{6}\frac{E_p}{E_g}, \tag{A.6b}$$

$$\gamma_3' = \gamma_3 - \frac{1}{6}\frac{E_p}{E_g}. \tag{A.6c}$$

- m' is the effective mass of the conduction band to be used in the 8×8 Hamiltonian, and is related to the experimental effective mass m_e by:

$$\frac{m_0}{m'} = \frac{m_0}{m_e} - \frac{E_p}{3}\left(\frac{2}{E_g} + \frac{1}{E_g + \Delta_0}\right). \tag{A.7}$$

A.1.2. Bir-Pikus Hamiltonian Matrix

Here we present the explicit form of the Bir-Pikus Hamiltonian matrix for the zincblende structure. It can be obtained formally from the $\boldsymbol{k}\cdot\boldsymbol{p}$ Hamiltonian according to the following prescription:[102]

$$\begin{aligned}
k_i k_j &\rightarrow \varepsilon_{ij}, \\
\frac{\hbar^2}{2m'} &\rightarrow C_1, \quad \equiv \quad a_c, \\
\frac{\hbar^2\gamma_1}{2m_0} &\rightarrow -D_d^v \quad \equiv \quad -a_v, \\
\frac{\hbar^2\gamma_2}{2m_0} &\rightarrow \frac{D_u}{3} \quad \equiv \quad -\frac{b}{2}, \\
\frac{\hbar^2\gamma_3}{2m_0} &\rightarrow \frac{D_u'}{3} \quad \equiv \quad -\frac{d}{2\sqrt{3}},
\end{aligned}$$

The notation of the deformation potential of the second column is employed by H.-R. Trebin *et al.*.[215] Those shown in the third column were defined by G. L. Bir and G. E. Pikus and are widely used in the literature.

$\left\vert c,\frac{1}{2},+\frac{\mathbf{1}}{\mathbf{2}}\right\rangle$	$\left\vert c,\frac{1}{2},-\frac{\mathbf{1}}{\mathbf{2}}\right\rangle$	$\left\vert v,\frac{3}{2},+\frac{\mathbf{3}}{\mathbf{2}}\right\rangle$	$\left\vert v,\frac{3}{2},+\frac{\mathbf{1}}{\mathbf{2}}\right\rangle$	$\left\vert v,\frac{3}{2},-\frac{\mathbf{1}}{\mathbf{2}}\right\rangle$	$\left\vert v,\frac{3}{2},-\frac{\mathbf{3}}{\mathbf{2}}\right\rangle$	$\left\vert v,\frac{1}{2},+\frac{\mathbf{1}}{\mathbf{2}}\right\rangle$	$\left\vert v,\frac{1}{2},-\frac{\mathbf{1}}{\mathbf{2}}\right\rangle$
$C_1\,\mathrm{tr}(\varepsilon)$	0	0	0	0	0	0	0
0	$C_1\,\mathrm{tr}(\varepsilon)$	0	0	0	0	0	0
0	0	$D_d\,\mathrm{tr}(\varepsilon)-\frac{1}{3}\,D_u\,\bar{\varepsilon}$	0	$\frac{1}{\sqrt{3}}\left[\left(\frac{D_u+D'_u}{2}\right)\varepsilon_{--}+\left(\frac{D_u-D'_u}{2}\right)\varepsilon_{++}\right]$	0	0	$-\sqrt{\frac{2}{3}}\left[\left(\frac{D_u+D'_u}{2}\right)\varepsilon_{--}+\left(\frac{D_u-D'_u}{2}\right)\varepsilon_{++}\right]$
0	0	0	$D_d\,\mathrm{tr}(\varepsilon)+\frac{1}{3}\,D_u\,\bar{\varepsilon}$	0	$\frac{1}{\sqrt{3}}\left[\left(\frac{D_u+D'_u}{2}\right)\varepsilon_{--}+\left(\frac{D_u-D'_u}{2}\right)\varepsilon_{++}\right]$	$-\frac{\sqrt{2}}{3}\,D_u\,\bar{\varepsilon}$	0
0	0	$\frac{1}{\sqrt{3}}\left[\left(\frac{D_u+D'_u}{2}\right)\varepsilon_{++}+\left(\frac{D_u-D'_u}{2}\right)\varepsilon_{--}\right]$	0	$D_d\,\mathrm{tr}(\varepsilon)+\frac{1}{3}\,D_u\,\bar{\varepsilon}$	0	0	$\frac{\sqrt{2}}{3}\,D_u\,\bar{\varepsilon}$
0	0	0	$\frac{1}{\sqrt{3}}\left[\left(\frac{D_u+D'_u}{2}\right)\varepsilon_{++}+\left(\frac{D_u-D'_u}{2}\right)\varepsilon_{--}\right]$	0	$D_d\,\mathrm{tr}(\varepsilon)-\frac{1}{3}\,D_u\,\bar{\varepsilon}$	$\sqrt{\frac{2}{3}}\left[\left(\frac{D_u+D'_u}{2}\right)\varepsilon_{++}+\left(\frac{D_u-D'_u}{2}\right)\varepsilon_{--}\right]$	0
0	0	0	$-\frac{\sqrt{2}}{3}\,D_u\,\bar{\varepsilon}$	0	$\sqrt{\frac{2}{3}}\left[\left(\frac{D_u+D'_u}{2}\right)\varepsilon_{--}+\left(\frac{D_u-D'_u}{2}\right)\varepsilon_{++}\right]$	$D_d\,\mathrm{tr}(\varepsilon)$	0
0	0	$-\sqrt{\frac{2}{3}}\left[\left(\frac{D_u+D'_u}{2}\right)\varepsilon_{++}+\left(\frac{D_u-D'_u}{2}\right)\varepsilon_{--}\right]$	0	$-\frac{\sqrt{2}}{3}\,D_u\,\bar{\varepsilon}$	0	0	$D_d\,\mathrm{tr}(\varepsilon)$

(A.8)

A.2. Wurtzite Structure

A.2.1. $\boldsymbol{k} \cdot \boldsymbol{p}$ Hamiltonian Matrix

Here we present the explicit form of the $\boldsymbol{k} \cdot \boldsymbol{p}$ Hamiltonian matrix for the wurtzite structure discussed in Sec. 2.2.3.

$$
\begin{array}{c|cc|ccc|ccc}
 & \left|c,0,+\frac{1}{2}\right\rangle & \left|c,0,-\frac{1}{2}\right\rangle & \left|v,1,+\frac{1}{2}\right\rangle & \left|v,-1,+\frac{1}{2}\right\rangle & \left|v,0,+\frac{1}{2}\right\rangle & \left|v,-1,-\frac{1}{2}\right\rangle & \left|v,1,-\frac{1}{2}\right\rangle & \left|v,0,-\frac{1}{2}\right\rangle \\
\hline
\left|c,0,+\frac{1}{2}\right\rangle & E_c+\frac{\hbar^2k^2}{2m_0} & 0 & -\frac{1}{\sqrt{2}}P_\perp k_+ & \frac{1}{\sqrt{2}}P_\perp k_- & P_z k_z & 0 & 0 & 0 \\
\left|c,0,-\frac{1}{2}\right\rangle & 0 & E_c+\frac{\hbar^2k^2}{2m_0} & 0 & 0 & 0 & \frac{1}{\sqrt{2}}P_\perp k_- & -\frac{1}{\sqrt{2}}P_\perp k_+ & P_z k_z \\
\hline
\left|v,1,+\frac{1}{2}\right\rangle & -\frac{1}{\sqrt{2}}P_\perp k_- & 0 & \begin{array}{c}E_v+\Delta_1+\Delta_2\\+\frac{\hbar^2}{2m_0}(A_2'+A_4')k_\perp^2\\+\frac{\hbar^2}{2m_0}(A_1'+A_3')k_z^2\end{array} & -\frac{\hbar^2}{2m_0}A_5'k_-^2 & -\frac{\hbar^2}{2m_0}A_6'k_-k_z & 0 & 0 & 0 \\
\left|v,-1,+\frac{1}{2}\right\rangle & \frac{1}{\sqrt{2}}P_\perp k_+ & 0 & -\frac{\hbar^2}{2m_0}A_5'k_+^2 & \begin{array}{c}E_v+\Delta_1-\Delta_2\\+\frac{\hbar^2}{2m_0}(A_2'+A_4')k_\perp^2\\+\frac{\hbar^2}{2m_0}(A_1'+A_3')k_z^2\end{array} & \frac{\hbar^2}{2m_0}A_6'k_+k_z & 0 & 0 & \sqrt{2}\Delta_3 \\
\left|v,0,+\frac{1}{2}\right\rangle & P_z k_z & 0 & -\frac{\hbar^2}{2m_0}A_6'k_+k_z & \frac{\hbar^2}{2m_0}A_6'k_-k_z & E_v+\frac{\hbar^2}{2m_0}A_2'k_\perp^2+\frac{\hbar^2}{2m_0}A_1'k_z^2 & 0 & \sqrt{2}\Delta_3 & 0 \\
\hline
\left|v,-1,-\frac{1}{2}\right\rangle & 0 & \frac{1}{\sqrt{2}}P_\perp k_- & 0 & 0 & 0 & \begin{array}{c}E_v+\Delta_1+\Delta_2\\+\frac{\hbar^2}{2m_0}(A_2'+A_4')k_\perp^2\\+\frac{\hbar^2}{2m_0}(A_1'+A_3')k_z^2\end{array} & -\frac{\hbar^2}{2m_0}A_5'k_+^2 & \frac{\hbar^2}{2m_0}A_6'k_+k_z \\
\left|v,1,-\frac{1}{2}\right\rangle & 0 & \frac{1}{\sqrt{2}}P_\perp k_+ & 0 & 0 & \sqrt{2}\Delta_3 & -\frac{\hbar^2}{2m_0}A_5'k_-^2 & \begin{array}{c}E_v+\Delta_1-\Delta_2\\+\frac{\hbar^2}{2m_0}(A_2'+A_4')k_\perp^2\\+\frac{\hbar^2}{2m_0}(A_1'+A_3')k_z^2\end{array} & -\frac{\hbar^2}{2m_0}A_6'k_-k_z \\
\left|v,0,-\frac{1}{2}\right\rangle & 0 & P_z k_z & 0 & \sqrt{2}\Delta_3 & 0 & \frac{\hbar^2}{2m_0}A_6'k_+k_z & -\frac{\hbar^2}{2m_0}A_6'k_+k_z & E_v+\frac{\hbar^2}{2m_0}A_2'k_\perp^2+\frac{\hbar^2}{2m_0}A_1'k_z^2
\end{array}
\tag{A.9}
$$

Below we will give the definition of the parameters appearing in the Hamiltonian matrix (A.9)

- The Kane-like parameters P_z and $P_\perp$ are defined as:

$$P_z = \frac{\hbar}{m_0}\langle S|p_z|Z\rangle, \tag{A.10a}$$

$$P_\perp = \frac{\hbar}{m_0}\langle S|p_x|X\rangle = \frac{\hbar}{m_0}\langle S|p_y|Y\rangle \quad , \tag{A.10b}$$

  and, as in the zincblende, they are purely imaginary numbers, i.e.,

$$P_z = -i|P_z| \, , \tag{A.11a}$$

$$P_\perp = -i|P_\perp| \, , \tag{A.11b}$$

  where $|P_\perp|$ and $|P_z|$ are positive values. From these parameters we introduce the energies $E_{p,z}$ and $E_{p,\perp}$:

$$E_{p,z} = \frac{2m_0}{\hbar^2}|P_z|^2, \tag{A.12a}$$

$$E_{p,\perp} = \frac{2m_0}{\hbar^2}|P_\perp|^2. \tag{A.12b}$$

- A_i', $i = 1, \ldots, 6$, are parameters equivalent to the Luttinger parameters appearing in the zincblende $\boldsymbol{k}\cdot\boldsymbol{p}$ Hamiltonian. They are related to A_i through the following expressions:[216]

$$A_1' = A_1 + \frac{E_{p,z}}{E_g} \tag{A.13a}$$

$$A_2' = A_2 \tag{A.13b}$$

$$A_3' = A_3 - \frac{E_{p,z}}{E_g} \tag{A.13c}$$

$$A_4' = A_4 + \frac{1}{2}\frac{E_{p,\perp}}{E_g} \tag{A.13d}$$

$$A_5' = A_5 + \frac{1}{2}\frac{E_{p,\perp}}{E_g} \tag{A.13e}$$

$$A_6' = A_6 + \frac{\sqrt{2}m_0}{\hbar^2}\frac{P_z P_\perp}{E_g} \, . \tag{A.13f}$$

  In this case the Kane-like parameters are obtained from the experimental

effective masses $m_{e,z}$ and $m_{e,\perp}$ and the energy parameters as follows:

$$P_z^2 = \frac{\hbar^2}{2m_0}\left(\frac{1}{m_{e,z}} - 1\right)\frac{(E_g + \Delta_1 + \Delta_2)(E_g + 2\Delta_2) - 2\Delta_3^2}{E_g + 2\Delta_2}, \tag{A.14}$$

$$P_\perp^2 = \frac{\hbar^2}{2m_0}\left(\frac{1}{m_{e,\perp}} - 1\right)\frac{(E_g + \Delta_1 + \Delta_2)(E_g + 2\Delta_2) - 2\Delta_3^2}{(E_g + \Delta_1 + \Delta_2)(E_g + \Delta_2) - \Delta_3^2}. \tag{A.15}$$

A.2.2. Bir-Pikus Hamiltonian Matrix

Here we present the explicit form of the Bir-Pikus Hamiltonian matrix for the zincblende structure. It can be obtained formally from the $\boldsymbol{k}\cdot\boldsymbol{p}$ Hamiltonian according to the following prescription:

$$\begin{aligned} k_i k_j &\rightarrow \varepsilon_{ij}\,, \\ \frac{\hbar^2 k_z^2}{2m_{0,z}} &\rightarrow a_z e_{zz}\,, \\ \frac{\hbar^2 k_\perp^2}{2m_{0,\perp}} &\rightarrow a_\perp(e_{xx} + e_{yy})\,, \\ \frac{\hbar^2 A_i}{2m_0} &\rightarrow D_i\,, \end{aligned} \tag{A.16}$$

where a_z and $a_\perp$ are deformation potentials of the conduction bands and D_i, $i = 1, \ldots 6$, are the deformation potentials of the valence bands.

$$
\begin{array}{c}
\begin{array}{cccccccc}
\left|c,0,+\tfrac{1}{2}\right\rangle & \left|c,0,-\tfrac{1}{2}\right\rangle & \left|v,1,+\tfrac{1}{2}\right\rangle & \left|v,-1,+\tfrac{1}{2}\right\rangle & \left|v,0,+\tfrac{1}{2}\right\rangle & \left|v,-1,-\tfrac{1}{2}\right\rangle & \left|v,1,-\tfrac{1}{2}\right\rangle & \left|v,0,-\tfrac{1}{2}\right\rangle
\end{array}
\\
\left(\begin{array}{cc|ccc|cc}
a_\perp(\varepsilon_{11}+\varepsilon_{22}) & 0 & 0 & 0 & 0 & 0 & 0 & 0 \\
+a_z\varepsilon_{33} & & & & & & & \\
0 & a_\perp(\varepsilon_{11}+\varepsilon_{22}) & 0 & 0 & 0 & 0 & 0 & 0 \\
 & +a_z\,\varepsilon_{33} & & & & & & \\
\hline
0 & 0 & (D_2+D_4)(\varepsilon_{11}+\varepsilon_{22}) & -D_5\,\varepsilon_{--} & 0 & 0 & 0 & 0 \\
 & & +(D_1+D_3)\varepsilon_{33} & & & & & \\
0 & 0 & -D_5\,\varepsilon_{++} & (D_2+D_4)(\varepsilon_{11}+\varepsilon_{22}) & 0 & 0 & 0 & 0 \\
 & & & +(D_1+D_3)\varepsilon_{33} & & & & \\
0 & 0 & 0 & 0 & D_2(\varepsilon_{11}+\varepsilon_{22}) & 0 & 0 & 0 \\
 & & & & +D_1\,\varepsilon_{33} & & & \\
\hline
0 & 0 & 0 & 0 & 0 & (D_2+D_4)(\varepsilon_{11}+\varepsilon_{22}) & -D_5\,\varepsilon_{++} & 0 \\
 & & & & & +(D_1+D_3)\varepsilon_{33} & & \\
0 & 0 & 0 & 0 & 0 & -D_5\,\varepsilon_{--} & (D_2+D_4)(\varepsilon_{11}+\varepsilon_{22}) & 0 \\
 & & & & & & +(D_1+D_3)\varepsilon_{33} & \\
0 & 0 & 0 & 0 & 0 & 0 & 0 & D_2(\varepsilon_{11}+\varepsilon_{22}) \\
 & & & & & & & +D_1\,\varepsilon_{33}
\end{array}\right)
\end{array}
\tag{A.17}
$$

Appendix B

Momentum Matrix Elements

In this appendix we give the explicit form of the momentum matrix elements $(\hat{\boldsymbol{e}} \cdot \boldsymbol{p}_{aa'})$ appearing in the expression of the interband optical matrix element (2.50), when expressed in the Bloch basis employed for the matrix representation of the $\boldsymbol{k} \cdot \boldsymbol{p}$ Hamiltonians for zincblende and wurtzite structures detailed in Appendix A.

B.1. Zincblende Structure

$$(\hat{\boldsymbol{e}} \cdot \boldsymbol{p}_{aa'}) \leftrightarrow P \left(\begin{array}{cc|cccc|cc} 0 & 0 & \left[-1\right]_- & \left[\sqrt{\frac{2}{3}}\right]_z & \left[\frac{1}{\sqrt{3}}\right]_+ & 0 & \left[-\frac{1}{\sqrt{3}}\right]_z & \left[-\sqrt{\frac{2}{3}}\right]_+ \\ 0 & 0 & 0 & \left[-\frac{1}{\sqrt{3}}\right]_- & \left[\sqrt{\frac{2}{3}}\right]_z & \left[1\right]_+ & \left[-\sqrt{\frac{2}{3}}\right]_- & \left[\frac{1}{\sqrt{3}}\right]_z \\ \hline \left[1\right]_+ & 0 & 0 & 0 & 0 & 0 & 0 & 0 \\ \left[-\sqrt{\frac{2}{3}}\right]_z & \left[\frac{1}{\sqrt{3}}\right]_+ & 0 & 0 & 0 & 0 & 0 & 0 \\ \left[-\frac{1}{\sqrt{3}}\right]_- & \left[-\sqrt{\frac{2}{3}}\right]_z & 0 & 0 & 0 & 0 & 0 & 0 \\ 0 & \left[-1\right]_- & 0 & 0 & 0 & 0 & 0 & 0 \\ \hline \left[\frac{1}{\sqrt{3}}\right]_z & \left[\sqrt{\frac{2}{3}}\right]_+ & 0 & 0 & 0 & 0 & 0 & 0 \\ \left[\sqrt{\frac{2}{3}}\right]_- & \left[-\frac{1}{\sqrt{3}}\right]_z & 0 & 0 & 0 & 0 & 0 & 0 \end{array}\right). \tag{B.1}$$

B.2. Wurtzite Structure

$$(\hat{\boldsymbol{e}}\cdot\boldsymbol{p}_{aa'}) \leftrightarrow \left(\begin{array}{cc|ccc|ccc} 0 & 0 & \left[-P_\perp\right]_- & \left[P_\perp\right]_+ & \left[P_z\right]_z & 0 & 0 & 0 \\ 0 & 0 & 0 & 0 & 0 & \left[P_\perp\right]_+ & \left[-P_\perp\right]_- & \left[P_z\right]_z \\ \hline \left[P_\perp\right]_+ & 0 & 0 & 0 & 0 & 0 & 0 & 0 \\ \left[-P_\perp\right]_- & 0 & 0 & 0 & 0 & 0 & 0 & 0 \\ \left[-P_z\right]_z & 0 & 0 & 0 & 0 & 0 & 0 & 0 \\ \hline 0 & \left[-P_\perp\right]_- & 0 & 0 & 0 & 0 & 0 & 0 \\ 0 & \left[+P_\perp\right]_+ & 0 & 0 & 0 & 0 & 0 & 0 \\ 0 & \left[-P_z\right]_z & 0 & 0 & 0 & 0 & 0 & 0 \end{array}\right). \tag{B.2}$$

Appendix C

Matrix Elements for the Envelope Function Model

In this appendix we present some necessary expressions for the calculation of the matrix elements:

$$\left\langle \xi_{\alpha}^{(m)} \left| H^{(\mathrm{NW})} \right| \xi_{\alpha'}^{(m')} \right\rangle$$

that appear in the multiband envelope function model introduced in Chapter 4 for the calculation of the nanowire electronic structure.

- $\boxed{\langle \xi_{\alpha}^{(m)} \left| T_{\rho}^{(m)} \right| \xi_{\beta}^{(m)} \rangle}$

$$\langle \xi_{\alpha}^{(m)} \left| T_{\rho}^{(m)} \right| \xi_{\beta}^{(m)} \rangle = \frac{\hbar^2}{2m_{\perp}^{*} R^2}\, \delta_{\alpha,\beta}\,. \tag{C.1}$$

- $\boxed{\langle \xi_{\alpha}^{(m)} \left| V^{(NW)}(\rho) \right| \xi_{\beta}^{(m)} \rangle}$

$$\langle \xi_{\alpha}^{(m)} \left| V^{(NW)}(\rho) \right| \xi_{\beta}^{(m)} \rangle = \int_0^R \rho\, d\rho\, R_{m,\alpha}^{*}(\rho)\, V^{(NW)}(\rho)\, R_{m,\beta}(\rho)\,. \tag{C.2}$$

- $\boxed{\langle \xi_{\alpha}^{(m\pm1)} \left| k_{\pm} \right| \xi_{\beta}^{(m)} \rangle}$

$$\langle \xi_{\alpha}^{(m\pm1)} \left| k_{\pm} \right| \xi_{\beta}^{(m)} \rangle = (-i)\frac{(\mp k_{\beta}^{(m)})}{R} \Pi_{m\pm1}\left(k_{\alpha}^{(m\pm1)}, k_{\beta}^{(m)} \right)\,. \tag{C.3}$$

- $\boxed{\langle \xi_\alpha^{(m\pm2)} \left| k_\pm^2 \right| \xi_\beta^{(m)} \rangle}$

$$\langle \xi_\alpha^{(m\pm2)} \left| k_\pm^2 \right| \xi_\beta^{(m)} \rangle = -\frac{(k_\beta^{(m)})^2}{R^2} \Pi_{m\pm2} \left(k_\alpha^{(m\pm2)}, k_\beta^{(m)} \right) . \tag{C.4}$$

Appendix D

Material Tensors

D.1. Voigt Notation

The tensor representation of the constitutive relations in Eq.(3.2) can be expressed in a compact matrix form using the Voigt notation explained in the table below:

tensor notation	ij or kl	11	22	33	23,32	13,31	12,21
matrix notation	I or K	1	2	3	4	5	6

Table D.1: Voigt notation.

In the case of the piezoelectric coupling matrix, which is a third rank tensor, the last two indices are replaced by a single index according to Voigt notation whereas the first index remains unchanged. The new matrix arrangement of the material constants will look like:

$$C_{ijkl} \rightarrow C_{IK}, \quad e_{nij} \rightarrow e_{nI} \, . \tag{D.1}$$

Using the Voigt notation, the fully-coupled constitutive relations (3.2) can be written in compact form as:

$$\sigma_I = C_{IK}\varepsilon_K - e_{nI}E_n \, , \tag{D.2a}$$

$$D_m = e_{mK}\varepsilon_K + \epsilon_{mn}E_n \, , \tag{D.2b}$$

or in matrix form as

$$\begin{pmatrix} \sigma_1 = \sigma_{11} \\ \sigma_2 = \sigma_{22} \\ \sigma_3 = \sigma_{33} \\ \sigma_4 = \sigma_{23} \\ \sigma_5 = \sigma_{13} \\ \sigma_6 = \sigma_{12} \\ D_1 \\ D_2 \\ D_3 \end{pmatrix} = \begin{pmatrix} C_{11} & C_{12} & C_{13} & C_{14} & C_{15} & C_{16} & e_{11} & e_{21} & e_{31} \\ C_{21} & C_{22} & C_{23} & C_{24} & C_{25} & C_{26} & e_{12} & e_{22} & e_{32} \\ C_{31} & C_{32} & C_{33} & C_{34} & C_{35} & C_{36} & e_{13} & e_{23} & e_{33} \\ C_{41} & C_{42} & C_{43} & C_{44} & C_{45} & C_{46} & e_{14} & e_{24} & e_{34} \\ C_{51} & C_{52} & C_{53} & C_{54} & C_{55} & C_{56} & e_{15} & e_{25} & e_{35} \\ C_{61} & C_{62} & C_{63} & C_{64} & C_{65} & C_{66} & e_{16} & e_{26} & e_{36} \\ e_{11} & e_{12} & e_{13} & e_{14} & e_{15} & e_{16} & -\epsilon_{11} & -\epsilon_{12} & -\epsilon_{13} \\ e_{21} & e_{22} & e_{23} & e_{24} & e_{25} & e_{26} & -\epsilon_{21} & -\epsilon_{22} & -\epsilon_{23} \\ e_{31} & e_{32} & e_{33} & e_{34} & e_{35} & e_{36} & -\epsilon_{31} & -\epsilon_{32} & -\epsilon_{33} \end{pmatrix} \begin{pmatrix} \varepsilon_1 = \varepsilon_{11} \\ \varepsilon_2 = \varepsilon_{22} \\ \varepsilon_3 = \varepsilon_{33} \\ \varepsilon_4 = 2\varepsilon_{23} \\ \varepsilon_5 = 2\varepsilon_{13} \\ \varepsilon_6 = 2\varepsilon_{12} \\ -E_1 \\ -E_2 \\ -E_3 \end{pmatrix}. \tag{D.3}$$

D.2. Material Tensors

In this section we give the elasticity, piezoelectric and dielectric Voigt matrices of zincblende and wurtzite semiconductors used in Chapter 3 for the study of elastic and piezoelectric properties of nanowires.

Material Tensors of the Diamond/Zincblende Structure

For crystalline materials belonging to the cubic system (crystal classes T and T_d), when referred to the crystallographic axes ($X_1 \parallel [100]$, $X_2 \parallel [010]$, $X_3 \parallel [001]$), these matrices are given by:[128]

$$C_{IK} \leftrightarrow \begin{pmatrix} C_{11} & C_{12} & C_{12} & 0 & 0 & 0 \\ C_{12} & C_{11} & C_{12} & 0 & 0 & 0 \\ C_{12} & C_{12} & C_{11} & 0 & 0 & 0 \\ 0 & 0 & 0 & C_{44} & 0 & 0 \\ 0 & 0 & 0 & 0 & C_{44} & 0 \\ 0 & 0 & 0 & 0 & 0 & C_{44} \end{pmatrix}, \tag{D.4}$$

$$e_{nI} \leftrightarrow \begin{pmatrix} 0 & 0 & 0 & e_{14} & 0 & 0 \\ 0 & 0 & 0 & 0 & e_{14} & 0 \\ 0 & 0 & 0 & 0 & 0 & e_{14} \end{pmatrix}, \tag{D.5}$$

$$\epsilon_{mn} \leftrightarrow \begin{pmatrix} \epsilon_{11} & 0 & 0 \\ 0 & \epsilon_{11} & 0 \\ 0 & 0 & \epsilon_{11} \end{pmatrix}, \tag{D.6}$$

where C_{11}, C_{12}, C_{44}, e_{14}, and ϵ_{11} are the only independent material constants. In the case of the crystal class O_h corresponding to non-piezoelectric materials, e_{14} must be taken to be zero.

If a rotated system of axes is to be used, then it is necessary to first transform accordingly the material tensors and only afterwards construct the associated Voigt matrices. This is the situation in Secs. 3.3.1 and 3.3.5, where a nanowire with $\hat{X}_3$ axis along the crystallographic direction [111] is studied. For that purpose it is convenient to employ a new system of axes ($\hat{X}_1 \parallel [10\bar{1}]$, $\hat{X}_2 \parallel [\bar{1}2\bar{1}]$, $\hat{X}_3 \parallel [111]$). The rotation matrix leading to this new reference frame is:

$$R = \begin{pmatrix} \frac{1}{\sqrt{2}} & 0 & -\frac{1}{\sqrt{2}} \\ -\frac{1}{\sqrt{6}} & \frac{2}{\sqrt{6}} & -\frac{1}{\sqrt{6}} \\ \frac{1}{\sqrt{3}} & \frac{1}{\sqrt{3}} & \frac{1}{\sqrt{3}} \end{pmatrix} \quad . \tag{D.7}$$

Following the procedure outlined above, one obtains the following Voigt matrices corresponding to the rotated system of axes:

$$\hat{C}_{IK} \leftrightarrow \begin{pmatrix} \hat{C}_{11} & \hat{C}_{12} & \hat{C}_{12} & \hat{C}_{14} & 0 & 0 \\ \hat{C}_{12} & \hat{C}_{11} & \hat{C}_{12} & -\hat{C}_{14} & 0 & 0 \\ \hat{C}_{12} & \hat{C}_{12} & \hat{C}_{33} & 0 & 0 & 0 \\ \hat{C}_{14} & -\hat{C}_{14} & 0 & \hat{C}_{44} & 0 & 0 \\ 0 & 0 & 0 & 0 & \hat{C}_{44} & \hat{C}_{14} \\ 0 & 0 & 0 & 0 & \hat{C}_{14} & \hat{C}_{66} \end{pmatrix} \quad , \tag{D.8}$$

$$\hat{e}_{nI} \leftrightarrow \begin{pmatrix} 0 & 0 & 0 & 0 & \hat{e}_{15} & -\hat{e}_{22} \\ -\hat{e}_{22} & \hat{e}_{22} & 0 & \hat{e}_{15} & 0 & 0 \\ \hat{e}_{31} & \hat{e}_{31} & \hat{e}_{33} & 0 & 0 & 0 \end{pmatrix} \quad , \tag{D.9}$$

$$\hat{\epsilon}_{mn} \leftrightarrow \begin{pmatrix} \epsilon_{11} & 0 & 0 \\ 0 & \epsilon_{11} & 0 \\ 0 & 0 & \epsilon_{11} \end{pmatrix} \quad , \tag{D.10}$$

where the elements of the matrices are:

$$\hat{C}_{11} = \frac{1}{2}(C_{11} + C_{12} + 2C_{44}) \, ,$$

$$\hat{C}_{12} = \frac{1}{6}(C_{11} + 5C_{12} - 2C_{44}) \, ,$$

$$\hat{C}_{13} = \frac{1}{3}(C_{11} + 2C_{12} - 2C_{44}) \, ,$$

$$\hat{C}_{14} = \frac{1}{3\sqrt{2}}(-C_{11} + C_{12} + 2C_{44})\,,$$
$$\hat{C}_{33} = \frac{1}{3}(C_{11} + 2C_{12} + 4C_{44})\,,$$
$$\hat{C}_{44} = \frac{1}{3}(C_{11} - C_{12} + C_{44})\,,$$
$$\hat{C}_{66} = \frac{1}{2}(\hat{C}_{11} - \hat{C}_{12})\,,$$

$$\hat{e}_{15} = -\sqrt{\frac{1}{3}}\,e_{14}\,,$$
$$\hat{e}_{22} = \sqrt{\frac{2}{3}}\,e_{14}\,,$$
$$\hat{e}_{31} = -\sqrt{\frac{1}{3}}\,e_{14}\,,$$
$$\hat{e}_{33} = \sqrt{\frac{4}{3}}\,e_{14}\,.$$

Material Tensors of the Wurtzite Structure

For wurtzite materials the elasticity tensor has five independent elements, given in Voigt notation as C_{11}, C_{12}, C_{13}, C_{44} and C_{66}. For $X_3 \parallel [0001]$ the elasticity matrix takes the form[217]

$$C_{IK} \leftrightarrow \begin{pmatrix} C_{11} & C_{12} & C_{13} & 0 & 0 & 0 \\ C_{12} & C_{11} & C_{13} & 0 & 0 & 0 \\ C_{13} & C_{13} & C_{33} & 0 & 0 & 0 \\ 0 & 0 & 0 & C_{44} & 0 & 0 \\ 0 & 0 & 0 & 0 & C_{44} & 0 \\ 0 & 0 & 0 & 0 & 0 & C_{66} \end{pmatrix}\,, \tag{D.11}$$

where $C_{66} = \frac{1}{2}(C_{11} - C_{12})$ and the piezoelectric coupling matrix is of the form

$$e_{nI} \leftrightarrow \begin{pmatrix} 0 & 0 & 0 & 0 & e_{15} & 0 \\ 0 & 0 & 0 & e_{15} & 0 & 0 \\ e_{31} & e_{31} & e_{33} & 0 & 0 & 0 \end{pmatrix}\,, \tag{D.12}$$

where e_{15}, e_{31} and e_{33} are the independent piezoelectric constants. The dielectric matrix of the wurtzite structure is given by

$$\epsilon_{mn} \leftrightarrow \begin{pmatrix} \epsilon_{11} & 0 & 0 \\ 0 & \epsilon_{11} & 0 \\ 0 & 0 & \epsilon_{33} \end{pmatrix} \quad , \tag{D.13}$$

where ϵ_{11} and ϵ_{33} are the relative permittivities along the a and c axis of the wurtzite structure respectively.

D.3. Strain and Electric Field Components in Cylindrical Coordinates

Here we give the relationship between the cartesian and cylindrical components for the strain and electric fields. First we give the relationships for the strain components:

$$\begin{aligned}
\varepsilon_{rr} &= \varepsilon_{11}\ \cos^2\phi + \varepsilon_{22}\ \sin^2\phi + \varepsilon_{12}\ \sin 2\phi\,, \\
\varepsilon_{\phi\phi} &= \varepsilon_{11}\ \sin^2\phi + \varepsilon_{22}\ \cos^2\phi - \varepsilon_{12}\ \sin 2\phi\,, \\
\varepsilon_{zz} &= \varepsilon_{33}\,, \\
\varepsilon_{r\phi} &= \frac{1}{2}(\varepsilon_{22} - \varepsilon_{11})\ \sin 2\phi + \varepsilon_{12}\ \cos 2\phi\,, \\
\varepsilon_{rz} &= \varepsilon_{23}\ \sin\phi + \varepsilon_{13}\ \cos\phi\,, \\
\varepsilon_{\phi z} &= \varepsilon_{23}\ \cos\phi - \varepsilon_{13}\ \sin\phi\,,
\end{aligned}$$

and for the electric fields we have the relationship:

$$\begin{aligned}
E_r &= \quad E_1\ \cos\phi + E_2\ \sin\phi\,, \\
E_\phi &= -E_1\ \sin\phi + E_2\ \cos\phi\,, \\
E_z &= E_3\,.
\end{aligned}$$

Appendix E

Material Parameters

In this appendix we show the numerical values of the parameters used in the calculations presented in this thesis.

E.1. Parameters for Diamond/Zincblende Materials

		Si	Ge	GaAs	InAs	InN	GaN
a_0	(Å)	5.430 [218]	5.652 [218]	5.645 [186]	6.053 [186]	4.98 [186]	4.5 [186]
C_{11}	(GPa)	162.0 [219]	128.5 [219]	124.2 [220]	92.2 [220]	204.1 [220]	316.9 [220]
C_{12}	(GPa)	62.8 [219]	45.7 [219]	51.4 [220]	46.5 [220]	119.4 [220]	152.0 [220]
C_{44}	(GPa)	77.2 [219]	66.8 [219]	63.4 [220]	44.4 [220]	114.1 [220]	197.6 [220]
e_{14}	(C/m^2)	–	–	-0.20 [221]	-0.05 [221]	0.84 [220]	0.59 [221]
ϵ_{11}	(ϵ_0)	11.97 [222]	16.00 [222]	12.80 [222]	15.15 [222]	8.4 [222]	9.7 [222]

Table E.1: Lattice, elastic, piezoelectric and dielectric constants.

Parameters		GaAs	InAs	AlAs
E_p	(eV)	23.81 [22]	19.33 [22]	21.1 [186]
E_g	(eV)	1.51 [22]	0.37 [22]	3.099 [186]
Δ_0	(eV)	0.34 [22]	0.43 [22]	0.28 [186]
m_e	(m_0)	0.067 [22]	0.023 [22]	0.15 [186]
γ_1		7.05 [22]	19.67 [22]	3.76 [186]
γ_2		2.33 [22]	8.37 [22]	0.82 [186]
γ_3		3.00 [22]	9.29 [22]	1.42 [186]

Table E.2: Bandstructure parameters.

Parameters		GaAs		InAs	
a_c	(eV)	-7.17	[186]	-5.08	[186]
a_v	(eV)	-1.16	[186]	-1.0	[186]
b	(eV)	-2.0	[186]	-1.8	[186]
d	(eV)	-4.8	[186]	-3.6	[186]

Table E.3: Deformation potentials.

E.2. Parameters for Wurtzite Materials

		InN		GaN		ZnO	
a_0	(Å)	3.535	[223]	3.187	[224]	3.248	[224]
c_0	(Å)	5.701	[223]	5.183	[224]	5.205	[224]
C_{11}	(GPa)	258.6	[220]	407.7	[220]	238	[225]
C_{12}	(GPa)	112.7	[220]	138.0	[220]	106	[225]
C_{13}	(GPa)	71.6	[220]	75.2	[220]	84	[225]
C_{33}	(GPa)	299.8	[220]	470.4	[220]	176	[225]
C_{44}	(GPa)	53.6	[220]	102.3	[220]	58	[225]
e_{15}	(C/m^2)	-0.43	[226]	-0.31	[226]	-0.53	[226]
e_{31}	(C/m^2)	-0.59	[226]	-0.44	[226]	-0.68	[226]
e_{33}	(C/m^2)	1.14	[226]	0.75	[226]	1.31	[226]
P_{sp}	(C/m^2)	-0.035	[226]	-0.027	[226]	-0.042	[226]
ϵ_{11}	(ϵ_0)	14.40	[227]	10.40	[227]	8.91	[228]
ϵ_{33}	(ϵ_0)	13.10	[227]	9.50	[227]	7.77	[228]

Table E.4: Lattice, elastic, piezoelectric and dielectric constants.

parameters		InN		ZnO	
E_g	(eV)	0.70	[229]	3.43	[57]
$E_{p,\perp}$	(ev)	7.04	*	10.32	*
$E_{p,z}$	(ev)	7.48	*	10.74	*
Δ_1	(eV)	0.0437	[229]	0.066	[57]
Δ_2	(eV)	-0,003167	[229]	-0.001167	
Δ_3	(eV)	-0,001967	[229]	-0.001167	
$m_{e,z}$	(m_0)	0.09	[229]	0.2460	[57]
$m_{e,\perp}$	(m_0)	0.09	[229]	0.250	[57]
A_1		-5.98	[229]	-2.743	[230]
A_2		-0.58	[229]	-0.393	[230]
A_3		5.44	[229]	2.377	[230]
A_4		-2.46	[229]	-2.069	[230]
A_5		-2.53	[229]	-2.051	[230]
A_6		-1.55	[229]	-2.099	[230]

* Numerical values of $E_{p,\perp}$ and $E_{p,z}$ are calculated using the relation given in (A.12).

Table E.5: Bandstructure parameters.

Parametrs		InN		ZnO	
a_1	(eV)	-3.5	[231]	0.84	**
a_2	(eV)	-3.5	[231]	1.67	**
D_1	(eV)	0.14	**	3.9	[232]
D_2	(eV)	1.08	**	4.13	[232]
D_3	(eV)	2.68	[230]	0.47	[230]
D_4	(eV)	-1.78	[230]	-0.84	[230]
D_5	(eV)	-2.07	[230]	-1.21	[230]
D_6	(eV)	-3.95	[230]	-1.77	[230]

** Numerical values of D_1 and D_2 are calculated values using (a_1) and (a_2) through the following expression: $a_g = a_1 - a_2$.[230]

Table E.6: Deformation potentials.

Bibliography

[1] A. S. Edelsteinm and R. S. Cammaratam. *Nanomaterials: synthesis, properties, and applications* (IOP Publishing, Bristol, 1996)

[2] H. S. Nalwa. *Handbook of Nanostructured Materials and Nanotechnology* (Academic Press, 2000)

[3] V. Shalaev and M. Moskovits. *Nanostructured materials: clusters, composites, and thin films* (American Chemical Society, Washington DC, 1997)

[4] S. G. Louie. Electronic properties, junctions, and defects of carbon nanotubes. En *Carbon Nanotubes*, págs. 113–145 (Springer Berlin Heidelberg, 2001)

[5] J. Hu, T. W. Odom, and C. M. Lieber. Chemistry and physics in one dimension: Synthesis and properties of nanowires and nanotubes. *Acc. Chem. Res.* **32**, 435–445 (1999), URL `http://dx.doi.org/10.1021/ar9700365`

[6] X. F. Duan, Y. Huang, Y. Cui, J. F. Wang, and C. M. Lieber. Indium phosphide nanowires as building blocks for nanoscale electronic and optoelectronic devices. *Nature* **409**, 66–69 (2001), URL `http://dx.doi.org/10.1038/35051047`

[7] Z. Zhang, X. Sun, M. S. Dresselhaus, J. Y. Ying, and J. Heremans. Electronic transport properties of single-crystal bismuth nanowire arrays. *Phys. Rev. B* **61**, 4850–4861 (2000), URL `http://dx.doi.org/10.1103/PhysRevB.61.4850`

[8] M. H. Huang, S. Mao, H. F. Feick, H. Yan, Y. Wu, H. Kind, E. Weber, R. Russo, and P. Yang. Room-temperature ultraviolet nanowire nanolasers. *Science* **292**, 1897–1899 (2001), URL `http://dx.doi.org/10.1126/science.1060367`

[9] M. Law, L. E. Greene, J. C. Johnson, R. Saykally, and P. Yang. Nanowire dye-sensitized solar cells. *Nature Mater.* **4**, 455–459 (2005), URL http://dx.doi.org/10.1038/nmat1387

[10] J. Wang, M. S. Gudiksen, X. Duan, Y. Cui, and C. M. Lieber. Highly polarized photoluminescence and photodetection from single indium phosphide nanowires. *Science* **293**, 1455–1457 (2005), URL http://dx.doi.org/10.1126/science.1062340

[11] E. D. Minot, F. Kelkensberg, M. Kouwen, J. A. Dam, L. P. Kouwenhoven, V. Zwiller, and M. T. Borgstrom. Single quantum dot nanowire LEDs. *Nano Lett.* **7**, 367–371 (2007), URL http://dx.doi.org/10.1021/nl062483w

[12] F. Qian, S. Gradecak, Y. Li, C. Y. Wen, and C. Lieber. Core/multishell nanowire heterostructures as multicolor, high-efficiency light-emitting diodes. *Nano Lett.* **5**, 2287–2291 (2005), URL http://dx.doi.org/10.1021/nl051689e

[13] X. F. Duan, Y. Huang, R. Agarwal, and C. M. Lieber. Single-nanowire electrically driven lasers. *Nature* **421**, 241–245 (2003), URL http://dx.doi.org/10.1038/nature01353

[14] A. M. Morales and C. M. Lieber. A laser ablation method for the synthesis of crystalline semiconductor nanowires. *Science* **279**, 208–211 (1998), URL http://dx.doi.org/10.1126/science.279.5348.208

[15] J. Johansson, K. A. Dick, P. Caroff, M. E. Messing, J. Bolinsson, K. Deppert, and L. Samuelson. Diameter dependence of the wurtzite-zincblende transition in InAs nanowires. *J. Phys. Chem. C* **114**, 3837–3842 (2010), URL http://dx.doi.org/10.1021/jp910821e

[16] D. Spirkoska, A. L. Efros, W. R. L. Lambrecht, T. Cheiwchanchamnangij, F. A. Morral, and G. Abstreiter. Valence band structure of polytypic zincblende/wurtzite GaAs nanowires probed by polarization-dependent photoluminescence. *Phys. Rev. B* **85**, 045309 (2012), URL http://dx.doi.org/10.1103/PhysRevB.85.045309

[17] A. L. Efros and W. R. L. Lambrecht. Theory of light emission polarization reversal in zincblende and wurtzite nanowires. *Phys. Rev. B* **89**, 035304 (2014), URL http://dx.doi.org/10.1103/PhysRevB.89.035304

[18] P. Redlisnski and F. M. Peeters. Optical properties of free-standing GaAs semiconductor nanowires and their dependence on the growth direction. *Phys.*

Rev. B **77**, 075329 (2008), URL http://dx.doi.org/10.1103/PhysRevB.77.075329

[19] C. L. Santos and P. Piquini. Diameter dependence of mechanical, electronic, and structural properties of InAs and InP nanowires: A first-principles study. *Phys. Rev. B* **81**, 075408 (2010), URL http://dx.doi.org/10.1103/PhysRevB.81.075408

[20] S. M. Bergin, Y. H. Chen, A. R. Rathmell, P. Charbonneau, Z. Li, and B. J. Wiley. The effect of nanowire length and diameter on the properties of transparent, conducting nanowire films. *Nanoscale* **4**, 1996–2004 (2012), URL http://dx.doi.org/10.1039/C2NR30126A

[21] B. Mandl, J. Stangl, T. Martensson, A. Mikkelsen, J. Eriksson, L. S. Karlsson, G. Bauer, L. Samuelson, and W. Seifert. Au-free epitaxial growth of InAs nanowires. *Nano Lett.* **6**, 1817–1821 (2006), URL http://dx.doi.org/10.1021/nl060452v

[22] I. Saidi, S. B. Radhia, and K. Boujdaria. Band parameters of GaAs, InAs, InP, and InSb in the 40-band k·p model. *J. Appl. Phys.* **107**, 043701 (2010), URL http://dx.doi.org/10.1063/1.3295900

[23] K. A. Dick, K. Deppert, L. S. Karlsson, L. Wallenberg, L. Samuelson, and W. Seifert. A new understanding of Au-assisted growth of III-V semiconductor nanowires. *Adv. Funct. Mater* **15**, 1603–1610 (2005), URL http://dx.doi.org/10.1002/adfm.200500157

[24] X. Zhou, S. A. Dayeh, D. Wang, and E. T. Yu. Scanning gate microscopy of InAs nanowires. *Appl. Phys. Lett.* **90**, 233118 (2007), URL http://dx.doi.org/10.1063/1.2746422

[25] H. D. Park, S. M. Prokes, M. E. Twigg, R. C. Cammarata, and A. C. Gaillo. Si-assisted growth of InAs nanowires. *Appl. Phys. Lett.* **89**, 223125 (2006), URL http://dx.doi.org/10.1063/1.2398917

[26] E. C. Heeres, E. P. A. M. Bakkers, A. L. Roest, M. Kaiser, T. H. Oosterkamp, and N. D. Jonge. Electron emission from individual indium arsenide semiconductor nanowires. *Nano Lett.* **7**, 536–540 (2007), URL http://dx.doi.org/10.1021/nl062554r

[27] L. C. Chuang, M. Moewe, C. Chase, N. P. Kobayashi, C. C. Hasnain, and S. Crankshaw. Critical diameter for III-V nanowires grown on lattice-

mismatched substrates. *Appl. Phys. Lett.* **90**, 04311 (2007), URL http://dx.doi.org/10.1063/1.2436655

[28] A. Ford, J. C. Ho, Z. Fan, O. Ergen, V. Altoe, S. Aloni, H. Razavi, and A. Javey. Synthesis, contact printing, and device characterization of Ni-catalyzed, crystalline InAs nanowires. *Nano Res.* **1**, 32–39 (2008), URL http://dx.doi.org/10.1007/s12274-008-8009-4

[29] Z. Fan, J. C. Ho, T. Takahashi, R. Yerushalmi, K. Takei, A. C. Ford, Y.-L. Chueh, and A. Javey. Toward the development of printable nanowire electronics and sensors. *Adv. Mater.* **21**, 3730–3743 (2009), URL http://dx.doi.org/10.1002/adma.200900860

[30] X. Duan, J. Wang, and C. M. Lieber. Synthesis and optical properties of gallium arsenide nanowires. *Appl. Phys. Lett.* **76**, 1116 (2000), URL http://dx.doi.org/10.1063/1.125956

[31] A. L. Roset, M. A. Verhiejen, O. Wunnicke, S. Serafi, H. Wondergem, and E. Bakkers. Position controlled epitaxial III-V nanowires on silicon. *Nanotechnology* **17**, S271–S275 (2006), URL http://stacks.iop.org/Nano/17/S271

[32] J. C. Harmand, G. Patriarche, N. Pere-Laperne, M. N. Merat-Combes, L. Travers, and F. Glas. Analysis of vapor-liquid-solid mechanism in Au-assisted GaAs nanowire growth. *Appl. Phys. Lett.* **87**, 203101 (2005), URL http://dx.doi.org/10.1063/1.2128487

[33] S. G. Ihn, J. I. Song, T. W. Kim, D. S. Leem, T. Lee, S. G. Lee, E. K. Koh, and K. Song. Morphology- and orientation-controlled gallium arsenide nanowires on silicon substrates. *Nano Lett.* **7**, 39–44 (2007), URL http://dx.doi.org/10.1021/nl0618795

[34] J. Johansson, B. A. Wacaser, K. A. Dick, and W. Seifert. Growth related aspects of epitaxial nanowires. *Nanotechnology* **17**, S355 (2006), URL http://stacks.iop.org/Nano/17/S355

[35] M. T. Borgstrom, M. A. Verheijen, G. Immink, T. Smet, and E. Bakkers. Interface study on heterostructured GaP-GaAs nanowires. *Nanotechnology* **17**, 4010–4013 (2006), URL http://stacks.iop.org/Nano/17/4010

[36] J. Noborisaka, J. Motohisa, and T. Fukui. Catalyst-free growth of GaAs nanowires by selective-area metalorganic vapor-phase epitaxy. *Appl. Phys. Lett.* **86**, 213102 (2005), URL http://dx.doi.org/10.1063/1.1935038

[37] K. Hiruma, K. Haraguchi, M. Yazawa, Y. Madokoro, and T. Katsuyama. Nanometre-sized GaAs wires grown by organo-metallic vapour-phase epitaxy. *Nanotechnology* **17**, S369–S375 (2006), URL http://dx.doi.org/10.1088/0957-4484/17/11/S23

[38] X. Dai, S. Zhang, Z. Wang, G. Adamo, H. Liu, Y. Huang, C. Couteau, and C. Soci. GaAs/AlGaAs nanowire photodetector. *Nano Lett.* **15**, 2688–2693 (2014), URL http://dx.doi.org/10.1021/nl5006004

[39] K. Peng, P. Parkinson, L. Fu, Q. Gao, N. Jiang, Y. Guo, F. Wang, H. J. Joyce, J. L. Boland, H. H. Tan, C. Jagadish, and M. B. Johnston. Single nanowire photoconductive terahertz detectors. *Nano Lett.* **15**, 206–210 (2015), URL http://dx.doi.org/10.1021/nl5033843

[40] J. Q. Wu. When group-III nitrides go infrared, new properties and perspectives. *J. Appl. Phys.* **106**, 011101 (2009), URL http://dx.doi.org/10.1063/1.3155798

[41] S. Strite and H. Morkoc. GaN, AlN, and InN - a review. *J. Vac. Sci. Technol.* **10**, 1237–1266 (1992), URL http://dx.doi.org/10.1116/1.585897

[42] A. G. Bhuiyan, A. Hashimoto, and A. Yamamoto. Indium nitride InN: A review on growth, characterization, and properties. *J. Appl. Phys.* **94**, 2779–2808 (2003), URL http://dx.doi.org/10.1063/1.1843281

[43] T. Kuykendall, P. Ulrich, S. Aloni, and P. Yang. Complete composition tunability of InGaN nanowires using a combinatorial approach. *Nat. Mater.* **6**, 951–956 (2007), URL http://dx.doi.org/10.1038/nmat2037

[44] T. Stoica, R. Meijers, R. Calarco, T. Richter, and H. Luth. MBE growth optimization of InN nanowires. *J. Cryst. Growth* **290**, 241–247 (2006), URL http://dx.doi.org/10.1016/j.jcrysgro.2005.12.106

[45] E. Calleja, M. S. Garcia, F. Sanchez, F. Calle, F. Naranjo, E. Munoz, S. Molina, A. Sanchez, F. Pacheco, and R. Garcia. Growth of III-nitrides on Si(111) by molecular beam epitaxy: Doping, optical, and electrical properties. *J. Cryst. Growth* **202**, 296–317 (1999), URL http://dx.doi.org/10.1016/S0022-0248(98)01346-3

[46] S. H. Lee, E. S. Jang, D. W. Kim, I. H. Lee, R. Navamathavan, S. Kannappan, and C. R. Lee. InN nanocolumns grown on a Si(111) substrate using Au+In solid solution by metal organic chemical vapor deposition. *Jpn. J. Appl.*

Phys. **48**, 04C141 (2009), URL http://stacks.iop.org/1347-4065/48/i=4S/a=04C141

[47] C. Chao, J. Chyi, C. Hsiao, C. Kei, S. Kuo, H. Chang, and T. Hsu. Catalyst-free growth of indium nitride nanorods by chemical beam epitaxy. *Appl. Phys. Lett.* **88**, 233111 (2006), URL http://dx.doi.org/10.1063/1.2210296

[48] T. Stoica, R. Meijers, R. Calarco, T. Richter, and H. Luth. MBE growth optimization of InN nanowires. *J. Cryst. Growth* **290**, 241–247 (2006), URL http://dx.doi.org/10.1016/j.jcrysgro.2005.12.106

[49] Y. L. Chang, F. Li, A. Fatehi, and Z. T. Mi. Molecular beam epitaxial growth and characterization of non-tapered InN nanowires on Si(111). *Nanotechnology* **20**, 345203 (2009), URL http://dx.doi.org/10.1088/0957-4484/20/34/345203

[50] S. H. Yun, S. Kissinger, D. W. Kim, J. H. Cha, Y. H. Ra, and C. R. Lee. Synthesis of InN nanowires grown on droplets formed with au and self catalyst on Si(111) by using metalorganic chemical vapor deposition. *Journal of Materials Research* **25**, 1778–1783 (2010), URL http://dx.doi.org/10.1557/JMR.2010.0219

[51] J. Grandal, M. A. Sanchez-Garcia, E. Calleja, E. Luna, and A. Trampert. Accommodation mechanism of InN nanocolumns grown on Si(111) substrates by molecular beam epitaxy. *Appl. Phys. Lett.* **91**, 021902 (2007), URL http://dx.doi.org/10.1021/nl300476d

[52] S. E. Cheng, G., E. D. Turner-Evans, and M. A. Reed. Electronic properties of InN nanowires. *Appl. Phys. Lett.* **87**, 253103 (2005), URL http://dx.doi.org/10.1063/1.2141927

[53] K. Kishino, J. Kamimura, and K. Kamiyama. Near-infrared InGaN nanocolumn light-emitting diodes operated at 1.46 μm. *Appl. Phys. Express* **5**, 031001 (2012), URL http://stacks.iop.org/1882-0786/5/i=3/a=031001

[54] S. Zhao, B. Le, D. Liu, X. Liu, M. Kibria, and T. Szkopek. p-Type InN nanowires. *Nano Lett.* **13**, 55090 (2013), URL http://stacks.iop.org/1882-0786/5/i=3/a=031001

[55] B. Le, S. Zhao, N. Tran, and Z. Mi. Electrically injected near-infrared light emission from single InN nanowire p-i-n diode. *Appl. Phys. Lett.* **105**, 231124 (2014), URL http://dx.doi.org/10.1063/1.4904271

[56] J. Fan, J. Xia, P. Agus, S. Tan, S. Yu, and X. Sun. Band parameters and electronic structures of wurtzite ZnO and ZnO/MgZnO quantum wells. *J. Appl. Phys.* **99**, 013702 (2006), URL http://dx.doi.org/10.1063/1.2150266

[57] Q. Yan, P. Rinke, M. Winkelnkemper, A. Qteish, D. Bimberg, M. Scheffler, and C. G. Van de Walle. Strain effects and band parameters in MgO, ZnO, and CdO. *Appl. Phys. Lett.* **101**, 152105 (2012), URL http://dx.doi.org/10.1063/1.4759107

[58] S. Baruah and J. Dutta. ph-dependent growth of zinc oxide nanorods. *J. Crys. Growth* **311**, 2549–2554 (2009), URL http://dx.doi.org/10.1016/j.jcrysgro.2009.01.135

[59] G. C. Yi, C. Wang, and W. I. Park. ZnO nanorods: synthesis, characterization and applications. *Semiconductor Science and Technology* **20**, S22–S34 (2005), URL http://dx.doi.org/10.1088/0268-1242/20/4/003

[60] E. W. Petersen, E. M. Likovich, K. J. Russell, and V. Narayanamurti. Growth of ZnO nanowires catalyzed by size-dependent melting of Au nanoparticles. *Nanotechnology* **20**, 405603 (2009), URL url={http://stacks.iop.org/0957-4484/20/i=40/a=405603}

[61] L. N. Protasova, E. V. Rebrov, and K. L. Choy. ZnO based nanowires grown by chemical vapour deposition for selective hydrogenation of acetylene alcohols. *Catal. Sci. Technol.* **1**, 768–777 (2011), URL http://dx.doi.org/10.1039/C1CY00074H

[62] B. Liu and H. C. Zeng. Hydrothermal synthesis of ZnO nanorods in the diameter regime of 50 nm. *J. Am. Chem. Soc.* **125**, 4430–4431 (2003), URL http://dx.doi.org/10.1021/ja0299452

[63] G. An, Z. Sun, and Y. Zhang. CO_2-mediated synthesis of ZnO nanorods and their application in sensing ethanol vapor. *Journal of Nanoscience and Nanotechnolog* **125**, 1252–1258 (2011), URL http://dx.doi.org/10.1166/jnn.2011.3087

[64] Q. Wan, Q. H. Li, Y. J. Chen, T. H. Wang, X. L. He, J. P. Li, and C. L. Lin. Fabrication and ethanol sensing characteristics of ZnO nanowire gas sensors. *Appl. Phys. Lett.* **84**, 3654 (2004), URL http://dx.doi.org/10.1063/1.1738932

[65] C. S. Rout, S. H. Krishna, S. R. C. Vivekchand, A. Govindaraj, and C. N. R. Rao. Hydrogen and ethanol sensors based on ZnO nanorods, nanowires and

nanotubes. *Chem. Phys. Lett.* **418**, 586–590 (2006), URL http://dx.doi.org/10.1016/j.cplett.2005.11.040

[66] Y. Li, F. D. Valle, M. Simonnet, I. Yamada, and J. J. Delaunay. High-performance UV detector made of ultra-long ZnO bridging nanowires. *Nanotechnology* **4**, 045501 (2009), URL http://stacks.iop.org/0957-4484/20/i=4/a=045501

[67] C. Y. Lu, S. P. Chang, S. Chang, T. J. Hsueh, C. L. Hsu, Y. Z. Chiou, and I. C. Chen. A lateral ZnO nanowire UV photodetector prepared on a ZnO:Ga/glass template. *Semiconductor Science and Technology* **7**, 075005 (2009), URL http://stacks.iop.org/0268-1242/24/i=7/a=075005

[68] K. J. Chen, F. Y. Hung, S. J. Chang, and S. J. Young. Optoelectronic characteristics of UV photodetector based on ZnO nanowire thin films. *J. Alloys Compounds* **479**, 674–677 (2009), URL http://dx.doi.org/10.1016/j.jallcom.2009.01.026

[69] F. Fang, J. Futter, A. Markwitz, and J. Kennedy. UV and humidity sensing properties of ZnO nanorods prepared by the arc discharge method. *Nanotechnology* **24**, 245502 (2009), URL http://stacks.iop.org/0957-4484/20/i=24/a=245502

[70] K. Burke. Perspective on density functional theory. *J. Chem. Phys.* **136**, 150901 (2012), URL http://dx.doi.org/10.1063/1.4704546

[71] F. Ning, L. M. Tang, Y. Zhang, and K. Q. Chen. First-principles study of quantum confinement and surface effects on the electronic properties of InAs nanowires. *J. Appl. Phys.* **114**, 224304 (2003), URL http://dx.doi.org/10.1063/1.4842735

[72] S. Cahangirov and S. Ciraci. First-principles study of GaAs nanowires. *Phys. Rev. B* **79**, 165118 (2009), URL http://dx.doi.org/10.1103/PhysRevB.79.165118

[73] C. L. Santos and P. Piquini. Electronic and structural properties of InAs/InP core/shell nanowires: A first principles study. *J. Appl. Phys.* **111**, 054315 (2012), URL http://dx.doi.org/10.1063/1.3692440

[74] X. Peng and P. Logan. Electronic properties of strained Si/Ge core-shell nanowires. *Appl. Phys. Lett.* **96**, 143119 (2010), URL http://dx.doi.org/10.1063/1.3389495

[75] A. Di Carlo. Microscopic theory of nanostructured semiconductor devices: beyond the envelope-function approximation. *Semicond. Sci. Technol.* **18**, R1 (2003), URL `http://stacks.iop.org/0268-1242/18/i=1/a=201`

[76] A. Molina Sánchez, A. García-Cristóbal, A. Cantarero, A. Terentjevs, and G. Cicero. LDA + U and tight-binding electronic structure of InN nanowires. *Phys. Rev. B* **82**, 165324 (2010), URL `http://link.aps.org/doi/10.1103/PhysRevB.82.165324`

[77] M. P. Persson and A. Di Carlo. Electronic structure and optical properties of freestanding [0001] oriented GaN nanowires and nanotubes. *J. Appl. Phys.* **104**, 073718 (2008), URL `http://jap.aip.org/resource/1/JAPIAU/v104/i7`

[78] Y. M. Niquet. Effects of a shell on the electronic properties of nanowire superlattices. *Nano Lett.* **7**, 1105–1109 (2007), URL `http://dx.doi.org/10.1021/nl0629097`

[79] H. Stillinger and A. T. Weber. Computer simulation of local order in condensed phases of silicon. *Phys. Rev. B.* **31**, 5262 (1985), URL `http://journals.aps.org/prb/abstract/10.1103/PhysRevB.33.1451`

[80] J. Tersoff. Empirical interatomic potential for silicon with improved elastic properties. *Phys. Rev. B* **38**, 9908 (1998), URL `http://dx.doi.org/10.1103/PhysRevB.38.9902`

[81] W. Jung, M. Cho, and M. Zhou. Strain dependence of thermal conductivity of [0001]-oriented GaN nanowires. *Appl. Phys. Lett.* **98**, 041909 (2011), URL `http://dx.doi.org/10.1063/1.3549691`

[82] M. Hu, K. P. Giapis, J. V. Goicochea, X. Zhang, and D. Poulikakos. Significant reduction of thermal conductivity in Si/Ge core-shell nanowires. *Nano Lett.* **11**, 618–623 (2011), URL `dx.doi.org/10.1021/nl103718a`

[83] J. Chen, G. Zhang, and B. Li. Impacts of atomistic coating on thermal conductivity of germanium nanowires. *Nano Lett.* **12**, 2826–2832 (2012), URL `dx.doi.org/10.1021/nl300208c`

[84] T. C. T. Ting. *Anisotropic Elasticity: Theory and Applications* (Oxford University Press, Oxford, 1996)

[85] C. Hwu. *Anisotropic elastic plates* (Springer, New York, 2010)

[86] E. Pan. Mindlin problem for an anisotropic piezoelectric half space with general boundary conditions. *Proc. R. Soc. Lond. A* **458**, 181–208 (2002), URL http://dx.doi.org/10.1098/rspa.2001.0875

[87] E. Panand and B. Yang. Elastic and piezoelectric fields in a substrate AlN due to a buried quantum dot. *J. Appl. Phys.* **93**, 2435 (2003), URL http://dx.doi.org/10.1063/1.1542670

[88] C. Q. Chenand and J. Zhu. Bending strength and flexibility of ZnO nanowires. *Appl. Phys. Lett.* **90**, 043105 (2007), URL http://dx.doi.org/10.1063/1.2432289

[89] M. A. Schubert, S. Senz, M. Alexe, D. Hesse, and U. Gosele. Finite element method calculations of ZnO nanowires for nanogenerators. *Appl. Phys. Lett.* **92**, 122904 (2008), URL http://dx.doi.org/10.1063/1.2903114

[90] S. R. Patil and R. V. N. Melnik. Coupled electromechanical effects in II-VI group finite length semiconductor nanowires. *J. Phys. D: Appl. Phys.* **42**, 145113 (2009), URL stacks.iop.org/JPhysD/42/145113

[91] F. Boxberg, N. Søndergaard, and H. Q. Xu. Photovoltaics with piezoelectric core-shell nanowires. *Nano Lett.* **10**, 1108–1112 (2010), URL http://dx.doi.org/10.1021/nl9040934

[92] F. Boxberg, N. Søndergaard, and H. Q. Xu. Elastic and piezoelectric properties of zincblende and wurtzite crystalline nanowire heterostructures. *Adv. Mater.* **24**, 4692–4706 (2012), URL http://dx.doi.org/10.1002/adma.201200370

[93] H. T. Mengistu and A. García-Cristóbal. Electronic and optical properties of InN nanowires. *Materials science in semiconductor processing* (2016), URL http://authors.elsevier.com/sd/article/S1369800116301019

[94] V. V. R. Kishore, B. Partoens, and F. M. Peeters. Electronic structure and optical absorption of GaAs/$Al_xGa_{1-x}As$ and $Al_xGa_{1-x}As$/GaAs core-shell nanowires. *Phys. Rev. B* **82**, 235425 (2010), URL http://dx.doi.org/10.1103/PhysRevB.82.235425

[95] V. V. R. Kishore, B. Partoens, and F. M. Peeters. Electronic structure of InAs/GaSb core-shell nanowires. *Phys. Rev. B* **100**, 165439 (2010), URL http://dx.doi.org/10.1103/PhysRevB.86.165439

[96] R. Winkler. *Spin-orbit Coupling Effects in Two-Dimensional Electron and Hole Systems* (Springer, Berlin, 2003)

[97] R. M. Martin. *Electronic Structure: Basic Theory and Practical Methods* (Cambridge University Press, 2008)

[98] E. O. Kane. *Semiconductors and Semimetals Vol. 1* (Academic Press, New York, 1966)

[99] P. O. Löwdin. A note on the quantum-mechanical perturbation theory. *J. Chem. Phys.* **19**, 1396–1401 (1951), URL http://dx.doi.org/10.1063/1.1748067

[100] G. L. Bir and G. E. Pikus. *Symmetry and Strain-Induced Effects in Semiconductors* (Wiley, New York, 1974)

[101] S. L. Chuang and C. S. Chang. k·p method for strained wurtzite semiconductors. *Phys. Rev. B* **54**, 2491–2504 (1996), URL http://dx.doi.org/10.1103/PhysRevB.54.2491

[102] S. L. Chuang. *Physics of Optoelectronic Devices* (Wiley-Interscience, 1995)

[103] M. Cardona and P. Yu. *Fundamentals of Semiconductors* (Springer-Verlag, 2010)

[104] C. Cohen-Tannoudji, B. Diu, and F. Laloë. *Quantum Mechanics* (Hermann and John Wiley and Sons, 1977)

[105] E. O. Kane. Band structure of indium antimonide. *J. Phys. Chem. Solids* **1**, 249–261 (1957), URL http://dx.doi.org/10.1016/0022-3697(57)90013-6

[106] Y. M. Sirenko, J. B. Jeon, K. W. Kim, M. A. Littlejohn, and M. A. Stroscio. Envelope-function formalism for valence bands in wurtzite quantum wells. *Phys. Rev. B* **53**, 1997–2009 (1996), URL http://dx.doi.org/10.1103/PhysRevB.53.1997

[107] J. M. Luttinger and W. Kohn. Motion of electrons and holes in perturbed periodic fields. *Phys. Rev.* **97**, 869 (1955), URL http://dx.doi.org/10.1103/PhysRev.97.869

[108] G. Bastard. Superlattice band-structure in the envelope-function approximation. *Phys. Rev. B* **24**, 5693–5697 (1981), URL http://dx.doi.org/10.1103/PhysRevB.24.5693

[109] M. G. Burt. The justification for applying the effective-mass approximation to microstructures. *Journal of Physics: Condensed Matter* **4**, 6651 (1992), URL http://stacks.iop.org/0953-8984/4/i=32/a=003

[110] M. G. Burt. An exact formulation of the envelope function method for the determination of electronic states in semiconductor microstructures. *Semiconductor Science and Technology* **3**, 79 (1988), URL http://stacks.iop.org/0268-1242/2/i=7/a=012

[111] M. G. Burt. Fundamentals of envelope function theory for electronic states and photonic modes in nanostructures. *Journal of Physics: Condensed Matter* **11**, 53 (1999), URL http://stacks.iop.org/0953-8984/11/i=9/a=002

[112] Y. Zhang. Motion of electrons in semiconductors under inhomogeneous strain with application to laterally confined quantum wells. *Phys. Rev. B* **49**, 14352–14366 (1994), URL http://dx.doi.org/10.1103/PhysRevB.49.14352

[113] W. Li, X. Qian, and J. Li. Envelope function method for electrons in slowly-varying inhomogeneously deformed crystals. *Journal of Physics: Condensed Matter* **26**, 455801 (2014), URL http://dx.doi.org/10.1088/0953-8984/26/45/455801

[114] G. Bastard. *Wave Mechanics Applied to Semiconductor Heterostructures* (Halstead Press, New York, 1988)

[115] B. A. Foreman. Effective-mass hamiltonian and boundary conditions for the valence bands of semiconductor microstructures. *Phys. Rev. B* **48**, 4964–4967 (1993), URL http://dx.doi.org/10.1103/PhysRevB.48.4964

[116] R. Loudon. *The Quantum Theory of Light* (Oxford University Press, New York, 2000)

[117] J. D. Jackson. *Classical Electrodynamics* (Wiley, 1998)

[118] C. R. Bowen, H. A. Kim, P. M. Weaver, and S. Dunn. Piezoelectric and ferroelectric materials and structures for energy harvesting applications. *Energy Environ. Sci.* **7**, 25–44 (2014), URL http://dx.doi.org/10.1039/C3EE42454E

[119] B. Kumara and S. W. Kima. Energy harvesting based on semiconducting piezoelectric nanostructures. *Nano Energy* **1** (2012), URL http://dx.doi.org/10.1016/j.nanoen.2012.02.001

[120] A. Erturk, W. G. R. Vieira, C. D. Marqui, and D. J. Inman. On the energy harvesting potential of piezoaeroelastic systems. *Appl. Phys. Lett.* **96**, 184103 (2010), URL http://dx.doi.org/10.1063/1.3427405

[121] H. Takeda, M. Hagiwara, H. Noguchi, T. Hoshina, T. Takahashi, N. Kodama, and T. Tsurumi. Calcium aluminate silicate $Ca_2Al_2SiO_7$ single crystal applicable to piezoelectric sensors at high temperature. *Appl. Phys. Lett.* **102**, 242907 (2013), URL http://dx.doi.org/10.1063/1.4811163

[122] H. S. Park and P. A. Klein. Surface stress effects on the resonant properties of metal nanowires: The importance of finite deformation kinematics and the impact of the residual surface stress. *J. Mech. Phys. Solids* **56**, 3144–3166 (2008), URL http://dx.doi.org/10.1016/j.jmps.2008.08.003

[123] Z. L. Wang and J. Song. Piezoelectric nanogenerators based on zinc oxide nanowire arrays. *Science* **312**, 242–246 (2006), URL http://dx.doi.org/10.1126/science.1124005

[124] M. M. Jolandan, R. A. Bernal, I. Kuljanishvili, V. Parpoil, and H. D. Espinosa. Individual GaN nanowires exhibit strong piezoelectricity in 3D. *Nano Lett.* **312**, 970–976 (2012), URL http://dx.doi.org/10.1103/PhysRevB.54.2491

[125] J. M. Wu, C. Y. Chen, Y. Zhang, K. H. Chen, Y. Yang, Y. Hu, J. H. He, and Z. L. Wang. Ultrahigh sensitive piezotronic strain sensors based on a $ZnSnO_3$ nanowire/microwire. *Nanotechnology* **6**, 4369–4374 (2012), URL http://dx.doi.org/10.1021/nn3010558

[126] X. Xue, Y. Nie, B. He, L. Xing, Y. Zhang, and Z. L. Wang. Surface free-carrier screening effect on the output of a ZnO nanowire nanogenerator and its potential as a self-powered active gas sensor. *Nanotechnology* **24**, 225501 (2013), URL http://stacks.iop.org/0957-4484/24/i=22/a=225501

[127] S. Niu, Y. Hu, X. Wen, Y. Zhou, F. Zhang, L. Lin, S. Wang, and Z. L. Wang. Enhanced performance of flexible ZnO nanowire based room-temperature oxygen sensors by piezotronic effect. *Adv. Mater.* **25**, 3701–3706 (2013), URL http://dx.doi.org/10.1002/adma.201301262

[128] J. F. Nye. *Physical properties of crystals* (Oxford university press, New York, 1985)

[129] J. D. Eshelby. *Elastic inclusions and inhomogeneities* (North-Holland, Amsterdam, 1961)

[130] T. Mura. *Micromechanics of defects in solids* (Martinus Nijhoff, Dordrecht, 1987)

[131] H. F. Tiersten. *Linear Piezoelectric Plate Vibrations: Elements of the Linear Theory of Piezoelectricity and the Vibrations Piezoelectric Plates* (Springer, 2013.)

[132] COMSOL Multiphysics, Release 4.2a (COMSOL Inc., Maine, 2010), URL `https://www.comsol.com`

[133] P. X. Gao, J. H. Song, J. Liu, and Z. L. Wang. Nanowire piezoelectric nanogenerators on plastic substrates as flexible power sources for nanodevices. *Adv. Mater* **19**, 67–72 (2007), URL `http://dx.doi.org/10.1002/adma.200601162`

[134] J. Song, J. Zhou, and Z. L. Wang. Piezoelectric and semiconducting coupled power generating process of a single ZnO belt/wire. A technology for harvesting electricity from the environment. *Nano Lett.* **6**, 1656–1662 (2006), URL `http://dx.doi.org/10.1021/nl060820v`

[135] L. C. Dai, W. L. Guo, and C. M. She. Plane strain problem of piezoelectric solid with an elliptic inclusion. *Appl. Math. Mech.* **26**, 1615–1622 (2005), URL `http://dx.doi.org/10.1007/BF03246271`

[136] R. K. N. D. Rajapakse. Plane strain/stress solutions for piezoelectric solids. *Composites Part B* **28**, 385–396 (1997), URL `http://dx.doi.org/10.1016/S1359-8368(96)00057-1`

[137] C. F. Gao and W. X. Fan. Exact solutions for the plane problem in piezoelectric materials with an elliptic or a crack. *Int. J. Solids Struct.* **36**, 2527–2540 (1999), URL `http://dx.doi.org/10.1016/S0020-7683(98)00120-6`

[138] A. N. Cleland. *Foundations of nanomechanics: from solid-state theory to device applications* (Springer Science & Business Media, 2013)

[139] C. O. Horgan. Recent developments concerning Saint-Venant's principle: An update. *Appl. Mech. Rev* **42**, 295–303 (1989), URL `http://dx.doi.org/10.1115/1.3152414`

[140] S. G. Lekhnitskii. *Theory of elasticity of an anisotropic elastic body* (Holden-Day, San Francisco, 1963)

[141] A. H. D. Cheng, J. J. Rencis, and Y. Abousleiman. Generalized plane strain elasticity problems. *Boundary elements XVII* **42**, 167–174 (1995), URL http://dx.doi.org/10.2495/BE950201

[142] A. Kotousov and C. H. Wang. A generalized plane-strain theory for transversally isotropic plates. *Acta Mechanica* **161**, 53–64 (2003), URL http://dx.doi.org/10.1007/BF02857343

[143] S. Li and S. H. Lim. Variational principles for generalized plane strain problems and their applications. *Composites Part A* **36**, 353–365 (2005), URL http://dx.doi.org/10.1016/j.compositesa.2004.06.036

[144] A. Blazquez, V. Mantic, and F. Paris. Application of BEM to generalized plane problems for anisotropic elastic materials in presence of contact. *Engineering Analysis with Boundary Elements* **30**, 489–502 (2006), URL http://dx.doi.org/10.1016/j.enganabound.2005.07.006

[145] C. P. T. Svensson, T. Mårtensson, J. Trägårdh, C. Larsson, M. Rask, D. Hessman, L. Samuelson, and J. Ohlsson. Monolithic GaAs/InGaP nanowire light emitting diodes on silicon. *Nanotechnology* **19**, 305201 (2008), URL http://dx.doi.org/10.1088/0957-4484/19/30/305201

[146] A. F. Morral, D. Spirkoska, J. Arbiol, M. Heigoldt, J. R. Morante, and G. Abstreiter. Prismatic quantum heterostructures synthesized on molecular-beam epitaxy GaAs nanowires. *Small* **4**, 899–903 (2008), URL http://dx.doi.org/10.1002/smll.200701091

[147] M. E. Pistol and C. E. Pryor. Band structure of core-shell semiconductor nanowires. *Phys. Rev. B* **78**, 115319 (2008), URL http://dx.doi.org/10.1103/PhysRevB.78.115319

[148] M. Montazeri, M. Fickenscher, L. M. Smith, H. E. Jackson, J. Yarrison-Rice, J. H. Kang, Q. Gao, H. H. Tan, C. Jagadish, Y. Guo, J. Zou, M. E. Pistol, and C. E. Pryor. Direct measure of strain and electronic structure in GaAs/GaP core-shell nanowires. *Nano Lett.* **10**, 880–886 (2010), URL http://dx.doi.org/10.1021/nl903547r

[149] M. Ben-Ishai and F. Patolsky. A route to high-quality crystalline coaxial core/multishell Ge@ Si $(GeSi)_n$ and Si@$(GeSi)_n$ nanowire heterostructures.

Adv. Mater. **22**, 902–906 (2010), URL http://dx.doi.org/10.1002/adma.200902815

[150] B. M. Wong, F. Leonard, Q. Li, and G. T. Wang. Nanoscale effects on heterojunction electron gases in *GaN/AlGaN* core/shell nanowires. *Nano Lett.,* **11**, 3074–3079 (2011), URL http://dx.doi.org/10.1021/nl200981x

[151] D. Ferrand and J. Cibert. Strain in crystalline core-shell nanowires. *Eur. Phys. J. Appl. Phys.* **67**, 30403 (2014), URL http://dx.doi.org/10.1051/epjap/2014140156

[152] H. T. Mengistu and A. García-Cristóbal. Generalized plane strain problem: Application to heterostructure nanowires. *Proceedings of Iberian COMSOL Multiphysics conference, Malaga, Spain* págs. 94–99 (2014), URL http://iberiancomsolconference.com/wp-content/uploads/2014/09/IberianCOMSOLMultiphysicsConferenceBook2014.pdf

[153] H. T. Mengistu and A. García-Cristóbal. Generalized plane piezoelectric problem: Application to heterostructure nanowires. *Proceedings of COMSOL Multiphysics conference, Cambridge, England* (2014), URL https://www.comsol.eu/paper/download/199911/mengistu_paper.pdf

[154] L. J. Lauhon, M. S. Gudiksen, D. Wang, and C. M. Lieber. Epitaxial core shell and core multishell nanowire heterostructures. *Nature* **420**, 57–61 (2002), URL http://dx.doi.org/10.1038/nature01141

[155] R. N. Musin and X. Q. Wang. Structural and electronic properties of epitaxial core-shell nanowire heterostructures. *Phys. Rev. B* **71**, 155318 (2005), URL http://dx.doi.org/10.1103/PhysRevB.71.155318

[156] I. A. Goldthorpe, A. F. Marshall, and P. C. Mclntyre. Synthesis and strain relaxation of Ge-core/Si-shell nanowire arrays. *Nano Lett.* **8**, 4081–4086 (2008), URL http://dx.doi.org/10.1021/nl802408y

[157] Y. H. Kim, H. J. Park, K. Kim, C. S. Kim, and W. Yun. Strain distribution and interface modulation of highly lattice-mismatched InN/GaN heterostructure nanowires. *Appl. Phys. Lett.* **95**, 033112 (2009), URL http://dx.doi.org/10.1063/1.3184541

[158] K. Cui, S. Fathololoumi, M. G. Kibria, G. A. Botton, and Z. Mi. Molecular beam epitaxial growth and characterization of catalyst-free InN/$In_xGa_{1-x}N$ core/shell nanowire heterostructures on Si(111) substrates. *Nanotechnology* **23**, 085205 (2012), URL http://stacks.iop.org/Nano/23/085205

[159] P. Sangeetha, K. Jeganathan, and V. Ramakrishnan. Micro-raman investigations of InN/GaN core-shell nanowires on Si (111) substrate. *AIP Advances* **3**, 062114 (2013), URL http://dx.doi.org/10.1063/1.4811365

[160] C. W. Wu and Y. R. Wu. Thermoelectric characteristic of the rough InN/GaN core-shell nanowires. *J. Appl. Phys.* **116**, 103707 (2014), URL http://dx.doi.org/10.1063/1.4894510

[161] M. Tchernycheva, P. Lavenus, H. Zhang, A. V. Babichev, G. Jacopin, M. Shahmohammadi, F. H. Julien, R. Ciechonski, G. Vescovi, and O. Kryliouk. InGaN/GaN core shell single nanowire light emitting diodes with graphene based p contact. *Nano Lett.* **14**, 2456–2465 (2014), URL http://dx.doi.org/10.1021/nl5001295

[162] M. Gómez-Gómez, N. Garro, J. Segura-Ruiz, G. Martinez-Criado, A. Cantarero, H. T. Mengistu, A. García-Cristóbal, S. Murcia-Mascarós, C. Denker, J. Malindretos, and A. Rizzi. Spontaneous core-shell elemental distribution in In-rich $In_xGa_{1-x}N$ nanowires grown by molecular beam epitaxy. *Nanotechnology* **25**, 075705 (2014), URL http://dx.doi.org/10.1088/0957-4484/25/7/075705

[163] F. M. Morales, D. González, J. G. Lozano, R. García, S. H. Frank, V. Lebedev, V. Cimalla, and O. Ambacher. Determination of the composition of $In_xGa_{1-x}N$ from strain measurements. *Acta Materialia* **57**, 5681–5692 (2009), URL http://dx.doi.org/10.1016/j.actamat.2009.07.063

[164] A. F. Wright. Elastic properties of zinc-blende and wurtzite AlN, GaN, and InN. *J. Appl. Phys.* **82**, 2833 (1997), URL http://dx.doi.org/10.1063/1.366114

[165] Y. C. Fung and P. Tong. *Classical and Computational Solid Mechanics* (World Scientific, 2001)

[166] S. Das, A. Moitra, M. Bhattacharya, and A. Dutta. Simulation of thermal stress and buckling instability in Si/Ge and Ge/Si core/shell nanowires. *Beilstein J. Nanotechnol* **6**, 1970–1977 (2016), URL http://dx.doi.org/10.3762/bjnano.6.201

[167] J. Y. Marzin and G. Bastard. Calculation of the energy-levels in InAs/GaAs quantum dots. *Solid State Commun.* **92**, 437–442 (1994), URL http://dx.doi.org/10.1016/0038-1098(94)90524-X

[168] G. A. Baraff and D. Gershoni. Eigenfunction-expansion method for solving the quantum-wire problem - formulation. *Phys. Rev. B* **43**, 4011–4022 (1991), URL http://dx.doi.org/10.1103/PhysRevB.43.4011

[169] A. Wojs, P. Hawrylak, S. Fafard, and L. Jacak. Electronic structure and magneto-optics of self-assembled quantum dots. *Phys. Rev. B* **54**, 5604–5608 (1996), URL http://dx.doi.org/10.1103/PhysRevB.54.5604

[170] M. Grundmann, O. Stier, and D. Bimberg. InAs/GaAs pyramidal quantum dots - strain distribution, optical phonons, and electronic-structure. *Phys. Rev. B* **52**, 11969–11981 (1995), URL http://dx.doi.org/10.1103/PhysRevB.52.11969

[171] P. Matagne, J. P. Leburton, J. Destine, and G. Cantraine. Modeling of the electronic properties of vertical quantum dots by the finite element method. *Computer Modeling in Engineering & Sciences* **1**, 1–10 (2000), URL http://www.techscience.com/doi/10.3970/cmes.2000.001.001.pdf

[172] F. Gelbard and K. J. Malloy. Modeling quantum structures with the boundary element method. *Journal of Computational Physics* **172**, 19–39 (2001), URL http://dx.doi.org/10.1006/jcph.2001.6751

[173] C. G. Smith. Low-dimensional quantum devices. *Reports on Progress in Physics* **59**, 235–282 (1996), URL http://stacks.iop.org/0034-4885/59/i=2/a=003

[174] K. J. Vahala and P. C. Sercel. Application of a total-angular-momentum basis to quantum-dot band-structure. *Phys. Rev. Lett.* **65**, 239–242 (1990), URL http://dx.doi.org/10.1103/PhysRevLett.65.239

[175] P. C. Sercel and K. J. Vahala. Analytical formalism for determining quantum-wire and quantum-dot band-structure in the multiband envelope-function approximation. *Phys. Rev. B* **42**, 3690–3710 (1990), URL http://dx.doi.org/10.1103/PhysRevB.42.3690

[176] M. Altarelli, U. Ekenberg, and A. Fasolino. Calculations of hole subbands in semiconductor quantum wells and superlattices. *Phys. Rev. B* **32**, 5138–5143 (1985), URL http://dx.doi.org/10.1103/PhysRevB.32.5138

[177] C. Kittel. *Quantum Theory of Solids* (John Wiley & Sons, Inc., 1963)

[178] K. Tomioka, P. Mohan, J. Noborisaka, S. Hara, J. Motohisa, and T. Fukui. Growth of highly uniform InAs nanowire arrays by selective-area MOVPE.

J. Cryst. Growth **28**, 644–647 (2007), URL http://dx.doi.org/10.1016/j.jcrysgro.2006.10.183

[179] L. E. Froberg, W. Seifert, and J. Johansson. Diameter-dependent growth rate of InAs nanowires. *Phys. Rev. B* **76**, 153401 (2007), URL http://dx.doi.org/10.1103/PhysRevB.76.153401

[180] N. Luo, G. Liao, and H. Q. Xu. $\boldsymbol{k}\cdot\boldsymbol{p}$ theory of free-standing narrow band gap semiconductor nanowires (2016), URL http://arxiv.org/abs/1603.00811

[181] M. P. Persson and H. Q. Xu. Electronic structure of [100]-oriented free-standing semiconductor nanowires. *Nano. Lett.* **4**, 2409–2414 (2004), URL http://dx.doi.org/10.1021/nl0485049

[182] Y. M. Niquet, A. Lherbier, N. H. Quang, M. V. Fernández-Serra, X. Blase, and C. Delerue. Electronic structure of semiconductor nanowires. *Phys. Rev. B* **73**, 165319 (2006), URL http://dx.doi.org/10.1103/PhysRevB.73.165319

[183] F. Wang, H. Yu, S. Jeong, J. M. Pietryga, J. A. Hollingsworth, P. C. Gibbons, and W. E. Buhro. The scaling of the effective band gaps in indium arsenide quantum dots and wires. *ACS Nano.* **2**, 1903–1913 (2008), URL http://dx.doi.org/10.1021/nn800356z

[184] Z. Zeng, A. Petoni, C. Garoufalis, S. Baskoutas, and G. Bester. Near-band-edge exciton polarization change in ZnO nanowires. *Phys. Chem. Chem. Phys.* **17**, 1197–1203 (2015), URL http://dx.doi.org/10.1039/C4CP04551C

[185] T. M. Schmidt and R. H. Miwa. Stability and electronic confinement of free-standing InP nanowires: Ab initio calculations. *Phys. Rev. B* **72**, 193404 (2005), URL http://dx.doi.org/10.1039/C4CP04551C

[186] I. Vurgaftman, J. R. Meyer, and L. R. Ram-Mohan. Band parameters for III-V compound semiconductors and their alloys. *J. Appl. Phys.* **89**, 5815 (2001), URL http://dx.doi.org/10.1063/1.1368156

[187] W. Yi, V. Narayanamurti, H. Lu, M. A. Scarpulla, A. C. Gossard, Y. Huang, J. H. Ryou, and R. D. Dupuis. Bandgap and band offsets determination of semiconductor heterostructures using three-terminal ballistic carrier spectroscopy. *Appl. Phys. Lett.* **95**, 112102 (2009), URL http://dx.doi.org/10.1063/1.3224914

[188] J. A. Czaban, D. A. Thompson, and R. R. LaPierre. GaAs core-shell nanowires for photovoltaic applications. *Nano Lett.* **9**, 148–154 (2009), URL http://dx.doi.org/10.1021/nl802700u

[189] M. Amato, M. S. Ossicini, and R. Rurali. Band-offset driven efficiency of the doping of SiGe core-shell nanowires. *Nano Lett.* **11**, 594–598 (2011), URL dx.doi.org/10.1021/nl103621s

[190] H. Lee and H. J. Choi. Single-impurity scattering and carrier mobility in doped Ge/Si core-shell nanowires. *Nano Lett.* **10**, 2207 (2011), URL dx.doi.org/10.1021/nl101109p

[191] T. Sadowski and R. Ramprasad. Core/shell CdSe/CdTe heterostructure nanowires under axial strain. *J. Phys. Chem. C* **114**, 1773–1781 (2010), URL http://dx.doi.org/10.1021/jp907150d

[192] A. W. Adeagbo, S. Thomas, S. K. Nayak, A. Ernst, and W. Hergert. First-principles study of uniaxial strained and bent ZnO wires. *Phys. Rev. B* **89**, 195135 (2014), URL http://dx.doi.org/10.1103/PhysRevB.89.195135

[193] Y. Yang, X. H. Yan, Y. Xiao, and D. Lu. Size-dependent strain effects on electronic and optical properties of ZnO nanowires. *Appl. Phys. Lett.* **97**, 033106 (2010), URL http://dx.doi.org/10.1063/1.3464974

[194] Y. Zhang, Y. H. Wen, J. C. Zheng, and Z. Z. Zhu. Direct to indirect band gap transition in ultrathin ZnO nanowires under uniaxial compression. *Appl. Phys. Lett.* **94**, 113114 (2009), URL http://dx.doi.org/10.1063/1.3104852

[195] X. Han, L. Kou, X. Lang, J. Xia, N. Wang, R. Qin, J. Lu, J. Xu, Z. Liao, X. Zhang, X. Shan, X. Song, J. Gao, W. Guo, and Y. Dapeng. Electronic and mechanical coupling in bent ZnO nanowires. *Adv. Mater.* **21**, 44937–494 (2009), URL http://dx.doi.org/10.1002/adma.200900956

[196] Z. Y. Zhang. Strain engineering for ZnO nanowires: First principle calculations. *Physics Letters A* **378**, 1174–1179 (1996), URL http://dx.doi.org/10.1016/j.physleta.2014.02.029

[197] S. Li, Q. Jiang, and G. W. Yang. Uniaxial strain modulated band gap of ZnO nanostructures. *Appl. Phys. Lett.* **96**, 213101 (2010), URL http://dx.doi.org/10.1063/1.3435479

[198] T. Pavloudis, K. Termentzidis, P. Komninou, C. D. Latham, P. R. Briddon, and J. Kioseoglou. The influence of structural characteristics on the electronic and thermal properties of GaN/AlN core/shell nanowires. *J. Appl. Phys.* **119**, 074304 (2016), URL `http://dx.doi.org/10.1063/1.4941827`

[199] S. Yang, D. Prendergast, and J. B. Neaton. Strain-induced band gap modification in coherent core/shell nanostructures. *Nano Lett.* **10**, 3156–3162 (2010), URL `http://dx.doi.org/10.1021/nl101999p`

[200] X. Pengand and P. Logan. Electronic properties of strained Si/Ge core-shell nanowires. *J. Appl. Phys.* **10**, 143119 (2010), URL `http://dx.doi.org/10.1063/1.3389495`

[201] F. Ning, D. Wang, L. M. Tang, Y. Zhang, and K. Chen. The effects of the chemical composition and strain on the electronic properties of GaSb/InAs core-shell nanowires. *J. Appl. Phys.* **116**, 094308 (2014), URL `http://dx.doi.org/10.1111/10.1063/1.4894707`

[202] N. Liu, N. Lu, Y. X. Yao, Y. R. Li, C. Z. Wang, and K. M. Ho. Strain effects in Ge/Si and Si/Ge core/shell nanowires. *J. Phys. Chem. C* **115**, 15739–15742 (2011), URL `http://dx.doi.org/10.1021/jp110379n`

[203] Y. Zhang, D. Q. Fang, S. L. Zhang, R. Huang, and Y. H. Wen. Structural and electronic properties of ZnO/GaN heterostructured nanowires from first-principles study. *Phys. Chem. Chem. Phys.* **18**, 3097–3102 (2016), URL `http://dx.doi.org/10.1039/C5CP06564J`

[204] R. W. Shao, K. Zheng, B. Wei, Y. F. Zhang, Y. J. Li, X. D. Han, Z. Zhang, and J. Zou. Bandgap engineering and manipulating electronic and optical properties of ZnO nanowires by uniaxial strain. *Nanoscale* **6**, 493 (2014), URL `http://dx.doi.org/10.1039/C4NR00059E`

[205] C. Song, J. Wang, W. Lin, H. Mao, Q. Zhao, P. Yang, and H. Xing. Manipulation of band structures in wurtzite and zinc-blende GaAs/InAs-core-shell nanowires. *J. Appl. Phys.* **114**, 113704 (2013), URL `http://dx.doi.org/10.1063/1.4821507`

[206] E. S. Kadantsev, M. Zielinski, and P. Hawrylak. Band engineering in nanowires: Ab initio model of band edges modified by (111) biaxial strain in group IIIA-VA semiconductors. *Phys. Rev. B* **86**, 085411 (2012), URL `http://dx.doi.org/10.1103/PhysRevB.86.085411`

[207] M. X. Xiao, M. Zhao, and Q. Jiang. Intrinsic and external strains modulated electronic properties of GaN/InN core-shell nanowires. *J. Appl. Phys* **110**, 054308 (2011), URL http://dx.doi.org/10.1063/1.3630122

[208] M. Pistol and C. E. Pryor. Band structure of core−shell semiconductor nanowires. *Phys. Rev. B* **78**, 491–505 (2008), URL http://dx.doi.org/10.1103/PhysRevB.78.115319

[209] Y. M. Niquet. Electronic and optical properties of InAs/GaAs nanowire superlattice. *Phys. Rev. B* **74**, 155304 (2006), URL http://dx.doi.org/10.1103/PhysRevB.74.155304

[210] A. Schliwa, M. Winkelnkemper, and D. Bimberg. Impact of size, shape, and composition on piezoelectric effects and electronic properties of In(Ga)As/GaAs quantum dots. *Phys. Rev. B* **76**, 205324 (2007), URL http://dx.doi.org/10.1103/PhysRevB.76.205324

[211] J. Zhou, Y. Gu, P. Fei, W. Mai, Y. Gao, R. Yang, G. Bao, and Z. L. Wang. Flexable piezoelectric sensor. *Nano Lett.* **8**, 3035–3040 (2008), URL http://dx.doi.org/10.1021/nl802367t

[212] R. W. Shao, K. Zheng, B. Wei, Y. F. Zhang, Y. J. Li, X. D. Han, Z. Zhang, and J. Zou. Bandgap engineering and manipulating electronic and optical properties of ZnO nanowires by uniaxial strain. *Nanoscale* **6**, 493 (2014), URL http://dx.doi.org/10.1039/C4NR00059E

[213] B. Wei, K. Zheng, Y. Ji, Y. Zhang, Z. Zhang, and X. Han. Size-dependent bandgap modulation of ZnO nanowires by tensile strain. *Nano Lett.* **12**, 4595–459 (2012), URL dx.doi.org/10.1021/nl301897q

[214] C. R. Pidgeon and R. N. Brown. Interband magneto-absorption and faraday rotation in InSb. *Phys. Rev.* **100**, 575 (1966), URL http://link.aps.org/doi/10.1103/PhysRev.146.575

[215] H. R. Trebin, U. Rossler, and R. Ranvaud. Quantum resonances in the valence bands of zincblende semiconductors. I. theoretical aspects. *Phys. Rev. B* **20**, 686–700 (1979), URL http://dx.doi.org/10.1103/PhysRevB.20.686

[216] A. D. Andreev and E. P. O'Reilly. Theory of the electronic structure of GaN/AlN hexagonal quantum dots. *Phys. Rev. B* **62**, 15851 (2000), URL http://dx.doi.org/10.1063/1.4811365

[217] B. Sen, M. Stroscio, and M. Dutta. Piezoelectricity in wurtzite polar semiconductor nanowires: A theoretical study. *J. Appl. Phys.* **110**, 024506 (2011), URL http://dx.doi.org/10.1063/1.3603036

[218] R. R. Reeber and K. Wang. Thermal expansion and lattice parameters of group IV semiconductors. *Materials Chemistry and Physics* **46**, 259–264 (1996), URL http://dx.doi.org/10.1016/S0254-0584(96)01808-1

[219] S. Q. Wang and H. Q. Ye. Ab initio elastic constants for the lonsdaleite phases of C, Si and Ge. *J. Phys.: Condens. Matter* **15**, 5307–5314 (2003), URL http://stacks.iop.org/0953-8984/15/i=30/a=312

[220] S. Q. Wang and H. Q. Ye. First-principles study on elastic properties and phase stability of III-V compounds. *phys. stat. sol. (b)* **240**, 45–54 (2003), URL http://dx.doi.org/10.1002/pssb.200301861

[221] J. Xin, Y. Zheng, and E. Shi. Piezoelectricity of zinc-blende and wurtzite structure binary compounds. *Appl. Phys. Lett.* **91**, 112902 (2007), URL http://scitation.aip.org/content/aip/journal/apl/91/11/10.1063/1.2783279

[222] O. Madelung. *Semiconductors Data Handbook* (Springer, Berlin, 2004)

[223] K. Wang and R. R. Reeber. Thermal expansion and elastic properties of InN. *Appl. Phys. Lett.* **79**, 1602–1604 (2001), URL http://dx.doi.org/10.1111/j.1151-2916.1967.tb14964.x

[224] R. R. Reeber and K. Wang. Lattice parameters and thermal expansion of important semiconductors and their substrates. *Mat. Res. Soc. Symp. Proc.* **622**, T6.35.1 (2000), URL http://journals.cambridge.org/article_S1946427400592197

[225] S. H. Jang and S. F. Chichibu. Structural, elastic, and polarization parameters and band structures of wurtzite ZnO and MgO. *J. Appl. Phys.* **112**, 073503 (2012), URL http://dx.doi.org/10.1063/1.4757023

[226] P. Y. Prodhomme, A. Beya-Wakata, and G. Bester. Nonlinear piezoelectricity in wurtzite semiconductors. *Phys. Rev. B* **88**, 121304(R) (2013), URL http://dx.doi.org/10.1103/PhysRevB.88.121304

[227] H. Morkoç. *Handbook of Nitride Semiconductors and Devices* (Wiley-VCH Verlag GmbH, Weinheim, 2008)

[228] H. Morkoc and U. Ozgur. *Zinc Oxide: Fundamentals, Materials and Device Technology* (Wiley-VCH, 2009)

[229] A. Punya and W. R. L. Lambrecht. Valence band effective-mass hamiltonians for the group-III nitrides from quasiparticle self-consistent GW band structures. *Phys. Rev. B* **85**, 195147 (2012), URL http://dx.doi.org/10.1103/PhysRevB.85.195147

[230] Q. Yan, P. Rinke, M. Winkelnkemper, A. Qteish, D. Bimberg, M. Scheffler, and C. Walle. Band parameters and strain effects in ZnO and group-III nitrides. *Semicond. Sci. Technol.* **26**, 014037 (2011), URL http://stacks.iop.org/0268-1242/26/i=1/a=014037

[231] I. Vurgaftman and J. R. Meyer. Band parameters for nitrogen-containing semiconductors. *J. Appl. Phys.* **94**, 3675 (2003), URL http://dx.doi.org/10.1063/1.1600519

[232] J. Wrzesinski and D. , Frohlich. Two-photon and three-photon spectroscopy of ZnO under uniaxial stress. *Phys. Rev. B* **56**, 13087 (1997), URL http://dx.doi.org/10.1103/PhysRevB.56.13087

[233] T. Chen and D. Lai. An exact correspondence between plane piezoelectricity and generalized plane strain in elasticity. *Proc. R. Soc. Lond. A* **453**, 2689–2713 (1997), URL http://dx.doi.org/10.1098/rspa.1997.0143

Resumen en Castellano

Simulaciones de las Propiedades Piezoeléctricas, Electrónicas y Ópticas de Nanohilos

Los nanohilos semiconductores han atraido un interés creciente debido a sus potenciales aplicaciones en electrónica, óptica y fotónica. Un amplio rango de dispositivos fotónicos y electrónicos basados en nanohilos han sido ya demostrados, incluyendo células solares,[1] fotodetectores,[2] diodos emisores de luz,[3,4] y láseres.[5,6] Para comprender las propiedades de los nanohilos es necesario conocer su estructura electrónica. Además, es importante conocer cómo estas propiedades dependen del tamaño, estructura cristalina y orientación, y cómo se ven afectadas por las deformaciones. El objetivo de esta tesis es desarrollar modelos teóricos realistas, pero manejables desde un punto de vista computacional, para estudiar el comportamiento piezoeléctrico y las propiedades electrónicas y ópticas de los nanohilos. Hemos considerado nanohilos con la estructura de la zincblenda y de la wurtzita. En lo que respecta a la composición, hemos considerado tanto nanohilos simples (*free standing*) como estructurados radialmente en una geometría coaxial de núcleo-corteza (*core-shell*).

Propiedades Piezoeléctricas de Nanohilos

Para estudiar las propiedades piezoeléctricas de los nanohilos con geometría núcleo-corteza, hemos desarrollado un nuevo procedimiento bi-dimensional (2D) apropiado para estudiar problemas piezoeléctricos totalmente acoplados con simetría traslacional. El procedimiento está basado en la idea de que para sistemas

con una relación de aspecto grande, se puede considerar que todas las secciones transversales se encuentran en idénticas condiciones, y por tanto la deformación y el campo eléctrico dependen sólo de las coordenadas en el plano.[7] Bajo esta única hipótesis, el problema tri-dimensional (3D) original puede ser muy bien aproximado por el que hemos denominado problema piezoeléctrico plano generalizado (en inglés, *generalized plane piezoelectric*, *GPP*, *problem*).[8]. En el caso de un sistema no piezoeléctrico, el problema GPP se convierte en puramente elástico y se reduce al llamado problema de deformación plana generalizada (en inglés, *generalized plane strain*, *GPS*, *problem*). Este procedimiento es completamente general y flexible dentro del marco de las hipótesis del modelo y permite una implementación numérica eficiente para el estudio de sistemas complejos. Los cálculos numéricos se han realizado sobre una forma discretizada del problema GPP mediante el método de los elementos finitos.

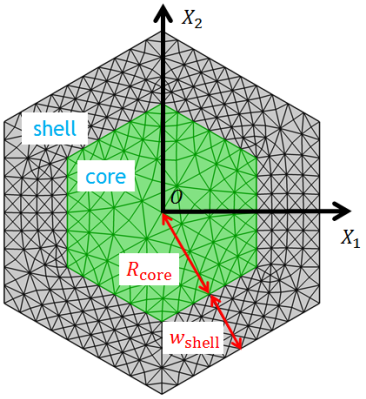

Figure E.1: Sección transversal del nanohilo con geometría núcleo-corteza estudiado, junto con el mallado empleado en los cálculos por el método de elemento finitos. La sección transversal se supone hexagonal y está caracterizada por los valores del radio del núcleo R_{core} y de la anchura de la corteza w_{shell}. El radio total del nanohilo es entonces $R_{\text{NW}} = R_{\text{core}} + w_{\text{shell}}$.

Los modelos desarrollados ha sido ilustrados estudiando las propiedades piezoeléctricas de nanohilos indefinidos constituidos por semiconductores piezoeléctricos tipo zincblenda InN(núcleo)/GaN(corteza) con desacuerdo de red. Los nanohilos están orientados a lo largo de la dirección [111]. La geometría de la sección transversal se muestra en la Fig. E.1.

En Fig. E.2 presentamos las componentes del campo, tal como se obtienen de un cálculo completo 3D, a lo largo de un eje longitudinal del nanohilo. A modo de comparación, también se indican, mediante líneas horizontales, los valores correspondientes obtenidos mediante el procedimiento GPP. En la Fig. E.2 distinguimos dos regiones. En la región central, para distancias a las superficies extremas mayores que $1.25(2R_{\text{NW}})$ (i.e., $|z| < 150$ nm), el campo es bastante uniforme a lo

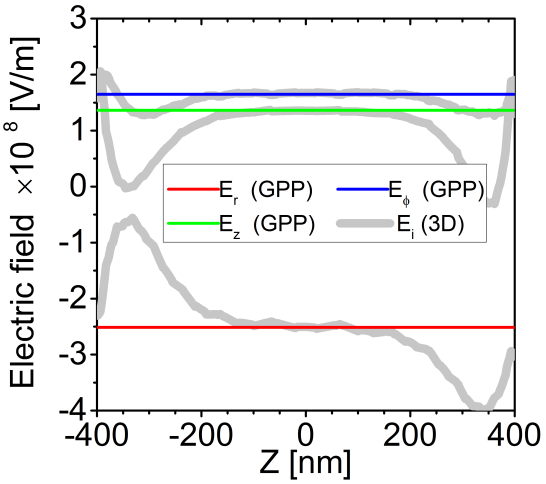

Figure E.2: Las líneas gruesas grises representan las componentes del campo eléctrico E_r, E_ϕ y E_z a lo largo de un eje longitudinal de un nanohilo finito largo que pasa a través de $(x = 0.5R_{NW}, y = 0.5R_{NW})$ tal como se obtienen a partir de los cálculos 3D. Por comparación, también se muestran como líneas horizontales los resultados correspondientes a un nanohilo infinito tal como se obtienen por medio del procedimiento GPP.

largo del eje. Por otro lado, a distancias de los extremos menores que $1.25(2R_{\mathrm{NW}})$, el campo varía considerablemente, principalmente como consecuencia del efecto de sobrerelajación de las componentes de la deformación. Los resultados para la sección transversal central del modelo finito son muy bien aproximados por los de un nanohilo infinito calculado por medio del procedimiento 2D GPP (el acuerdo en $z = 0$ es mejor del 99.3 % para E_z y mejor que 98 % para E_r y E_ϕ). Estos resultados representan una confirmación numérica de que el principio de Saint-Venant, inicialmente formulado para problemas elásticos, también funciona para el problema totalmente acoplado de un nanohilo piezoeléctrico.

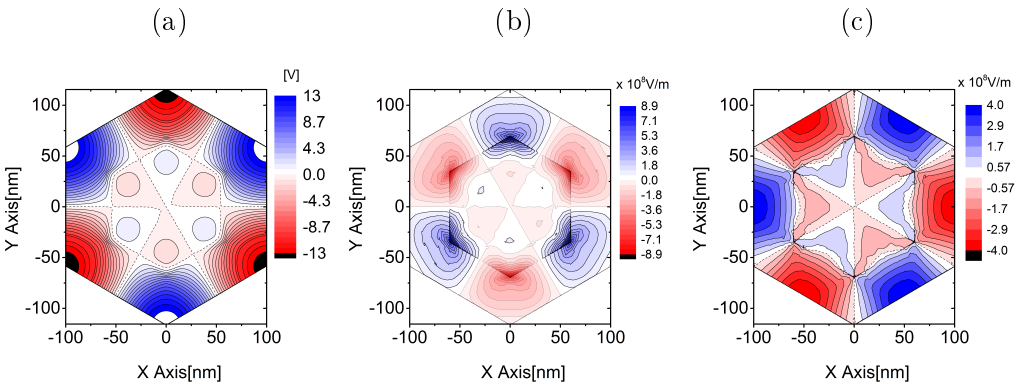

Figure E.3: Distribución en el plano de: (a) el potencial Φ, y de las componentes del campo (b) E_r y (c) E_ϕ en un nanohilo núcleo-corteza, según los cálculos del procedimiento GPP.

En la Fig. E.3 se muestra la distribución sobre el plano XY del perfil del potencial piezoeléctrico $\Phi(x, y)$ y de las componentes en el plano del campo eléctrico, para un hilo infinito modelizado usando el problema GPP. El procedimiento GPP da un campo axial $E_z = E_{\|} = 1.36 \times 10^8$ V/m, que es uniforme en toda la sección transversal. La Fig. E.3a muestra que los valores máximo/mínimo del potencial piezoeléctrico ($\pm 13.6V$) se sitúan alternadamente en las esquinas externas de la capa de GaN, mientras que el núcleo de InN se encuentra esencialmente a potencial cero. La distribución asociada del campo en el plano se muestra en Figs. E.3b y E.3c: Los valores máximos de la componente radial $E_{r,\max} = 8.95 \times 10^8$ V/m están situados en las esquinas de la intercara núcleo-corteza. Por otro lado, $E_{\phi,\max} = 3.97 \times 10^8$ V/m está localizado entre las esquinas de la superficie externa del nanohilo, .

Estructura Electrónica y Absorción Óptica de Nanohilos con Estructura Zincblenda

En esta tesis se ha utilizado el método de la función envolvente multibanda, en combinación con el Hamiltoniano $\boldsymbol{k} \cdot \boldsymbol{p}$ de ocho bandas, para estudiar la estructura electrónica de nanohilos simples (*free-standing*) y núcleo-corteza (*core shell*). Empezamos nuestra investigación con nanohilos simples de InAs orientados a lo largo de la dirección [001]. La geometría del hilo, que está alineado a lo largo del eje Z, se describe por su radio R, como se muestra en la Fig. E.4.

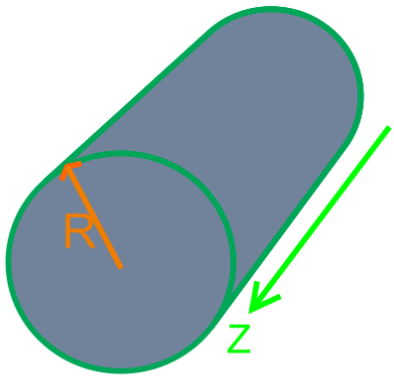

Figure E.4: Nanohilo cilíndrico simple con radio R alineado a lo largo de la dirección [001], que tomamos como eje Z.

La energía de los estados de la banda de conducción en el punto Γ aumenta monótonamente al decrecer el radio. Dichos estados tienen un carácter dominante S. Por el contrario, la dispersión con el tamaño de los estados de la banda de valencia

muestra un comporatmiento más complejo con multitud de cruces y anticruces. Las curvas de dispersión con el radio de los dos estados más altos de la banda de valencia (v_1 and v_2) se cruzan en un radio crítico R_c ∼4.6 nm como se muestra en Fig. E.5: Para nanohilos con ($R \leq R_c$), v_1 and v_2 tienen caracteres dominantes $lh(\uparrow)$ y $lh(\downarrow)$, respectivamente, mientras que intercambian ese carácter para radios mayores ($R > R_c$). En el caso de nanohilos de InAs orientados a lo largo de la direccción [111], el radio crítico del cruce adopta un valor menor de R_c ∼3.2 nm.

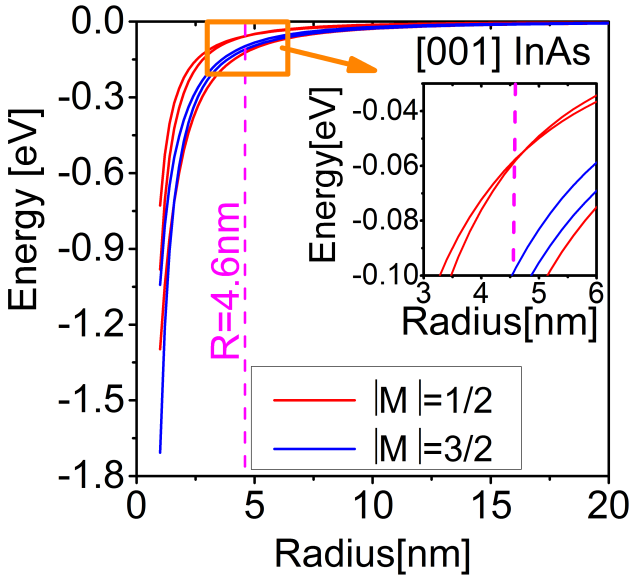

Figure E.5: Dependencia con el tamaño de los cinco estados más altos de la banda de valencia en el punto Γ. La línea vertical discontinua muestra el radio en que se cruzan las curvas asociadas a los dos primeros estados. Los estados están etiquetados según su momento angular | M |.

Las estructuras de bandas de nanohilos de [001] InAs con radios R =2.5 y 10 nm se presentan en Fig. E.6. Las subbandas están etiquetadas según su momento angular. Las subbandas de conducción en los nanohilos de InAs no son parabólicas alrededor del punto Γ debido a su acoplamiento con la banda de valencia. Las subbandas de valencia más altas del nanohilo de radio R =2.5 nm exhiben claramente una estructura de "joroba de camello"(en ingles, *camelback*) que da lugar a una masa efectiva negativa. La estructura *camelback* es más visible en los hilos de InAs más pequeños y va desapareciendo a medida que el tamaño de los hilos aumenta.

En la absorpción óptica encontramos que las transiciones ópticas alrededor del gap óptico fundamental dependen acusadamente del tamaño del nanohilo. Como resultado del comentado cruce de las curvas de dispersión con el tamaño de los dos estados más altos de la banda de valencia, para nanohilos de [001] InAs con $R \leq R_c$ la absorción óptica está polarizada a lo largo el eje del nanohilo y el gap óptico fundamental coincide exactamente con el gap de banda del nanohilo,

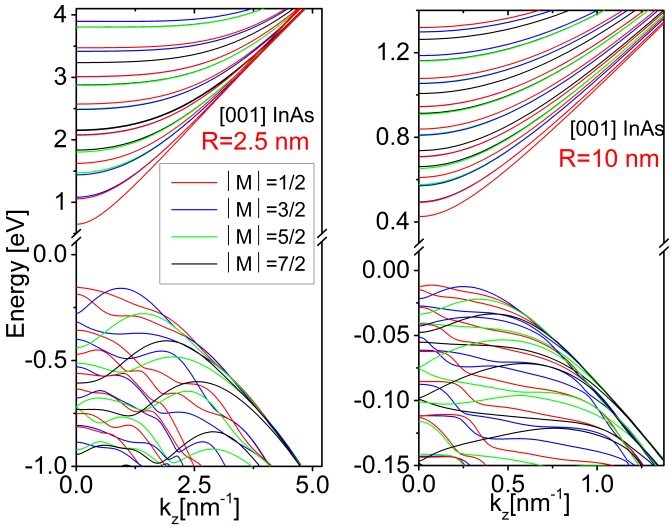

(a) (b)

Figure E.6: Estructura de subbandas de nanohilos [001] InAs con radios R=2.5 y 10 nm.

como se muestra en Fig. E.7a para el caso de radio R =2.5 nm. Sin embargo, para ($R > R_c$) el gap fundamental se desplaza hacia el azul con una separación de energía $v_2 - v_1$ con respecto al gap de banda del nanohilo (ver Fig. E.7b para nanohilos de [001] InAs con radio R =5 nm). La magnitud del desplazamiento al azul disminuye con el aumento del tamaño del nanohilo.

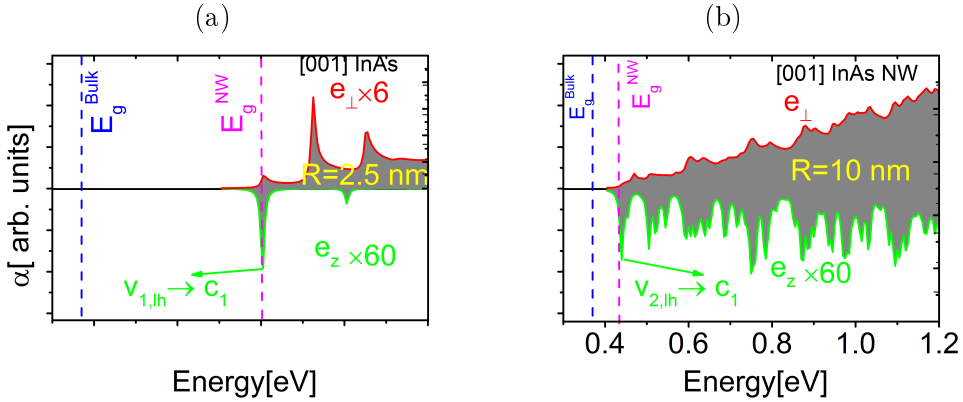

Figure E.7: Los gráficos (a) y (b) muestran la absorción óptica de los nanohilos de InAs con radio R=2.5 nm y R=10 nm, respectivamente. Las líneas discontinuas verticales roja y azul muestran el correspondiente gap fundamental los nanohilos de InAs y del cristal masivo de InAs, respectivamente.

También se han estudiado en esta tesis las propiedades electrónicas y ópticas de nanohilos núcleo-corteza con la estructura de la zincblenda. En primer lugar se ha estudiado el caso de nanohilos núcleo-corteza [111] $Al_{0.4}Ga_{0.6}As/GaAs$ con

acuerdo de red. La geometría del sistema está descrita por el radio del núcleo R_{core} y el espesor de la corteza w_{shell} (ver Fig. E.8). Encontramos que la presencia de la aleación de aluminio aumenta el gap debido al aumento de los desalineamientos de las bandas. Particularmente, el cambio en el gap de banda es mayor para dimensiones pequeñas del núcleo y la corteza, como se muestra en Fig. E.9. La presencia de la concentración de Al convierte en opticamente inactivo el estado más alto de la banda de valencia en el punto Γ, lo que resulta en un corrimiento hacia el azul de la absorción óptica polarizada axialmente.

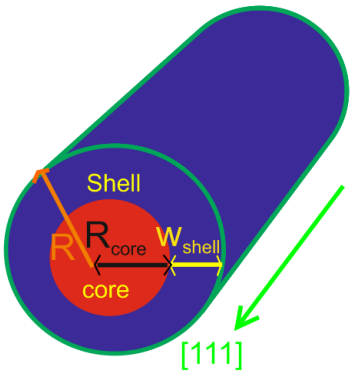

Figure E.8: Descripción geométrica de un hilo cilíndrico núcleo-corteza $Al_xGa_{1-x}As/GaAs$ con radio del núcleo R_{core} y anchura de la corteza w_{shell}. El nanohilo está orientado a lo largo de la dirección [111], que se toma como eje Z.

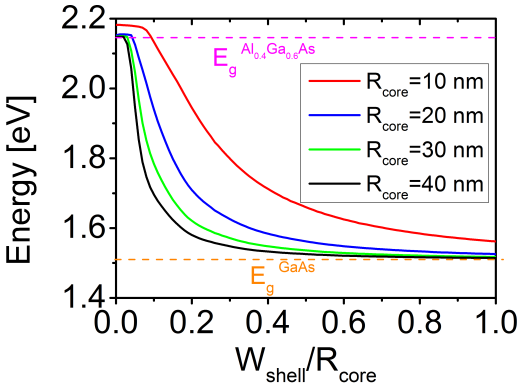

Figure E.9: Gap de banda E_g^{NW} de nanohilos núcleo-corteza $Al_{0.4}Ga_{0.6}As/GaAs$ en función del espesor de la corteza w_{shell}. Las líneas discontinuas púrpura y naranja corresponden respectivamente a los gaps de los materiales masivos $Al_{0.4}Ga_{0.6}As$ y GaAs.

También hemos considerado nanohilos núcleo-corteza GaAs/InAs con desacuerdo de red orientados en la dirección [001]. El desacuerdo de red del núcleo (InAs) respecto a la corteza (GaAS) es 6.87 %. La distribución de la deformación inducida por el desacuerdo de red en el sistema núcleo-corteza se ha obtenido haciendo uso del procedimiento GPS discutido más arriba. A continuación se han incluido

los efectos de la deformación sobre la estructura electrónica usando el Hamiltoniano Bir-Pikus. En Fig. E.10 presentamos el gap de nanohilos GaAs/InAs sin deformación y deformados en función del grosor de la corteza w_{shell} para un radio fijo del núcleo R_{core} =10 nm. Lo primero que llama la atención es que, sólo con el cambio en las dimensiones de la corteza, sin tener en cuenta la deformación intrínseca, ya se produce una variación apreciable del gap. El gap tiene valores más altos para cortezas más estrechas y decrece a medida que la corteza es más gruesa. En el caso de los nanohilos GaAs/InAs deformados, observamos una tendencia cualitativamente similar con el aumento en el espesor de la corteza, pero ahora la deformación hidrostática da lugar a una disminución apreciable del gap comparado con el caso libre de deformación. Así, globalmente el gap disinuye con el aumento del espesor de la corteza como un efecto combinado de la disminución del confinamiento y de la deformación. También observamos que el cambio en el gap de los nanohilos deformados es debido principalmente a la disminución en la energía del borde de la banda de conducción.

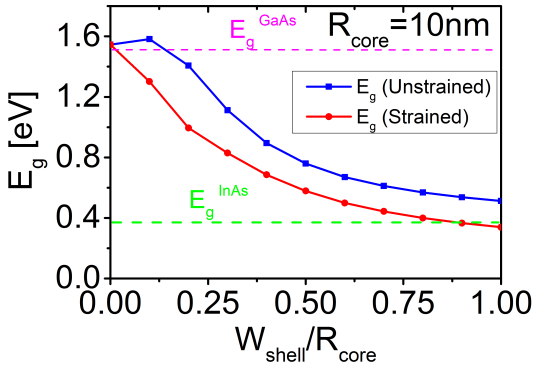

Figure E.10: Gap de los nanohilos núcleo-corteza de GaAs/InAs sin y con deformación. El radio del núcleo está fijado en $R_{\text{core}} = 10$ nm y la anchura de la corteza varía entre $1 \leq w_{\text{shell}} \leq 10$.

En Fig. E.11 presentamos la absorción óptica de los nanohilos de GaAs/InAs en función del espesor de la corteza para un radio del núcleo R_{core} =10 nm. Para w_{shell} =0, que representa el caso de un nanohilo simple de GaAs, la fuerza de oscilador de la transición $v_{1,lh} \rightarrow c_1$ es no nula, y por tanto la dirección de polarización de la absorción óptica es a lo largo de la orientación del nanohilo [001] y el gap óptico coincide con el gap fundamental del nanohilo, como se muestra en Fig. E.11(a). En contraste, la fuerza de oscilador de la transición $v_{1,lh} \rightarrow c_1$ en el nanohilo deformado GaAs/InAs (w_{shell} >0) se anula, y esa transición se hace invisible. Sin embargo, la dirección de polarización de la absorción óptica continúa siendo la dirección Z (en este caso la dirección [001]) debido a que la transición $v_{2,lh} \rightarrow c_1$ tiene una fuerza de oscilador no nula. Así, el borde de absorción fun-

damental se desplaza hacia el azul por la separación de energía $v_1 - v_2$, como se muestra en Fig. E.11(b)-(d) para $w_{\text{shell}} \geq 1$ nm. De la discusión precedente vemos que el efecto de la deformación es convertir en ópticamente inactivo al estado más alto de la banda de valencia.

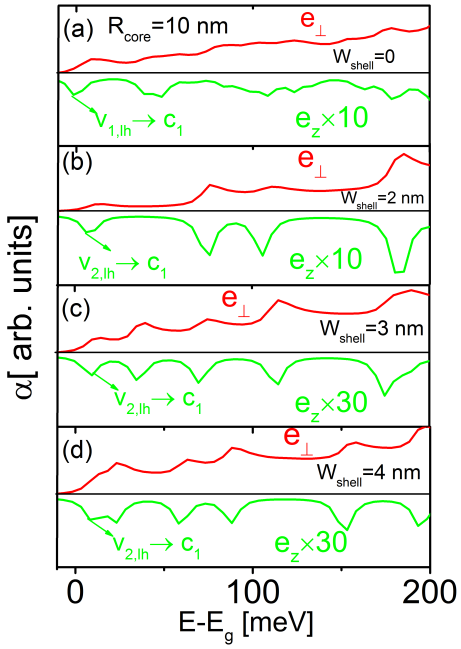

Figure E.11: Absorción óptica de nanohilos deformados núcleo-corteza de GaAs/InAs con radio del núcleo R_{core} =10 nm y anchura de la corteza w_{shell} =0-4 nm.

Estructura Electrónica y Absorción Óptica de Nanohilos con Estructura Wurtzita

En la parte final de la tesis hemos estudiado las propiedades electrónicas y ópticas de nanohilos con la estructura de la wurtzita. En los nanohilos de InN orientados a lo largo de la dirección [0001] hemos encontrado que la energía de los estados de la banda de conducción exhibe un decrecimiento monótono al aumentar el radio del nanohilo, y tienen carácter dominante S. La dispersión con el tamaño de los dos estados más altos de la banda de valencia se cruza en un radio crítico $R_c \sim 2$ nm. Este cruce no sólo resulta en un desplazamiento hacia el azul del gap óptico, como en el caso de los nanohilos de InAs, sino que va acompañado también de un cambio en la dirección de la polarización para la absorción óptica: Para nanohilos de InN con $R \leq 2$ nm, la absorción óptica está polarizada a lo largo del

eje del nanohilo y el gap óptico coincide con el gap fundamental como se muestra en Fig. E.12a para R =2 nm. Para nanohilos con 2< $R \leq$ 3nm, el gap óptico se desplaza hacia el azul aunque la absorción óptica continúa polarizada a lo largo del eje del nanohilo, como se ve en Fig. E.12b para R =2.5 nm. Por el contrario, para nanohilos de InN con R >3 nm, la absorción óptica se encuentra polarizada en el plano transversal al nanohilo como se muestra en Fig. E.12c para un nanohilo de radio R =10 nm.

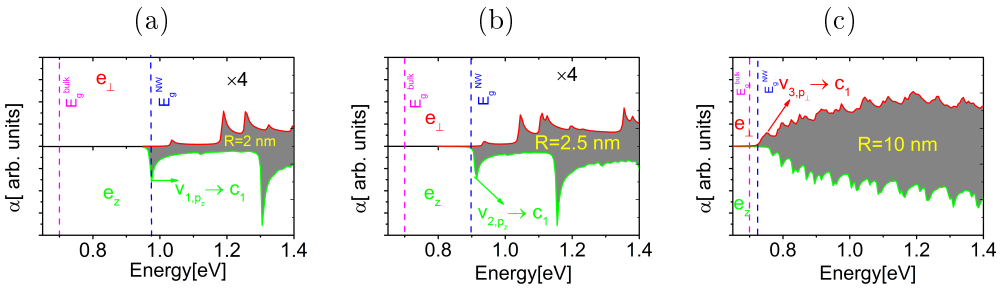

Figure E.12: Espectros de absorción óptica dependientes de la polarización para nanohilos de InN con radios (a) R=2 nm, (b) R=2.5 nm y (c) R=10 nm. En cada caso se han representado de forma separada, en los ejes verticales positivo y negativo, los espectros correspondientes a las polarizaciones $\boldsymbol{e}_\perp$ y $\boldsymbol{e}_z$, respectivamente. Las líneas verticales azul y roja marcan el gap del correspondiente nanohilo y del cristal masivo de InN, respectivamente.

Finalmente, investigamos el caso de nanohilos de ZnO tensionados uniaxialmente. En este caso, los gaps muestran una relación lineal con la tensión aplicada: la tensión compresiva aumenta el gap mientras que la tensión extensiva lo disminuye. En la absorción óptica encontramos una tensión crítica mínima en que la dirección de polarización puede ser cambiada de $\boldsymbol{e}_z$ a $\boldsymbol{e}_\perp$ y viceversa, dependiendo del tamaño del nanohilo. Así, aplicando tensión extensiva, más allá de un valor crítico, se cambia la dirección de polarización para nanohilos con $R \leq$ 2 nm de $\boldsymbol{e}_z$ hacia $\boldsymbol{e}_\perp$, como se muestra en Figs. E.13(a) y (b) para nanohilos de ZnO con R =1.4 nm bajo una tensión de $F = 0$ y $F = 20$ GPa, respectivamente. Por el contrario, para nanohilos con R >2 nm, al aplicar una tensión compresiva más allá del valor crítico, se cambia la dirección de polarización de la absorción óptica de $\boldsymbol{e}_\perp$ a $\boldsymbol{e}_z$ (ver Figs. E.13(c) y (d) para $R = 5$ nm bajo tensión $F = 0$ y $F = -20$ GPa, respectivamente). La magnitud de la tensión crítica requerida depende mucho del tamaño de los nanohilos de ZnO.

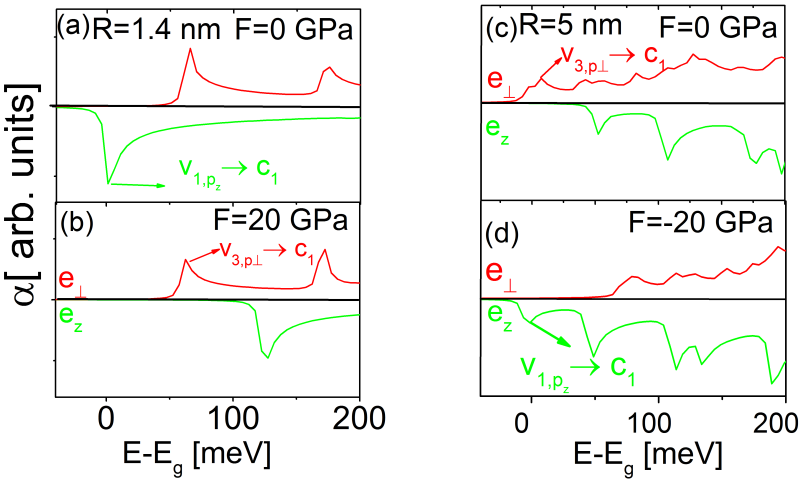

Figure E.13: Espectro de absorción óptica dependiente de la polarización de los nanohilos de ZnO bajo una tensión uniaxial de (a) $F = 0$ GPa y (b) $F = 20$ GPa, para radio R =1.4, y (c) $F = 0$ GPa y (b) $F = -20$ GPa, para radio R =5 nm. En cada caso se han representado separadamente, en los ejes verticales positivo y negativo, los espectros correspondientes a las polarizaciones $\boldsymbol{e}_\perp$ y $\boldsymbol{e}_z$, respectivamente.

Conclusiones

En esta tesis hemos estudiado primero los campos piezoeléctricos en nanohilos y luego hemos explorado los efectos del tamaño, orientación y deformación sobre sus propiedades electrónicas y ópticas. Los resultados concretos obtenidos se resumen a continuación:

- Desarrollo de un modelo bidimiensional de elementos finitos, general, flexible y computacionalmente eficiente, para estudiar las propiedades piezoeléctricas de nanohilos con geometría núcleo-corteza.

- Investigación de la dependencia con el tamaño y la orientación ([001] y [111]) de las propiedades electrónicas y ópticas de nanohilos con la estructura de la zincblenda (InAs y GaAs).

- Investigación de las propiedades electrónicas y ópticas de nanohilos con la estructura de la zincblenda y con geometría núcleo-corteza en los casos en que hay un acuerdo de red entre ambos materiales ([111] $Al_xGa_{1-x}As$/GaAs) y cuando hay un desacuerdo importante ([001] GaAs/InAs).

- Investigación de las propiedades electrónicas y ópticas de nanohilos con la estructura de la wurtzita (InN) orientados a lo largo de la dirección [0001].

- Investigación de la dependencia con la tensión uniaxial de las propiedades electrónicas y ópticas de nanohilos de ZnO.

Referencias

[1] M. Law, L. E. Greene, J. C. Johnson, R. Saykally and P. Yang, Nature Mater **4**, 455-459 (2005).

[2] J. Wang, M. S. Gudiksen, X. Duan, Y. Cui and C. M. Lieber, Science **293**, 1455-1457 (2005).

[3] E. D. Minot , F. Kelkensberg, M. Kouwen, J. A. Dam, L. P. Kouwenhoven, V. Zwiller and M. T. Borgstrom, Nano Lett. **7**, 367-371 (2007).

[4] F. Qian, S. Gradecak , Y. Li, C. Y. Wen and C. Lieber, Nano Lett. **5**, 2287-2291 (2007).

[5] M. H. Huang , S. Mao, H. F. Feick, H. Yan, Y. Wu, H. Kind, E. Weber, R. Russo and P. Yang, Science **292**, 1897-1899 (2001).

[6] X. F. Duan, Y. Huang, R. Agarwal and C. M. Lieber, Nature **421**, 241-245 (2003).

[7] Liangbin Hwu, Anisotropic elastic plates (Springer, New York, 2005).

[8] T. Chen and D. Lai, Proc. R. Soc. Lond. A **453**, 2689-2713 (1997).